

AD-A268 010

MENTATION PAGE

Form Approved
OMB No. 0704-0185



ESTIMATE TO AVERAGE 10 BUS PER RESPONSE, INCLUDING THE TIME FOR REVIEWING INSTRUCTIONS, SEARCHING EXISTING DATA, AND REVIEWING THE OPERATION OF THE MACHINE. Send comments regarding this burden estimate or any other aspect of this burden to Washington Headquarters Services, Directorate for Information Operations and Reports, 1215 Jefferson Davis Highway, Suite 1204, Arlington, VA 22202-4302, and to the Office of Management and Budget, Paperwork Reduction Project (704-0185), Washington, DC 20503.

1. REPORT DATE: June 1992
3. REPORT TYPE AND DATES COVERED: THESIS/DISSERTATION

4. TITLE AND SUBTITLE: A Derivation Of The Topside Heat Flux Using Incoherent Scatter Radar Observations
5. FUNDING NUMBERS:

6. AUTHOR(S): Capt Devin James Della-Rose

7. PERFORMING ORGANIZATION NAME(S) AND ADDRESS(ES): AFIT Student Attending: Utah State University
8. PERFORMING ORGANIZATION REPORT NUMBER: AFIT/CI/CIA- 93-124

9. SPONSORING / MONITORING AGENCY NAME(S) AND ADDRESS(ES): DEPARTMENT OF THE AIR FORCE
AFIT/CI
2950 P STREET
WRIGHT-PATTERSON AFB OH 45433-7765
10. SPONSORING / MONITORING AGENCY REPORT NUMBER:

**DTIC
ELECTE
AUG 17 1993
S E D**

11. SUPPLEMENTARY NOTES:

12a. DISTRIBUTION AVAILABILITY STATEMENT: Approved for Public Release IAW 190-1
Distribution Unlimited
MICHAEL M. BRICKER, SMSgt, USAF
Chief Administration
12b. DISTRIBUTION CODE:

13. ABSTRACT (Maximum 200 words):

93-18815

14. SUBJECT TERMS:
15. NUMBER OF PAGES: 197
16. PRICE CODE:

17. SECURITY CLASSIFICATION OF REPORT:
18. SECURITY CLASSIFICATION OF THIS PAGE:
19. SECURITY CLASSIFICATION OF ABSTRACT:
20. LIMITATION OF ABSTRACT:

DISCLAIMER NOTICE



THIS DOCUMENT IS BEST QUALITY AVAILABLE. THE COPY FURNISHED TO DTIC CONTAINED A SIGNIFICANT NUMBER OF COLOR PAGES WHICH DO NOT REPRODUCE LEGIBLY ON BLACK AND WHITE MICROFICHE.

A DERIVATION OF THE TOPSIDE HEAT FLUX
 USING INCOHERENT SCATTER
 RADAR OBSERVATIONS

by

Devin James Della-Rose

A thesis submitted in partial fulfillment
 of the requirements for the degree

of

MASTERS OF SCIENCE

in

Physics
 (Upper Atmospheric Option)

Accession For	
NTIS CRA&I	<input checked="" type="checkbox"/>
DTIC TAB	<input type="checkbox"/>
Unannounced	<input type="checkbox"/>
Justification	
By	
Distribution /	
Availability Codes	
Dist	Avail and/or Special
A-1	

Approved:

DTIC QUALITY INSPECTED 3

Vincent Wickwar

 Dr. Vincent B. Wickwar
 Major Professor

Jan J. Sojka

 Dr. Jan J. Sojka
 Committee Member

W. Farrell Edwards

 Dr. W. Farrell Edwards
 Committee Member

James P. Shaver

 Dr. James P. Shaver
 Dean of Graduate Studies

UTAH STATE UNIVERSITY
 Logan, Utah

1992

Copyright Devin James Della-Rose 1992

All Rights Reserved

DEDICATION

This work is dedicated to the memory of my mother, Monema Della-Rose.

ACKNOWLEDGMENTS

This study made use of the CEDAR database at the National Center for Atmospheric Research (NCAR), which, along with the Millstone Hill and Sondre Stromfjord radars, is supported by the National Science Foundation.

This research would have been much more difficult - if not impossible - had it not been for the cooperation and support of many people. A warm "thank you" goes to the following individuals:

To Dr. Jan Sojka and Dr. Bob Schunk, for providing me with the T_e solver, and to Mike Bowline, for helping me adapt the T_e solver to the purposes of this research.

To Mr. Roy Barnes (NCAR), for all his instruction in the use of the CEDAR Data Base and its application programs. He was never too busy to help me, and I am convinced that this research would have been near impossible without his support.

To Don Thompson, Hal Lynch, and David Haroldson, for all their help in the use of the DEC computers and the UNIX command language. Thanks also goes to Don Thompson for introducing me to the plotting program used throughout most of this research.

To Ian Monson and Carolyn Vadnais, for being the best officemates a person could want. Thanks, Ian, for writing the subroutine that allowed me to keep my output files in order.

To Peter Engelmann, for providing me with the color ion convection plot.

To Dr. John Raitt and the USU Physics Department, for allowing me to use their laser printers for my output.

To Melanie Oldroyd, for producing the T_e solver flow chart and compiling my reference section.

To Dr. Bela Fejer, who helped spark my interest in aeronomy. Our discussions were always enlightening.

To my life-long friends, John Shergold, Kevin Weaver, and Mike Moore. You were always there to give me much-needed encouragement, and the times we've spent together over the last two years have been a lot of fun.

To Trey, Beth, and Kelsi Lauren Cade. No one goes looking for good friends, and so it's very special when you find them. I always looked forward to spending time with you three, and I hope we never fall out of touch. God bless you.

Immeasurable thanks go to Dr. Vincent Wickwar for being my advisor and introducing me to this topic. I really learned a tremendous amount under his guidance, and the "ground breaking" nature of the research was very exciting. Thanks, Vince, for inviting me to present my results at the two scientific conferences. It was a great time.

Finally, I would like to say a special thank you to my wife, Corinne. You always stood beside me, especially through all the stressful times. I never would have made it through these past two years without you. I love you very much.

Devin James Della-Rose

CONTENTS

	Page
DEDICATION	ii
ACKNOWLEDGMENTS	iii
LIST OF TABLES	vii
LIST OF FIGURES	x
ABSTRACT	xv
CHAPTER	
1. INTRODUCTION	1
2. ELECTRON ENERGY BALANCE	9
2.1. ELECTRON ENERGY SOURCES	9
2.2. ELECTRON ENERGY SINKS	11
2.3. ELECTRON ENERGY TRANSPORT	14
3. THE METHOD	19
3.1. TECHNIQUE DEVELOPMENT	19
3.2. FINDING THE BEST FIT	23
3.3. TESTING THE METHOD	26
3.3.1. χ^2 Convergence	26
3.3.2. Testing the Algorithm on Theoretical Data	31
3.3.3. Comparison with <i>Kofman and Wickwar</i> [1984]	31
3.3.4. Determination of the "Zero" Heat Flux	36
4. THE DATA	38
4.1. ISR THEORY	38
4.2. ISR DATA	41
4.2.1. Sondrestrom Data	49
4.2.2. Millstone Hill Data	51

5. THE RESULTS	59
5.1. SONDRESTROM DATA	59
5.2. MILLSTONE HILL DATA	78
5.3. OTHER PARAMETERS THAT AFFECT THE FIT	93
5.4. PRECISION AND ACCURACY	108
6. CONCLUSIONS	113
7. AREAS FOR FURTHER STUDY	116
REFERENCES	118
APPENDICES	120
1. ION COMPOSITION ALGORITHMS	121
2. DATA RETRIEVAL PROCEDURES	123
3. SONDRESTROM DATA	126
4. MILLSTONE HILL DATA	162

LIST OF TABLES

Table	Page
1	Locations for Figure 1 Electron Temperature Profiles 2
2	Heat Flux Key for Figure 1 2
3	IS Radar Locations 4
4	TDIM Tests 32
5	Sondrestrom Days 50
6	Millstone Hill Days 53
A3.1	Sondrestrom Heat Flux Values for 24 April 1983 127
A3.2	Sondrestrom Heat Flux Values for 18 May 1983 128
A3.3	Sondrestrom Heat Flux Values for 15 June 1983 129
A3.4	Sondrestrom Heat Flux Values for 13 July 1983 130
A3.5	Sondrestrom Heat Flux Values for 26 June 1984 131
A3.6	Sondrestrom Heat Flux Values for 27 June 1984 135
A3.7	Sondrestrom Heat Flux Values for 28 June 1984 138
A3.8	Sondrestrom Heat Flux Values for 15 January 1985 141
A3.9	Sondrestrom Heat Flux Values for 16 January 1985 142
A3.10	Sondrestrom Heat Flux Values for 17 January 1985 143
A3.11	Sondrestrom Heat Flux Values for 18 January 1985 144
A3.12	Sondrestrom Heat Flux Values for 21 March 1985 145
A3.13	Sondrestrom Heat Flux Values for 12 April 1985 146
A3.14	Sondrestrom Heat Flux Values for 22 May 1985 147

LIST OF TABLES

Table	Page
A3.15 Sondrestrom Heat Flux Values for 13 August 1985	148
A3.16 Sondrestrom Heat Flux Values for 12 November 1985	149
A3.17 Sondrestrom Heat Flux Values for 28 August 1986	150
A3.18 Sondrestrom Heat Flux Values for 1 April 1987	152
A3.19 Sondrestrom Heat Flux Values for 27 August 1987	153
A3.20 Sondrestrom Heat Flux Values for 10 November 1987	154
A3.21 Sondrestrom Heat Flux Values for 25 November 1987	156
A3.22 Sondrestrom Heat Flux Values for 15 January 1988	157
A3.23 <i>Sondrestrom Heat Flux Values for 17 March 1988</i>	<i>158</i>
A4.1 Millstone Hill Heat Flux Values for 15 January 1985	163
A4.2 Millstone Hill Heat Flux Values for 16 January 1985	164
A4.3 Millstone Hill Heat Flux Values for 17 January 1985	165
A4.4 Millstone Hill Heat Flux Values for 20 March 1985	167
A4.5 Millstone Hill Heat Flux Values for 23 April 1985	169
A4.6 Millstone Hill Heat Flux Values for 21 May 1985	170
A4.7 Millstone Hill Heat Flux Values for 25 June 1985	171
A4.8 Millstone Hill Heat Flux Values for 1 April 1986	172
A4.9 Millstone Hill Heat Flux Values for 2 April 1986	174
A4.10 Millstone Hill Heat Flux Values for 28 August 1986	176
A4.11 Millstone Hill Heat Flux Values for 23 September 1986	178

LIST OF TABLES

Table	Page
A4.12 Millstone Hill Heat Flux Values for 24 September 1986179
A4.13 Millstone Hill Heat Flux Values for 7 October 1986181
A4.14 Millstone Hill Heat Flux Values for 8 October 1986182
A4.15 Millstone Hill Heat Flux Values for 29 October 1986183
A4.16 Millstone Hill Heat Flux Values for 30 October 1986184
A4.17 Millstone Hill Heat Flux Values for 10 December 1986186
A4.18 Millstone Hill Heat Flux Values for 11 December 1986187
A4.19 Millstone Hill Heat Flux Values for 3 June 1987189
A4.20 Millstone Hill Heat Flux Values for 25 November 1987191
A4.21 Millstone Hill Heat Flux Values for 3 February 1989192
A4.22 Millstone Hill Heat Flux Values for 9 May 1989193
A4.23 Millstone Hill Heat Flux Values for 10 May 1989194
A4.24 Millstone Hill Heat Flux Values for 20 September 1990196
A4.25 Millstone Hill Heat Flux Values for 18 December 1990197

LIST OF FIGURES

Figure	Page
1	Altitude profiles of electron temperature (K) at six geomagnetic locations for different heat fluxes at the upper boundary 2
2	Locations of present and former, middle and high latitude IS radars 4
3	Geomagnetic conjugate region heating by photoelectrons 6
4	Schematic diagram of the process acting within a SAR arc 6
5	Schematic diagram of the main features of the coulomb collision mechanism of SAR arc formation 7
6	Electron energy loss rate profiles for Sondrestrom 24 April 1983 at 1729UT (1429LT) 12
7	Electron energy loss rate profiles for Sondrestrom 17 March 1988 at 0121UT (2221LT) 13
8	An example of a solar EUV volume heating rate profile used in the T_e algorithm 21
9	Flow chart showing the inputs and outputs of the T_e solver 22
10	Sondrestrom T_e , T_i , and N_e data for 21 March 1985 at 1759UT (1459LT) 25
11	Convergence contour plot for Sondrestrom on 24 April 1983 at 0558UT (0258LT) 27
12	Cross section of Figure 11 for $Q_e \approx 1$ 28
13	Convergence contour plot for Sondrestrom on 21 March 1985 at 1311UT (1011LT) 29
14	Cross section of Figure 13 for $Q_e \approx 1$ 30
15	Results of TDIM test #1 33
16	Results of TDIM test #2 34

LIST OF FIGURES

Figure	Page
17 Sondrestrom T_e , T_i , and N_e data for 24 April 1983 at 1346UT (1046LT)	35
18 Heat flux versus height for Sondrestrom on 24 April 1983 at 1346UT (1046LT)	37
19 Sketch of the ion component of the incoherent scatter spectrum	40
20(a) Sondrestrom T_e , T_i , and N_e data for 17 January 1985 at 1308UT (1008LT)	43
20(b) Heat flux versus height for the calculated $T_e(h)$ profile of Figure 20(a)	44
21(a) Sondrestrom T_e , T_i , and N_e data for 17 March 1988 at 2005UT (1705LT)	45
21(b) Heat flux versus height for the calculated $T_e(h)$ profile of Figure 21(a)	46
22(a) Sondrestrom T_e , T_i , and N_e data for 24 April 1983 at 1346UT (1046LT)	47
22(b) Heat flux versus height for the calculated $T_e(h)$ profile of Figure 22(a)	48
23 Heat flux versus time for 17 March 1988 at Sondrestrom	52
24 Raw and corrected N_e profiles for 1 April 1986 at 1505UT (1005LT)	56
25 Convolution of the final N_e profile (from Figure 24) with a 96 km long square pulse	57
26 Downward heat flux versus date for the Sondrestrom days analyzed (see Table 5)	60

LIST OF FIGURES

Figure		Page
27	Scatter plot of heat flux versus $F_{10.7}$ for the Sondrestrom days analyzed (see Table 5)	61
28	Scatter plot of heat flux versus A_p for the Sondrestrom days analyzed (see Table 5)	63
29	Scatter plot of heat flux versus K_p for the Sondrestrom days analyzed (see Table 5)	64
30	Downward heat flux versus time for 21 March 1985 at Sondrestrom	65
31	Heat flux versus time for 24 April 1983 at Sondrestrom	67
32(a)	Electron temperature profiles versus time for 24 April 1983 at Sondrestrom	68
32(b)	Ion temperature profiles versus time for 24 April 1983 at Sondrestrom	69
32(c)	Electron density profiles versus time for 24 April 1983 at Sondrestrom	70
33	Heat flux versus time for 28 June 1984 at Sondrestrom	72
34(a)	Electron temperature profiles versus time for 28 June 1984 at Sondrestrom	73
34(b)	Ion temperature profiles versus time for 28 June 1984 at Sondrestrom	74
34(c)	Electron density profiles versus time for 28 June 1984 at Sondrestrom	75
35	Ion convection velocities (versus invariant latitude and time) at Sondrestrom on 28 June 1984	77
36	Downward heat flux versus date for the Millstone Hill days analyzed (see Table 6)	79

LIST OF FIGURES

Figure	Page
37 Scatter plot of heat flux versus $F_{10.7}$ for the Millstone Hill days analyzed (see Table 6)	80
38 Scatter plot of heat flux versus A_p for the Millstone Hill days analyzed (see Table 6)	81
39 Scatter plot of heat flux versus K_p for the Millstone Hill days analyzed (see Table 6)	82
40 Millstone Hill heat flux data for 15 January 1985	84
41 Millstone Hill heat flux data for 16 January 1985	86
42 Millstone Hill heat flux data for 28 August 1986	87
43(a) Millstone Hill heat flux versus conjugate solar zenith angle for 20 March 1985	90
43(b) Millstone Hill heat flux versus conjugate solar zenith angle for 7 October 1986	91
43(c) Millstone Hill heat flux versus conjugate solar zenith angle for 8 October 1986	92
44(a) Sondrestrom T_e , T_i , and N_e data for 23 April 1983 at 2000UT (1700LT)	94
44(b) Same as Figure 44(a), but here the calculated T_e profile is for $Q_e = 4$	96
44(c) Same as Figure 44(a), but here we have introduced a particle precipitation energy flux of $10 \text{ erg cm}^{-2} \text{ s}^{-1}$ ($= 6.24 \times 10^{12} \text{ eV cm}^{-2} \text{ s}^{-1}$)	97
44(d) Same as Figure 44(a), but here we have reduced the MSIS90 $T_n(h)$ profile by 50 percent	98
45 Heat flux versus time for 20 September 1990 at Millstone Hill	99

LIST OF FIGURES

Figure		Page
46	Millstone Hill T_e , T_i , and N_e data for 20 September 1990 at 1620UT (1120LT)	100
47	Same as Figure 46, but here the calculated T_e profile is for $Q_e = 4$	101
48	Sondrestrom T_e , T_i , and N_e data for 28 June 1984 at 1354UT (1054LT)	103
49	Assumed ion composition profiles for the Millstone Hill (solid line) and Sondrestrom (dashed line) data reduction algorithms	105
50	Ion composition for Sondrestrom on 28 June 1984	106
51	Downward heat flux versus time for Sondrestrom on 17 March 1988	110
52	Downward heat flux versus time for Millstone Hill on 2 April 1986	111

ABSTRACT

A Derivation of the Topside Heat Flux
Using Incoherent-Scatter
Radar Observations

by

Devin J. Della-Rose, Master of Science

Utah State University, 1992

Major Professor: Dr. Vincent B. Wickwar
Department: Physics

Heat conduction plays a major role in determining the electron temperature at high altitudes. Even though the importance of heat conduction has been recognized for over 20 years, our research is the first to attempt to rigorously examine this parameter. We do this by comparing (in a least-squares sense) calculated T_e profiles (from a T_e solver provided by Drs. R.W. Schunk and J.J. Sojka) with incoherent-scatter (IS) radar T_e observations from the Sondrestrom and Millstone Hill IS radars. For Sondrestrom we analyzed 23 days between 1983 and 1988. For Millstone Hill we analyzed 25 days between 1985 and 1990. We were able to find the heat flux within an uncertainty of about \pm six percent. In addition, we found a method to determine the asymptotic value of the heat flux. We found that typical downward heat flux values vary between about 10^9 and 10^{10} eV cm⁻² s⁻¹, with extremes of 10^8 eV cm⁻² s⁻¹ (summer night at Millstone) and

$3 \times 10^{11} \text{ eV cm}^{-2} \text{ s}^{-1}$ (Sondrestrom "spike" associated with the afternoon convection reversal). The Sondrestrom heat fluxes displayed variability associated with the radar's high invariant latitude (74.2 degrees). Millstone Hill heat fluxes displayed much less of this variability (it is inside the plasmapause most of the time). We did find conjugate heating effects at Millstone; however, the heat flux enhancement due to this process (a few times $10^8 \text{ eV cm}^{-2} \text{ s}^{-1}$) is small compared to the daytime heat flux increase (due to local effects). We found that the cross-correlation between the heat flux and the solar EUV heating rate is small, i.e., the heat flux mainly determines the high altitude electron temperatures, whereas the solar EUV heating controls the low altitude T_e profile. Finally, as an "offshoot" of the heat flux research, we found a new method of determining the molecular ion concentration in the F-region.

(213 pages)

CHAPTER 1

INTRODUCTION

It is well-established that heat flow has a significant impact on the electron energy balance in the thermosphere [Banks, 1966; Hoegy and Brace, 1978; Schunk and Nagy, 1978; Kofman and Wickwar, 1984; Schunk et al., 1986; Rasmussen et al., 1988]. However, it was only 14 years ago that comparison of satellite data and theory verified the importance of electron heat flow [Hoegy and Brace, 1978]. Prior to this time, some researchers held that resolution of the electron energy balance problem depended on improving our knowledge of electron heating and cooling rates [Brace et al., 1976].

Even though heat flow is known to make a sizable contribution to thermospheric electron energy balance, few attempts have been made to rigorously examine this parameter. I note two studies that we will return to in later chapters. The first is Kofman and Wickwar [1984], who examined high electron temperatures at the Sondrestrom Incoherent Scatter Radar (ISR). Second is Rasmussen et al. [1988], who compared ISR electron temperature data with ionospheric model predictions. Aside from these two papers, most of the thermospheric heat flow research has remained theoretical. In other words, journal publications will show how heat conduction affects theoretical electron temperature (T_e) profiles. For example, Schunk and Walker [1973] showed the important role that heat flux plays in determining the electron temperature profile. In a more recent example, Schunk et al. [1986] examined T_e versus height for six different magnetic locations (see Figure 1 and Table 1). For each location, the electron temperature profile is computed for six different values of heat flux (see Table 2). The dimensions of heat flux are energy per area per time. Heat flux is a vector; however, as we will see in

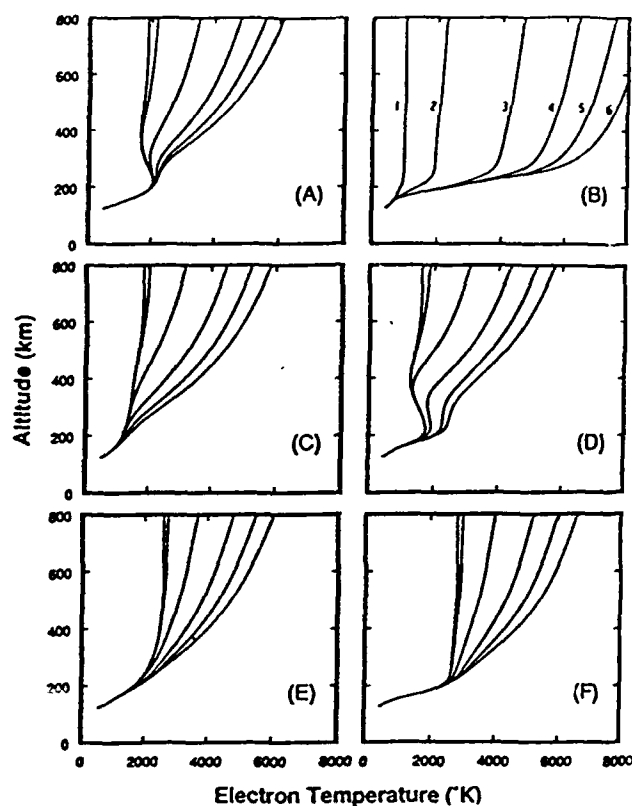


Fig. 1. Altitude profiles of electron temperature (K) at six geomagnetic locations for different heat fluxes at the upper boundary. The profiles are for 1700UT. The locations are given in Table 1 and the heat fluxes in Table 2 [Schunk *et al.*, 1986].

TABLE 1. Locations for Figure 1 Electron Temperature Profiles

Panel in Figure 9	Magnetic Coordinates		
	MLT	Latitude	Description
A	1100	44°	dayside, mid-latitude
B	0300	47°	night sector trough
C	0400	71°	morning sector oval
D	1200	80°	poleward of cusp
E	1900	71°	old hot spot
F	1600	65°	new hot spot

TABLE 2. Heat Flux Key for Figure 1

Curve Label	Heat Flux, $eV\ cm^{-2}\ s^{-1}$
1	0
2	-1.0E9*
3	-1.0E10
4	-3.0E10
5	-5.0E10
6	-7.0E10

*1.0E9 = 1.0×10^9 .

chapter two, we have a one-dimensional situation. The vector is thus represented by a positive number (upward heat flow) or by a negative number (downward heat flow). Notice how curve one (no heat flux) results in an almost isothermal temperature profile above about 200 kilometers, whereas a strong heat flux results in a significant positive temperature gradient ($\partial T/\partial z > 0$) throughout the altitude range of the graph. Again, the Schunk paper illustrates the importance of heat flux on a purely theoretical level. The next logical step is to combine theory with temperature data in order to derive the heat flux in real situations. Deriving the heat flux from ISR data is difficult, since it requires the first and second height derivatives of electron temperature. *Kofman and Wickwar* [1984] estimated the heat flux at a few altitudes using only ISR data and a simplified version of the electron energy equation (for a pure plasma). One cannot proceed any further without computer modelling for the derivatives. Again, scant progress has been made along these lines.

My research combines model calculations with data in an effort to derive the heat flux into the topside ionosphere. This method (to be described in chapter three) has never been used before. I applied the method to data from the Sondrestrom and Millstone Hill incoherent-scatter (IS) radars; however, this technique will eventually be applied to a large body of data from several IS radars. Figure 2 shows the location of these radars. Table 3 gives additional information about the location and coverage of these radars. As can be seen, analysis of temperature data from these radars allows us to study the heat flux in distinct geophysical regions: cusp and cleft, polar cap, auroral zone, trough, and plasmasphere. Additionally, we can study how the heat flux depends on factors such as

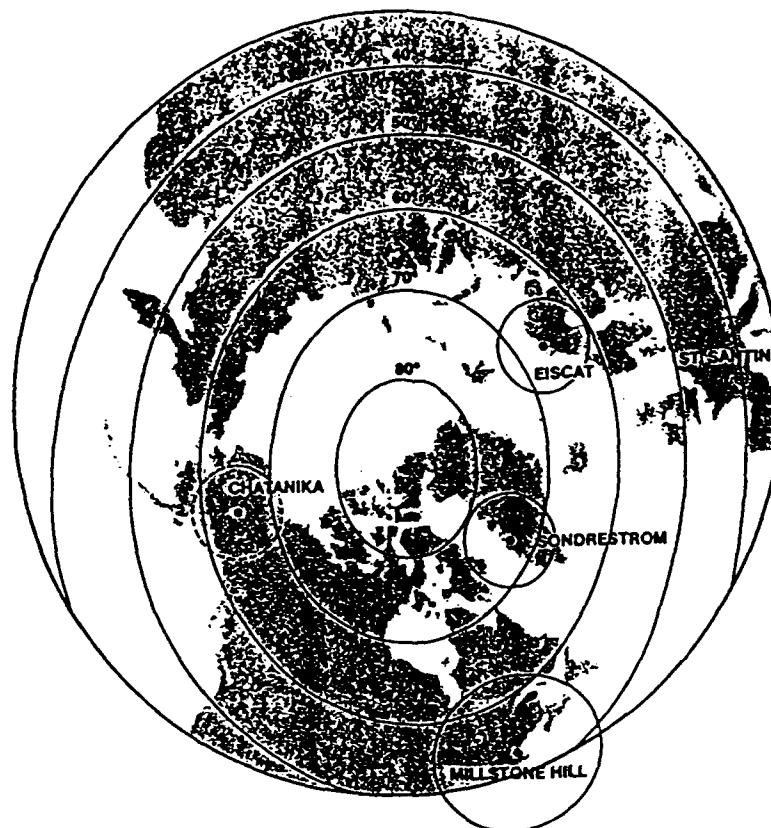


Fig. 2. Locations of present and former, middle and high latitude IS radars. Approximate F-region fields of view are indicated along with the land masses and invariant latitudes. Chatanika and St. Santin are no longer operating [Wickwar, 1991].

TABLE 3. IS Radar Locations

INCOHERENT-SCATTER RADARS				
RADAR	NORTH LATITUDE	EAST LONGITUDE	INVARIANT LATITUDE	REGION
<i>Sondrestrom</i>	67.0	-51.0	74.2	Nighttime—Polar Cap Daytime—Auroral
<i>EISCAT (Tromso)</i>	69.6	19.2	66.8	Nighttime—Auroral Daytime—Mid Latitude
<i>Millstone Hill</i>	42.6	-71.5	55.0	Mid Latitude
<i>Arecibo</i>	18.3	-66.8	34.4	Lower Mid Latitude
<i>Jicamarca</i>	-11.9	-76.0	17.8	Equatorial
<i>Chatanika</i>	65.1	-147.4	65.6	Nighttime—Auroral Daytime—Mid Latitude
<i>St. Santin</i>	44.6	2.2	42.3	Mid latitude

season, magnetic activity, conjugate photoelectrons, and solar cycle. All of these results will be new. The main goal of this research is to learn about the heat flux and its variations. In the process we expect to learn more about the volume heating rate model that is built into the T_e algorithm. Having examined both of these, we will have developed a technique that will allow us to better use ISR $T_e(h)$ observations as a diagnostic tool, and we will be in a position to better specify electron heat fluxes to be used in model calculations.

At this point, one may well wonder about the various energy sources for topside ionospheric heat flow. There are many possibilities, but I will only mention three of them here. The first possibility is that, at high latitudes, local field lines may be connected to regions of the magnetosphere with hot electron populations. There will be heat conduction from these regions into the local ionosphere. The second involves *conjugate point heating* (see Figure 3). Each geomagnetic field line connects to the earth at two points. For a given field line these two points are called *conjugate points*. Because of the tilt of the geographic and geomagnetic axes (relative to each other and to the ecliptic plane), certain conjugate points (at certain times of the year) will not be sunlit at the same time. Solar input in the sunlit region can then result in energetic photoelectrons that travel along field lines and deposit energy in the conjugate hemisphere [Carlson, 1966]. These photoelectrons also deposit energy in the flux tube between the two ends of the field line. Another energy source is the stable auroral red (SAR) arc [Rees and Roble, 1975; Kozyra et al., 1987]. During the main phase of a geomagnetic storm, high energy ring current plasma will interact with the relatively cold, plasmaspheric plasma (Figures

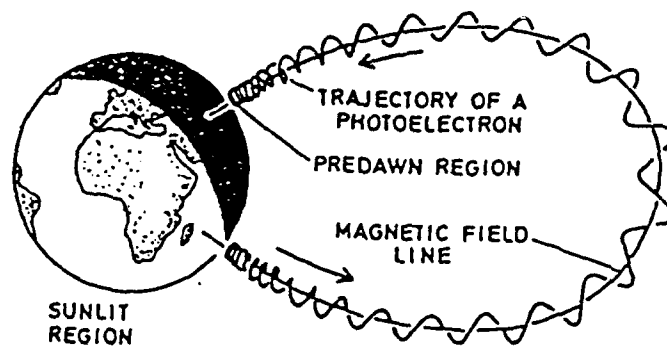


Fig. 3. Geomagnetic conjugate region heating by photoelectrons [Banks and Kockarts, 1973].

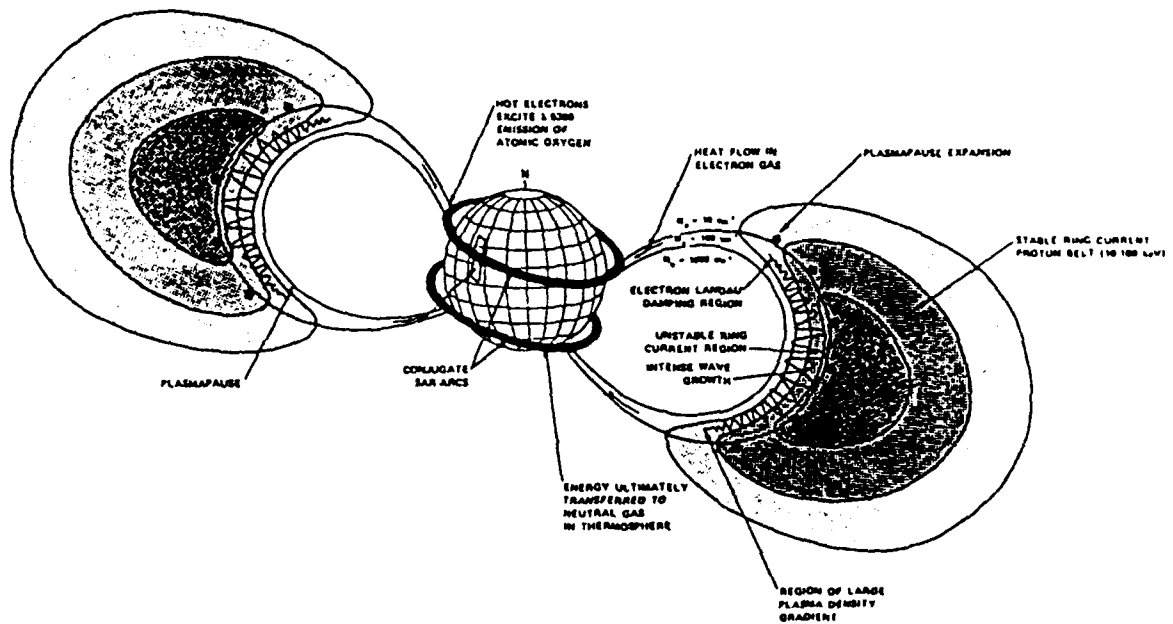
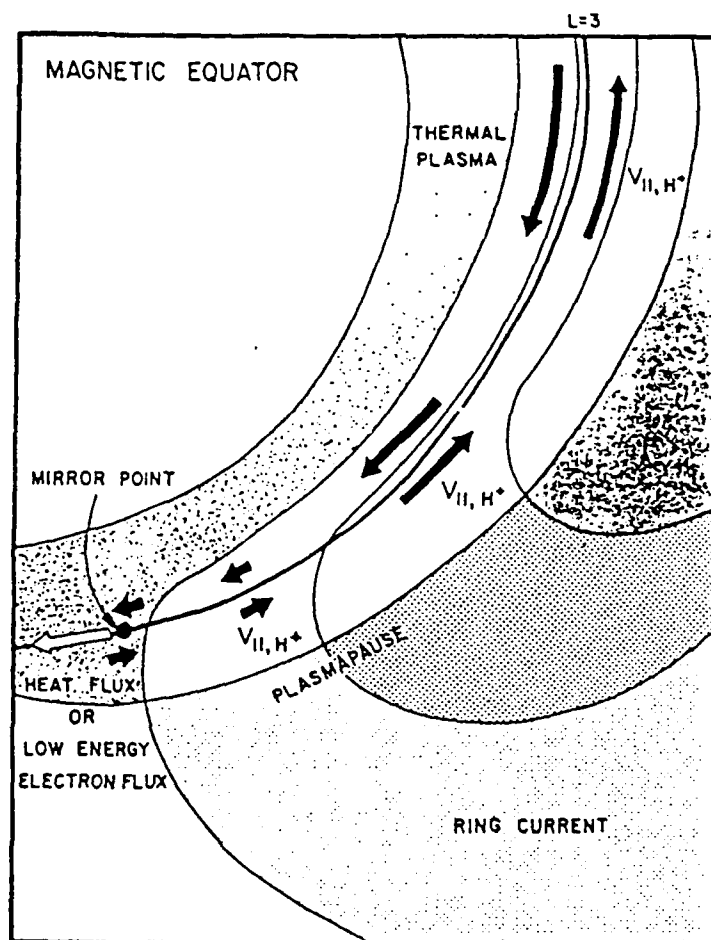


Fig. 4. Schematic diagram of the process acting within a SAR arc [Rees and Roble, 1975].



COULOMB COLLISIONS

Fig. 5. Schematic diagram of the main features of the coulomb collision mechanism of SAR arc formation. The only change between this graph and present-day theory is the fact that O^+ ions play an important role in the ring current (this graph shows only H^+ ions in the ring current).

4 and 5). Energy is transferred from the ring current plasma to the plasmaspheric plasma via coulomb collisions. Energy from the heated electrons then conducts downward (along field lines) into the topside ionosphere, setting up an electron temperature gradient ($\partial T_e / \partial z > 0$).

In chapter two we will examine electron energy balance in the thermosphere. Chapter three will discuss the T_e algorithm and how it was used to analyze the data. Data acquisition and reduction will be covered in chapter four. We present the results of the data analysis in chapter five, and conclusions in chapter six. Suggestions for further research will be addressed in chapter seven.

CHAPTER 2

ELECTRON ENERGY BALANCE

This chapter will review electron energy balance in the thermosphere. The thermosphere extends upward from the mesopause, and derives its name from the fact that temperatures increase with height. Electron energy balance in the thermosphere is governed by three competing processes: energy sources, energy sinks, and energy transport. The relative importance of these processes is determined by many factors, such as altitude, local time, invariant latitude, season, and solar activity. The following sections discuss these processes. Most of the information is taken from *Schunk and Nagy* [1978] and *Schunk et al.* [1986].

2.1. ELECTRON ENERGY SOURCES

Before we examine electron heating, we must distinguish between the two different components of the electron energy distribution function. For ionospheric electrons, the two components are *thermal* (or *ambient*) electrons and *suprathermal* electrons. Thermal electrons (in the thermosphere) are usually thought of as having a Maxwellian velocity distribution with a mean thermal energy of about 0.1 eV. The electron temperature is defined as the average energy of the thermal electron gas. Conversely, suprathermal electrons have energies that range from thermal energies up to about 100 eV. These electrons have a non-Maxwellian distribution, and originate from one of two sources: photoionization and particle ionization.

Solar EUV radiation ($\lambda < 1027\text{\AA}$) ionizes the neutral atmosphere. The photon

ionization energy is usually greater than the required ionization energy of the atmospheric constituents. The excess energy goes into ion excitation energy, ion kinetic energy, and electron kinetic energy. Because of momentum and energy conservation, the electron will carry away most of the kinetic energy. Such electrons are called *photoelectrons*. Photoelectron collisions with thermal electrons account for most of the electron gas heating in the ionosphere. However, photoelectrons with high energies (10's of eV) must lose most of their energy before coulomb collisions with the ambient electrons become important. The various processes that de-energize the photoelectrons are described in *Schunk and Nagy [1978]*. Briefly, for photoelectron energies greater than about 50 eV, ionization and optically allowed excitation of the neutral constituents are the dominant energy loss processes. At energies of about 20 eV, the energy loss via excitation of metastable levels of the major constituents is comparable to the energy loss through allowed transitions, becoming of increasing importance as the energy decreases. At photoelectron energies below about 5 eV, energy loss through excitation of N_2 and O_2 vibrational levels becomes important. Finally, below about 2 eV, energy loss to the thermal electrons through coulomb collisions is the dominant photoelectron energy loss process. At this point, most of the initial photoelectron energy has been lost to the neutrals.

In addition to photoelectrons, high energy electrons of magnetospheric origin can flow down into the ionosphere along geomagnetic field lines and ionize the local constituents. This is the second source of suprathermal electrons. Once in the ionosphere, these electrons lose energy in the same manner as photoelectrons. Again, the heating of

thermal electrons is one of the energy loss processes.

Thermal electrons can also be heated by deactivation (or *electron quenching*) of excited neutral and ion species. *Torr and Torr* [1978] have shown that a significant population of excited species exists in the upper atmosphere. However, the relative importance of quenching as a heat source has not yet been established.

2.2. ELECTRON ENERGY SINKS

Thermal electrons lose energy via the following processes:

- (1) Rotational excitation of N_2 and O_2 .
- (2) Fine structure excitation of O.
- (3) Vibrational excitation of N_2 and O_2 ($T_e > 1500K$).
- (4) Electronic excitation of N and O ($T_e > 3000K$).
- (5) Elastic collisions with neutrals (including H and He). This mechanism is not very efficient.
- (6) Coulomb collisions with ions. This is the primary heat source for the ions.

Figures 6 and 7 show the relative importance of these loss rates as a function of height. These two graphs were calculated by the T_e solver using Sondrestrom data. Figure 6 is for 24 April 1983 at 1729UT and is representative of daytime conditions, while Figure 7 is for 17 March 1988 at 0121UT and is representative of nighttime conditions. Also shown on these graphs are the sums of the local heating and cooling terms, as well as the heat conduction term (to be discussed in section 2.3). Notice in Figure 6 that heat conduction becomes very important above about 300 km. In addition, both figures show

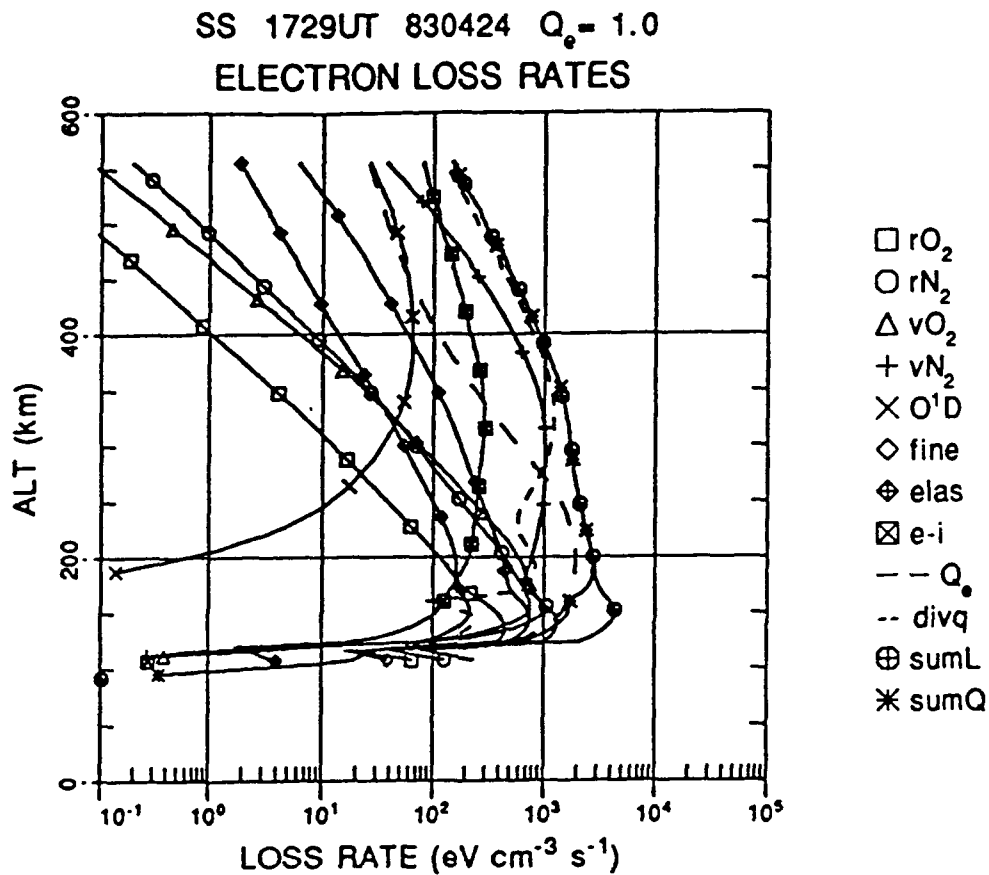


Fig. 6. Electron energy loss rate profiles for Sondrestrom on 24 April 1983 at 1729UT (1429LT). The curves labeled $v\text{N}_2$ and $v\text{O}_2$ represent losses due to the excitation of the vibrational states of N_2 and O_2 , respectively. The $r\text{N}_2$ and $r\text{O}_2$ curves represent losses in the excitation of rotational levels of N_2 and O_2 . The *elas* curve represents the sum of the losses due to elastic collisions between electrons and the neutral species. The O^1D curve represents losses in the excitation of O to the ^1D state, and that labeled *fine* represents the losses due to the excitation of fine structure levels in O . The *e-i* curve represents the losses in coulomb collisions between electrons and ions. Q_e is the solar EUV input, *divq* is the heat conduction term, *sumL* is the sum of the local losses, and *sumQ* is the sum of the local heat sources.

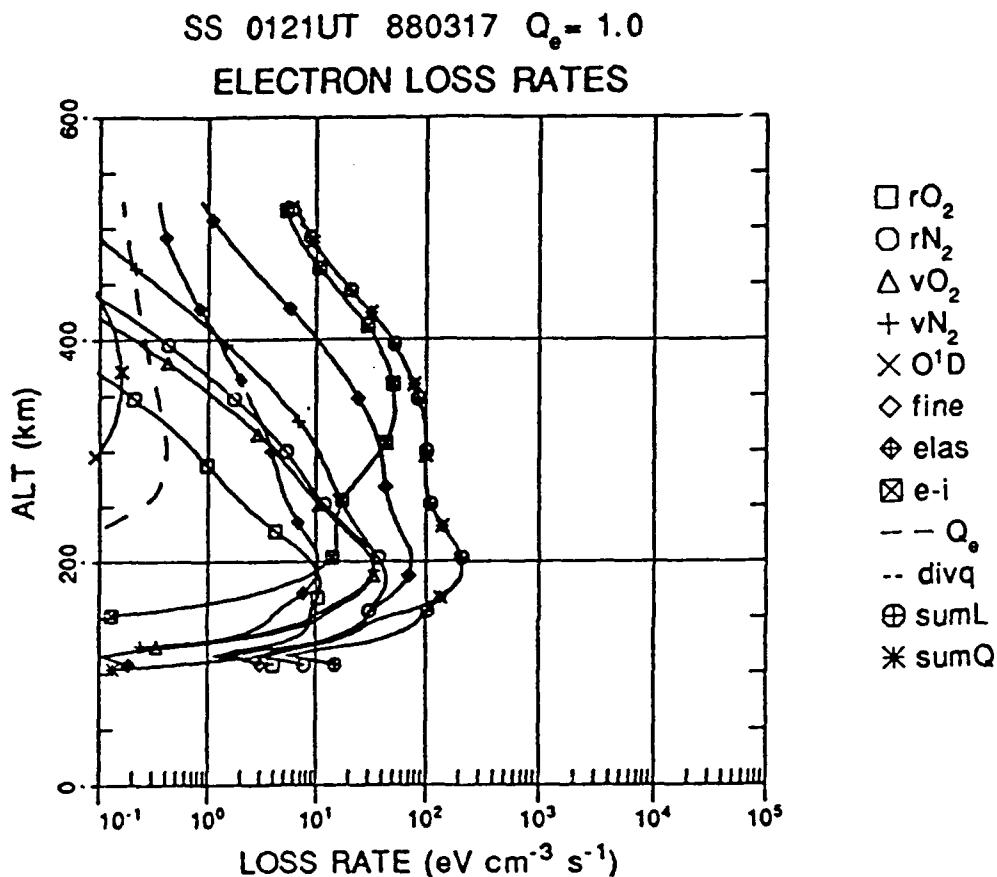


Fig. 7. Electron energy loss rate profiles for Sondrestrom on 17 March 1988 at 0121UT (2221LT). The curves labeled vN_2 and vO_2 represent losses due to the excitation of the vibrational states of N_2 and O_2 , respectively. The rN_2 and rO_2 curves represent losses in the excitation of rotational levels of N_2 and O_2 . The *elas* curve represents the sum of the losses due to elastic collisions between electrons and the neutral species. The $O(^1D)$ curve represents losses in the excitation of O to the 1D state, and that labeled *fine* represents the losses due to the excitation of fine structure levels in O . The *e-i* curve represents the losses in coulomb collisions between electrons and ions. Q_e is the solar EUV input, *divq* is the heat conduction term, *sumL* is the sum of the local losses, and *sumQ* is the sum of the local heat sources. In this example, in contrast to Fig. 2.1, *divq* cannot be seen because it is equal to *sumQ* (this is expected at night).

an apparent discontinuity in the curves at about 108 km. This discontinuity results because 108 km is the lower boundary at which the T_e algorithm solves the electron energy balance differential equation. Below this altitude we simply equate local heating and cooling. Finally, we notice that, in both of these figures, the sum of the local heating rates ($sumQ$) and sum of the local cooling rates ($sumL$) are not equal below about 175 km. This represents a problem in the T_e algorithm at low altitudes. However, as we will see, the derivation of heat flux is almost independent of the physical situation at low altitudes. Again, the processes listed in section 2.1 heat the ambient electron gas, whereas the processes in this section cool the electrons. The balance of thermal electron heating and cooling processes results in an thermospheric electron temperature that is usually greater than either the ion or the neutral temperature.

2.3. ELECTRON ENERGY TRANSPORT

The neutral density in the lower regions of the thermosphere is about one million times greater than the plasma density N_e . Therefore, collisions between the thermal electrons and the neutrals almost completely inhibit energy transport from one portion of the electron gas to another. However, as altitude increases, N_n / N_e decreases, and energy transport begins to play a role in thermal electron energy balance.

The electron energy balance equation is obtained by taking the third velocity moment of the Boltzmann Equation:

$$\begin{aligned} & \frac{1}{2} m_e \int_{-\infty}^{+\infty} v_e^2 dv_x dv_y dv_z \left[\frac{\partial f}{\partial t} + \mathbf{v}_e \cdot \nabla_r f + \mathbf{a} \cdot \nabla_v f \right] \\ & = \frac{1}{2} m_e \int_{-\infty}^{+\infty} v_e^2 dv_x dv_y dv_z \left(\frac{\delta f}{\delta t} \right)_{coll} \end{aligned} \quad (2.1)$$

where m_e is the electron mass, \mathbf{v}_e is the electron velocity, \mathbf{a} is the acceleration, f is the electron distribution function, ∇_r is the coordinate space gradient, ∇_v is the velocity space gradient, and $(\delta f/\delta t)_{coll}$ is the time rate of change of f due to collisions with other species.

Evaluation of equation 2.1 gives the electron energy equation:

$$\frac{3}{2} \left(\frac{D}{Dt} (N_e T_e) \right) = -\frac{5}{2} N_e k T_e \nabla \cdot \mathbf{u}_e - \nabla \cdot \mathbf{q}_e + \left(\frac{\delta E_e}{\delta t} \right)_{coll} \quad (2.2)$$

where $D/Dt = \partial/\partial t + \mathbf{u}_e \cdot \nabla$ is the convective derivative, k is Boltzmann's constant, N_e is the electron density, T_e is the electron temperature, \mathbf{u}_e is the electron drift velocity, \mathbf{q}_e is the heat flux, and $(\delta E_e/\delta t)_{coll}$ is the time rate of change of electron gas energy due to collisions with other species. Viscous heating is neglected in equation 2.2. Now $(\delta E_e/\delta t)_{coll}$ can be written [Schunk, 1975]:

$$\frac{\delta E_e}{\delta t} = -\sum_j \frac{N_e m_e \nu_{ej}}{m_e + m_j} [3k(T_e - T_j)] \quad (2.3)$$

where ν_{ej} is the collision frequency for momentum transfer, and the subscript j covers all neutral and ion species. Equation 2.3 can be thought of as the sum of all the heating and cooling rates discussed in the previous two sections. Thus, using equation 2.3 along with the electron continuity equation:

$$\frac{\partial N_e}{\partial t} + \nabla \cdot (N_e \mathbf{u}_e) = 0 \quad (2.4)$$

equation 2.2 becomes:

$$\begin{aligned} \frac{3}{2} N_e k \left(\frac{\partial T_e}{\partial t} \right) = & -N_e k T_e \nabla \cdot \mathbf{u}_e - \frac{3}{2} N_e k \mathbf{u}_e \cdot \nabla T_e \\ & -\nabla \cdot \mathbf{q}_e + \Sigma Q_e - \Sigma L_e \end{aligned} \quad (2.5)$$

where ΣQ_e and ΣL_e represent the sums of the ambient electron heating and cooling rates, respectively. These terms are usually referred to as the volume heating and volume cooling rates. The first term on the right-hand side of equation 2.5 represents adiabatic expansion, the second term is the advection term, and the third term is the divergence of heat flow. Equation 2.5 can be further altered by writing \mathbf{u}_e and \mathbf{q}_e as:

$$\mathbf{u}_e = -\frac{\mathbf{J}}{eN_e} \quad (2.6)$$

$$\mathbf{q}_e = -K^e \nabla T_e - \beta_e \mathbf{J} \quad (2.7)$$

where \mathbf{J} is the current, K^e is the thermal conductivity, and β_e is the thermoelectric transport coefficient. Equation 2.6 says that the ionospheric current is carried by the electrons, while equation 2.7 states that heat flow results from temperature gradients and currents. We now assume that \mathbf{J} and \mathbf{q}_e are parallel to the geomagnetic field, and that ∇T_e is in the vertical direction. If no field-aligned currents are present, we can use equations 2.6 and 2.7 to rewrite equation 2.5 as:

$$\frac{3}{2} N_e k \frac{\partial T_e}{\partial t} = \sin^2 I \frac{\partial}{\partial z} \left(K^e \frac{\partial T_e}{\partial z} \right) + \Sigma Q_e - \Sigma L_e \quad (2.8)$$

where I is the geomagnetic field dip angle. A further simplification is usually possible since F region electron temperatures respond rapidly to changing conditions. With this assumption, the left-hand side of equation 2.8 is negligible, and we can write:

$$\sin^2 I \frac{\partial}{\partial z} \left(K_e \frac{\partial T_e}{\partial z} \right) + \Sigma Q_e - \Sigma L_e = 0 \quad (2.9)$$

This is the form of the electron energy balance equation used by the T_e solver. Once again, the first term on the left-hand side of equation 2.9 is the divergence of heat flow. This term is positive if heat converges into a given volume (a heating mechanism for the electron gas), and is negative if heat diverges out of a given volume (a cooling mechanism for the electron gas). Referring back to Figures 2.1 and 2.2, the first term in equation 2.9 corresponds to $divq$, the second term to $sumQ$, and the third term to $sumL$.

As one might expect, the terms in equation 2.9 vary in importance with altitude. At low altitudes, where local heating and cooling dominate, equation 2.9 reduces to:

$$\Sigma Q_e = \Sigma L_e \quad (2.10)$$

At higher altitudes, energy transport becomes significant, and equation 2.9 describes electron energy balance. At high altitudes, energy transport dominates, and equation 2.9 becomes:

$$\frac{\partial}{\partial z} \left(K_e \frac{\partial T_e}{\partial z} \right) = 0 \quad (2.11)$$

For this research, heat flow is one of the parameters of interest (along with the volume heating rate). As stated previously, heat flow results from currents and temperature gradients. For the purposes of this research, we will, for the most part, ignore the current

flow term. As far as temperature gradients are concerned, it is instructive to examine the thermal conductivity, which is given by *Schunk and Nagy* [1978]:

$$K^e = \frac{5n_e k^2 T_e}{m_e} \frac{1}{\nu_{ei} + \sum_n \nu_{en}} \left[\frac{1}{g_k} - \frac{g_\sigma}{2g_\tau g_{\mu_n}} \right] \quad (2.12)$$

where ν_{ei} is the electron-ion collision frequency, $\sum_n \nu_{en}$ is the electron-neutral collision frequency summed over all neutral species, and the g terms represent correction factors which account for the variation with velocity of the electron-neutral collision frequency as well as for electron-ion and electron-electron effects (the expression in the braces is approximately equal to 0.5). If we substitute for ν_{ei} and ν_{en} as follows:

$$\nu_{ei} = 54.5 \frac{N_i}{T_e^{3/2}}$$

and

$$\nu_{en} = \frac{4}{3} N_n \left(\frac{8kT_e}{\pi m_e} \right)^{1/2} Q_D$$

where N_i is the ion density, Q_D is the Maxwellian-averaged momentum transfer cross section, and N_n is the neutral density, then we obtain:

$$K^e = \frac{7.7 \times 10^5 T_e^{5/2}}{1 + 3.22 \times 10^4 (T_e^2/N_e) \sum_n N_n Q_D} \quad (2.13)$$

which is the form of the thermal conductivity given by *Banks* [1966]. From equations 2.12 and 2.13, we see that energy transport depends strongly on T_e , and that neutral atoms and molecules inhibit energy transport. Heat flow is most efficient for a fully ionized gas at high temperature.

CHAPTER 3

THE METHOD

In this chapter we discuss the algorithm used to determine the topside heat flux. Data acquisition / reduction will be covered in chapter four.

3.1. TECHNIQUE DEVELOPMENT

We use an algorithm [Schunk *et al.*, 1986] that solves the electron energy balance equation (equation 2.9) to obtain a match to the incoherent-scatter T_e data. The match is accomplished by varying the volume heating rate Q_e and the heat flux q_e . The T_e algorithm requires the following inputs (the densities and temperatures listed are required above 88 km at four-km intervals):

(1) Neutral temperatures / densities. The Mass Spectrometer and Incoherent Scatter (MSIS90) model provides neutral temperature (T_n) height profiles as well as density profiles for O_2 , N_2 , O , He , and H . These T_n profiles must be compared with ISR T_i data for consistency ($T_i \approx T_n$ up to about 300 km).

(2) Ion temperatures. Incoherent-scatter radar T_i data (obtained at roughly 50 km intervals) are fit (in a least-squares sense) by a cubic spline. This enables the T_i to be interpolated to values at the required four-km intervals and ensures that the first and second height derivatives of T_i are continuous (a requirement of the algorithm).

(3) Ion densities. Incoherent-scatter radar electron density (N_e) data provide this information. We assume charge neutrality, then perform an interpolation of the $N_e(h)$ profile to obtain values at the required altitudes. Ion composition is determined as

follows. An existing routine (see appendix one) used in ISR data reduction is used to compute the percentage of O^+ at a given altitude ($[O^+] / [N_e]$). We then assume: (a) $[N_2^+] = [N^+] = 0$, and (b) 75 percent of molecular ions are NO^+ , and 25 percent are O_2^+ (a mean molecular weight of 30.5 amu).

(4) Geophysical data. We need values for the 10.7-cm flux (the 81-day average, the value from the previous day, and the value for the day of interest), the daily A_p value, and the magnetic field dip angle. The geophysical data have been tabulated in the CEDAR database at the National Center for Atmospheric Research; the dip angle is calculated from the IGRF model of the geomagnetic field.

(5) At 225 km and below, we force $T_n = T_i = T_e$ (ISR data points only). Since equation 2.10 applies below 225 km, this adjustment has no impact on the results of our study. However, this adjustment does prevent inaccurate low-altitude data points from generating unnecessary perturbations in the $T_i(h)$ spline. An inaccurate T_i spline (above about 350 km) would certainly have an adverse affect on the heat flux estimate.

(6) The algorithm also incorporates the volume heating rate, Q_e , which consists of two components: the solar EUV heating rate [*Richards and Torr, 1984*], and the particle heating rate (we set the particle heating rate to zero). An example of the solar EUV heating rate is shown in Figure 8. The solar EUV heating rate varies according to time of day (solar zenith angle), season, solar cycle, and geomagnetic activity. Finally, the algorithm includes a heat flux incident at the top of the atmosphere.

With this information, the algorithm solves the electron energy equation for the $T_e(h)$ profile. The flow chart shown in Figure 9 illustrates the flow of information into and out

SZA = 0.0

1987 173 f10.7 = 70 Ap = 200

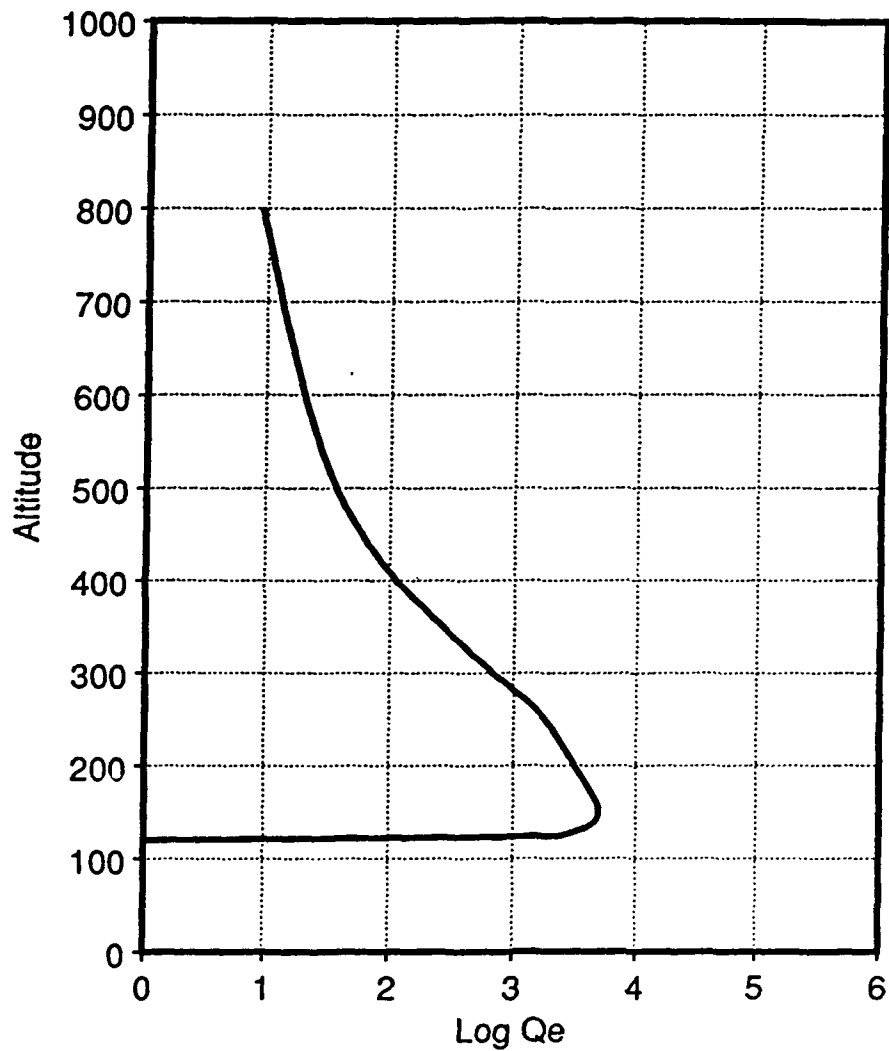


Fig. 8. An example of a solar EUV volume heating rate profile used in the T_e algorithm. The units of Q_e are $\text{eV cm}^{-3} \text{sec}^{-1}$. Volume heating rate profiles vary with solar zenith angle, season, solar cycle, and magnetic activity. This particular profile is for overhead sun, day number 173 of 1987, 10.7-cm flux of 70 ($70 \times 10^{-22} \text{ W m}^{-2} \text{ Hz}^{-1}$), and A_p of 200.

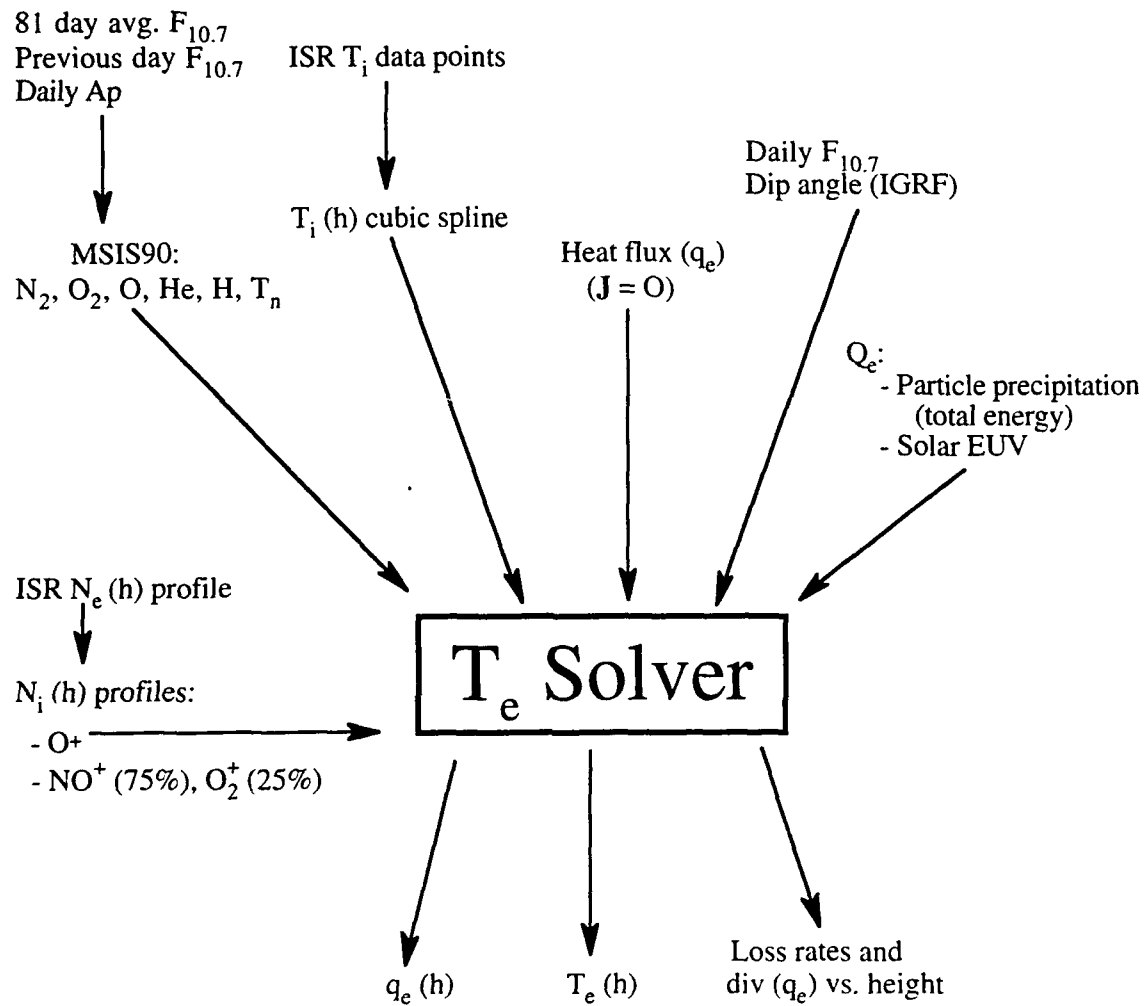


Fig. 9. Flow chart showing the inputs and outputs of the T_e solver.

of the T_e solver.

3.2. FINDING THE BEST FIT

Once the T_e algorithm generates an electron temperature profile, it is compared with the ISR T_e profile (in a weighted least-squares sense). As stated earlier, the volume heating rate and heat flux are then varied until the best fit is found. During this process, the heat flux and volume heating rate are not varied simultaneously. Rather, for each data set, we multiply the "standard" volume heating rate by four different factors: 0.5, 1, 2, and 4. The T_e algorithm is then applied four times to the given data set -- once for each factor of Q_e . This procedure ensures that Q_e varies in a physically reasonable fashion throughout the day. With Q_e fixed at each of the four different values, the best fit is found by changing only the heat flux. The best fit is then found by a least-squares technique. Stated mathematically, we try to minimize χ^2 , which is given by:

$$\chi^2 = \frac{1}{N} \sum_i \left[\frac{(T_m(h_i) - T_d(h_i))^2}{\sigma_i^2} \right] \quad (3.1)$$

where N is the number of data points in the profile, h_i is the altitude of the i^{th} data point, $T_m(h_i)$ is the calculated electron temperature at height h_i , $T_d(h_i)$ is the ISR T_e data point at height h_i , and σ_i is the uncertainty in $T_d(h_i)$. Ideally, the sum covers all data points for a given ISR T_e profile. The $T_m(h_i)$ are found by interpolation of the $T_m(h)$ profile. Note that χ^2 is a function of Q_e and q_e because of the $T_m(h)$ dependence on these quantities.

A golden search routine [Press et al., 1989] is used to select the sequence of q_e values used to minimize χ^2 . The search is completed when the q_e 's that "bracket" the χ^2

minimum differ by one percent or less. This tolerance is significantly better than the uncertainty in the derived q_e (see section 3.3.2).

In practice we did not use all the data points in a given data set to compute χ^2 (the sum in equation 3.1). This is because the low altitude T_e data points, which physically (as we will see) are determined almost entirely by solar EUV absorption, have smaller error bars and dominate the χ^2 calculation. When tried, the inclusion of these low altitude data points often resulted in overestimated heat fluxes. For example, Figure 10 shows the ISR data and T_e algorithm fit for 21 Mar 85 at 1759UT. Panel (a) shows the least-squares fit T_e profile (dashed line) when all data points are used to compute χ^2 . Notice how the calculated T_e profile fits the low altitude points well, but is a poor fit to the high altitude points. Panel (b) shows the best fit when data points below 350 km are excluded from the χ^2 sum. Notice that the calculated profile now falls within the error bars of two of the three highest data points. Correspondingly, the heat flux is 29 percent lower than in panel (a). In this study, only data points above 350 km are used to compute the least-squares fit.

This example was chosen to illustrate this effect. Usually the modeled T_e profile would also fit the low altitude (below 350 km) observations. The low altitude discrepancy in panel (b) of Figure 10 probably arises from an uncertainty in Q_e (see section 5.3). However, our study revealed that uncertainties in Q_e have minimal effect on the heat flux. In other words, the high-altitude T_e profile is not influenced heavily by the volume heating rate. Instead, the high-altitude profile is largely determined by the heat flux. The reverse is true at low altitudes. The evidence for this is shown in sections 3.3.1, 5.1, and 5.3.

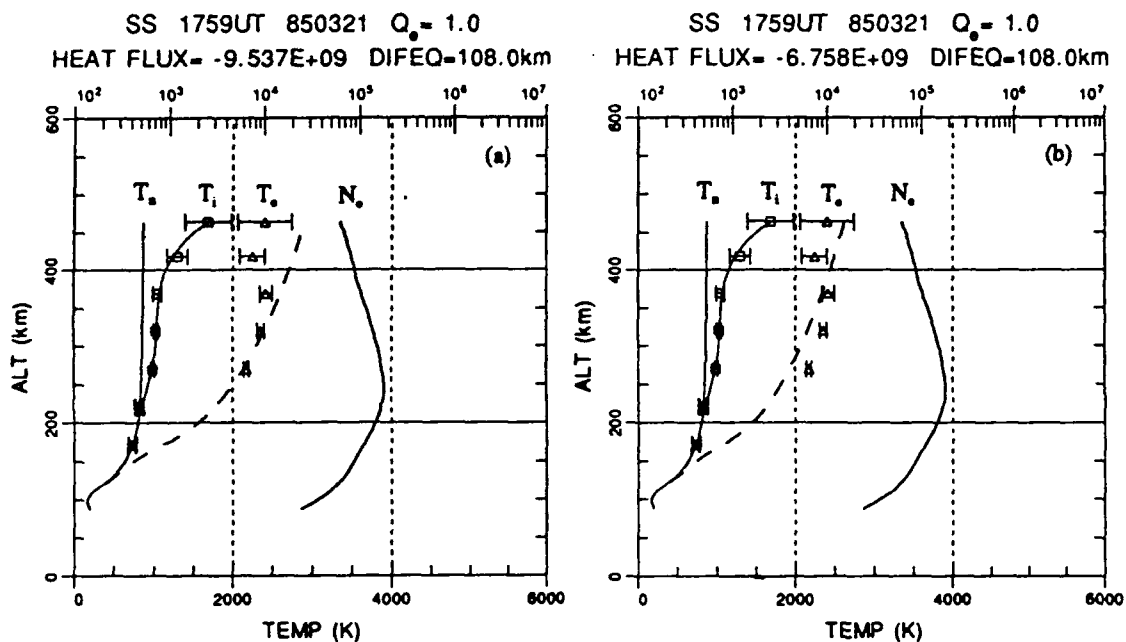


Fig. 10. Sondrestrom T_e , T_i , and N_e data for 21 March 1985 at 1759UT (1459LT). Triangles denote T_e data points; squares are for T_i data points. Note that $T_e = T_i = T_n$ for the data points below 250 km (as discussed in section 3.1). The N_e curve is the solid line to the right of the temperature profiles. The N_e scale, in cm^{-3} , is located on the upper x-axis. The solid line through the T_i data points is the T_i spline, and the other solid line is the MSIS90 $T_n(h)$ curve. The long-dashed line is the calculated T_e profile for $Q_e = 1$. The heat flux shown in the legend is for the altitude of the highest ISR data point, and DIFEQ is the lower bound for which we solve equation 2.9. Panel (a) shows the best fit when all T_e data points are used in the χ^2 sum; in panel (b) only data points above 350 km are used.

3.3. TESTING THE METHOD

The T_e algorithm will provide a q_e estimate for a given ISR data set. Before any conclusions can be made, however, one must have confidence in the q_e estimate. This section describes four tests used on the T_e algorithm to determine a "confidence level" in the results.

3.3.1. χ^2 Convergence

Once χ^2 is minimized, it is important to know whether the minimum is "narrow" or "wide" (referring to the range Δq_e over which χ^2 is small). If the minimum is narrow, then the q_e estimate is well-defined. However, if the minimum is wide, then the q_e estimate has a large uncertainty (related to the width of the minimum). Figure 11 is the convergence contour plot for Sondrestrom on 24 Apr 83 at 0558UT (0258LT). The contours show the different values of χ^2 . Notice that the minimum χ^2 is less than 0.17; however, from this plot, the width of the minimum appears to extend from 9.8 to 10.1 (a Δq_e of about 6×10^9). By taking a cross section of this plot through $Q_e = 1$ (Figure 12) we see that the minimum is much narrower. Figures 13 and 14 illustrate this same point for Sondrestrom on 21 Mar 85 at 1311UT (1011LT). In addition to the well-defined minimum, it is apparent in these four figures that the χ^2 function is not symmetric about the minimum. The sharper increase in χ^2 for large q_e indicates that it is extremely unlikely that the derived q_e would be overestimated. Figures 11 and 13 also illustrate the minimal dependence of q_e on Q_e . The smallness of this dependence strengthens the significance of the value of q_e that is found.

SS 830424 0558UT
CONVERGENCE

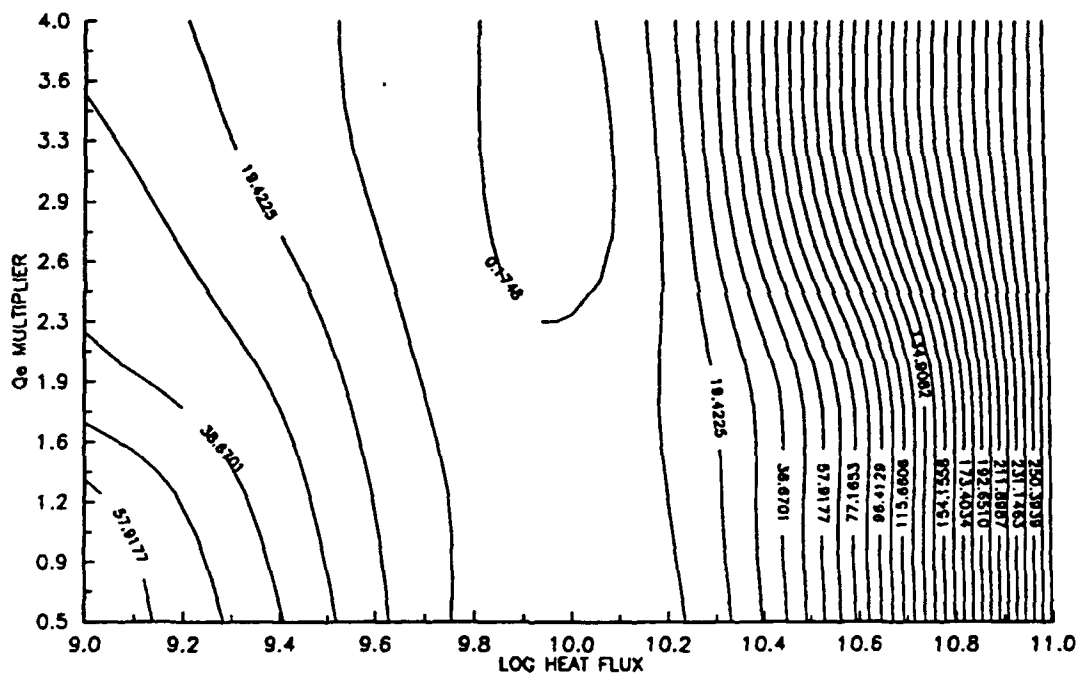


Fig. 11. Convergence contour plot for Sondrestrom on 24 April 1983 at 0558UT (0258LT). The contours show the different values of χ^2 .

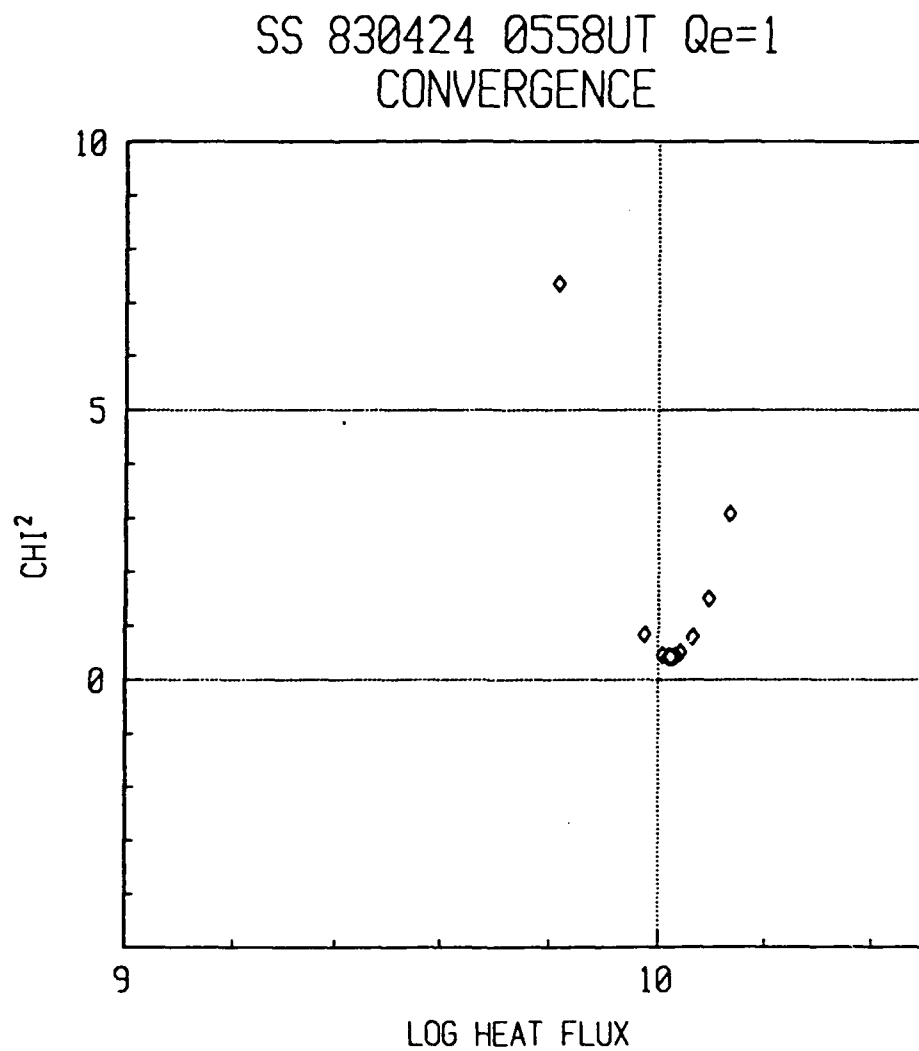


Fig. 12. Cross section of Figure 11 for $Q_e = 1$. The diamonds show the heat fluxes for which the golden search routine calculated χ^2 .

SS 850321 1311 UT
CONVERGENCE

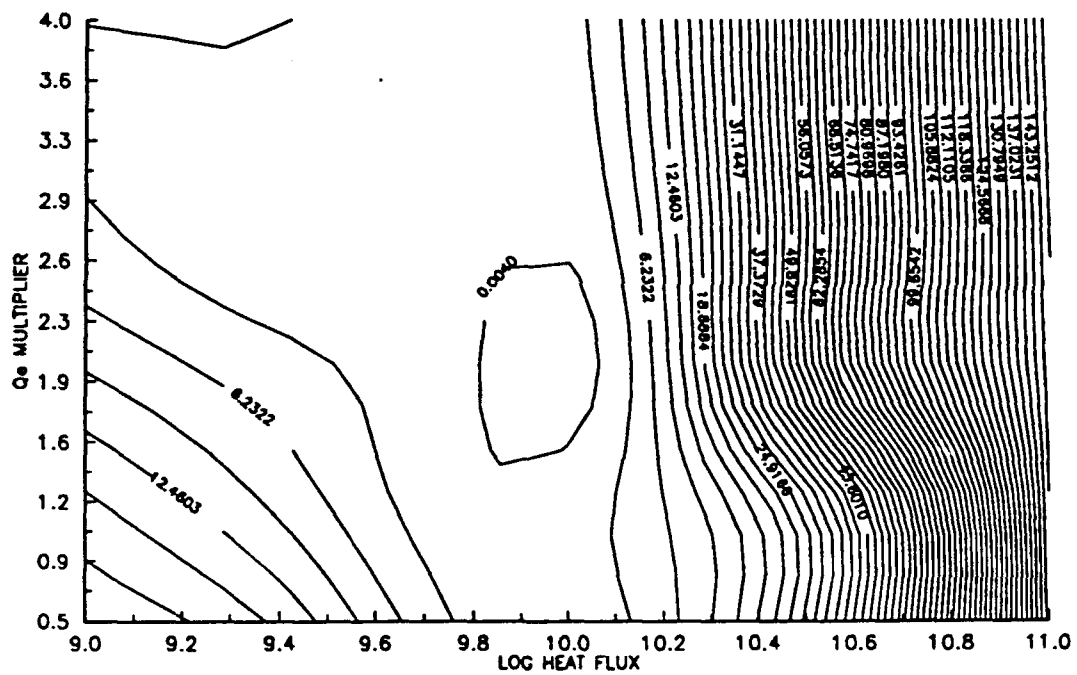


Fig. 13. Convergence contour plot for Sondrestrom on 21 March 1985 at 1311 UT (1011 LT). The contours show the different values of χ^2 .

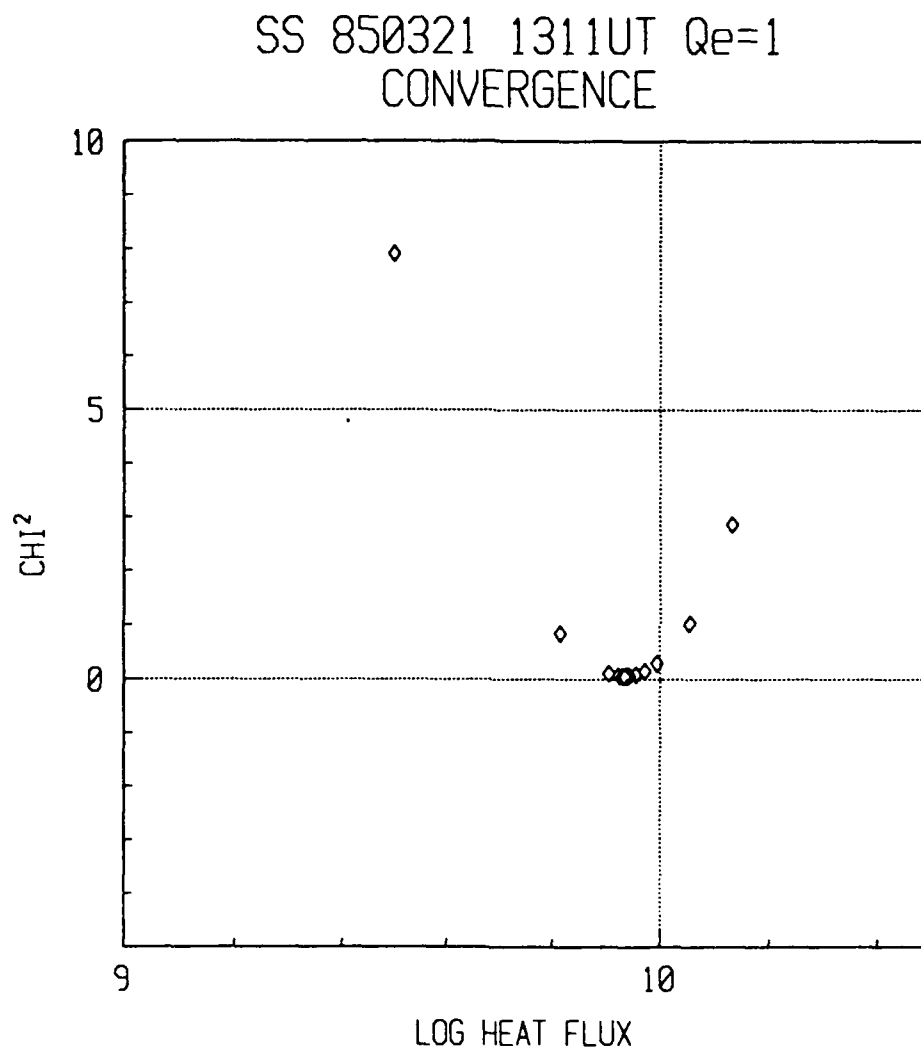


Fig. 14. Cross section of Figure 13 for $Q_e = 1$. The diamonds show the heat fluxes for which the golden search routine calculated χ^2 .

3.3.2. Testing the Algorithm on Model Data

Dr. Jan Sojka provided two sets of theoretical N_e , T_e , and T_i profiles to test on the T_e algorithm. These data were produced using the USU Time Dependent Ionospheric Model (TDIM). The test was to see whether the T_e algorithm could reproduce the heat fluxes that were used to generate the TDIM data sets. The results of the two tests are shown in Table 4, and in Figures 15 and 16. Test #1 represents nighttime conditions (with an unusually high heat flux), while test #2 represents daytime conditions. These TDIM tests show that one can have high confidence in the q_e estimates produced by the T_e solver.

One might wonder why there are any differences between the TDIM and the T_e solver electron temperature profiles. A potentially significant reason is that the TDIM uses the MSIS86 model of the neutral atmosphere, whereas the T_e solver uses the MSIS90 model. As a result, the neutral atmospheres -- hence the electron energy losses to the neutrals -- were not identical.

3.3.3. Comparison with *Kofman and Wickwar* [1984]

Figure 17 shows the ISR data, MSIS90 T_n profile, and calculated T_e profile for Sondrestrom on 24 April 1983 at 1346UT (1046LT). This ISR T_e profile represents one of the most extreme temperature gradients we saw in the data ($T_e = 6000\text{K}$ at 500 km). This situation has been studied by *Kofman and Wickwar* [1984]. They showed that the very intense heating for this case was caused by particle precipitation (associated with the afternoon convection reversal) and by a large downward heat flux. They calculated this heat flux using two different methods. The first method involved use of the thermal conductivity and the electron temperature gradients. The second method assumed that the

TABLE 4. TDIM Tests

Test #1

Theoretical q_e : $-3.00 \times 10^{10} \text{ eV cm}^{-2} \text{ s}^{-1}$
 T_e solver q_e estimate: $-3.11 \times 10^{10} \text{ eV cm}^{-2} \text{ s}^{-1}$
percent difference: 3.6

Test #2

Theoretical q_e : $-4.926 \times 10^9 \text{ eV cm}^{-2} \text{ s}^{-1}$
 T_e solver q_e estimate: $-5.155 \times 10^9 \text{ eV cm}^{-2} \text{ s}^{-1}$
percent difference: 4.6

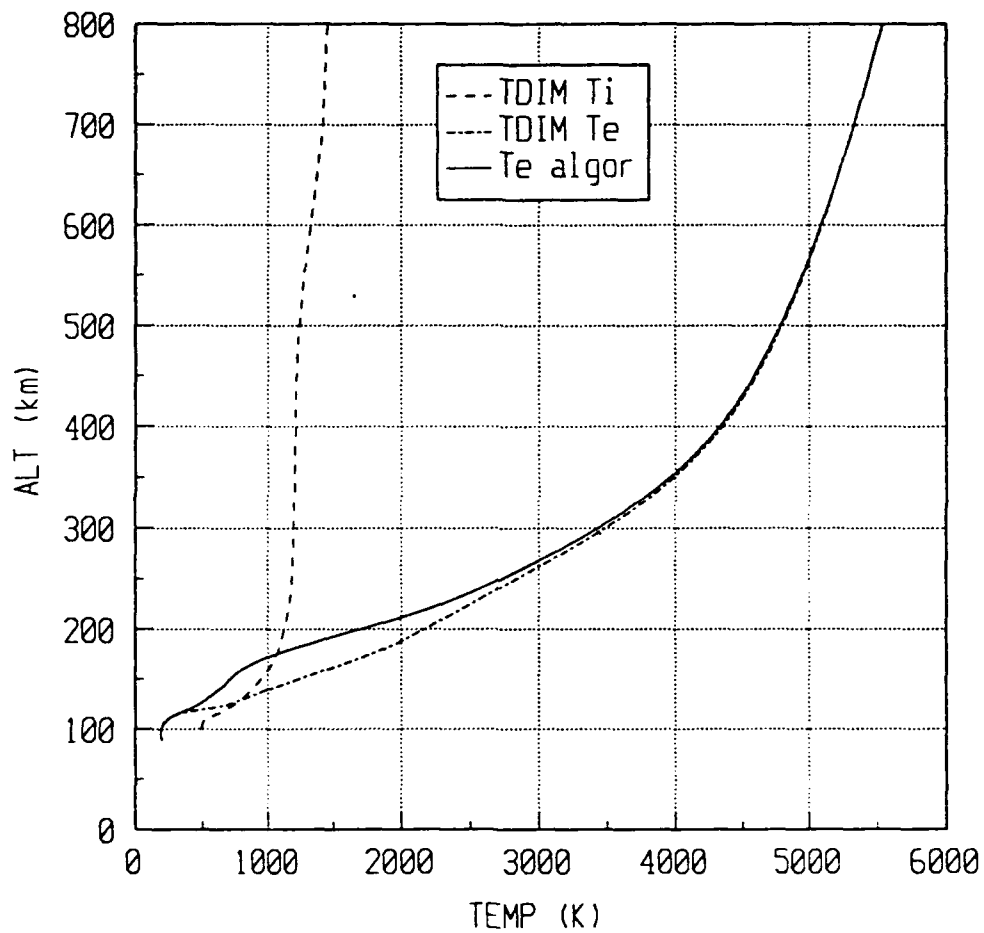
TDIM VS. T_e ALGORITHM
TEST #1

Fig. 15. Results of TDIM test #1. The long dash curve is the T_i profile from the TDIM, the dash-dot curve is the TDIM T_e curve, and the solid line is the electron temperature curve calculated by the T_e solver.

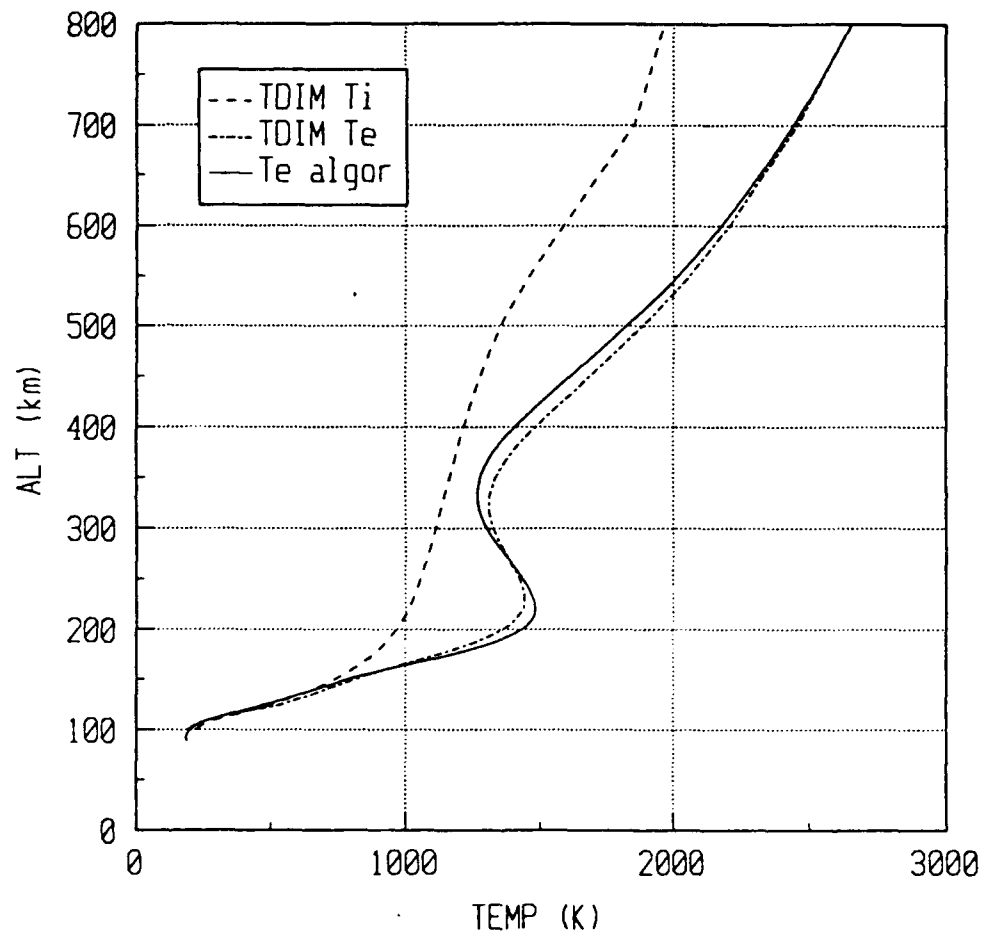
TDIM VS. T_e ALGORITHM
TEST #2

Fig. 16. Results of TDIM test #2. The long dash curve is the T_i profile from the TDIM, the dash-dot curve is the TDIM T_e curve, and the solid line is the electron temperature curve calculated by the T_e solver.

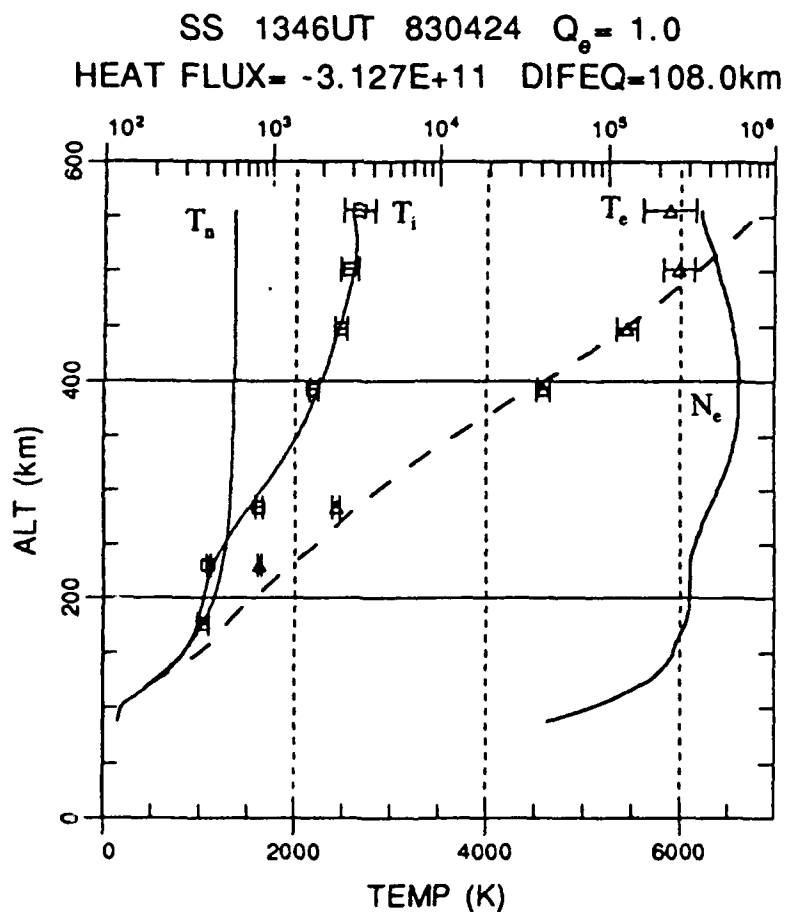


Fig. 17. Sondrestrom T_e , T_i , and N_e data for 24 April 1983 at 1346UT (1046LT). Triangles denote T_e data points; squares are for T_i data points. The N_e curve is the solid line to the right of the temperature profiles. The N_e scale, in cm^{-3} , is located on the upper x-axis. The solid line through the T_i data points is the T_i spline, and the other solid line is the MSIS90 $T_a(h)$ curve. The long-dashed line is the calculated T_e profile for $Q_0 = 1$. The heat flux shown in the legend is for the altitude of the highest ISR data point, and DIFEQ is the lower bound for which we solve equation 2.9.

heat flux is constant along the magnetic field line, then solved for the heat flux using the integrated electron energy equation (equation 2.9 with $\Sigma Q_e = \Sigma L_e = 0$). Both these methods assume a pure plasma. We used the T_e solver to compute the heat flux for this same situation (results shown in Figure 17). Thus we can compare the T_e solver results with the results of the two other (very different) techniques for computing heat flux. Figure 18 shows the results of this comparison. There is very good agreement between the T_e solver and both of the *Kofman and Wickwar* methods, and this is another boost to our confidence level in the T_e solver results.

3.3.4. Determination of the "Zero" Heat Flux

For a given state of the topside ionosphere, q_e and T_e vary proportionally. In other words, T_e increases as q_e increases, and vice versa. However, if q_e drops below a certain value (call it q_0), then the effect of heat flux on the T_e profile becomes undetectable. The heat flux q_0 is the minimum detectable heat flux and for our data and method is equivalent to $q_e = 0$. Therefore, any meaningful results out of this research must be based on heat flux values larger than q_0 . With this in mind, we conducted two tests to obtain an estimate for q_0 . One test involved typical daytime ionospheric parameters; the other test was for nighttime conditions. In both tests we started with $q_e = 0$, then increased the heat flux until the high-altitude T_e values increased by 20 percent (above the T_e values for zero heat flux). For both experiments, a heat flux of about -1×10^7 eV cm⁻² s⁻¹ was equivalent to $q_e = 0$, and T_e had increased by 20 percent when q_e reached about -5×10^7 eV cm⁻² s⁻¹. This places q_0 below -5×10^7 eV cm⁻² s⁻¹ for both daytime and nighttime conditions. As we will see in chapter five, this estimate of the "zero" heat flux is well

below the heat flux values we use to establish our conclusions.

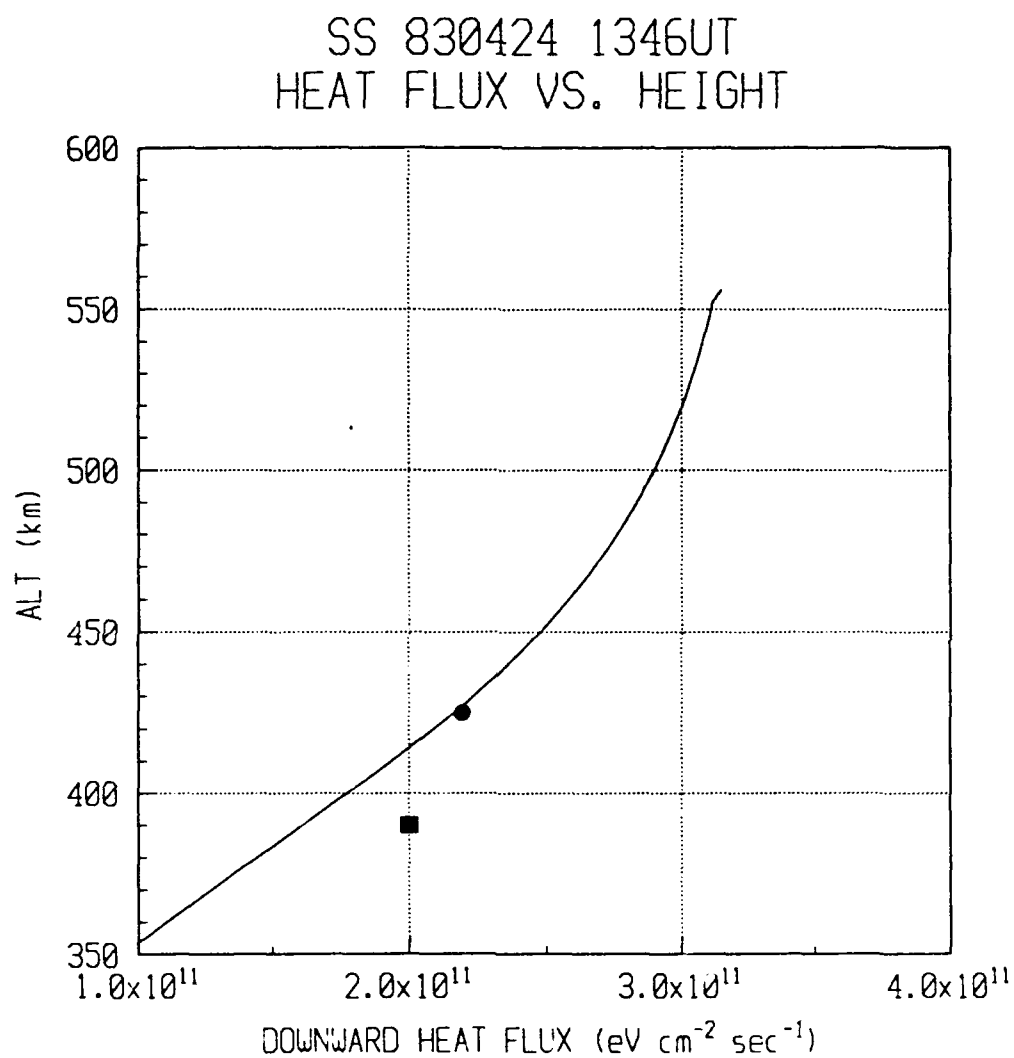


Fig. 18. Heat flux versus height for Sondrestrom on 24 April 1983 at 1346UT (1046L). The solid curve is the T_e solver heat flux profile. The filled circle and filled square are the *Kofman and Wickwar* heat flux values. The circle represents the integrated electron energy equation method; the square is the T_e gradient method.

CHAPTER 4

THE DATA

The data used in this research were obtained from the CEDAR database. This database is located at the National Center for Atmospheric Research (NCAR) in Boulder, Colorado (see appendix two for an outline of data retrieval procedures). Data from the Sondrestrom and Millstone Hill IS radars were used in this study. Sondrestrom data analysis extended from 1983 to 1988; Millstone Hill analysis extended from 1985 to 1990. These dates were determined by the data and type of data available in the database. For instance, there were no data for Sondrestrom from later than 1988, while the earlier data from Millstone Hill did not include a detailed density profile. Thus roughly half a solar cycle was included for each radar. Additionally, for each radar, an average of five days of data per year were analyzed -- about 30 percent of the available data set. Since we want to examine the effects of season and magnetic activity on the heat flux, we chose days in which these two parameters took on a range of values.

In this chapter we look at the criteria that the Sondrestrom and Millstone Hill data had to meet before they could be used in the T_e solver. We begin with a brief review of how ionospheric plasma parameters are derived from ISR measurements.

4.1. ISR THEORY

The incoherent scatter radar is an indispensable tool in ionospheric research. These radars emit electromagnetic signals at a frequency that is much higher than the ionospheric plasma frequency f_p (the Sondrestrom radar operates at a frequency of 1290

MHz, the Millstone Hill radar operates at 440 MHz, and the plasma frequency is usually 10 MHz or less). With these high operating frequencies, most of the radar energy passes through the ionosphere and is lost. However, a minute fraction of the incident energy back-scatters off the ionospheric electrons. The scattered signal carries a wealth of information on the state of the ionospheric plasma. Extraction of this information (density and temperature in our case) from the radar signal, however, is a nontrivial problem, and depends heavily on our theoretical model of the back-scatter mechanism, which is well understood.

Now the transmitted wavelength λ_t is usually much greater than the Debye length λ_d ($\lambda_t \approx 68$ cm for Millstone Hill, 23 cm for Sondrestrom). This fact means that the returned signal is divided into two parts: an electron component (which we are not concerned with), and an ion component (see Figure 19). The ion component of the signal comes from scattering off of damped ion acoustic waves. At F-region altitudes, the shape of this component depends on the ratio of T_e to T_i and the ion mass m_i . Determination of the plasma temperatures from the returned signal depends on the mixture of ion masses that is assumed. Overestimation of m_i results in overestimated temperatures, and vice versa.

Ionospheric parameters (N_e , T_e , and T_i) are derived by comparing (in a least-squares sense) the autocorrelation function (ACF) of the received radar signal with calculated ACF's that are modified to include effects from the way the data are acquired. Once the best fit is found, the plasma density and temperatures are taken to be the ones used to produce the theoretical ACF. The actual algorithms are for a nonlinear least-squares fit, e.g., similar to the algorithms found in *Bevington* [1969]. It starts with an initial "guess"

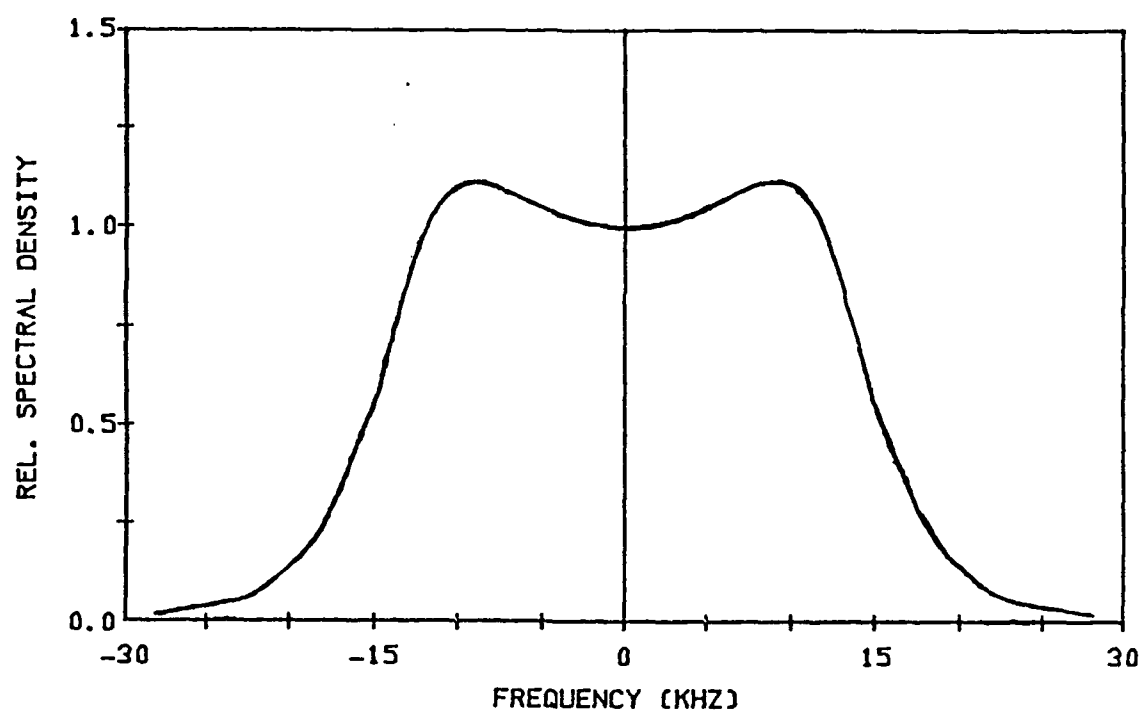


Fig. 19. Sketch of the ion component of the incoherent scatter spectrum. For this theoretical example, the transmitted frequency is about 1290 MHz [R.S.V. Raman, 1980].

of the plasma parameters, then iterates until the suitably modified theoretical ACF matches the observed ACF. In so doing, it also provides an estimate of the uncertainty of the derived parameters. Convergence of the algorithm is very rapid [*private communication, V. B. Wickwar, 1991*].

4.2. ISR DATA

Several factors must be taken into account when using Sondrestrom and Millstone Hill data. We will first consider those factors common to both radars. Issues that are unique to Sondrestrom or Millstone Hill will be covered in sections 4.2.1 and 4.2.2, respectively.

Both of these radars make observations at many different azimuths and elevation angles. However, since heat is conducted mainly along geomagnetic field lines, we are interested in radar observations taken along the field line, or in a direction in which there are no spatial gradients in heat flux. In the data examined, the Sondrestrom radar looks along the field line (azimuth 141 degrees, elevation 80 degrees) at intervals ranging between five and thirty minutes. At Millstone Hill, however, observations are seldom carried out along the magnetic field line (azimuth 166 degrees, elevation 70 degrees). The best data for this study were obtained with the 45-m antenna that is fixed almost vertical. This means that the T_e data points in a given profile lie along different field lines. At 300 km, for example, the plasma from which T_e is derived is on a field line that is about 65 km south of the field line whose plasma will determine the 500 km T_e measurement (65 km is based on the simple geometry of parallel field lines; in reality, the lines get farther apart with altitude). We expect this problem to have minimal impact

on this study. This is because the meridional T_e gradient is usually small at mid-latitudes. The exception to this rule is during periods of magnetic activity; heat flux estimates must be scrutinized in such cases.

Another reality of the data is that the altitude of the highest data point varies between about 450 and 600 km. Since heat flux varies with height, we need to extrapolate all of the q_e estimates up to the same altitude (about 600 km). This extrapolation is crucial if we want to make any conclusions based on variations in heat flux. Fortunately, the results of the research indicate that, for virtually all the data analyzed, q_e has become constant at the top of the ISR T_e profile. To show this, we examined three cases for which the T_e gradient at the top of the profile is substantial, i.e., q_e is still increasing with height. Hence, these are worst-case situations. In each of these cases, we used an exponential function to extend the heat flux curve up to 600 km. The equation we used is given by:

$$q_e(h) = q_\infty - (q_\infty - q_{h_0}) \exp\left(-\frac{h - h_0}{H}\right) \quad (4.1)$$

where q_∞ is the asymptotic value of the heat flux, q_{h_0} is the heat flux at the height h_0 (we used 400 km for h_0), and H is a "scale height-like" factor. For each case, we iterated q_∞ and H until the proper fit was achieved (determined visually). The profiles for these three cases are shown in Figures 20 through 22. Panel (a) in each figure shows the ISR T_e profile, while panel (b) shows heat flux versus height (solid curve) for high altitudes, along with the graph of equation 4.1 (up to 600 km). Panel (b) also gives the q_{h_0} , q_∞ , and the H used for the fitted function. In Figures 20(b) and 21(b) it is obvious that q_e has gone

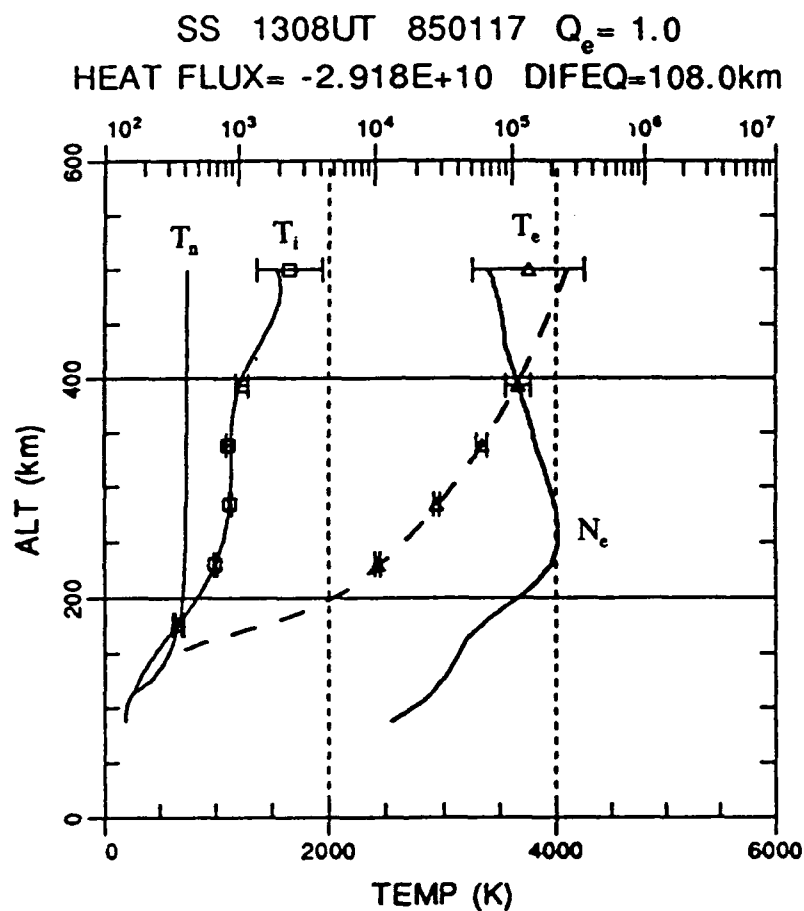


Fig. 20(a). Sondrestrom T_e , T_i , and N_e data for 17 January 1985 at 1308UT (1008LT). Triangles denote T_e data points; squares are for T_i data points. The N_e curve is the solid line to the right of the temperature profiles. The N_e scale, in cm^{-3} , is located on the upper x-axis. The solid line through the T_i data points is the T_i spline, and the other solid line is the MSIS90 $T_n(h)$ curve. The long-dashed line is the calculated T_e profile for $Q_e = 1$. The heat flux shown in the legend is for the altitude of the highest ISR data point, and DIFEQ is the lower bound for which we solve equation 2.9.

SS 850117 1308UT
HEAT FLUX VS. HEIGHT

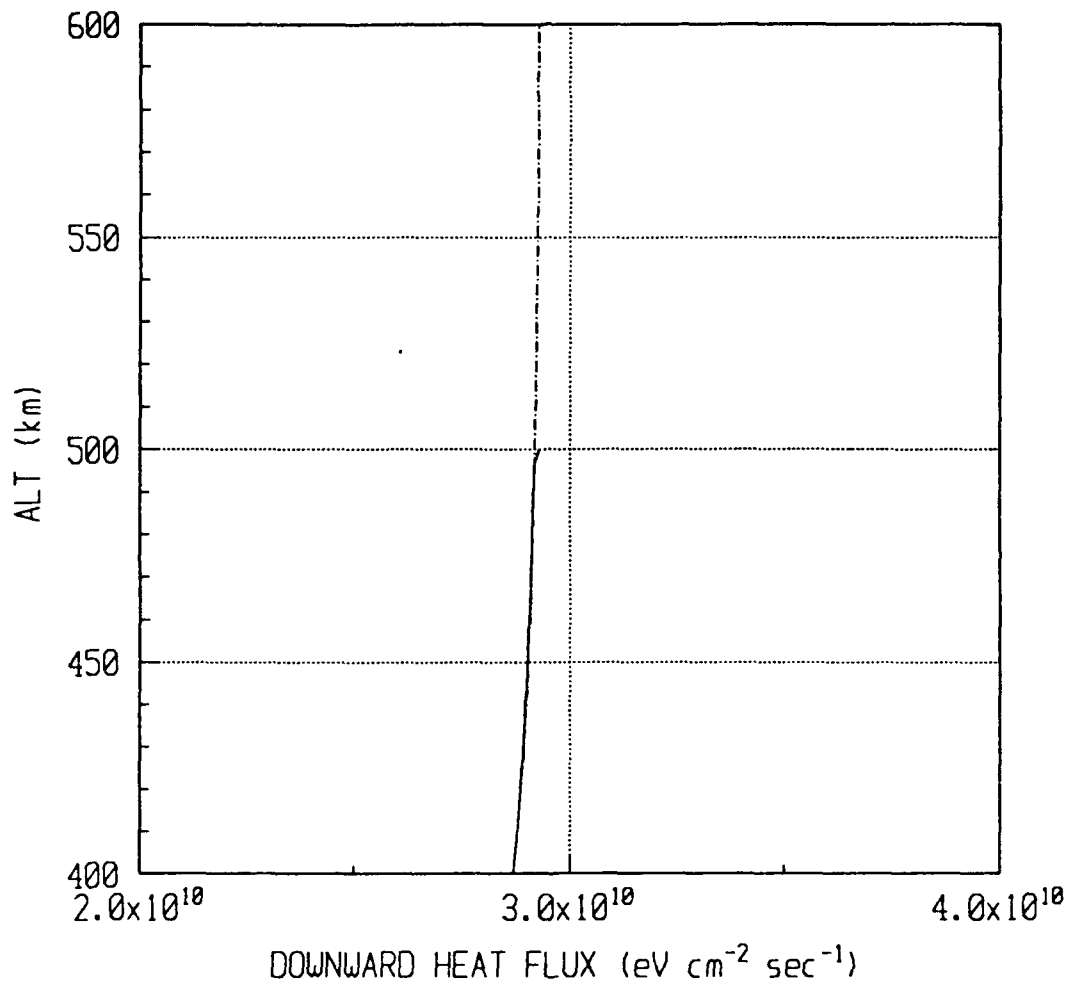


Fig. 20(b). Heat flux versus height for the calculated $T_e(h)$ profile of Figure 20(a). The solid curve is q_e from the T_e solver, and the dash-dot curve is the fitted function. For this case, $q_e(400) = 2.87 \times 10^{10}$, $q_e(500) = 2.93 \times 10^{10}$ (from the solid curve), $q_e(600) = 2.93 \times 10^{10}$, $q_\infty = 2.93 \times 10^{10}$, and $H = 60$ km.

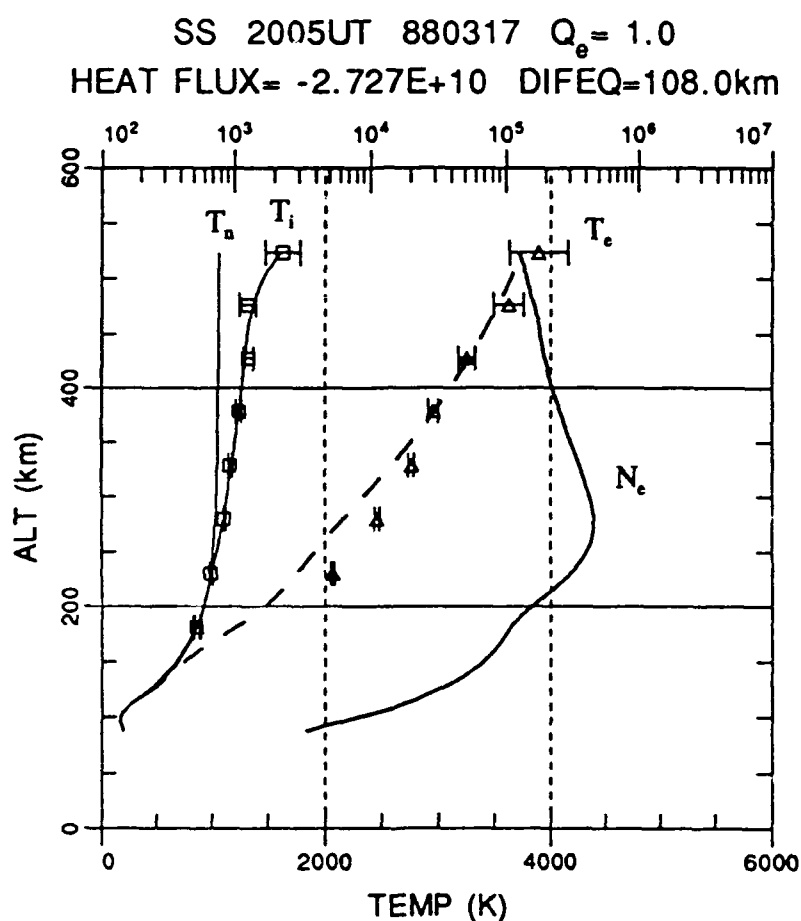


Fig. 21(a). Sondrestrom T_e , T_i , and N_e data for 17 March 1988 at 2005UT (1705LT). Triangles denote T_e data points; squares are for T_i data points. The N_e curve is the solid line to the right of the temperature profiles. The N_e scale, in cm^{-3} , is located on the upper x-axis. The solid line through the T_i data points is the T_i spline, and the other solid line is the MSIS90 $T_n(h)$ curve. The long-dashed line is the calculated T_e profile for $Q_e = 1$. The heat flux shown in the legend is for the altitude of the highest ISR data point, and DIFEQ is the lower bound for which we solve equation 2.9.

SS 880317 2005UT
HEAT FLUX VS. HEIGHT

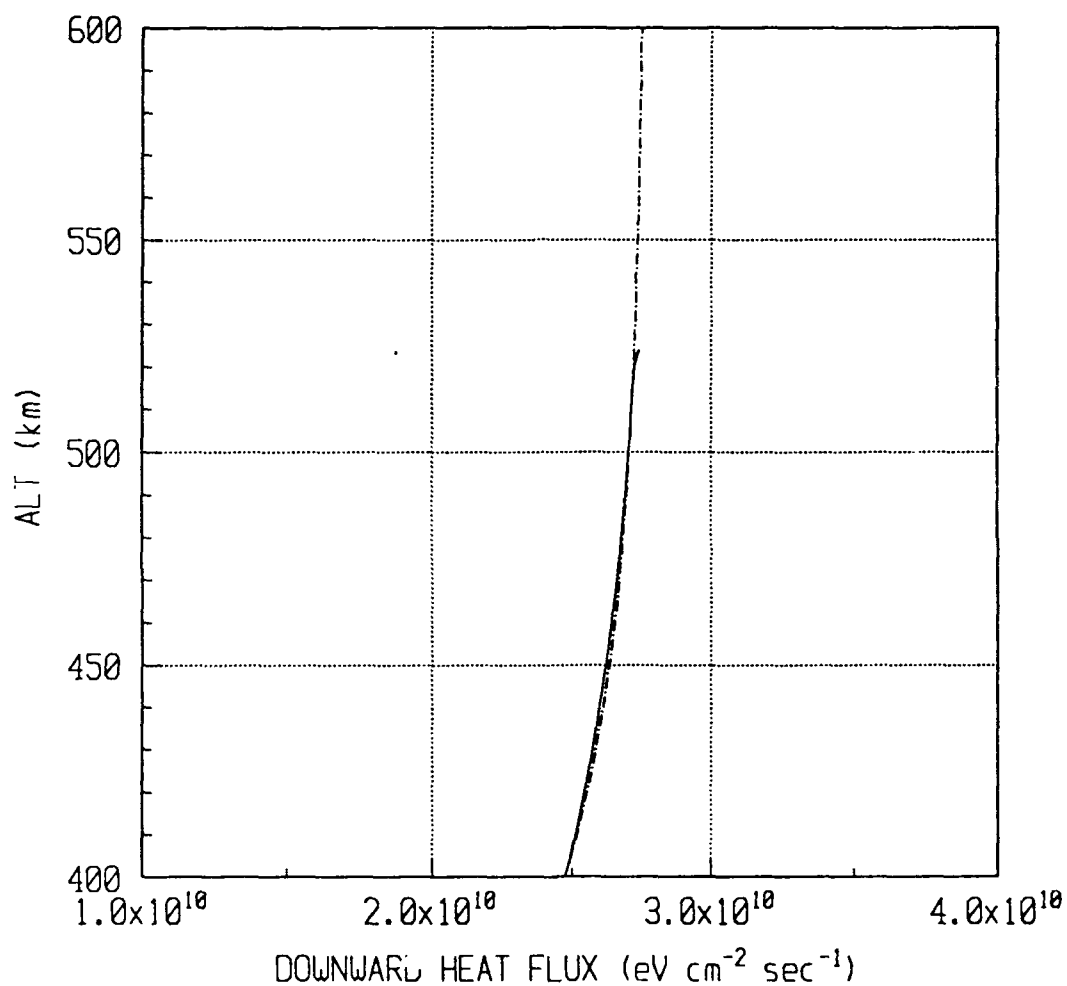


Fig. 21(b). Heat flux versus height for the calculated $T_e(h)$ profile of Figure 21(a). The solid curve is q_e from the T_e solver, and the dash-dot curve is the fitted function. For this case, $q_e(400) = 2.48 \times 10^{10}$, $q_e(524) = 2.74 \times 10^{10}$ (from the solid curve), $q_e(600) = 2.75 \times 10^{10}$, $q_\infty = 2.76 \times 10^{10}$, and $H = 60$ km.

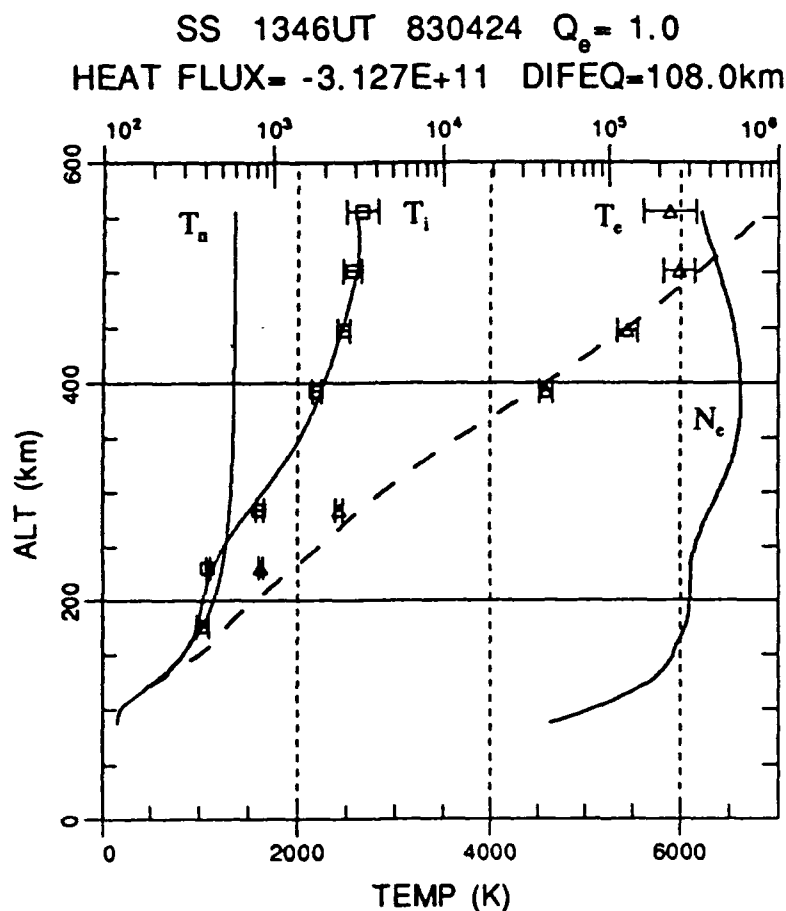


Fig. 22(a). Sondrestrom T_e , T_i , and N_e data for 24 April 1983 at 1346UT (1046LT). Triangles denote T_e data points; squares are for T_i data points. The N_e curve is the solid line to the right of the temperature profiles. The N_e scale, in cm^{-3} , is located on the upper x-axis. The solid line through the T_i data points is the T_i spline, and the other solid line is the MSIS90 $T_a(h)$ curve. The long-dashed line is the calculated T_e profile for $Q_e = 1$. The heat flux shown in the legend is for the altitude of the highest ISR data point, and DIFEQ is the lower bound for which we solve equation 2.9.

SS 830424 1346UT
HEAT FLUX VS. HEIGHT

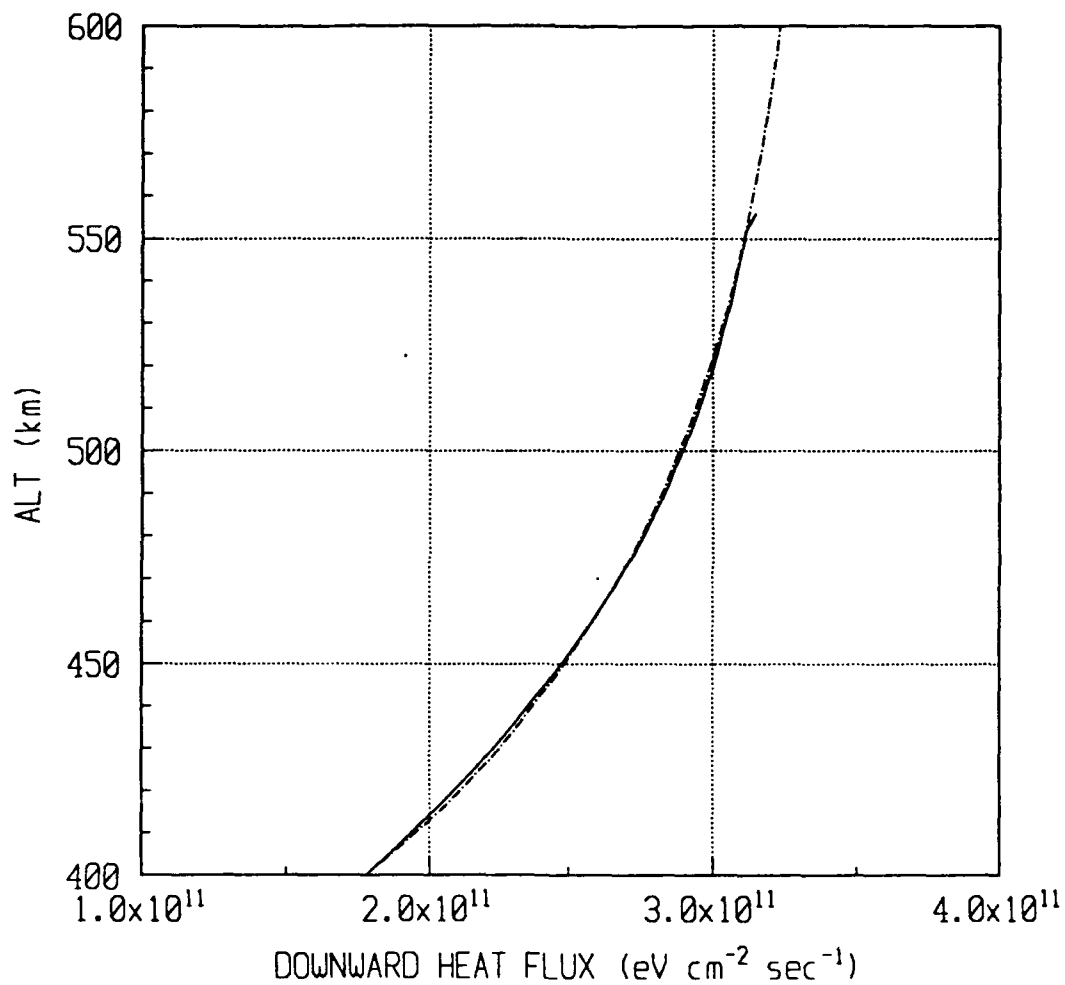


Fig. 22(b). Heat flux versus height for the calculated $T_e(h)$ profile of Figure 22(a). The solid curve is q_e from the T_e solver, and the dash-dot curve is the fitted function. For this case, $q_e(400) = 1.78 \times 10^{11}$, $q_e(556) = 3.13 \times 10^{11}$ (from the solid curve), $q_e(600) = 3.23 \times 10^{11}$, $q_\infty = 3.39 \times 10^{11}$, and $H = 86$ km.

asymptotic and thus can easily be extended up to 600 km. The situation shown in Figure 22 has already been introduced as an extreme case. The heat flux for the ISR T_e profile in panel (a) is -3.127×10^{11} eV cm⁻² s⁻¹. From Figure 22(b), the $q_e(600 \text{ km})$ given by equation 4.1 is -3.23×10^{11} , which corresponds to only a three percent increase in the heat flux. It is also interesting to note that H is approximately equal to the neutral scale height.

Finally, we had to deal with bad data and missing data (bad data will be discussed in section 4.2.1). A given temperature profile was skipped when bad or missing data reduced the number of T_i data points to five or less. This was done because profiles with five or fewer T_i data points tended to produce an erratic T_i spline.

4.2.1. Sondrestrom Data

Table 5 lists the days for which Sondrestrom data were analyzed. Also listed in Table 5 is the average highest heat flux for the day (not including short-term "peaks" or "valleys" in the heat flux -- these features will be discussed separately), the daily 10.7-cm flux value, the 24-hour A_p value, the 3-hour K_p value for the time of highest average heat flux, and the A_p values for one and two days prior (K_p is written such that 3⁻ is represented by 2.7 and 3⁺ by 3.3). Table 5 also lists the "daily" volume heating rate multiplier, Q_e , which, for a given day, resulted in calculated T_e profiles that best fit the low-altitude (below about 350 km) ISR T_e data points. This "daily" Q_e multiplier was determined by visually comparing the low-altitude T_e profiles and data points for each data set throughout a particular day.

To illustrate how the heat fluxes in Table 5 were obtained, we look at 17 March 1988

TABLE 5. Sondrestrom Days

Date	heat flux	f10.7	Ap	Qe	Kp	Ap - 1	Ap - 2
24-Apr-83	3.00E+10	142.7	61	1	5.7	17	17
18-May-83	2.00E+10	137.6	12	1	2.7	64	9
15-Jun-83	2.00E+10	128.7	16	1	3.3	12	70
13-Jul-83	2.50E+10	123.5	19	1	3	16	4
26-Jun-84	1.50E+10	100.1	8	1	2	10	22
27-Jun-84	1.50E+10	101.5	10	1	1.7	8	10
28-Jun-84	2.00E+10	99.5	21	1	3.7	10	8
15-Jan-85	8.00E+09	72.4	9	1	2	9	14
16-Jan-85	7.00E+09	74.7	8	1	2	9	9
17-Jan-85	2.00E+10	75.8	9	1	2.3	8	9
18-Jan-85	6.00E+09	74.1	6	1	1	9	8
21-Mar-85	9.00E+09	76.1	5	1	1.3	5	9
12-Apr-85	1.00E+10	69.6	5	1	1.3	11	11
22-May-85	7.00E+09	82.7	5	1	1.3	8	5
13-Aug-85	2.00E+10	68.9	41	1	3.3	27	5
12-Nov-85	7.00E+09	74.7	4	1	1.7	10	19
28-Aug-86	1.00E+10	68.8	12	1	4	13	12
1-Apr-87	1.20E+10	72.5	10	1	1.7	4	4
27-Aug-87	1.80E+10	85.1	21	1	4.3	40	39
10-Nov-87	1.50E+10	89.2	11	1	2.3	10	4
25-Nov-87	1.00E+10	104.9	12	1	3.7	24	35
15-Jan-88	9.00E+09	112.4	63	2	3.7	48	7
17-Mar-88	1.00E+10	117.4	9	2	1.3	14	20

at Sondrestrom. Figure 23 shows heat flux versus UT time for this day. Notice the relatively stable heat flux pattern from about 1300UT (1000LT) to about 1700UT (1400LT). The horizontal line on the graph represents the mean maximum heat flux for the day (1×10^{10} eV cm⁻² s⁻¹). Notice that the heat flux "spikes" before 1300UT and after 1700UT do not enter into the average. Likewise, the heat flux "valleys" between 1300UT and 1700UT are not included in this average. One word of warning: these "average" heat flux values were determined subjectively by "eyeballing" the heat flux versus time graphs; therefore, the values listed should be used with caution. The Sondrestrom data in the CEDAR database could be used immediately by the T_e algorithm -- no further data processing was required. We were able to avoid further data processing because detailed N_e profiles (values sampled every 6 to 9 km) were available in the database. However, during the original data reduction, Sondrestrom analysts did assign a "usability" code to each of the temperature data points determined from the ACF's. This code involved such factors as the percentage uncertainty of T_e and T_i , the reduced χ^2 of the ACF fit, and the differences between the two Doppler velocity determinations [*private communication, V.B. Wickwar, 1992*]. Only data points that had a usability code of 2 were included in this study.

4.2.2. Millstone Hill Data

Table 6 lists the days for which Millstone Hill data were analyzed (format is the same as Table 5). Unlike Sondrestrom data, Millstone Hill N_e data required further reduction before we could use it in the T_e algorithm. Millstone Hill N_e data are of two types: short-pulse (~ 40 μ s) data, and long-pulse data (320 μ s or 640 μ s). The short-pulse

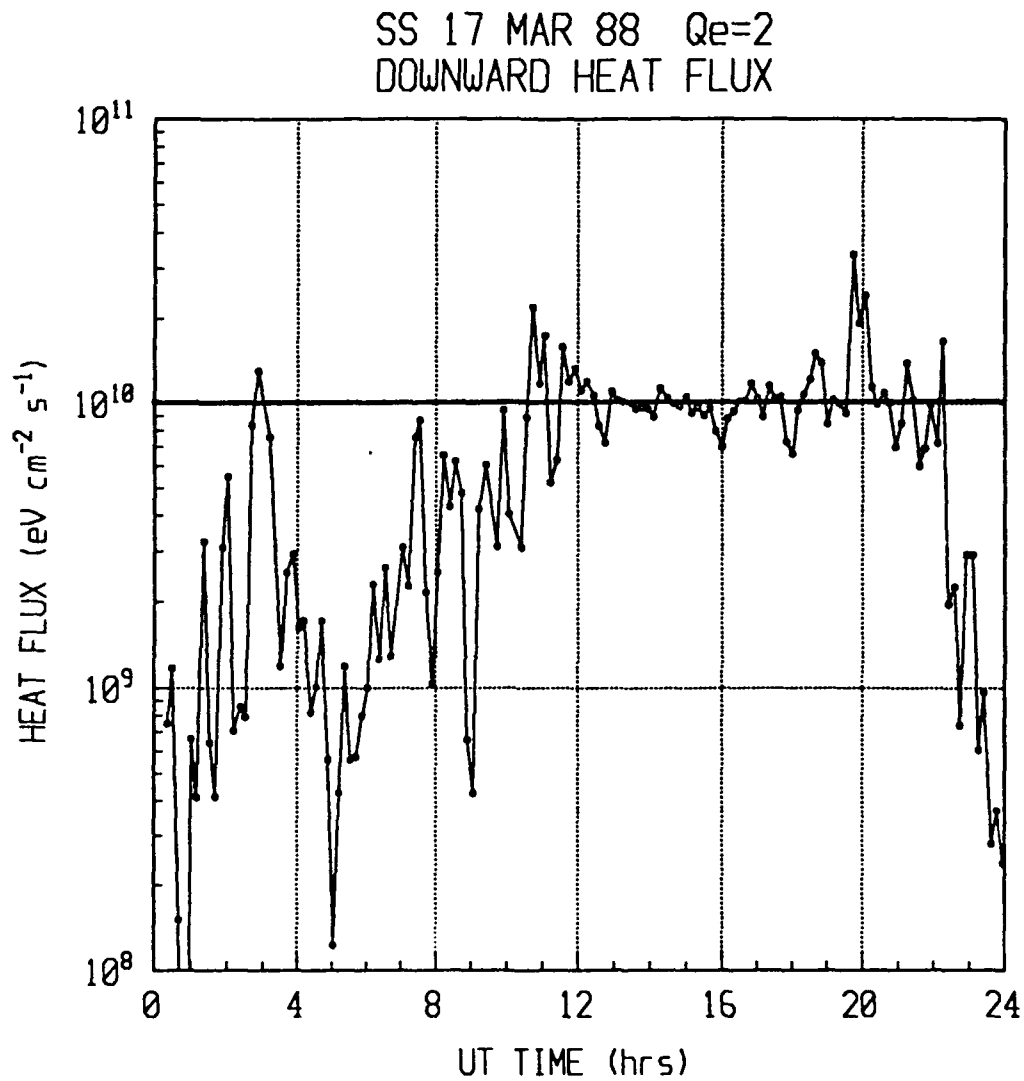


Fig. 23. Heat flux versus time for 17 March 1988 at Sondrestrom. The solid horizontal line represents the mean maximum heat flux for this day. Caution: these mean maximum heat flux values were determined by "eyeballing" graphs such as this one; therefore, the values in Tables 5 and 6 should be used with caution.

TABLE 6. Millstone Hill Days

Date	heat flux	f10.7	Ap	Qe	Kp	Ap - 1	Ap - 2
15-Jan-85	9.00E+09	72.4	9	1	3	9	14
16-Jan-85	1.00E+10	74.7	8	1	1	9	9
17-Jan-85	1.10E+10	75.8	9	1	2.7	8	9
20-Mar-85	1.10E+10	74.2	5	1	2	9	11
23-Apr-85	1.10E+10	93.3	12	1	3	11	103
21-May-85	1.10E+10	84.4	8	1	2.7	5	9
25-Jun-85	8.00E+09	71	12	1	3	5	7
1-Apr-86	1.20E+10	71.8	8	1	3	7	5
2-Apr-86	9.00E+09	70.6	5	1	1.3	8	7
28-Aug-86	1.00E+10	68.8	12	1	3.3	13	12
23-Sep-86	9.00E+09	68.7	43	1	4.7	4	11
24-Sep-86	9.00E+09	68.8	22	1	3.3	43	4
7-Oct-86	1.00E+10	74.3	5	1	1.3	12	19
8-Oct-86	1.10E+10	74.8	6	1	2.7	5	12
29-Oct-86	1.30E+10	91.4	15	1	2	9	16
30-Oct-86	1.10E+10	89.8	14	1	3	15	9
10-Dec-86	8.00E+09	72.3	12	1	2.7	6	4
11-Dec-86	8.00E+09	73	8	1	1.3	12	6
3-Jun-87	3.00E+10	76.4	4	4	1	8	8
25-Nov-87	1.20E+10	104.9	12	1	3	24	35
3-Feb-89	2.00E+10	185.8	44	4	4.7	21	29
9-May-89	2.00E+10	205.1	5	4	2	5	46
10-May-89	2.50E+10	208.7	4	4	1	5	5
20-Sep-90	1.80E+10	204	16	4	3	16	19
18-Dec-90	2.00E+10	201.6	5	4	2	6	8

provides higher resolution, but the short duration of the pulse causes the signal-to-noise ratio to drop below acceptable levels at high altitudes (above the F2 peak). This means that short-pulse N_e data are too noisy above the F2 peak to be of use. Conversely, the long-pulse gives a better signal-to-noise ratio above the F2 peak, but because of the long pulse length, the resolution is poor near the F-region peak and below. This makes long-pulse N_e data ideal above the F2 peak since the plasma scale height is large and thus the coarse resolution is adequate. The obvious thing to do then was to use short-pulse N_e data up to and through the F2 peak, then transition smoothly to the long-pulse N_e data.

Now the short-pulse N_e data is in "raw" form in the CEDAR database and had to be corrected before it could be "joined" with the long-pulse data. The correction is for the T_e / T_i ratio and Debye length according to:

$$N_c = \frac{1}{2} \left(1 + \alpha^2 + \frac{T_e}{T_i} \right) (1 + \alpha^2) N' \quad (4.1)$$

$$\alpha = \frac{4\pi\lambda_d}{\lambda}$$

$$\lambda_d = \left(\frac{\epsilon_0 k T_e}{e^2 N_c} \right)^{1/2}$$

where N' is the uncorrected (raw) electron density, λ_d is the Debye length (MKS units), λ is the radar wavelength, ϵ_0 is the permittivity of free space, k is Boltzmann's constant, e is the electron charge, and N_c is the corrected electron density. Since $\alpha^2 \propto 1 / N_c$, the correction must be done iteratively. We used the procedure outlined in *Wickwar* [1974].

The long-pulse N_e data did not need this correction because the N_e values were

determined in the fitting to the ACFs, which took the radar wavelength, Debye length, and temperature ratio into account.

Figure 24 gives an example of the joining process for Millstone Hill 1 Apr 86 at 1505UT (1005LT). The long-dash curve is the long-pulse N_e curve, the dot-dash curve is the short-pulse (raw) N_e curve, and the solid curve is the final N_e profile. Application of equation 4.1 shifts the raw short-pulse curve toward the long-pulse curve.

Finally, we found that, even after we applied equation 4.1, the short-pulse densities were still less than the long-pulse densities (but not by more than a factor of about 1.2). This difference occurs because the radar constant is derived for the long-pulse data. Therefore, the long-pulse data are fully corrected, and the short-pulse data had to be scaled up to the long-pulse data. This scale factor varied for each profile, but again was never larger than about 1.2.

We then tested the accuracy of the final N_e profile by assuming that the long-pulse N_e profile is simply the convolution of the actual N_e profile with a 96 km long square pulse (the radar pulse). Therefore, if we convolve our final N_e profile with a 96 km long square pulse, we should recover the long-pulse N_e profile. Figure 25 shows the results of the convolution procedure for the N_e profile of Figure 24. The dot-dash curve is the long-pulse profile, and the solid curve is the final N_e profile convolution. Overall, the fit is excellent. The portion of the long-pulse profile below about 190 km is not a real feature. Likewise, the sharp bend in the convolution curve above about 525 km is not real, but is due to the fact that the joined N_e profile in this example stops at 568 km.

One last potential problem with Millstone Hill data is high-altitude H^+ contamination.

MLH 860401 1505UT
RAW AND CORRECTED N_e PROFILES

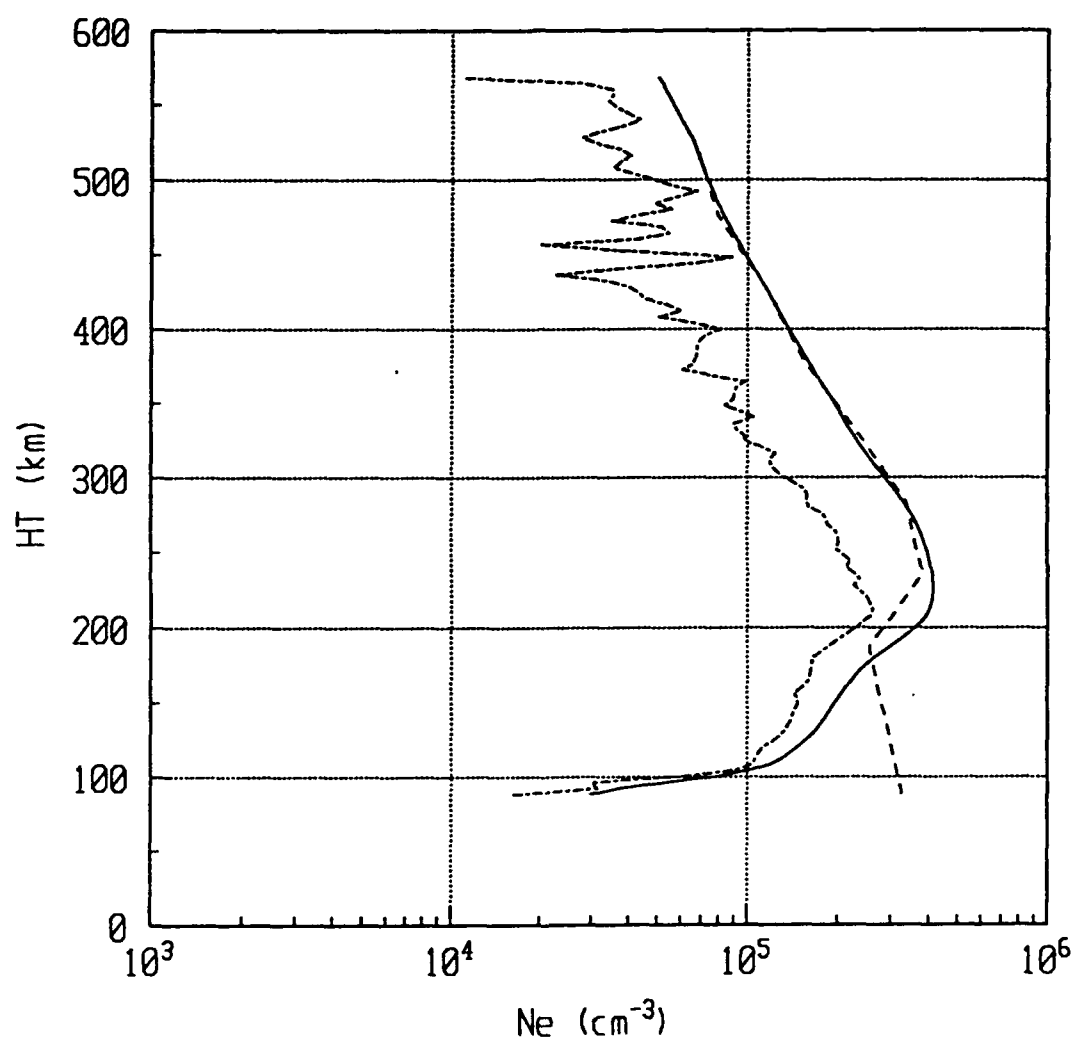


Fig. 24. Raw and corrected N_e profiles for 1 April 1986 at 1505UT (1005LT). The dot-dash curve is the raw short-pulse N_e data, the long-dash curve is the long-pulse N_e data, and the solid curve is the final (joined and corrected) N_e profile.

MLH 860401 1505UT
CONVOLUTION OF Ne PROFILE

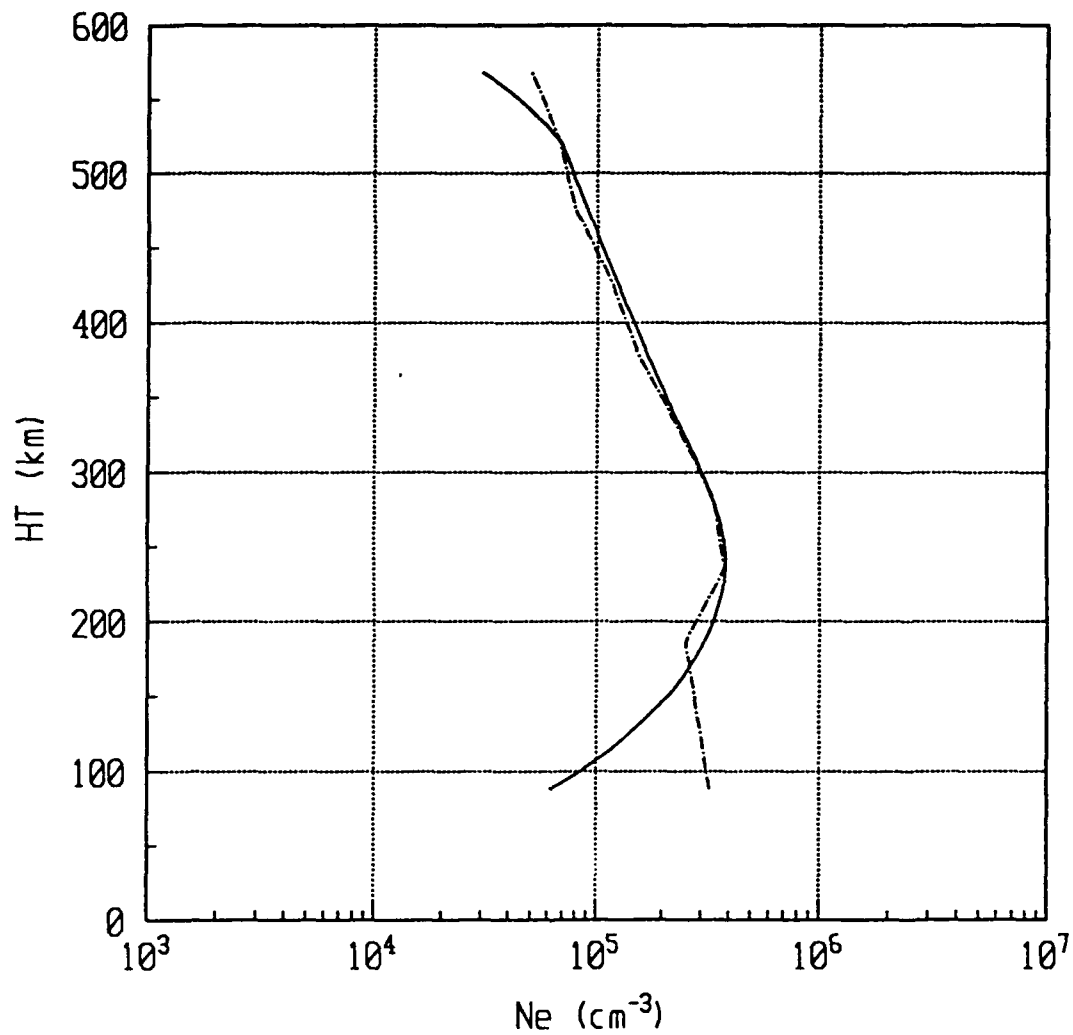


Fig. 25. Convolution of the final N_e profile (from Figure 24) with a 96 km long square pulse. The solid curve is the convolution, and the dot-dash curve is the long-pulse N_e profile.

The data reduction algorithm at Millstone Hill assumes an ion composition of 100 percent O^+ at high altitudes. At certain times, however, H^+ may be present in significant amounts above 400 km. At such times T_i may be overestimated (see section 4.1). This, in turn, would result in underestimated cooling rates. Since H^+ is most abundant at night and during solar minimum, these are the most likely times for contamination to occur [*private communication, S.A. Gonzalez, 1992*].

CHAPTER 5

RESULTS

Many interesting features resulted from the heat flux analysis of the Sondrestrom and Millstone Hill data. Sections 5.1 and 5.2 will cover the noteworthy findings from the Sondrestrom and Millstone Hill q_e analysis, respectively. Appendices III and IV contain tables of heat flux versus time, solar zenith angle, and conjugate point solar zenith angle for all the Sondrestrom and Millstone Hill days we analyzed, respectively.

5.1. SONDRESTROM DATA

Figure 26 shows heat flux versus date for 20 of the 23 days analyzed. The three days omitted from this graph were left off because no daytime measurements were taken, and so a heat flux comparison with the other days becomes questionable. The heat fluxes in this graph are the mean maximum heat fluxes from Table 5. This figure alone does not give us much information except that the mean maximum, q_e , varies from about -7×10^9 to about -3×10^{10} eV cm⁻² s⁻¹. More information can be gained by examining the variation of other geophysical parameters for the days of data we analyzed. Figure 27 shows a scatter plot of the mean heat flux versus the 10.7-cm flux (also called $F_{10.7}$). The line on the graph represents the linear least-squares fit through the data. The magnitude of the $F_{10.7}$ solar radio emission is often used as a surrogate for the level of overall solar activity. Accordingly, Figure 27 shows that the 10.7-cm flux varies from about 68 (solar minimum conditions) up to about 144 (active conditions). From the linear regression it is apparent that q_e is positively correlated with $F_{10.7}$.

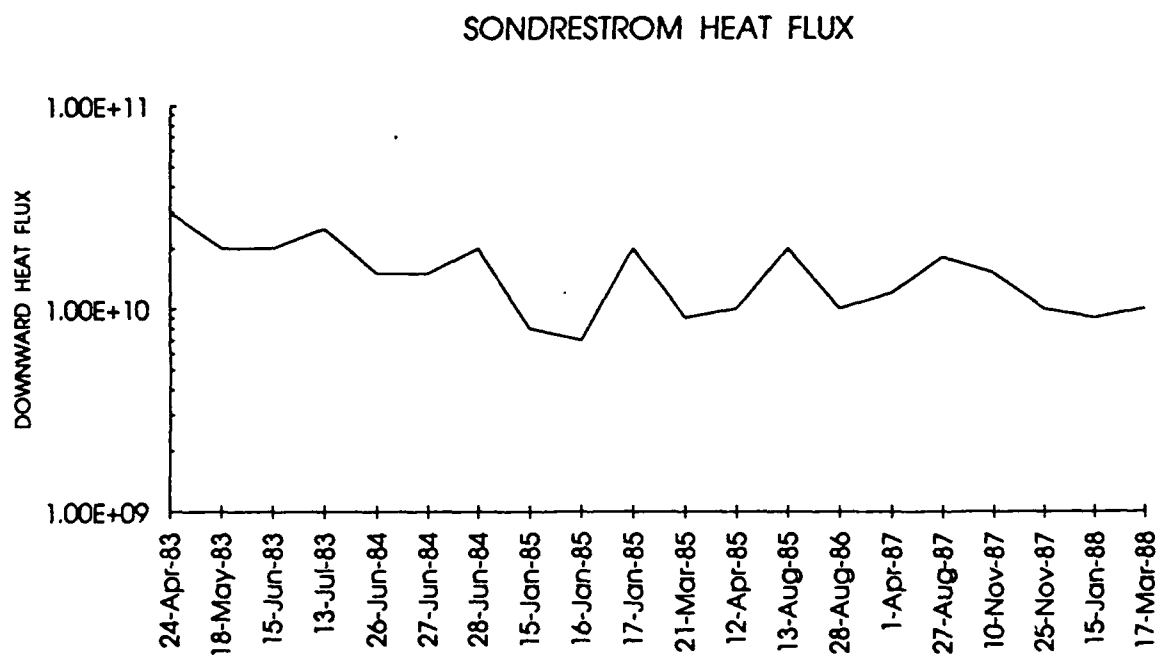


Fig. 26. Downward heat flux versus date for the Sondrestrom days analyzed (see Table 5). The units of heat flux are $\text{eV cm}^{-2} \text{s}^{-1}$.

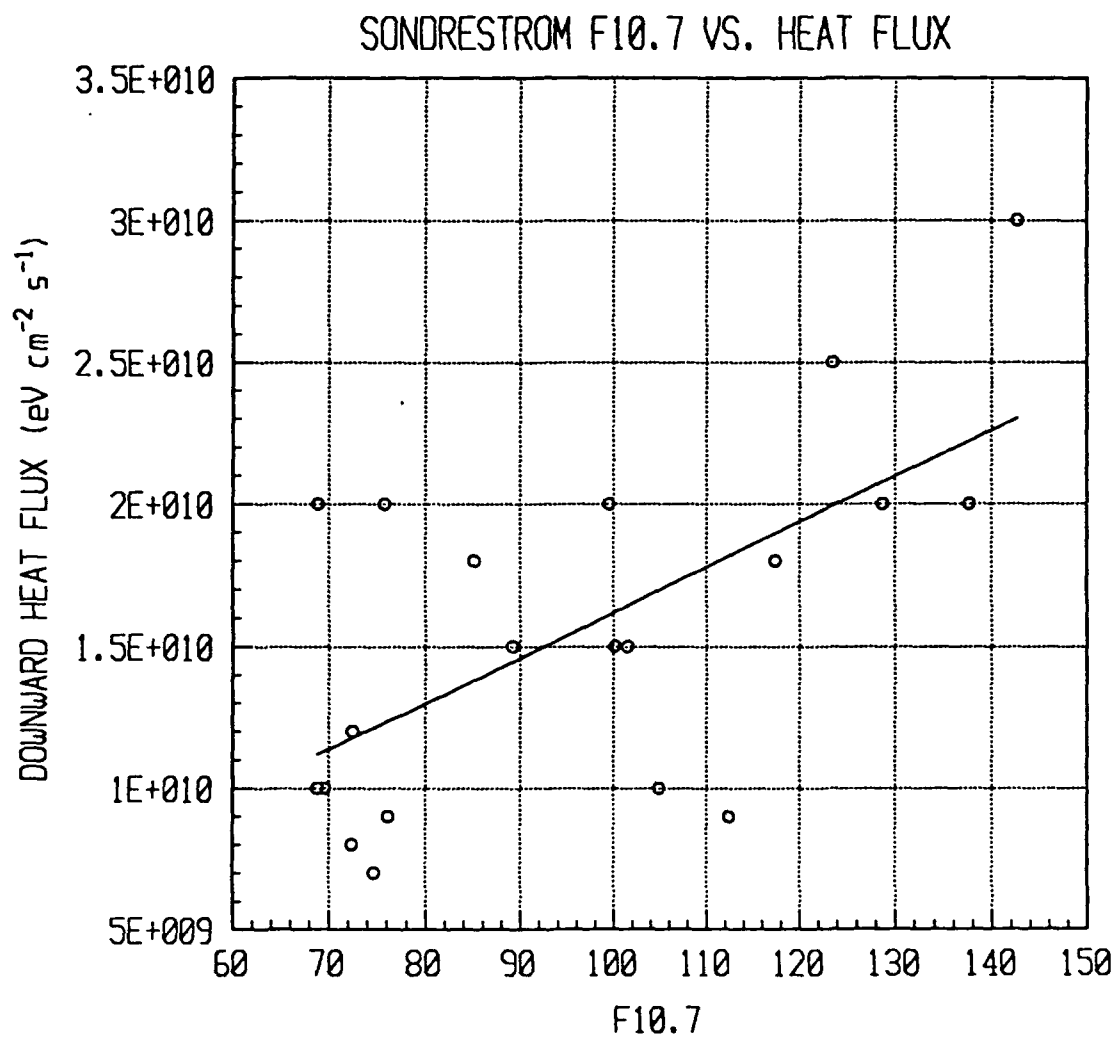


Fig. 27. Scatter plot of heat flux versus $F_{10.7}$ for the Sondrestrom days analyzed (see Table 5). The line represents the least-squares fit through the data points.

Figure 26 illustrates a long-term variability of heat flux. By analyzing many days throughout the solar cycle, one may also find dependences (of heat flux) on parameters that vary on shorter time scales. One example is geomagnetic activity. Figures 28 and 29 show scatter plots (and linear least-squares fits) of q_e versus the geomagnetic indices A_p and K_p , respectively. Both of these graphs show a positive correlation between heat flux and the level of geomagnetic activity, although the correlation with K_p is more convincing.

Heat flux during the day also exhibits other short-term variations. While a few of these variations were due to bad data, or to a calculated T_e profile that did not fit the data well, most of the variations are "real" and worthy of study (the only way to tell the difference between real and false q_e variations is to look at the individual calculated T_e profiles and compare them with the corresponding ISR data sets). Figure 30 shows heat flux versus time for 21 March 1985 at Sondrestrom. The four curves represent the heat flux for the different Q_e multipliers shown in the legend. There are several things to notice in this graph. First, the $Q_e = 0.5$, $Q_e = 1$, and $Q_e = 2$ curves are very similar, while the $Q_e = 4$ curve obviously represents too much solar input for this day (it caused the calculated T_e 's to be overestimated). For the remaining three curves, the heat flux is fairly independent of the Q_e multiplier (a fact we introduced in chapter 3). In fact, for this day, a factor of four change in Q_e (0.5 - 2) resulted in only a 50 percent change in heat flux. Thus the cross-correlation between q_e and Q_e is small for this day, and was equally small for the other 47 days of data we analyzed.

In addition, q_e in the figure shows a definite diurnal variation; the higher heat fluxes

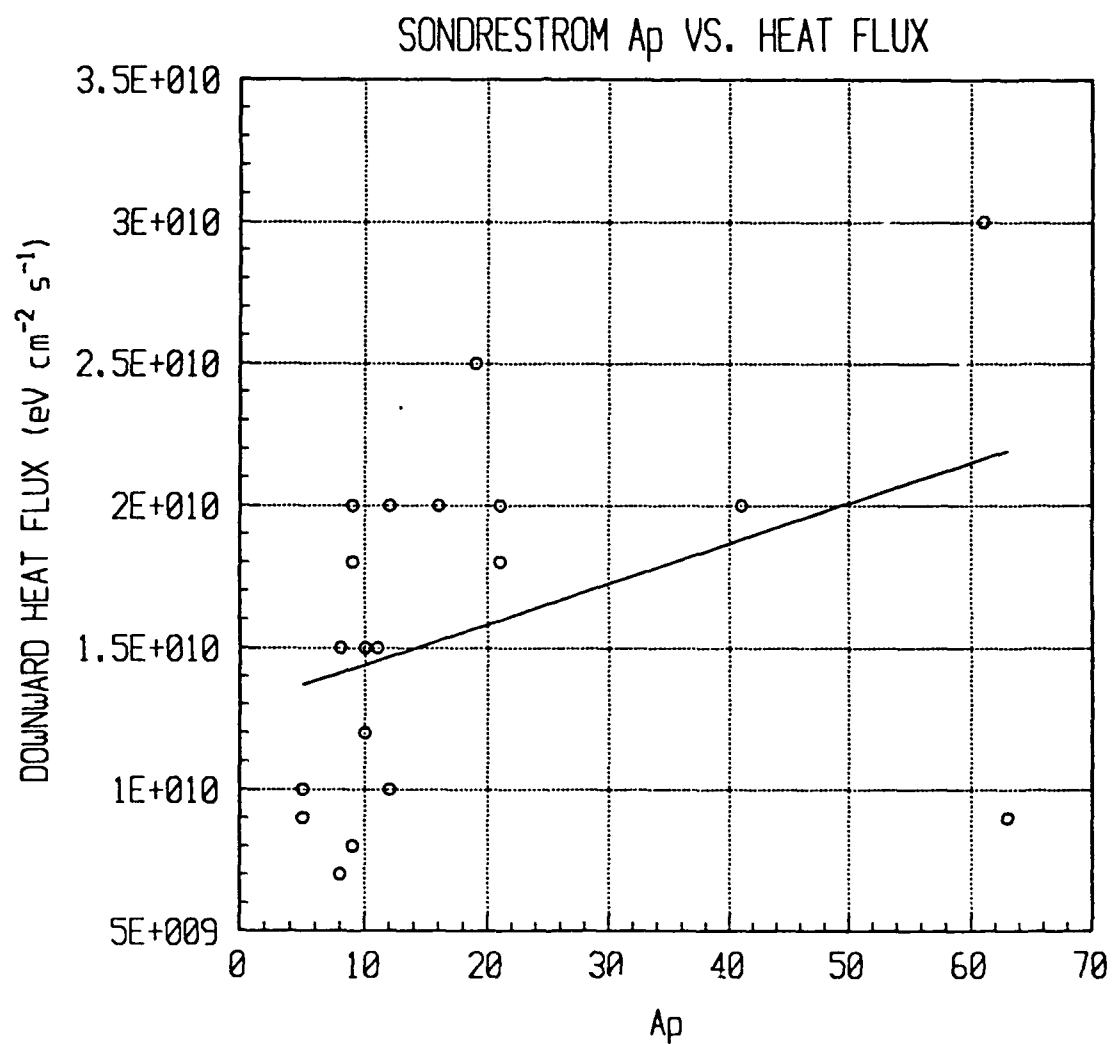


Fig. 28. Scatter plot of heat flux versus A_p for the Sondrestrom days analyzed (see Table 5). The line represents the least-squares fit through the data points.

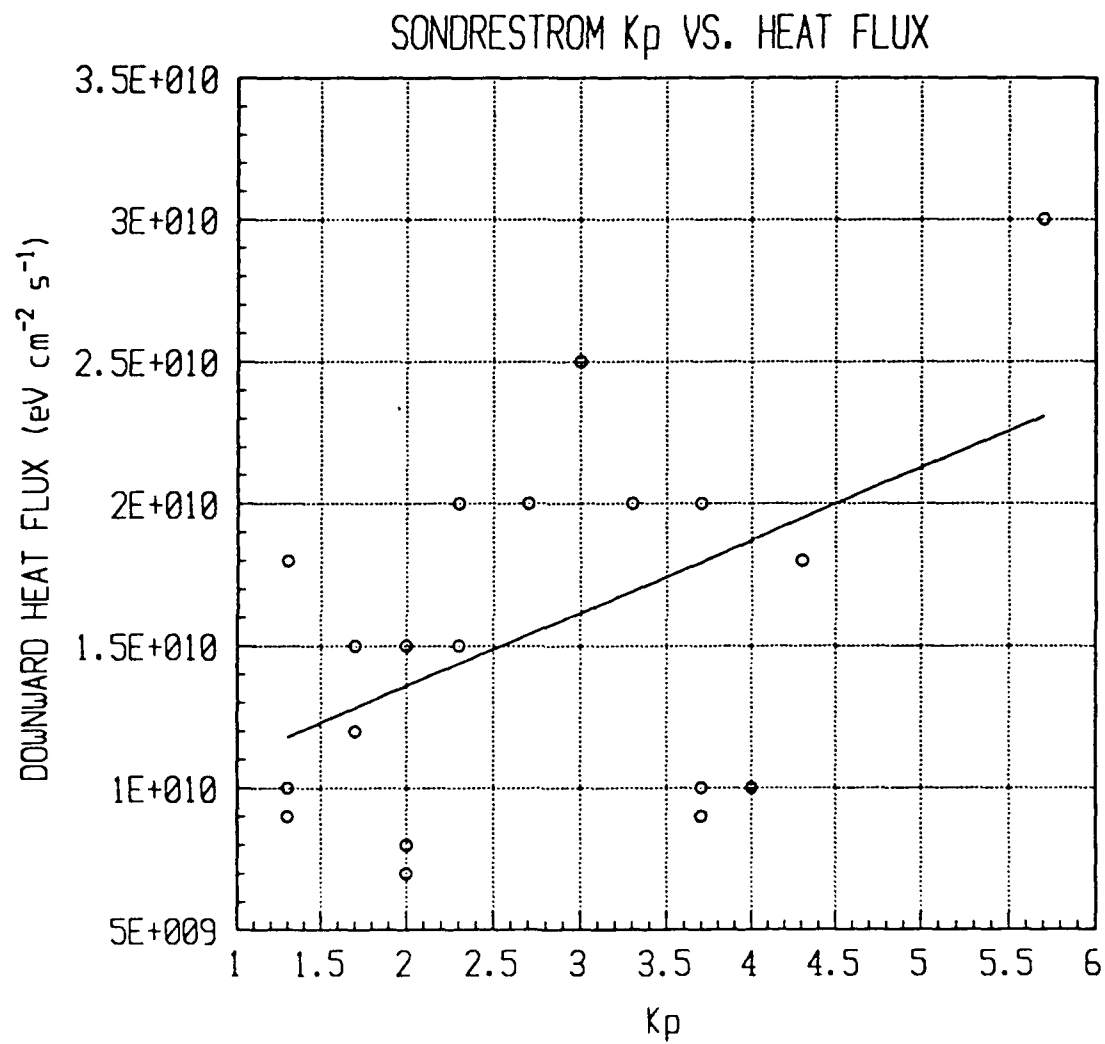


Fig. 29. Scatter plot of heat flux versus K_p for the Sondrestrom days analyzed (see Table 5). The line represents the least-squares fit through the data points.

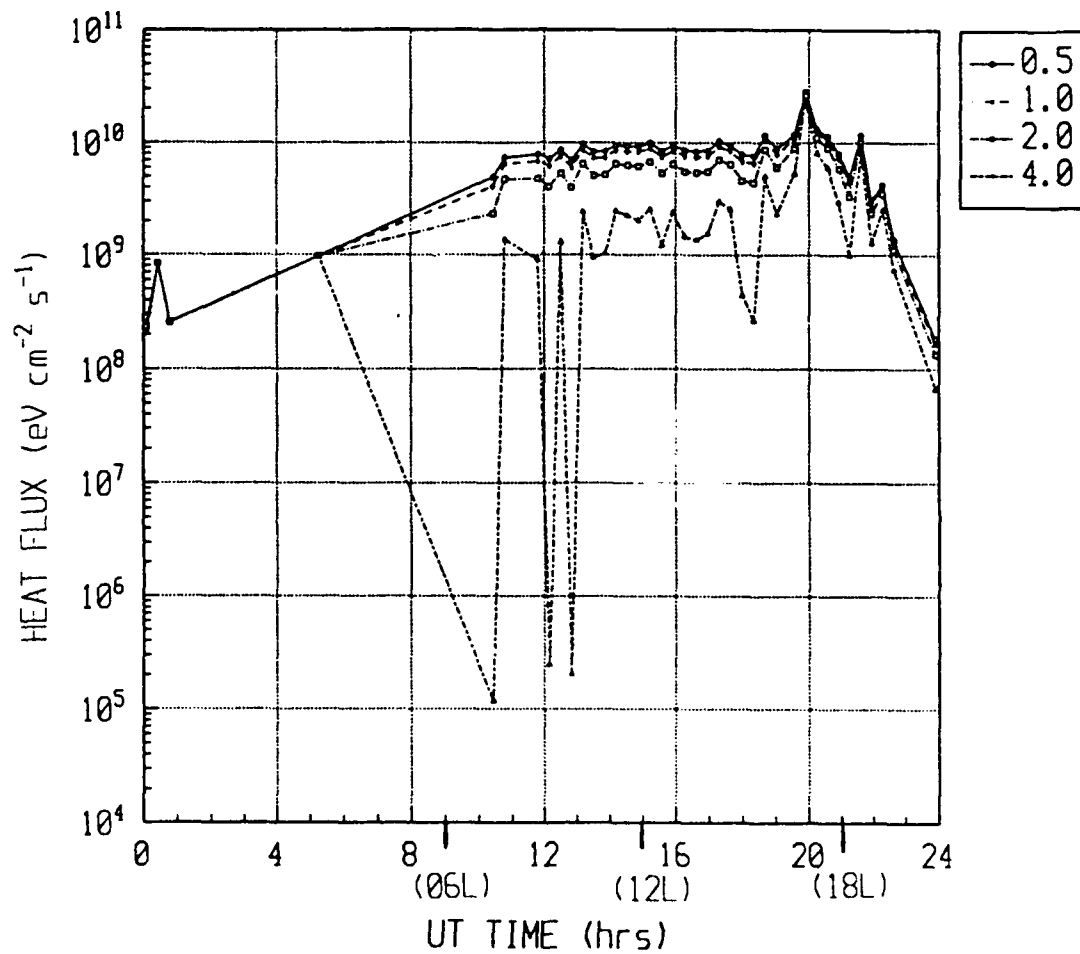
SS 21 MAR 85
DOWNWARD HEAT FLUX

Fig. 30. Downward heat flux versus time for 21 March 1985 at Sondrestrom. The units of heat flux are $\text{eV cm}^{-2} \text{s}^{-1}$. The four curves shown correspond to the volume heating rate multipliers given in the legend.

occur mainly during the day. One also sees shorter time scale q_e variations superimposed on the diurnal variations. For example, the heat flux curve is quite smooth between about 1200UT (0900LT) and 1900UT (1600LT). After this time, however, two heat flux "spikes" occur: one near 2000UT (1700LT), and the second around 2130UT (1830LT). Notice that, during these "spikes," q_e is especially independent of the volume heating rate multiplier. As stated above, we found that some q_e spikes were not "real." However, these two spikes were accompanied by an increase in T_e at high altitudes. To study the spike phenomenon more closely, we move on to two more dramatic examples.

Figure 31 shows another q_e versus time plot for 24 April 1983 at Sondrestrom. We have already identified this day as unusual (sections 3.3.3 and 4.2). We will examine $\Delta q_e / \Delta t$ (and its relation to $\Delta T_e / \Delta t$) between 1028UT (0728LT) and 1757UT (1457LT). To aid in this comparison, we will use Figures 32(a) through 32(c). Figure 32(a) shows a 3-D plot of $T_e(h)$ versus time (1000UT - 1800UT). Each T_e profile is color-coded (see legend), and time increases from upper right to lower left. Figures 32(b) and 32(c) show the T_i and N_e profiles for the same period, respectively. These two graphs are color-coded exactly the same as Figure 32(a), i.e., a given time has the same color profile in all three graphs. In Figure 31 there are three noticeable heat flux spikes: the first (and the biggest) is at 1346UT (1046LT), the second at 1442UT (1142LT), and the third at 1633UT (1333LT). Comparing these spikes with the corresponding T_e curves in Figure 32(a), we see that the T_e (at high altitudes) is increased at the times of the q_e spikes. Conversely, at those times during the period when q_e is smaller, T_e is also reduced. This positive correlation between T_e and q_e is consistent with theory. In Figure 32(b) we see

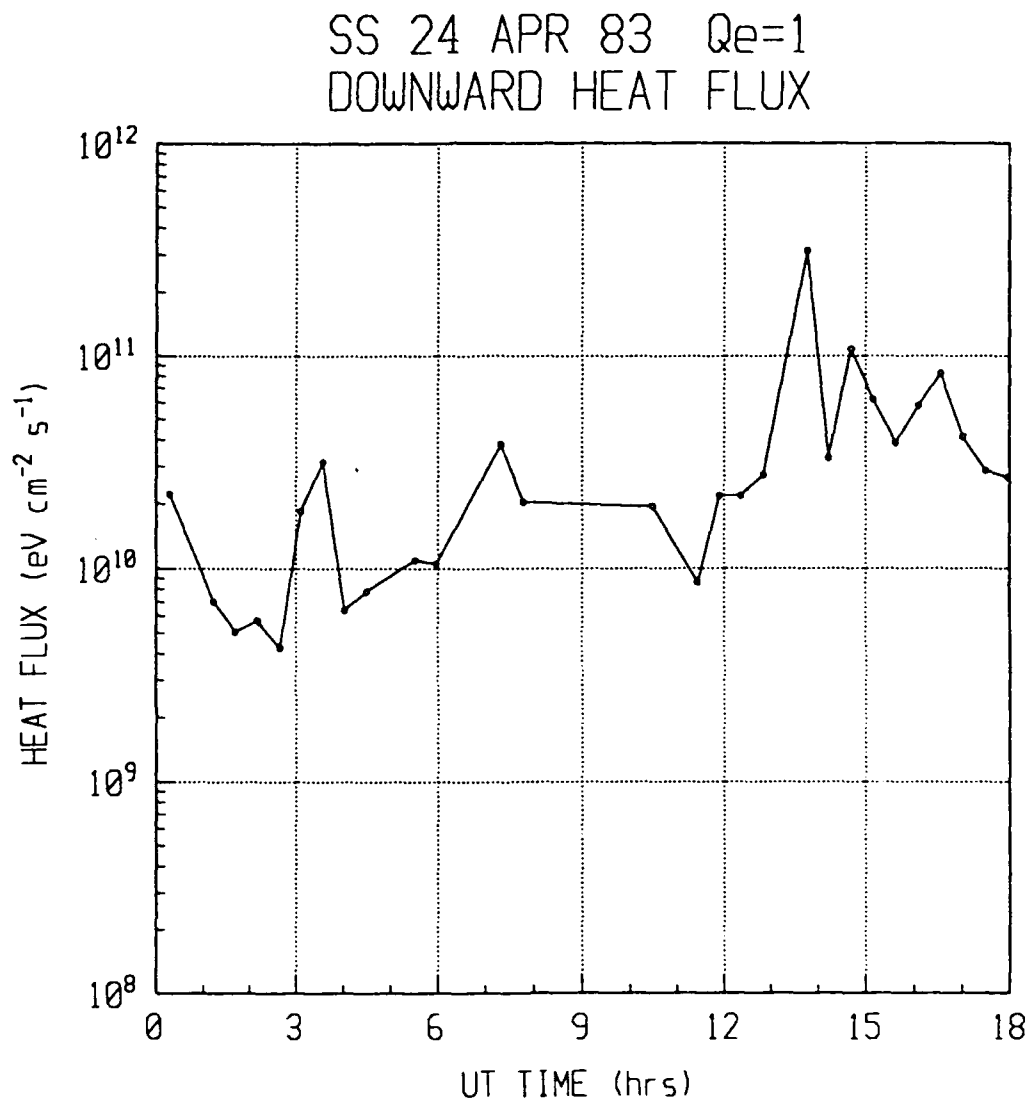


Fig. 31. Heat flux versus time for 24 April 1983 at Sondrestrom. The heat flux curve is for $Q_e = 1$.

SS 830424

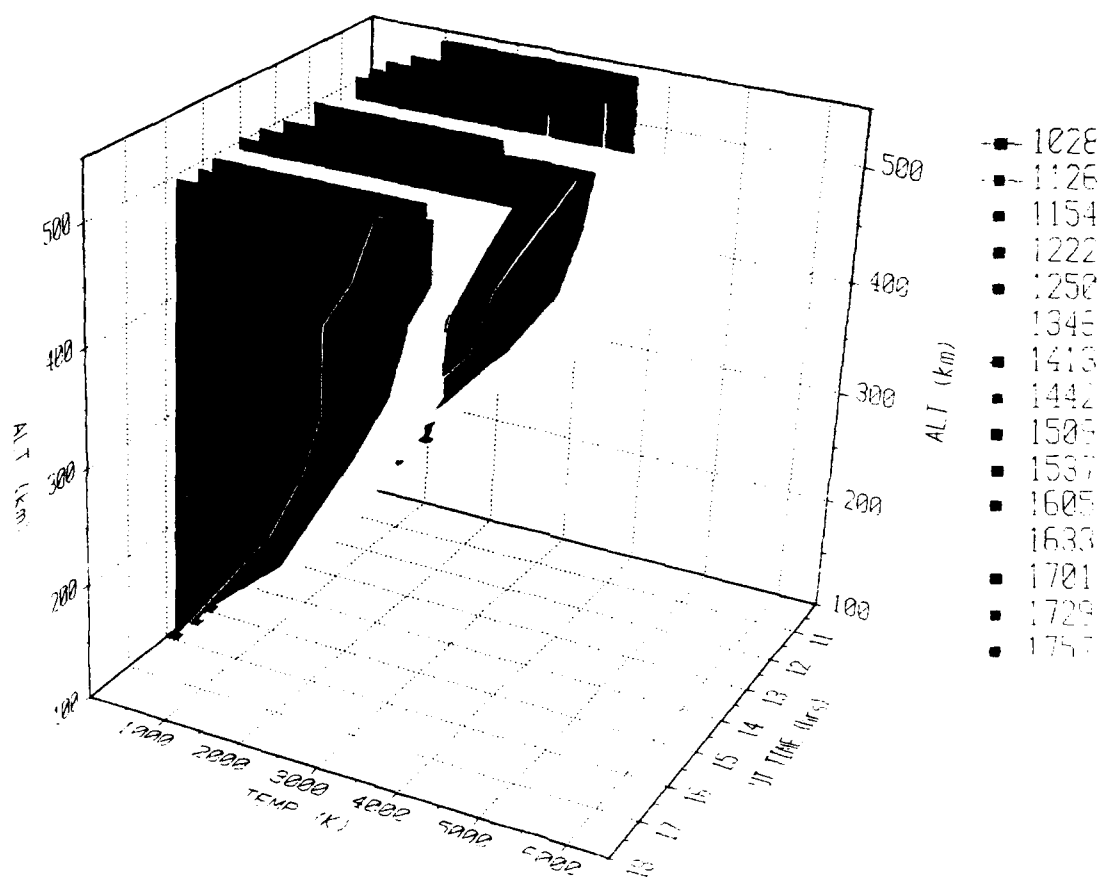
 T_e HEIGHT PROFILES vs TIME

Fig. 32(a). Electron temperature profiles versus time for 24 April 1983 at Sondrestrom. The T_e profiles are color-coded according to the legend. Time progresses in the graph from upper right to lower left.

SS 830424

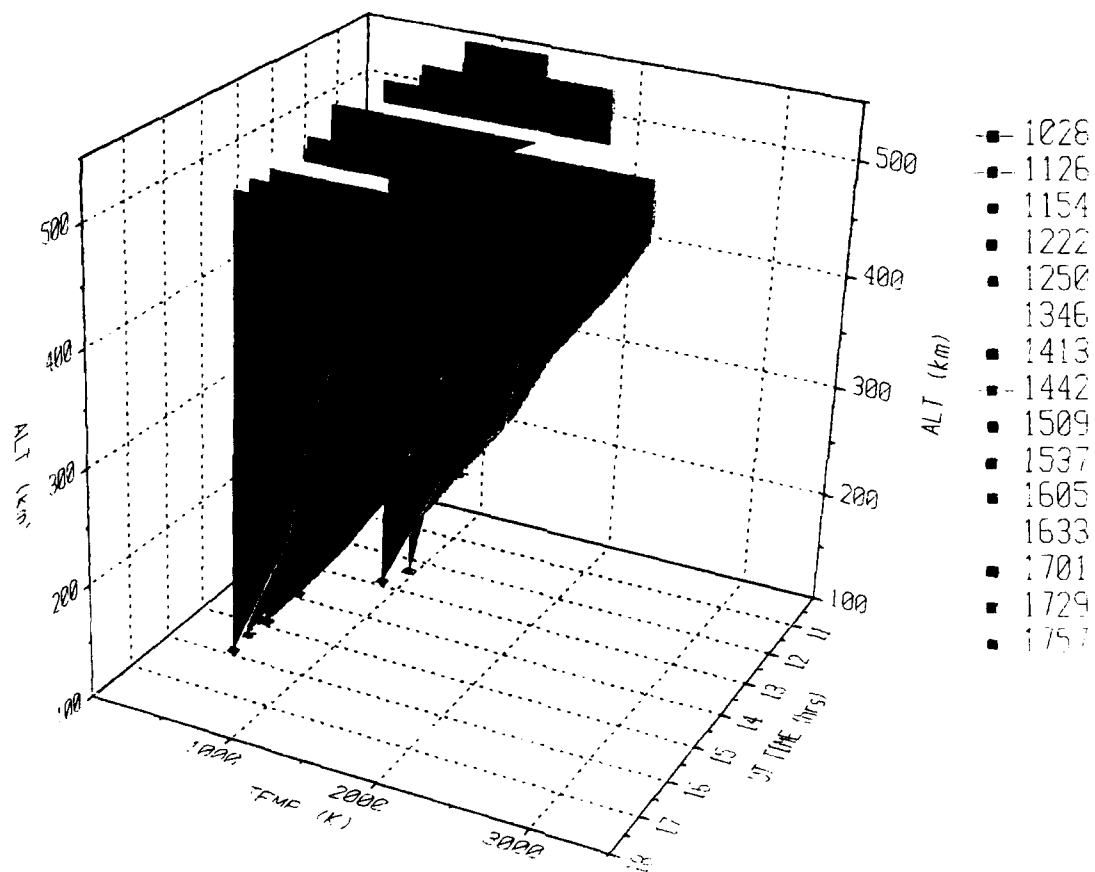
 T_i HEIGHT PROFILES vs TIME

Fig. 32(b). Ion temperature profiles versus time for 24 April 1983 at Sondrestrom. The T_i profiles are color-coded according to the legend. Time progresses in the graph from upper right to lower left.

SS 830424

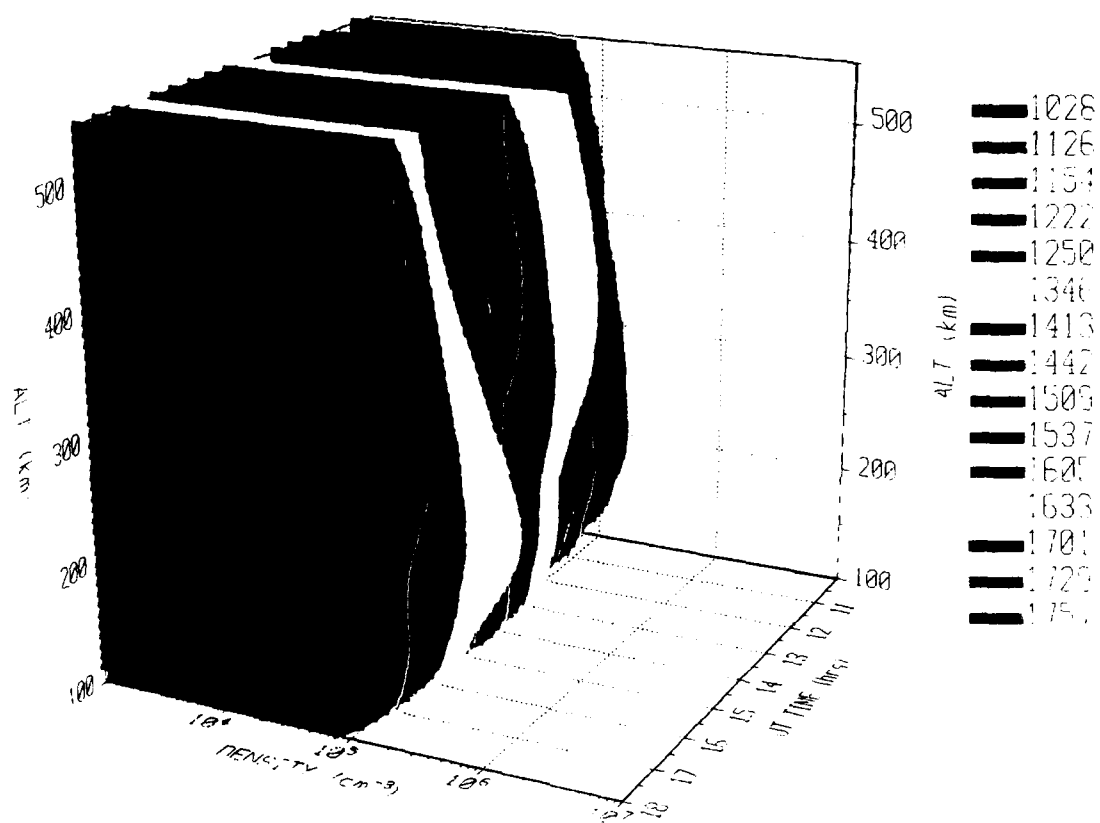
 N_e HEIGHT PROFILES vs TIME

Fig. 32(c). Electron density profiles versus time for 24 April 1983 at Sondrestrom. The N_e profiles are color-coded according to the legend. Time progresses in the graph from upper right to lower left.

that T_i is also increased at 1346UT and 1442UT. This increase in T_i may well be caused by ion heating ($\propto N_e^2$) due to coulomb collisions with the hot electrons; at both 1346UT and 1442UT the electron density is enhanced. However, by 1633UT the electron density has decreased at high altitudes (relative to N_e at 1346UT and 1442UT). This means that ion heating has decreased, and, as we see from Figure 32(c), T_i has decreased. Finally, Figure 32(c) shows that N_e (at F-region altitudes) is enhanced during the three heat flux spikes. The association of the N_e increase with the T_e increase is indicative of particle precipitation. With the N_e increases occurring higher in the F-region during the first two events, one can infer they arise from lower energy particles than during the third event. The primary electron energy in all three cases has to be less than the usual auroral energies that give rise to enhanced N_e layers at 120 km and below. As discussed in section 3.3.3, the unusual activity on this day has been studied by *Kofman and Wickwar* [1984]. The increased T_e values (at least for 1346UT) occurred at the afternoon convection reversal, and came about because of a large downward heat flux.

Another series of graphs, including Figures 33 and 34(a)-(c), illustrate this same correlation between T_e and q_e for 28 June 1984 at Sondrestrom. As shown in Table 5, this day was also geomagnetically active, with an A_p of 21 and a 3-hr K_p of 4⁻ (for the time frame of interest). In Figure 33, we see that the period of increased heat flux values begins at 1140UT (0840LT), and continues through about 1400UT (1100LT). The heat flux maxima during this period occur at 1232UT (0932LT), 1318UT (1013LT), and 1402UT (1102LT). The electron temperature and heat flux during this period show a definite correlation, while q_e and T_i have a weaker correlation. This weak correlation is

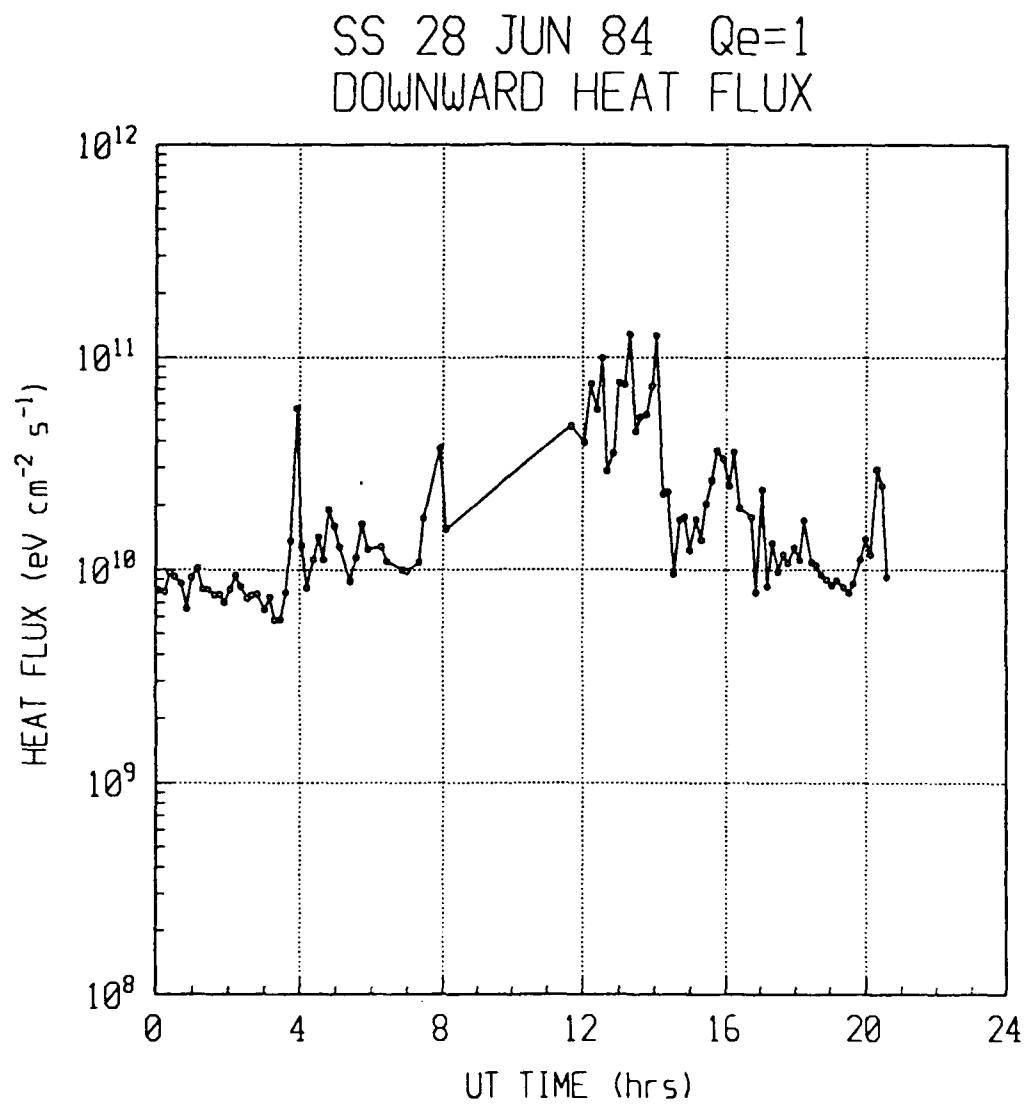


Fig. 33. Heat flux versus time for 28 June 1984 at Sondrestrom. The heat flux curve is for $Q_e = 1$.

SS 840628

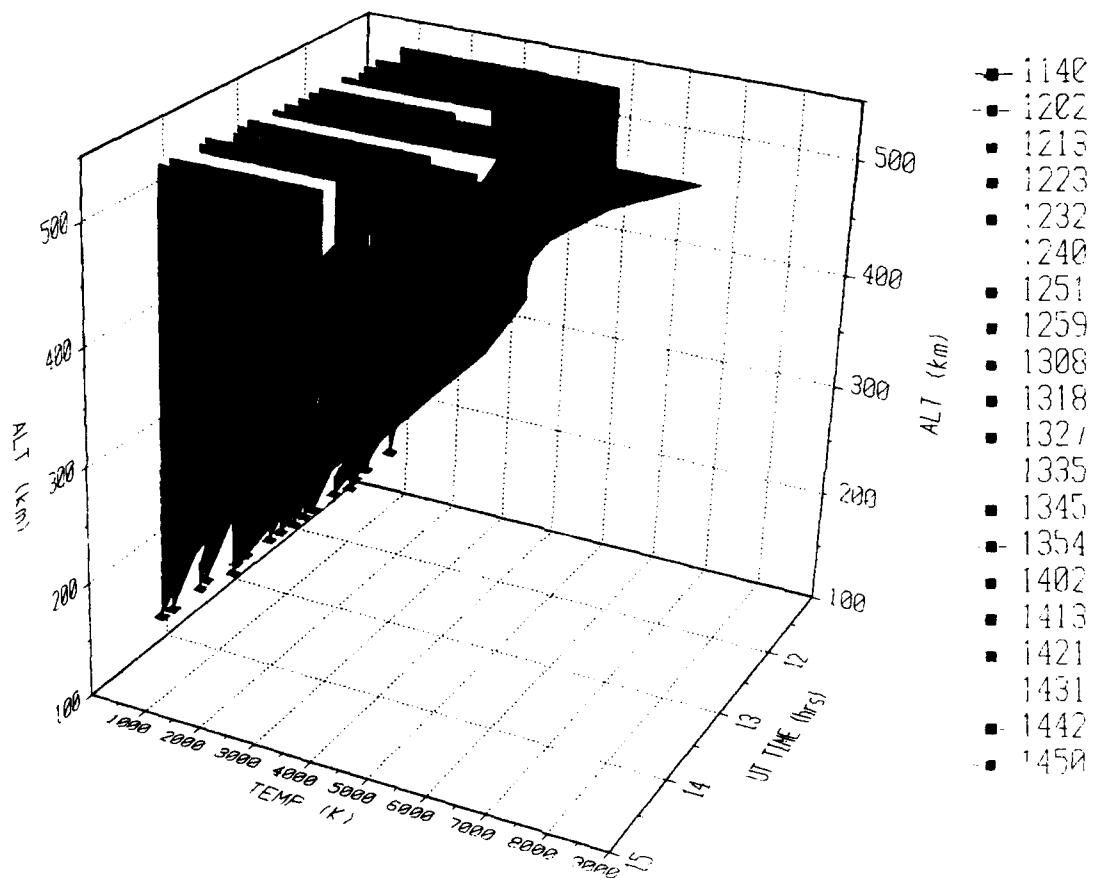
 T_e HEIGHT PROFILES vs TIME

Fig. 34(a). Electron temperature profiles versus time for 28 June 1984 at Sondrestrom. The T_e profiles are color-coded according to the legend. Time progresses in the graph from upper right to lower left.

SS 840628

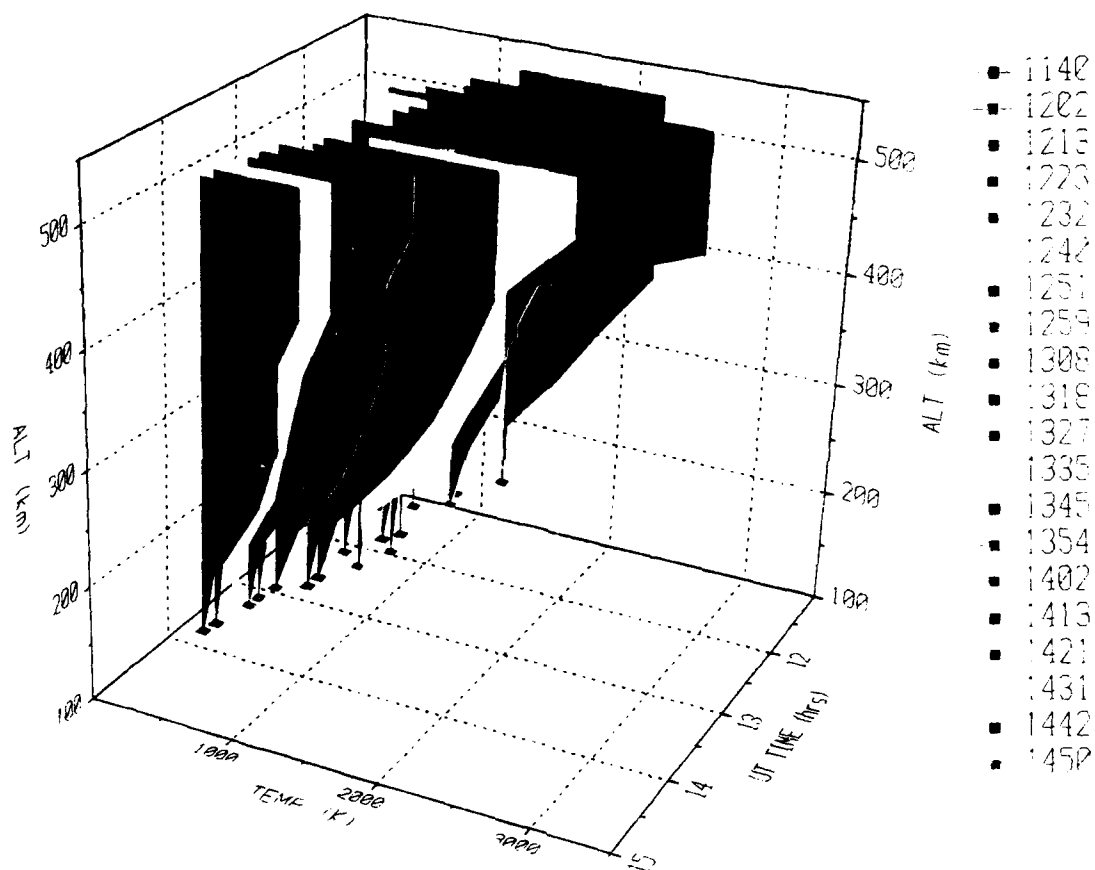
T_i HEIGHT PROFILES vs TIME

Fig. 34(b). Ion temperature profiles versus time for 28 June 1984 at Sondrestrom. The T_i profiles are color-coded according to the legend. Time progresses in the graph from upper right to lower left.

SS 840628

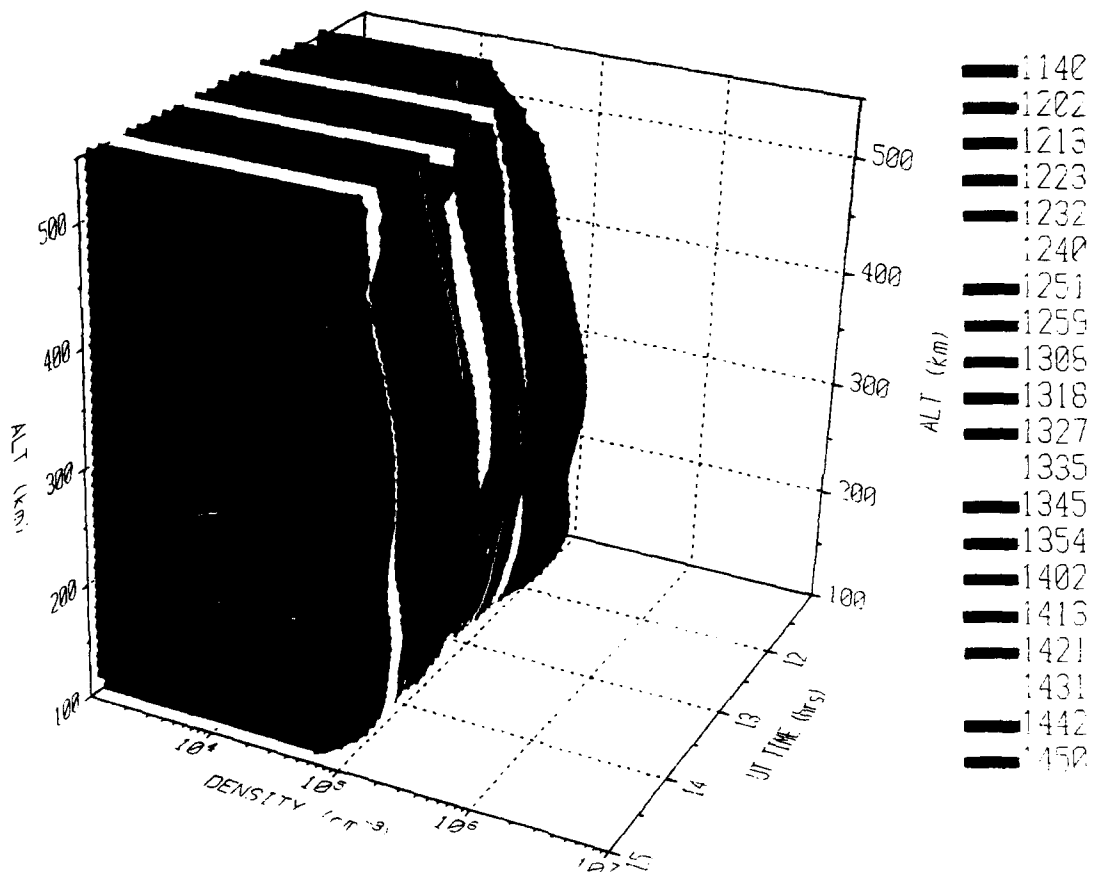
 N_e HEIGHT PROFILES vs TIME

Fig. 34(c). Electron density profiles versus time for 28 June 1984 at Sondrestrom. The N_e profiles are color-coded according to the legend. Time progresses in the graph from upper right to lower left.

due to the fact that the N_e profiles in Figure 34(c) are significantly smaller (on average) than those in Figure 32(c). Thus the ion heating is much smaller (recall that this heating is $\propto N_e^2$). The ISR ion convection velocity observations prove that large joule heating occurred on this day (see Figure 35); however, the event was over at Sondrestrom by 1140UT (0840LT). The T_e solver did not analyze any of the data sets during the joule heating event because too many of the high-altitude data points had large uncertainties, i.e., a usability code value of one (see section 4.2.1). These uncertainties were presumably caused by relatively small N_e values.

Finally, the heat flux variations are also positively correlated with N_e changes (Figure 34(c)), suggesting the presence of particle precipitation during this period (1140UT to 1400UT). As further evidence of particle precipitation, we look at the Sondrestrom ion velocities on this day (Figure 35). This graph shows ion convection velocities versus invariant latitude. Red arrows indicate that the zonal component of the velocity is westward, while blue arrows indicate an eastward component. The Sondrestrom radar is at about 74 degrees invariant latitude, hence the area in the center of the graph that has no data. We point out two major features on this graph. First, there are very large (2 - 4 km/s) eastward ion velocities prior to 1140UT (0840LT) below 73 invariant, and between 1000UT (0700LT) and 1400UT (1100LT) above 75 invariant. In addition, after 1140UT, the ion velocities below 73 invariant are small. Thus, after 1140UT, it appears that the radar is located in a region of strong gradients in the electric field and presumably the Pedersen current (current is converging). This is the same situation as on 24 April 1983, except that, in the June 1984 case, the electric field gradients are on

SONDRESTROM 28 JUN 1984

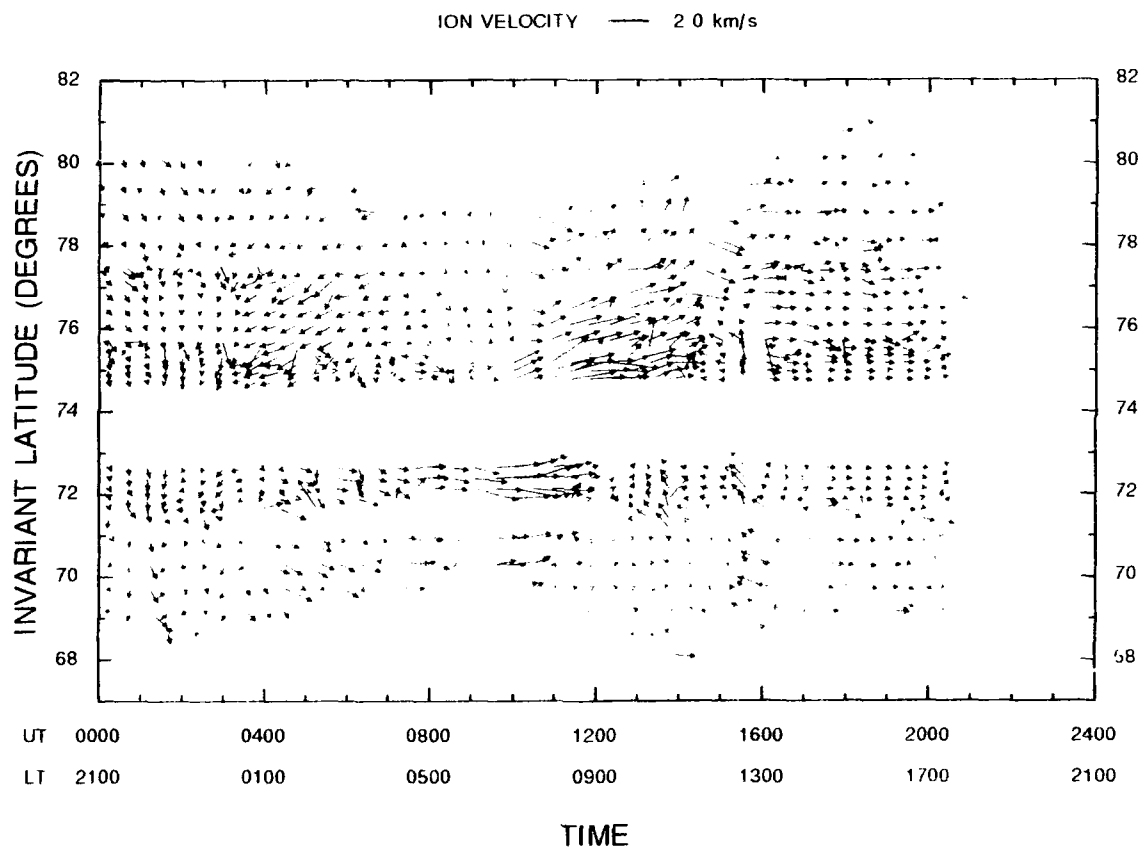


Fig. 35. Ion convection velocities (versus invariant latitude and time) at Sondrestrom on 28 June 1984. Red arrows indicate a westward zonal velocity component; Blue arrows indicate an eastward zonal component. Sondrestrom is at 74.2 invariant latitude; hence the absence of data around that latitude. The length of the arrows is scaled to the ion velocity according to the legend.

the equatorward side of the strong sunward convection in the morning convection cell (recall the April 1983 case was associated with the convection reversal in the afternoon cell). In both cases, the Pedersen current converges, and current continuity is preserved by electron precipitation in the region. This precipitation is accompanied by a strong heat flux.

The data quality for Sondrestrom was such that we have heat fluxes mostly from the daytime periods. These show a positive correlation to solar activity during the solar cycle, i.e., to $F_{10.7}$. These daytime heat fluxes also show a positive correlation (in the average behavior) to geomagnetic activity, i.e., to both A_p and K_p . Furthermore, big increases in the heat flux can be related to the convection pattern and to the precipitation of relatively low energy auroral particles, i.e., to specific magnetospheric features.

5.2. MILLSTONE HILL DATA

Figure 36 shows the heat flux versus date for the Millstone Hill days we analyzed. Again, the heat flux values shown are the mean maximum heat fluxes from Table 6. Notice in the figure that q_e remains at about the 10^{10} level for the 1985 and 1986 days, then increases significantly for the 1989 and 1990 data (this increase is unduly sharp due to the lack of 1987 and 1988 data). This apparent solar cycle correlation is seen again in Figure 37, where we plot heat flux versus $F_{10.7}$. A similar positive correlation with $F_{10.7}$ was seen in the Sondrestrom data. In Figures 38 and 39, however, we see that the Millstone Hill heat fluxes show a very different geomagnetic correlation than was found at Sondrestrom. The Millstone Hill data for A_p and K_p show a negative correlation.

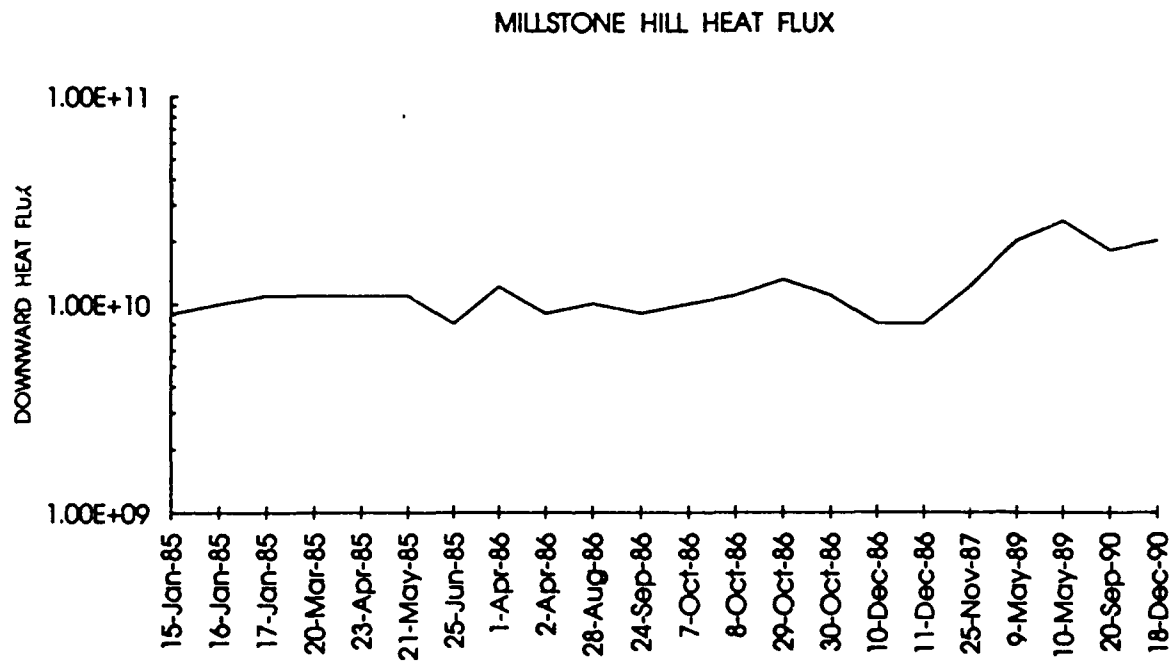


Fig. 36. Downward heat flux versus date for the Millstone Hill days analyzed (see Table 6). The units of heat flux are $\text{eV cm}^2 \text{s}^{-1}$.

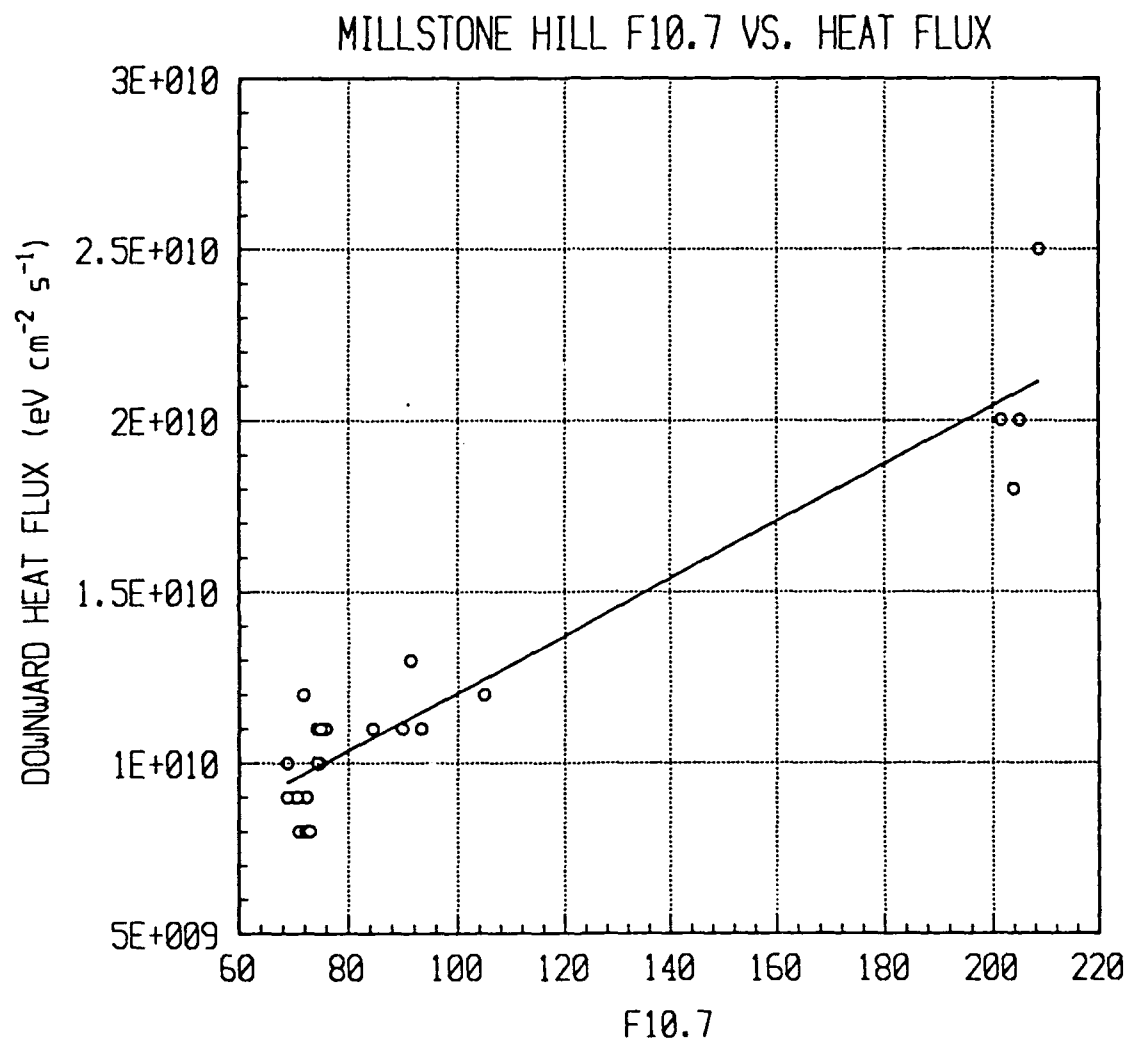


Fig. 37. Scatter plot of heat flux versus $F_{10.7}$ for the Millstone Hill days analyzed (see Table 6). The line represents the least-squares fit through the data points.

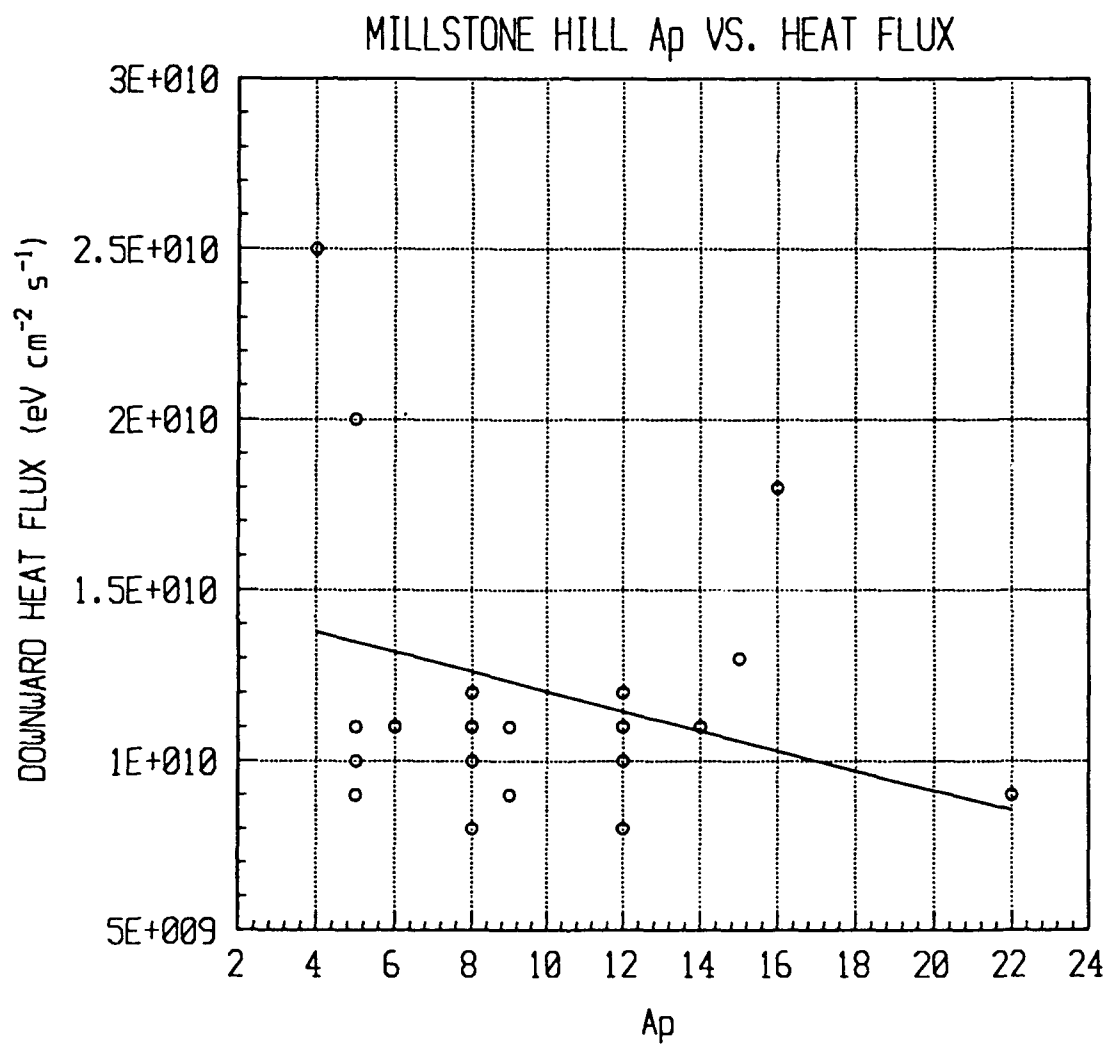


Fig. 38. Scatter plot of heat flux versus A_p for the Millstone Hill days analyzed (see Table 6). The line represents the least-squares fit through the data points.

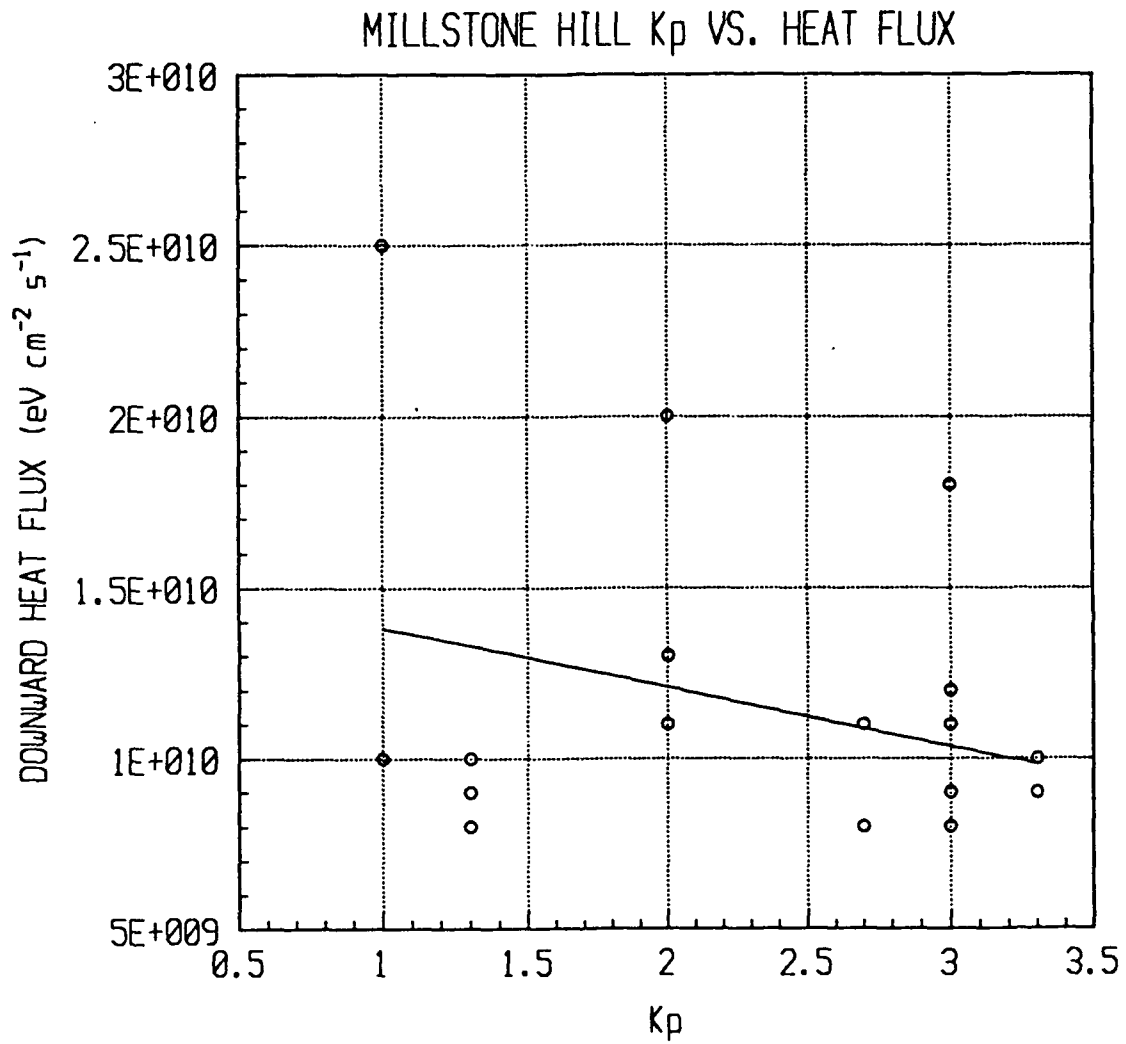


Fig. 39. Scatter plot of heat flux versus K_p for the Millstone Hill days analyzed (see Table 6). The line represents the least-squares fit through the data points.

However, the correlation depends on a few of the data points. If we were to remove the large heat flux points that occur for low geomagnetic activity, the regression lines in both graphs would become almost horizontal, i.e., no correlation. This difference in geomagnetic behavior between Sondrestrom and Millstone Hill seems plausible because Millstone Hill is 20 geomagnetic degrees equatorward of Sondrestrom. At $L = 3$, it is usually inside the plasmapause for the K_p values encountered during the days analyzed. In contrast, the field lines at Sondrestrom usually extend into parts of the magnetosphere.

Although we noted some nighttime heat flux "spikes" in the Millstone Hill data, far more interesting were the magnetic conjugate point heat flux effects we discovered (see Figure 3 and the related discussion). Figure 40 shows a representative example of a "hysteresis" pattern we found in *all* of the Millstone data. Panel (a) plots solar zenith angle versus heat flux, and panel (b) plots conjugate point solar zenith angle versus heat flux. Time progression is marked with arrows in the panels. In this figure, the data begin just after 0000UT (1900LT), and continue almost through 2400UT. The heat flux begins at a certain value, drops to a nighttime "floor" for several hours, increases in the morning hours up to a "ceiling," then decreases again in the evening hours. Notice that the heat flux in the evening hours is higher than the morning heat flux for the same solar zenith angle (hence the use of the term hysteresis). The heat flux pattern in Figure 40 is consistent with the view that the magnetic flux tubes are energized in the morning hours, and this energy is then conducted back out later in the day. The hysteresis shows that this process is almost symmetric about 1200LT, but that the maximum flux tube energy is shifted slightly towards the afternoon. In other words, there is a significant time con-

MLH 15 JAN 85
HEAT FLUX VS. SZA/CPSZA

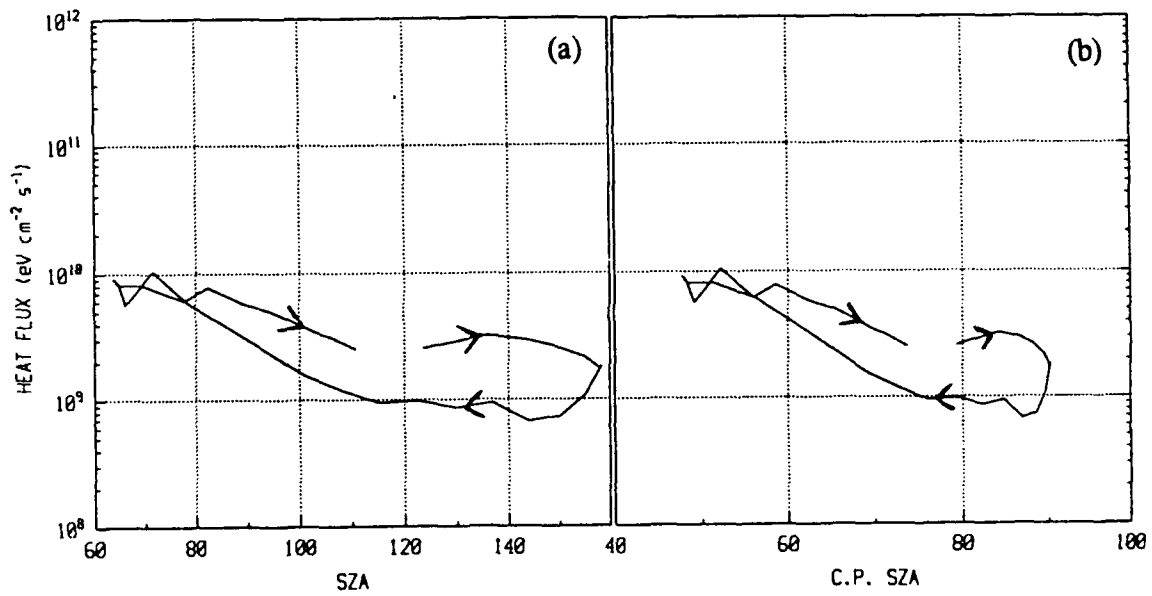


Fig. 40. Millstone Hill heat flux data for 15 January 1985. Panel (a) shows heat flux versus Millstone Hill solar zenith angle; panel (b) shows heat flux versus conjugate solar zenith angle. The arrows along the curve indicate the progression of time. Note: heat flux values that correspond to a poor agreement between the calculated and ISR T_e profiles are not included in this plot (see Appendix four).

stant associated with this process.

In our study of conjugate effects, we wish to determine at what solar zenith angle the heat flux begins to rise. In examining the data, we found that, on average, the heat flux is still at its nighttime minimum value at a zenith angle of 100 degrees, but had significantly increased when the angle dropped to 97 degrees. Recalling that photoelectron effects (red-line enhancement and plasma lines) begin between 100 and 105 degrees at Arecibo [Wickwar, 1971], this onset of heat flux increase suggests the need for some time for "hot" photoelectrons to heat the electrons in the flux tube.

As discussed above, the heat flux tends to decrease at night to a "floor" value and stay there throughout the night. However, we found that the magnitude of this "floor" minimum varies. In the northern hemisphere summer, when the conjugate point (relative to Millstone Hill) solar zenith angle becomes more than 100 degrees, we found that the nighttime "floor" heat flux at Millstone Hill averaged about $2 \times 10^8 \text{ eV cm}^{-2} \text{ s}^{-1}$. However, during winter in the northern hemisphere, conjugate sunset never occurs. The corresponding winter nighttime heat fluxes at Millstone Hill averaged $9 \times 10^8 \text{ eV cm}^{-2} \text{ s}^{-1}$, which represents a significant increase over the summertime "floor." This phenomenon is illustrated in Figures 41 and 42. Figure 41 shows solar zenith angle plots for 16 January 1985, and Figure 42 shows the same plots for 28 August 1986. In Figure 41(a) notice how the nighttime "floor" is about $1 \times 10^9 \text{ eV cm}^{-2} \text{ s}^{-1}$, while in panel (b) of the same figure the conjugate solar zenith angle never drops below 90 degrees. However, in Figure 42(a) the nighttime heat flux is about $2 \times 10^8 \text{ eV cm}^{-2} \text{ s}^{-1}$, while on panel (b) of this graph the conjugate solar zenith angle increases far beyond 100 degrees. The reason

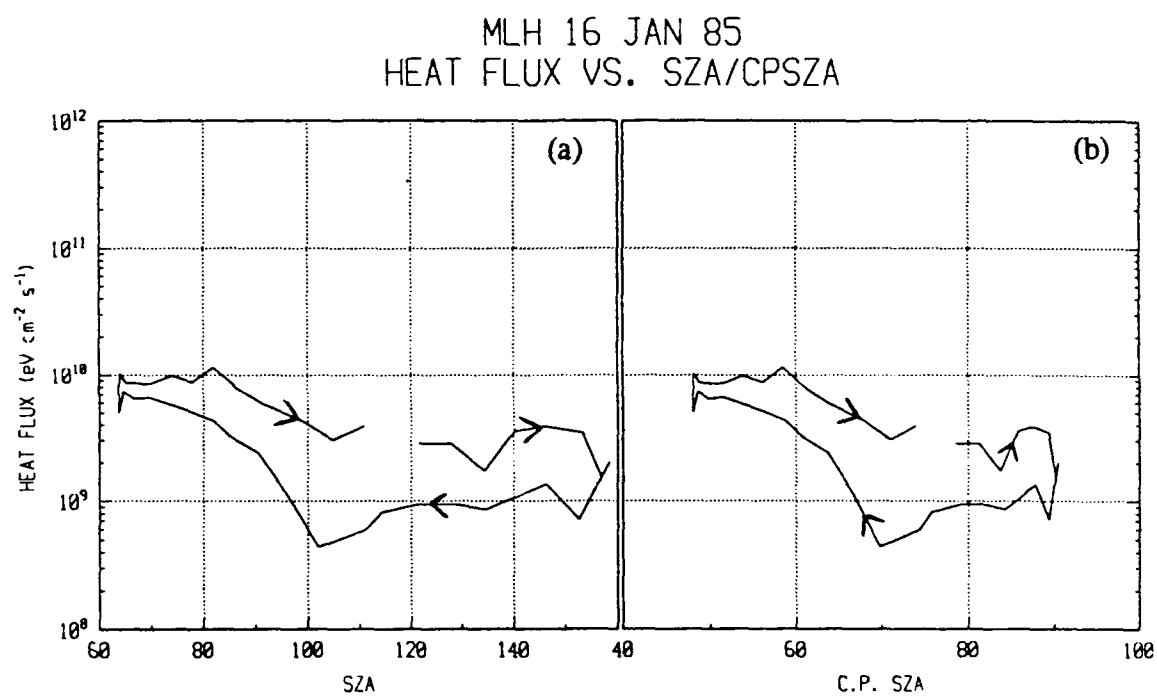


Fig. 41. Millstone Hill heat flux data for 16 January 1985. Panel (a) shows heat flux versus Millstone Hill solar zenith angle; panel (b) shows heat flux versus conjugate solar zenith angle. The arrows along the curve indicate the progression of time. Note: heat flux values that correspond to a poor agreement between the calculated and ISR T_e profiles are not included in this plot (see Appendix four).

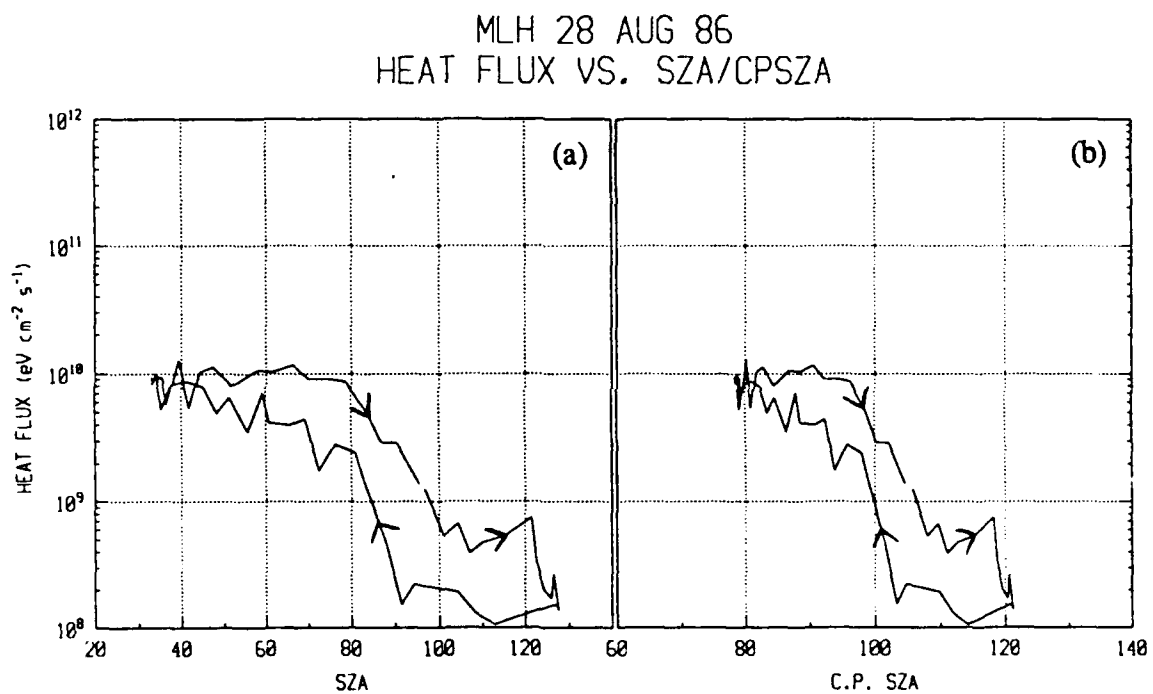


Fig. 42. Millstone Hill heat flux data for 28 August 1986. Panel (a) shows heat flux versus Millstone Hill solar zenith angle; panel (b) shows heat flux versus conjugate solar zenith angle. The arrows along the curve indicate the progression of time. Note: heat flux values that correspond to a poor agreement between the calculated and ISR T_e profiles are not included in this plot (see Appendix four).

for this difference in the nighttime heat fluxes between summer and winter is that, during the winter, the conjugate ionosphere is sunlit throughout the night, and thus provides a continuous source of energy for the local ionosphere and flux tube. Conversely, this heat source disappears during summer nights after conjugate sunset occurs, and thus the nighttime heat flux decreases. It is important to note that we observed this same "summer nighttime versus winter nighttime" pattern in all the Millstone Hill data we analyzed.

Notice that the impact of conjugate heating is only a few times 10^8 , whereas daytime heat fluxes at Millstone Hill are in the $10^9 - 10^{10}$ range. This order of magnitude difference suggests that conjugate effects do not contribute significantly to daytime heating. It further suggests that the reservoir of hot particles that give rise to the observed daytime heat fluxes is at the local end of the field line.

Now, during the summer nights at Millstone Hill (when conjugate sunset occurs), one may wonder why the nighttime heat flux "floor" does not drop to zero (or the equivalent of zero; see section 3.3.4). We speculate that it could be related to the low-level nighttime ionization that presumably occurs because of EUV scattering by the geocorona and because of galactic radiation. Another possibility is heating of plasmaspheric electrons by ring current ions -- the mechanism used to excite SAR arcs. If this latter source is active, it would be expected to be small because it would involve heat conduction perpendicular to the magnetic field.

It is likely that we could think of physical mechanisms other than conjugate heating to explain the phenomenon shown in Figures 41 and 42. To further test our assertion that conjugate effects are present in the Millstone Hill heat flux curves, we looked for

evidence of conjugate heating in the equinox data. During equinox it is possible for the conjugate solar zenith angle to pass from being greater than 100 degrees to being less than 100 degrees, while the local solar zenith angle remains above 100 degrees. Conjugate heating effects should be noticeable under such conditions. Our previous argument is weakened if conjugate heating is not evident in the data. Figures 43(a)-(c) show examples of equinox conjugate effects for 20 March 1986, 7 October 1986, and 8 October 1986. These plots show the heat flux versus conjugate solar zenith angle for each day. The arrow on each curve marks the point at which the local solar zenith angle is 100 degrees. Notice that, in each case, the heat flux begins to rise near 100 degrees conjugate solar zenith angle; this rise in heat flux is prior to local F-region sunrise. Therefore, our original (solstice) conjugate heating argument is strengthened by the equinox data.

One important point we have yet to touch on is the physical mechanism by which the local ionosphere is heated. There are two possibilities. The first involves heat conduction along the magnetic field line. The second involves "hot" photoelectrons that travel the length of the field tube from the conjugate hemisphere, then deposit their energy in the local F-region. Because the T_e solver does not take into account direct heating by conjugate photoelectrons, there is a possibility that our heat flux estimates are too large. Given the data available during this research, it was impossible to tell uniquely which of these mechanisms is responsible for the heating. However, given the proper experiment, these two mechanisms can be separated (discussed in chapter seven).

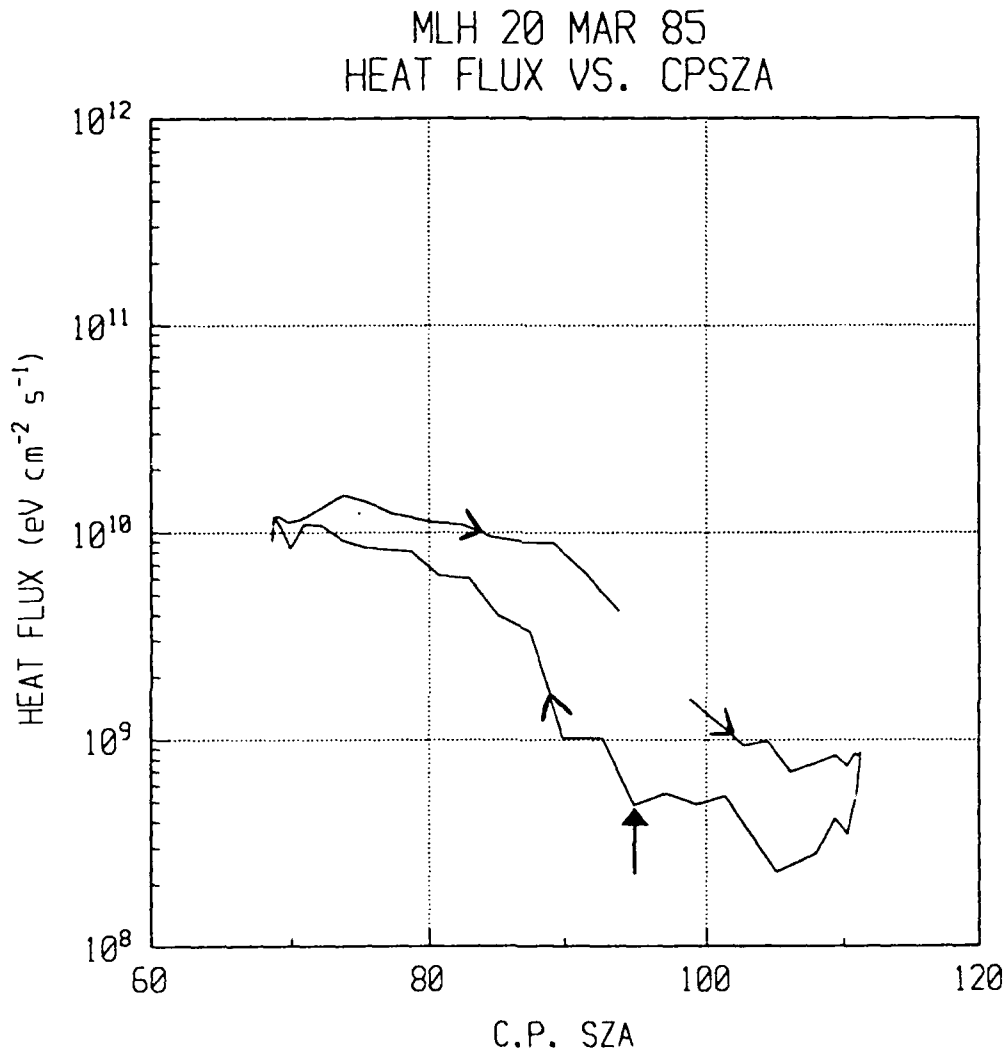


Fig. 43(a). Millstone Hill heat flux versus conjugate solar zenith angle for 20 March 1985. The arrows along the curve indicate the progression of time, and the large arrow off the curve indicates when the *Millstone Hill* solar zenith angle drops below 100 degrees. Note: heat flux values that correspond to a poor agreement between the calculated and ISR T_e profiles are not included in this plot (see Appendix four).

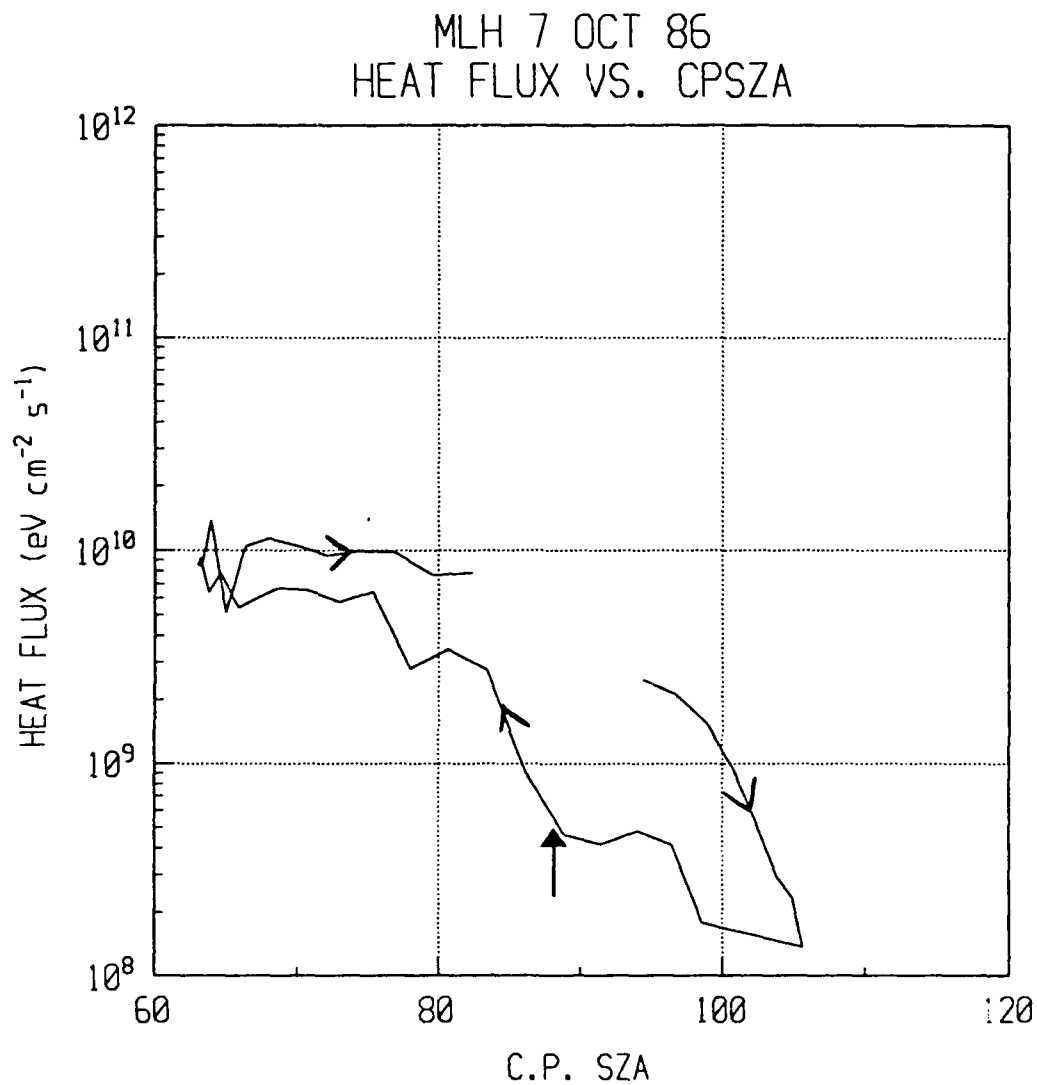


Fig. 43(b). Millstone Hill heat flux versus conjugate solar zenith angle for 7 October 1986. The arrows along the curve indicate the progression of time, and the large arrow off the curve indicates when the *Millstone Hill* solar zenith angle drops below 100 degrees. Note: heat flux values that correspond to a poor agreement between the calculated and ISR T_e profiles are not included in this plot (see Appendix four).

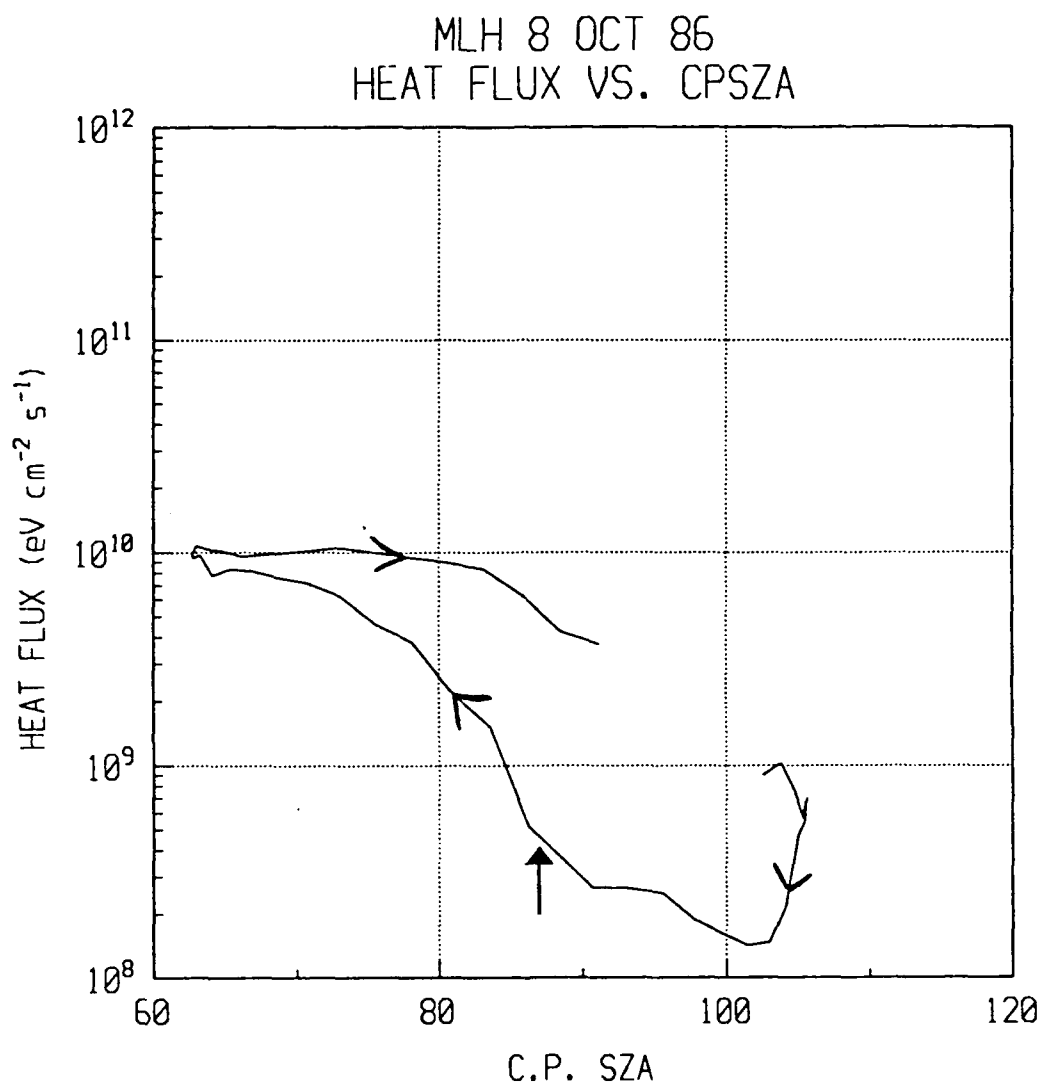


Fig. 43(c). Millstone Hill heat flux versus conjugate solar zenith angle for 8 October 1986. The arrows along the curve indicate the progression of time, and the large arrow off the curve indicates when the *Millstone Hill* solar zenith angle drops below 100 degrees. Note: heat flux values that correspond to a poor agreement between the calculated and ISR T_e profiles are not included in this plot (see Appendix four).

5.3. OTHER PARAMETERS THAT AFFECT THE FIT

So far we have only discussed situations in which the "best fit" heat flux corresponds to a calculated T_e profile that fits the data well (as verified visually). We now turn our attention to examples where the calculated T_e profile *does not* fit the data well. Before we move on to examples, we should mention the altitude range in which these discrepancies occur. They are typically below the altitudes of the T_e data points that determine the heat flux (below about 350 km). Instead, the data points we will refer to in this section are controlled mostly by Q_e from solar EUV. The observed data points are also affected by particle heating and ion composition, as we will see.

There are two ways in which the fit between the ISR T_e data and the calculated T_e values can fail: either the calculated T_e values are too small, or they are too big (relative to the ISR T_e values). We will examine the former situation first. We found that underestimated (model) electron temperatures occurred on two time scales: short (a few minutes up to two or three hours), and long (days). An example of a short time scale case is shown in Figure 44(a). In this case, the calculated T_e profile is almost 500 degrees below the T_e data points (between about 250 km and 350 km). Several things could cause this, including:

- (1) Underestimation of the solar EUV heating rate.
- (2) Overestimation of the neutral and / or electron densities.
- (3) Exclusion of additional heat sources, such as field-aligned currents or particle precipitation.

To gain insight into which of these factors might be causing the problem, we ran

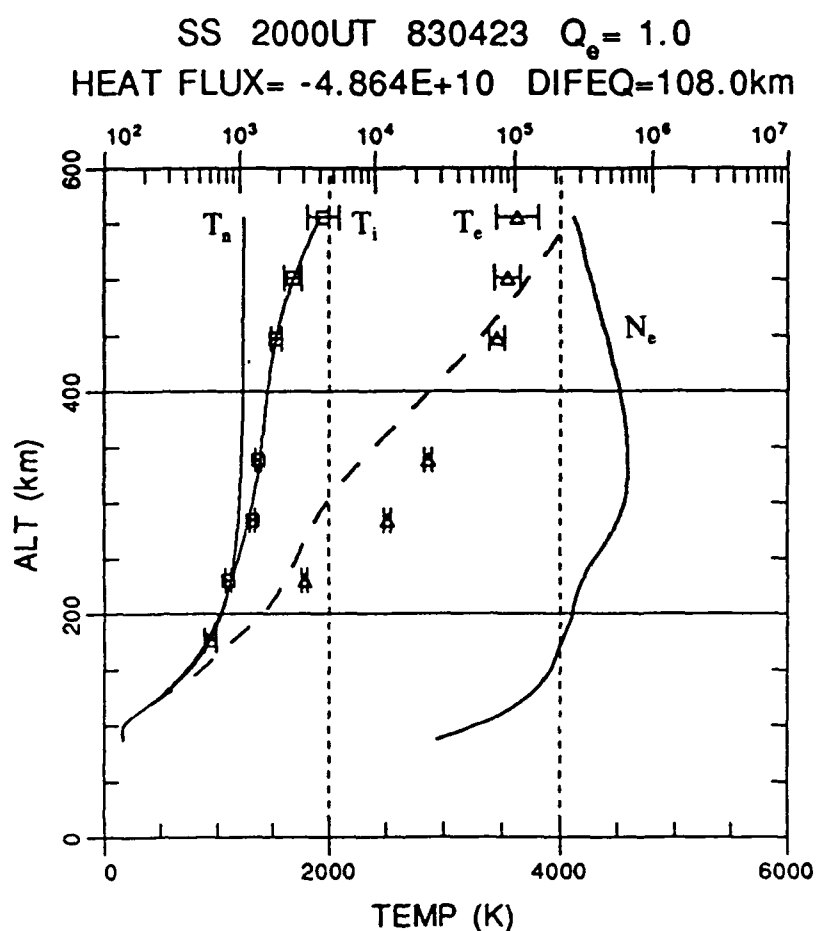


Fig. 44(a). Sondrestrom T_e , T_i , and N_e data for 23 April 1983 data at 2000UT (1700L). Triangles denote T_e data points; squares are for T_i data points. The N_e curve is the solid line to the right of the temperature profiles. The N_e scale is in cm^{-3} and is located on the upper x-axis. The solid line through the T_i data points is the T_i spline, and the other solid line is the MSIS90 $T_n(h)$ profile. The long-dash line is the calculated T_e profile for $Q_e = 1$. The heat flux shown in the legend is for the altitude of the highest ISR data point, and DIFEQ is the lower bound for which we solve equation 2.9.

several tests. In the first test, we tried $Q_e = 4$ to boost the solar EUV input. This test was only partially successful (see Figure 44(b)). It is unlikely, however, that the solar EUV should change significantly for a short period during the day. We then tried an energy flux of $10 \text{ erg cm}^{-2} \text{ s}^{-1}$ ($= 6.24 \times 10^{12} \text{ eV cm}^{-2} \text{ s}^{-1}$; a huge energy input) of auroral particles. The T_e solver assumes an average particle energy of about 3 KeV. Again, as Figure 44(c) shows, only partial success was achieved. However, less energetic auroral particles would deposit their energy at higher altitudes. The final test was to reduce N_e by 50 percent. As Figure 44(d) shows, this adjustment produced the best agreement between calculation and data. However, it seems unlikely that the $N_e(h)$ profile (obtained from ISR measurements) would be overestimated by 50 percent for a short period during the day. It appears that the most likely explanation is an additional heat source (particle precipitation). For the energy to be deposited at these altitudes, the primary electrons would have to have very low energies, i.e., for energy to be deposited above 200 km, the primary electron would have to have an energy less than 500 eV [Omholt, 1971; Jones, 1974]. Examples of short-term discrepancies such as these also exist for Millstone Hill.

As stated above, underestimated T_e values (from the solver) occurred on the time scale of a few minutes up to two or three hours. However, all of the 1989 and 1990 Millstone Hill data we analyzed (see Table 6) had significant long time-scale underestimations between about 200 and 400 km. $F_{10.7}$ was near 200 for all of these days. Figures 45, 46, and 47 illustrate this phenomenon for 20 September 1990 at Millstone Hill. Figure 45 shows q_e versus time for this day. Notice that, in contrast to Figure 30, $Q_e = 4$ does not represent an overestimated volume heating rate. Also notice, as already mentioned in

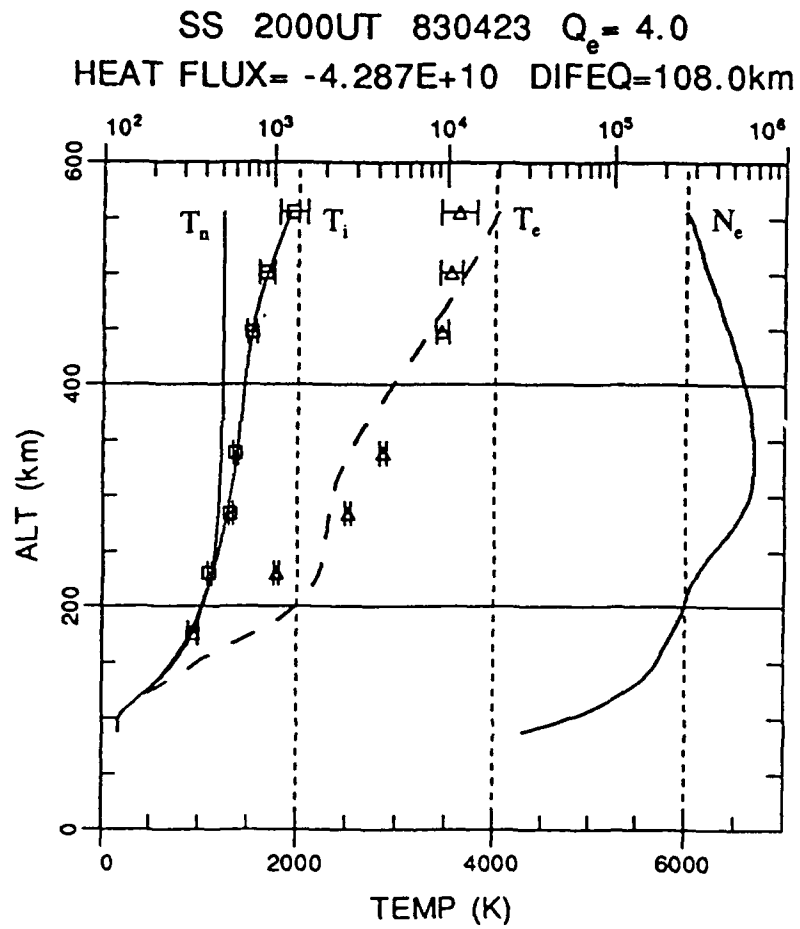


Fig. 44(b). Same as Figure 44(a), but here the calculated T_e profile is for $Q_e = 4$.

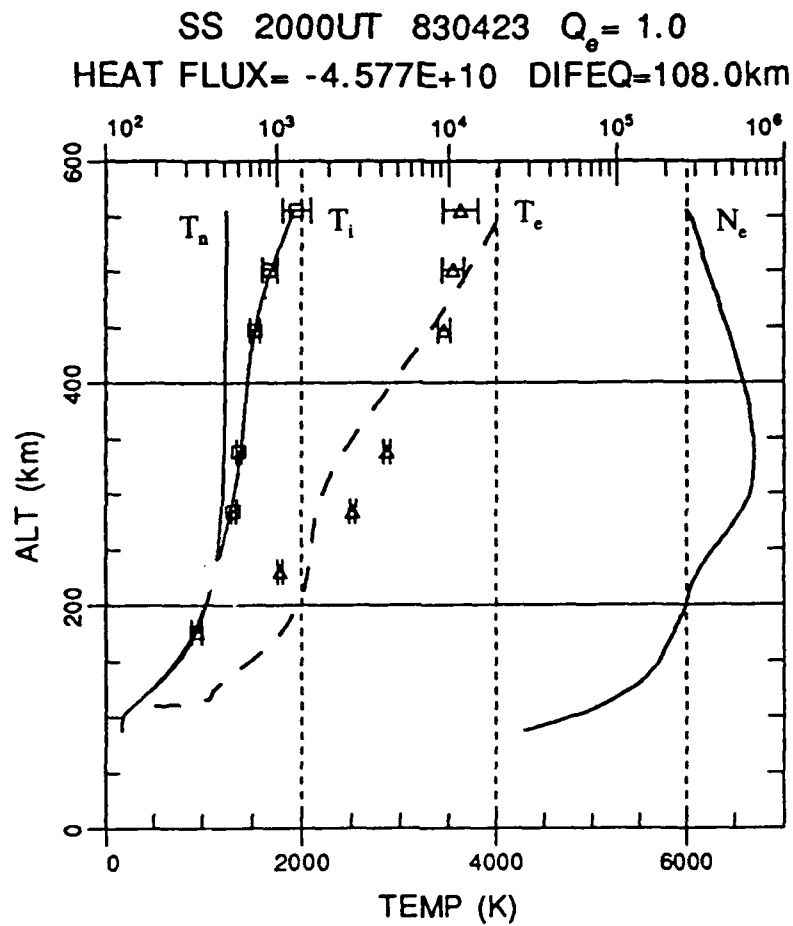


Fig. 44(c). Same as Figure 44(a), but here we have introduced a particle precipitation energy flux of $10 \text{ erg cm}^{-2} \text{ s}^{-1}$ ($= 6.24 \times 10^{12} \text{ eV cm}^{-2} \text{ s}^{-1}$).

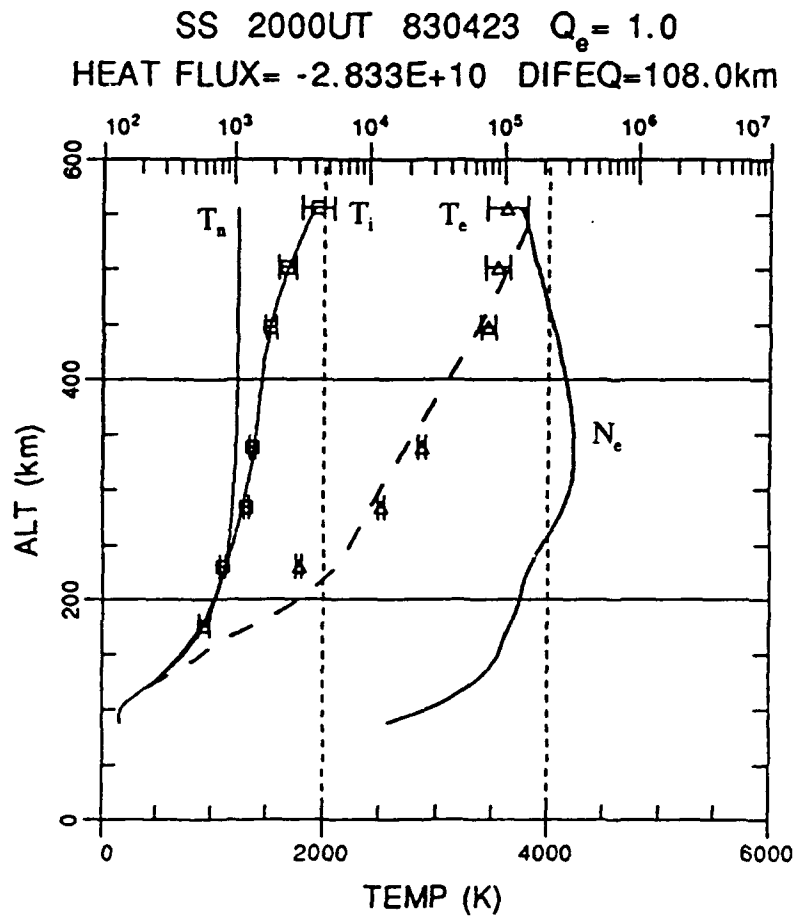


Fig. 44(d). Same as Figure 44(a), but here we have reduced the MSIS90 $T_n(h)$ profile by 50 percent.

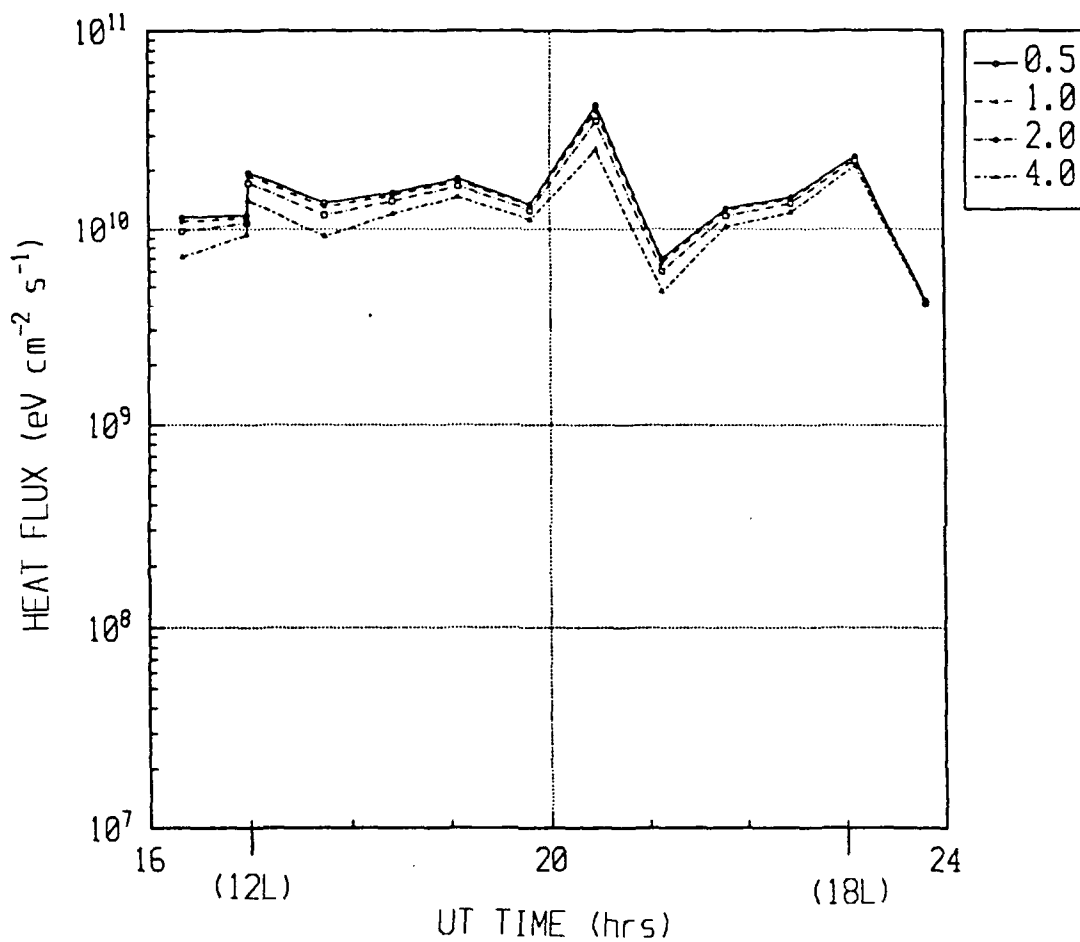
MLH 20 SEP 90
DOWNWARD HEAT FLUX

Fig. 45. Heat flux versus time for 20 September 1990 at Millstone Hill. The four curves represent the four volume heating rate profiles shown in the legend.

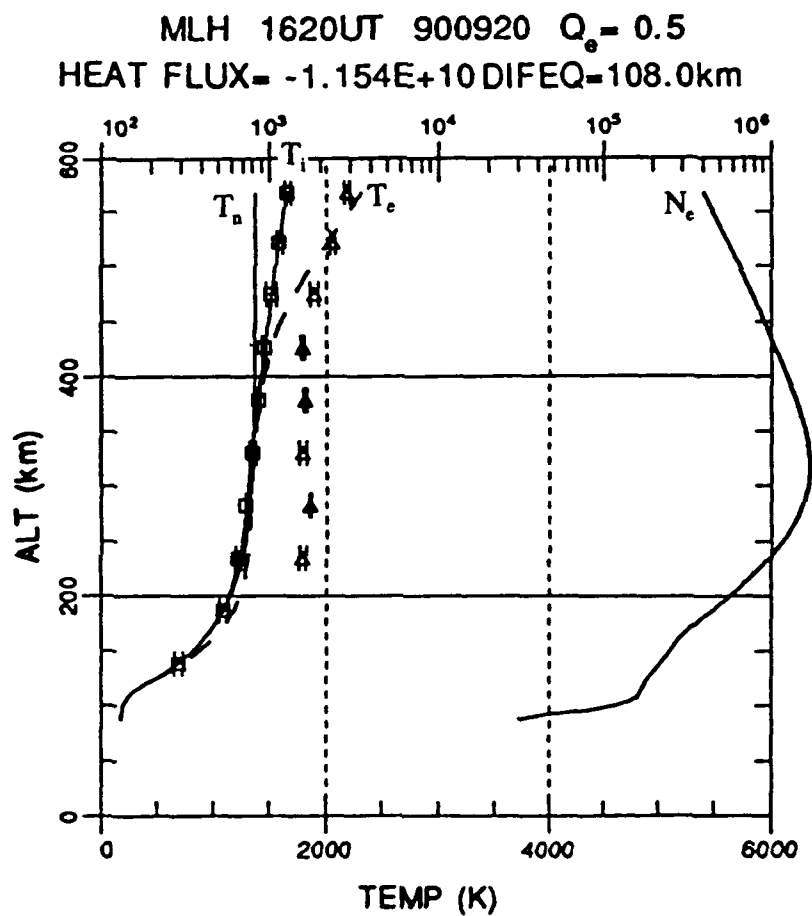


Fig. 46. Millstone Hill T_e , T_i , and N_e data for 20 September 1990 data at 1620UT (1120L). Triangles denote T_e data points; squares are for T_i data points. The N_e curve is the solid line to the right of the temperature profiles. The N_e scale is in cm^{-3} and is located on the upper x-axis. The solid line through the T_i data points is the T_i spline, and the other solid line is the MSIS90 $T_n(h)$ profile. The long-dash line is the calculated T_e profile for $Q_e = 0.5$. The heat flux shown in the legend is for the altitude of the highest ISR data point, and DIFEQ is the lower bound for which we solve equation 2.9.

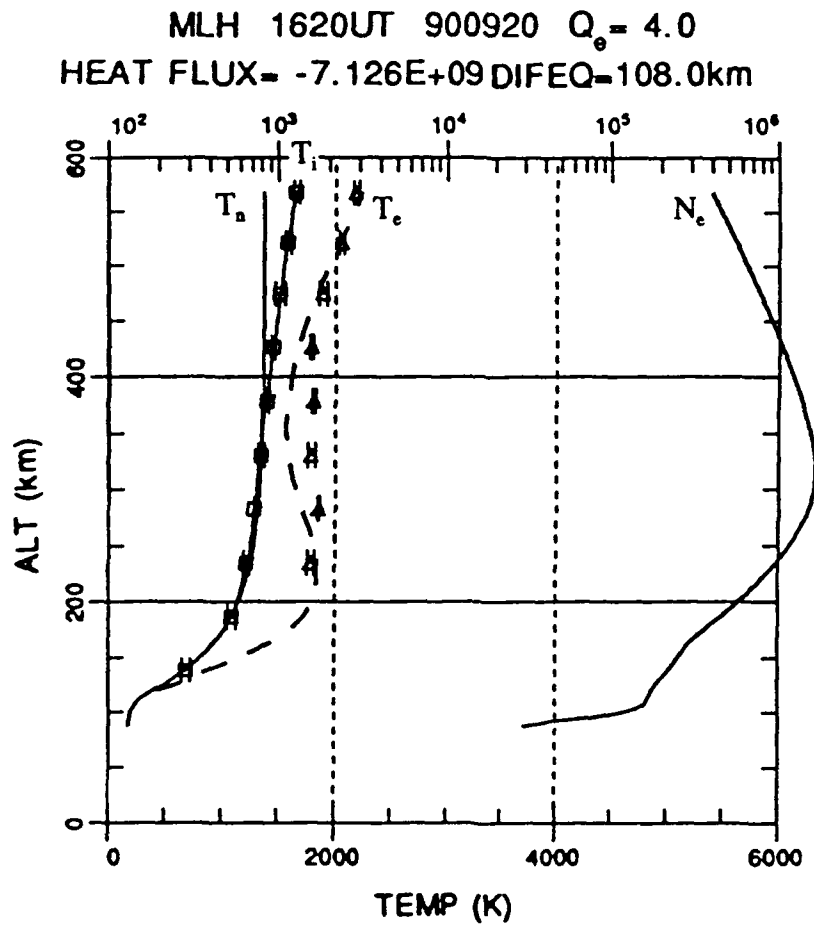


Fig. 47. Same as Figure 46, but here the calculated T_e profile is for $Q_e = 4$.

sections 3.3.1 and 5.1, the strong independence of q_e and Q_e .

Figures 46 and 47 show the ISR data, MSIS90 output, and model T_e profile for 1620UT (1120LT) on this day. Figure 46 is for $Q_e = 0.5$, and Figure 47 is for $Q_e = 4$. It is quite obvious that $Q_e = 0.5$ does not provide enough heating at lower altitudes, and that even $Q_e = 4$ is not enough. For these cases, because of the long time scale of the problem, we believe that the T_e solver solar EUV input is incorrect. The solver uses a solar EUV heating profile representative of solar minimum conditions. For high $F_{10.7}$ conditions the entire profile is "scaled up" by some factor (a linear interpolation based on $F_{10.7}$). However, we know that the shape of the solar EUV curve changes for high $F_{10.7}$. This is because, in general, the increase in solar EUV is greater for shorter wavelengths. Thus the scaling in the T_e solver appears to be inadequate for high $F_{10.7}$ conditions.

The second way for the fit to fail is that the calculated T_e values are greater than the ISR T_e values. The reason for this type of failure relates to ion composition. Figure 48 illustrates this situation for 28 June 1984 at Sondrestrom. Notice how the ISR T_e data points below 350 km are less than the calculated T_e 's in the same altitude range. Recalling section 4.1, we must assume a mean ion mass in order to derive T_e and T_i from the received radar signal. If we underestimate the ion mass, then we underestimate the temperatures. Therefore, in cases like the one shown in Figure 48, we assert that the mean ion mass has been underestimated in the Sondrestrom data reduction. Following Wickwar [1974] we can estimate the ion composition required to increase the ISR T_e values up to the calculated T_e values. We can only do this if we assume that the T_e solver solution is not sensitive to ion composition. We believe that the T_e solver is not

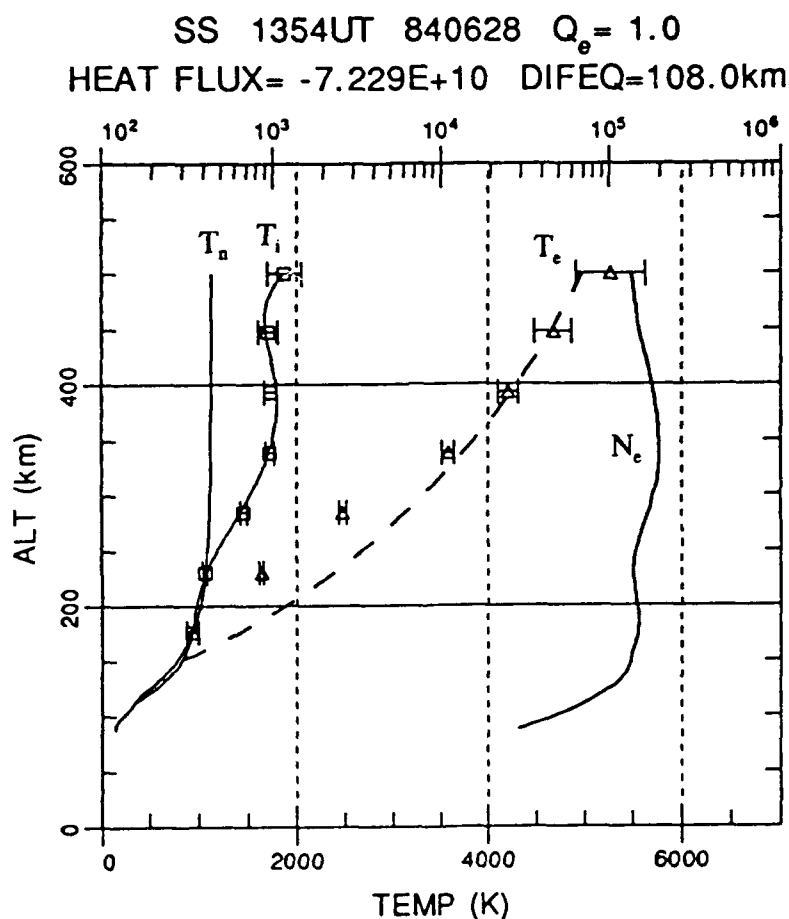


Fig. 48. Sondrestrom T_e , T_i , and N_e data for 28 June 1984 data at 1354UT (1054L). Triangles denote T_e data points; squares are for T_i data points. The N_e curve is the solid line to the right of the temperature profiles. The N_e scale is in cm^{-3} and is located on the upper x-axis. The solid line through the T_i data points is the T_i spline, and the other solid line is the MSIS90 $T_n(h)$ profile. The long-dash line is the calculated T_e profile for $Q_0 = 1$. The heat flux shown in the legend is for the altitude of the highest ISR data point, and DIFEQ is the lower bound for which we solve equation 2.9.

sensitive to ion composition because, at these altitudes, losses to the neutrals dominate ΣL_e . In the solver we assume the same ion composition profile as is used in the respective radar data reduction algorithms. These profiles are shown in Figure 49 and the algorithms are given in appendix two.

Wickwar develops a method in the 1974 report to find the electron temperature for a given q value (q is the ratio $[O^+] / [N_2]$). Assuming a mean ion mass of 30.5 (at $q = 0$), and a mean ion mass of 16 (at $q = 1$), Wickwar's relation can be written:

$$c(q) = 1.906 - 0.906q \quad (5.1)$$

where $c(q)$ is the correction factor for the assumed q . This correction factor is defined such that

$$\frac{T_e(q)}{c(q)} = T_e(1)$$

where $T_e(q)$ is the electron temperature for the assumed q , $T_e(1)$ is the electron temperature when only O^+ is present. Applying equation 5.1 to our situation, we get:

$$q_{actual} = 2.104 - 1.104c(q_{assumed}) \frac{T_{calc}}{T_{ISR}} \quad (5.2)$$

where T_{calc} is the T_e solver value, T_{ISR} is the radar data point, and q_{actual} is the q necessary to make $T_{calc} = T_{ISR}$. We used this method on Sondrestrom data for 28 June 1984. The results are shown in Figure 50. For this analysis we used the ISR T_e data points at 235 km. From Figure 49, this corresponds to a q of 0.94 (the ion composition model value used at Sondrestrom). In panel (a) of Figure 50 we show the calculated T_e values at 235 km (solid line), and the ISR T_e values (dot-dash line). Panel (b) shows the difference in the two T_e 's, and panel (c) plots q_{actual} . The long-dash reference line in panel (c) is for

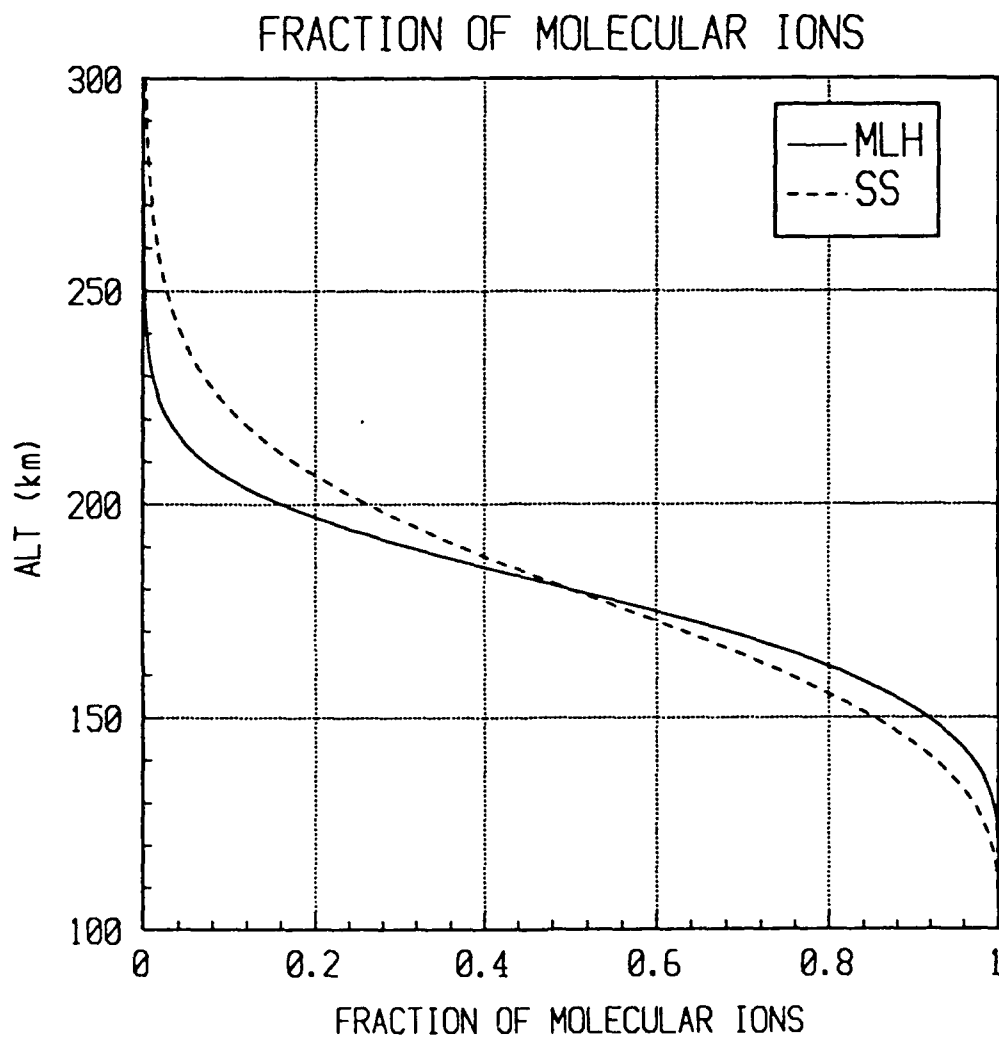


Fig. 49. Assumed ion composition profiles for the Millstone Hill (solid line) and Sondrestrom (dashed line) data reduction algorithms. These profiles were also used by the T_e solver.

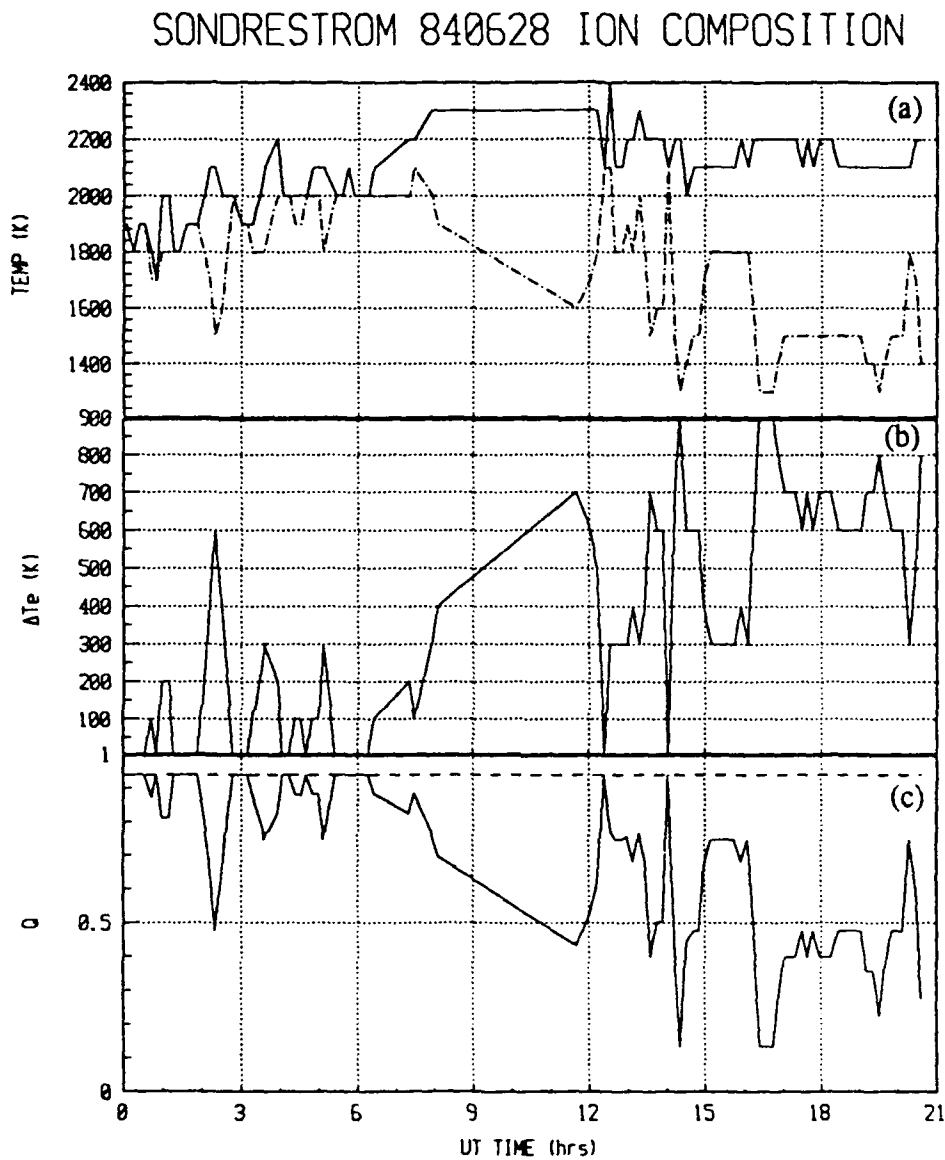


Fig. 50. Ion composition for Sondrestrom on 28 June 1984. Panel (a) shows both the ISR T_e values (dot-dash line) at 235 km and the calculated T_e values (solid line) at 235 km. Panel (b) shows $(T_{CALC} - T_{ISR})$. Panel (c) shows the q value ($= [O^+] / [N_2]$) necessary to make $T_{CALC} = T_{ISR}$. The long-dash line in panel (c) at $q = 0.94$ is the $q(235 \text{ km})$ used in the Sondrestrom data reduction algorithm and in the T_e solver.

$q = 0.94$ (the ion composition model value for Sondrestrom). Notice that ΔT_e is largest (and q_{actual} smallest, i.e., molecular composition the largest) after 1200UT (0900LT). As shown in Figure 35, the change in ion composition occurs at about the time of the large ion velocities and continues through the time of the strong particle and heat flux input. It is well-known that joule heating (especially a large event like this one) increases the percentage of molecular ions [Lathuillere, 1987]. This occurs because the energetic ions transfer large amounts of energy to the neutral gas (increases T_n). An increase in T_n will, through the ion / neutral chemistry, raise the transition altitude between molecular and atomic ions. Because of the large heat capacity of the neutral gas, T_n will remain elevated for a period of time after the joule heating is over. Thus, the molecular ion concentration will remain enhanced (Figure 50(c)).

A word of caution is in order. Physically, we know that the neutral scale height will increase during such an event. However, the MSIS90 input to the T_e solver does not adjust for the increased neutral densities. Therefore, the local loss rates computed by the T_e solver will be too small, the calculated T_e 's will be too big (at 235 km), and our molecular ion concentration will be overestimated. To estimate the size of this error, we conducted a test on the Sondrestrom 1746UT data set for 28 June 1984. In the test we reduced the neutral density profile by 50 percent. This resulted in only a 13 percent overestimation of the molecular concentration. Although one test is not conclusive, it does lead one to believe that the error is probably small.

One final point should be made here. In the first part of this section we said that calculated T_e 's that are underestimated indicates the need for an additional heat source.

Using the composition argument (in reverse), one could argue that the percentage of moleculars is too high (as opposed to the need for additional heating). While increasing the q ratio does decrease the ISR T_e values, we feel that this approach to the problem is incorrect for two reasons. First, the radar assumes a "quiet-time" $q(h)$ profile in the data reduction (see Figure 49), and any disturbances would act to decrease q (i.e., *increase* the ISR T_e values). Second, for an altitude near 235 km, as discussed above, q is almost 1, and increasing q up to 1 probably would not decrease the ISR T_e value enough.

5.4. PRECISION AND ACCURACY

Estimation of the uncertainty in our results is both a necessary and nontrivial matter. We have already mentioned two sources of error. First is the uncertainty in the ISR T_e and T_i data points -- varying between 5 and 20 percent. Second is the uncertainty generated by the T_e algorithm in finding the least-squares fit heat flux. The former source of uncertainty is random, i.e., it results from the statistical nature of the measurement and can vary in either direction. Thus, in the long-run, this uncertainty should be quite small.

With this in mind, we decided to conduct our "overall" uncertainty analysis in the following fashion. We examine the mid-day hours of a geomagnetically quiet day (one day for each radar). During such a period, the heat flux should remain essentially constant. Deviations in the heat flux during this period, then, would be due to the uncertainty in the method. In order to estimate the uncertainty, we calculate the observed variance about the mean (e.g., *Bevington*, 1969):

$$s^2 = \frac{1}{N-1} \sum_{i=1}^N (x_i - \bar{x})^2 \quad (5.3)$$

where N is the number of heat flux values in the time period, x_i stands for each heat flux, \bar{x} is the average of all N heat fluxes in the period, and s^2 is the estimated variance for each x_i (it is the estimate of σ^2). The square root of the variance gives the uncertainty.

For Sondrestrom, we chose to examine 17 March 1988 between 1300UT and 1530UT. Figure 51 shows the q_e versus time for this day, and the inset in this figure highlights the time interval of interest. A Q_e multiplier of two provided the best fit for this day. The K_p index for this period was 1⁺; the A_p for this day was 9. Application of equation 5.3 gave an uncertainty of about ± 6 percent.

For Millstone Hill, we looked at 2 April 1986 between 1300UT and 1600UT. Figure 52 shows the heat flux versus time plot for this day (same format as Figure 51). For this period K_p was 1; A_p was 5. In this case, we again calculated an uncertainty of about ± 6 percent. It is important to note that these uncertainties are *relative* (as opposed to *absolute*).

To the extent that there is some geophysical variation in the heat flux during these two periods, these estimated uncertainties are probably upper bounds for the daytime periods. The uncertainties are undoubtedly somewhat larger at night because the N_e and T_i values are less certain.

In addition to random errors, the derivation of the heat flux may also be subject to possible systematic errors, i.e., errors that are consistently in one direction and therefore bias the answer. There are three potential sources of systematic errors that should be

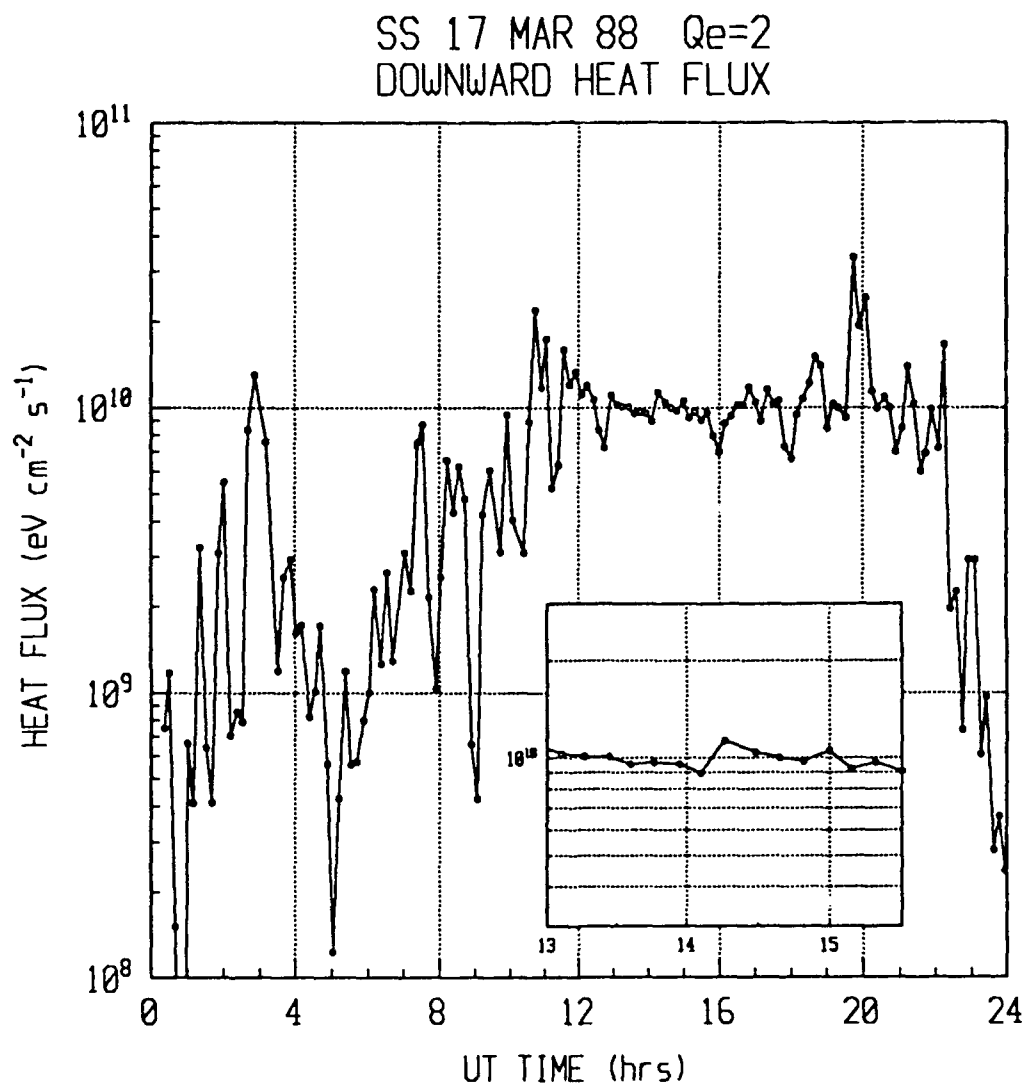


Fig. 51. Downward heat flux versus time for Sondrestrom on 17 March 1988. This curve is for a volume heating rate multiplier (Q_e) of two. The inset shows the heat flux for the time interval from 1300UT (1000LT) to 1530UT (1230LT).

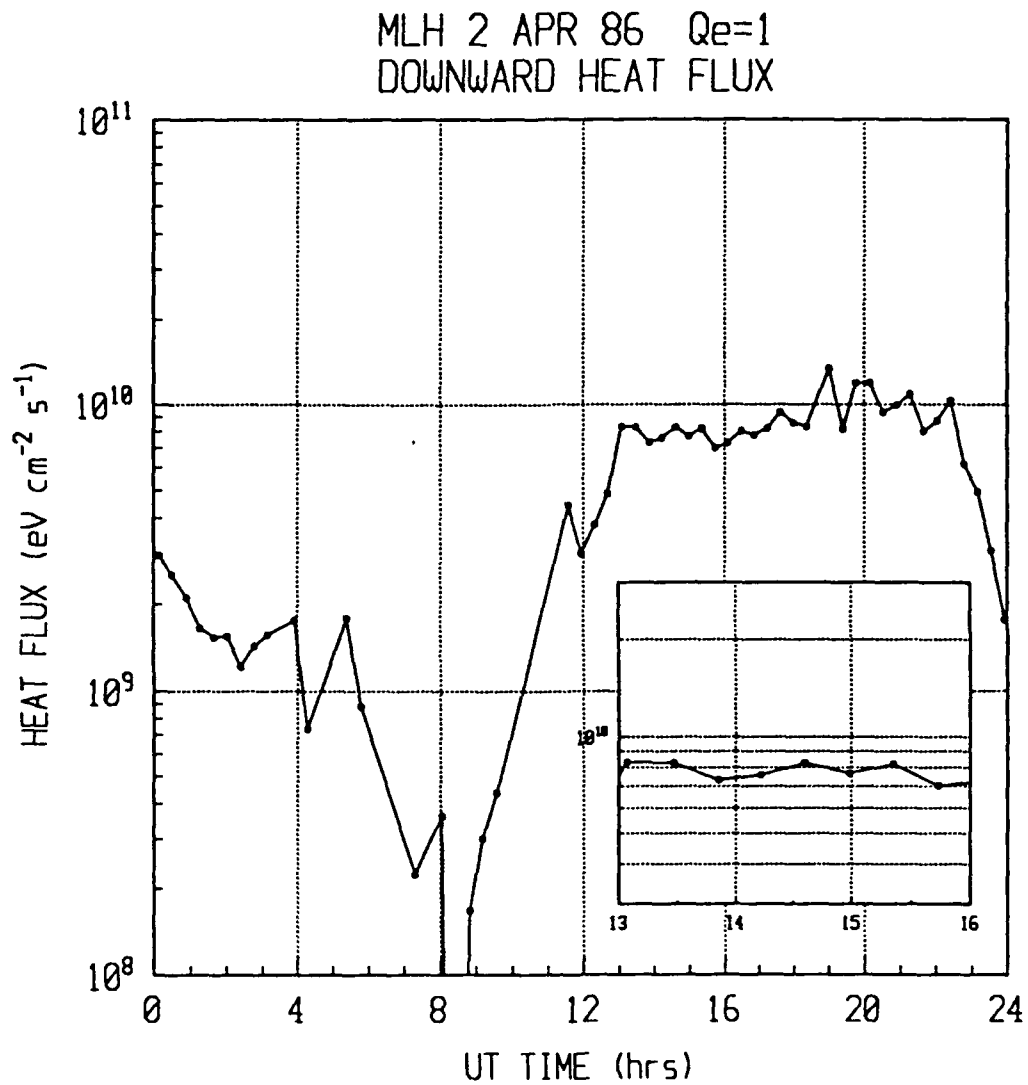


Fig. 52. Downward heat flux versus time for Millstone Hill on 2 April 1986. This curve is for a volume heating rate multiplier (Q_e) of one. The inset shows the heat flux for the time interval from 1300UT (0800LT) to 1600UT (1100LT).

mentioned. First is error in the MSIS90 densities. We ran tests (Sondrestrom data set for 28 June 1984 at 1746UT) in which the neutral densities were increased (and reduced) by 50 percent. This resulted in a heat flux increase (decrease) of about 15 percent. Second is the possible underestimation of the heat flux discussed in section 4.2. Recall that this error is due to the assumption that all our heat flux estimates are valid at 600 km. As shown in section 4.2, this could cause the heat flux to be underestimated by 1 to 3 percent. The third source of error involves the ISR electron-density profiles. We ran tests (Sondrestrom data set for 17 March 1988 at 1214UT) in which we increased N_e by 20 percent; we also tried decreasing N_e by 20 percent. In both cases, we found that the heat flux changed by almost 20 percent.

One source of error that we can probably dismiss is the uncertainty in the MSIS90 exospheric temperature. General agreement was found between the ISR T_i data points and the MSIS90 T_n profile (below 300 km) for the days we analyzed. This implies that the exospheric temperatures calculated by MSIS90 were reasonable.

CHAPTER 6

CONCLUSIONS

Many interesting results have come out of this research. Most importantly, we have developed a method to calculate the heat flux from IS radar data. This method is completely new and both very accurate and very precise. Using this method on the limited number of days we had time to analyze, we found downward heat fluxes that ranged from about $1 \times 10^8 \text{ eV cm}^{-2} \text{ s}^{-1}$ (a summer night at Millstone Hill) up to about $3 \times 10^{11} \text{ eV cm}^{-2} \text{ s}^{-1}$ (a Sondrestrom "spike"). Between these extremes, we found that the "usual" values of heat flux were somewhere in the 10^9 to 10^{10} range.

We also found that heat flux at both radars is positively correlated with the solar cycle, i.e., to $F_{10.7}$. In addition, the heat flux at Sondrestrom is positively correlated with geomagnetic activity. This latter correlation is not present at Millstone Hill. The difference is probably related to the fact that the Sondrestrom field lines extend into different regions of the magnetosphere, whereas the Millstone Hill field lines are usually within the plasmopause for the K_p values during the observations. Millstone Hill, however, is more subject to conjugate effects. This conjugate heating is small compared with daytime heat flux sources (which are local).

In addition to learning about q_e , this research provided an opportunity to learn about the volume heating rate, Q_e . There is only a small cross-correlation between q_e and Q_e . Again, the heat flux dominates the T_e profile above 350 km, while the volume heating rate largely determines the T_e profile below 350 km.

For most of our analyses, we have found that the calculated and observed T_e profiles

match each other well. However, we found periods when the calculated and observed T_e profiles are significantly different. When the calculated T_e 's were too high (this effect always occurred below 350 km), we found that the molecular ion concentration had to be increased to produce agreement between calculation and data. The best example of this occurred during (and after) a major joule heating event. We also observed underestimated model T_e values, on both short and long time scales. We found that the long time scale problems occurred in the high $F_{10.7}$ cases and affected all the sunlit profiles. This suggests that the solar EUV is not being scaled properly for these conditions. In other words, scaling an EUV curve (representative of solar minimum conditions) is not sufficient when analyzing data with high $F_{10.7}$ (especially true for solar maximum data). However, when the calculated T_e 's are too low *on a short time scale*, then the "missing" heat source is either particle precipitation or field-aligned currents. Our solver only allows us to input the total energy of the particles, and assumes a mean energy of several KeV (typical of energetic auroral precipitation). Including this flux was insufficient to provide the needed heating at the required altitudes. The clear implication is that if heating comes from particles as opposed to currents, then much lower energy particles are involved.

We also obtained valuable information about the asymptotic behavior of heat flux. Recall that our data sets stop somewhere between 450 km and 550 km. The heat flux we calculate is then representative of the altitude where the data stops. If we want to compare heat fluxes, however, we have to be able to extrapolate the heat flux up to a common height (600 km), or determine an asymptotic value. Our analysis showed that, wherever the data stop, the heat flux at that altitude can be used as the value at 600 km

(with minimal error). We also demonstrated how the asymptotic value of the heat flux could be estimated.

Finally, we investigated the precision and accuracy of the results: the precision in the afternoon was shown to be better than six percent. The accuracy can depend on such factors as the accuracy of the neutral densities and the accuracy of the radar calibration.

CHAPTER 7

AREAS FOR FURTHER STUDY

This research provided many answers about heat flux (and other ionospheric parameters), but also generated many questions. There are several areas that require follow-up study.

First of all, many more days must be analyzed -- not only for Sondrestrom and Millstone Hill, but also for other IS radars. This analysis is mandatory if we wish to fully understand the heat flux and its variations (on a world-wide scale). These include variations with respect to solar cycle, geomagnetic activity, location, season, and magnetic conjugate effects. The Sondrestrom data may need extensive averaging to determine the nighttime values, or special experiments may be needed. These experiments could be more easily carried out at the proposed European radar in Svalbard. This is because its lower transmitter frequency gives better results at low electron densities.

In addition, the solar EUV heating rate must be re-examined for high $F_{10.7}$ conditions. As mentioned before, scaling a curve representative of solar minimum conditions appears to be insufficient for high $F_{10.7}$.

On a shorter time scale (hours), we know that particle precipitation and field-aligned currents are important in some cases. This will surely become more evident as more data are analyzed. Thus, these heat sources must be taken into account. This means refinement of the particle precipitation input in the T_e solver. Additionally, we may have to include the effects of currents, which could be determined in the future with appropriate plasma line observations.

For Millstone Hill, we stated that, with our data, we could not differentiate between conjugate heating due to particle precipitation or due to heat conduction. It is possible, however, to distinguish between these two mechanisms. Soft particles are energetic enough to excite the 6300Å emission of atomic oxygen. However, heat conduction is a thermal process, and the electron energies involved are usually not high enough to excite the 6300Å oxygen emission. What is needed in the future is a special experiment with complete measurements of T_e , T_i , N_e , and the 6300Å emission line. In addition, the experiment should include plasma line measurements, since the presence of these lines implies the presence of photoelectrons [Wickwar, 1971; Carlson et al., 1977]. Detailed modelling should be carried out for these observations.

Finally, we have found another way of calculating the concentration of molecular ions. This method should be pursued in the future. Critical to this method is the assumption that the T_e solver is independent of the ion composition. This fact must be confirmed with suitable tests.

REFERENCES

- Banks, P. M., Charged particle temperatures and electron thermal conductivity in the upper atmosphere, *Ann. Geophys.*, 22, 577-587, 1966.
- Banks, P. M., and G. Kockarts, *Aeronomy*, Academic Press, New York, NY, 1973.
- Bevington, P. R., *Data Reduction and Error Analysis for the Physical Sciences*, McGraw-Hill, New York, NY, 1969.
- Brace, L. H., W. R. Hoegy, H. G. Mayr, G. A. Victor, W. B. Hanson, C. A. Reber, and H. E. Hinteregger, Discrepancy between electron heating and cooling rates derived from Atmosphere Explorer-C measurements, *J. Geophys. Res.*, 81, 5421-5429, 1976.
- Carlson, H. C., Ionospheric Heating by Magnetic Conjugate-Point Photoelectrons, *J. Geophys. Res.*, 71, 195-199, 1966.
- Carlson, H. C. J., V. B. Wickwar, and G. P. Mantas, The plasma line revisited as an aeronomical diagnostic: Suprathermal electrons, solar EUV, electron-gas thermal balance, *Geophys. Res. Lett.*, 4, 565-567, 1977.
- Hoegy, W. R., and L. H. Brace, The importance of electron heat conduction in the energy balance of the F-region, *Geophys. Res. Lett.*, 5, 269-272, 1978.
- Jones, A. V., *Aurora*, D. Riedel Publishing Co., Boston, MA, 1974.
- Kofman, W., and V. B. Wickwar, Very high electron temperatures in the daytime F-region at Sondrestrom, *Geophys. Res. Lett.*, 9, 919-922, 1984.
- Kozyra, J. U., E. G. Shelley, R. H. Comfort, L. H. Brace, T. E. Cravens, and A. F. Nagy, The role of ring current O^+ in the formation of stable auroral red arcs, *J. Geophys. Res.*, 92, 7487-7502, 1987.
- Lathuillere, C., Ion composition response to auroral energy inputs in the lower F-region, *Ann. Geophysicae*, 5A, 449-454, 1987.
- Omholt, A., *The Optical Aurora*, Springer-Verlag, New York, NY, 1971.
- Press, W. H., B. P. Flannery, S. A. Teukolsky, and W. T. Vetterling, *Numerical Recipes (FORTRAN Version)*, Cambridge University Press, New York, NY, 1989.
- Raman, R.S.V., *Incoherent scattering of radar waves in the auroral ionosphere*, Ph.D. thesis, Univ. of Michigan, Ann Arbor, MI, 1980.

- Rasmussen, C. E., J. J. Sojka, R. W. Schunk, V. B. Wickwar, O. de la Beaujardiere, J. Foster, and J. Holt, Comparison of simultaneous Chatanika and Millstone Hill temperature measurements with ionospheric model predictions, *J. Geophys. Res.*, **93**, 1922-1932, 1988.
- Rees, M. H., and R. G. Roble, Observations and theory of the formation of stable auroral red arcs, *Rev. Geophys. Space Phys.*, **13**, 201-242, 1975.
- Richards, P. G., and D. G. Torr, An investigation of the consistency of the ionospheric measurements of the photoelectron flux and solar EUV flux, *J. Geophys. Res.*, **89**, 5625-5635, 1984.
- Schunk, R. W., Transport equations for aeronomy, *Planet. Space Sci.*, **23**, 437-485, 1975.
- Schunk, R. W., and A. F. Nagy, Electron temperatures in the F region of the ionosphere: Theory and observations, *Rev. Geophys.*, **16**, 355-399, 1978.
- Schunk, R. W., and J. C. G. Walker, The theory of charged particle temperatures in the upper atmosphere, in *Progress in High Temperature Physics and Chemistry*, edited by C. A. Rouse, pp. 1-62, Pergamon Press, New York, NY, 1973.
- Schunk, R. W., J. J. Sojka, and M. D. Bowline, Theoretical study of the electron temperature in the high latitude ionosphere for solar maximum and winter conditions, *J. Geophys. Res.*, **91**, 12041-12054, 1986.
- Torr, D. G., and M. R. Torr, Review of rate coefficients of ionic reactions determined from measurements made by the Atmosphere Explorer satellites, *Rev. Geophys. Space Phys.*, **16**, 327-340, 1978.
- Wickwar, V. B., *Photoelectrons from the magnetic conjugate point studied by means of the 6300A predawn enhancement and the plasma line enhancement*, Ph.D. thesis, Rice Univ., Houston, TX, 1971.
- Wickwar, V. B., *Analysis techniques for incoherent-scatter data interpretation in the 100-to-300 km region*, Tech. Rep. 3, SRI Project 1703, Stanford Research Institute, Menlo Park, CA, 1974.
- Wickwar, V. B., proposal for *Validation of First-Principles Model Calculations of the Upper Atmosphere*, Utah State University, 1991.

APPENDICES

APPENDIX 1

ION COMPOSITION ALGORITHMS

This appendix gives the FORTRAN function subprograms used to determine the fraction of molecular ions (versus altitude). The first subprogram listed was used in Millstone Hill data reduction, and was also used by the T_e solver (when analyzing Millstone data). This function subprogram, called PMF, is as follows:

```

REAL FUNCTION PMF(X)
Z1=AMIN1(-(X-120.)/40.,50.)
H=10.-6.*EXP(Z1)
Z2=AMIN1(-(X-180.)/H,50.)
PMF=1.-2./(1.+SQRT(1.+8.*EXP(Z2)))
IF (X .LT. 110.) PMF=1.
RETURN
END

```

where X is the input altitude in kilometers, and the output gives the ratio of molecular ions to the total number of ions. The graph of the output of this subprogram is shown in Figure 49, page 105.

The second function subprogram was used in Sondrestrom data reduction, and was also used by the T_e solver (when analyzing Sondrestrom data). This function subprogram, called COMPQ, is as follows:

```

FUNCTION COMPQ(AL)
DATA TINF,HINF,HTR,SEXP,T120/1000.,60.,180.,.01,335./
ALTITU = AMAX1(AL,88.)
HT=HINF*(1.-(1.-T120/TINF)*EXP(-SEXP*(ALTITU-120.)))
TEMP=1.+8.*EXP(-3.*(ALTITU-HTR)/HT)
COMPQ=2./(1.+SQRT(TEMP))
RETURN
END

```

where AL is the input altitude in kilometers, and the output gives the ratio of *atomic* ions

to the total number of ions. Therefore, one obtains the percentage of molecular ions by computing $1.0 - COMPQ(AL)$. Again, the graph of the output of this subprogram is shown in Figure 49, page 105.

APPENDIX 2

DATA RETRIEVAL PROCEDURES

The CEDAR database, located at the National Center for Atmospheric Research (NCAR), contains the incoherent-scatter radar data used in this research. Two routines developed by Mr. Roy Barnes of NCAR, *gfiles* and *migsget*, were used to extract data from the database. The procedure is as follows:

1. Use the CEDAR database catalogue along with the AKAVSNS listing to determine the designators for the experiment / file(s) you wish to extract.

2. Logon to the CEDAR database (a UNIX-based system). Copy the *gfiles* command file to your home directory (instructions for doing this are contained in the database documentation provided to all new users). Edit the input / output lines of *gfiles*. The *gfiles* input lines are used to specify the experiment / file(s) to be extracted. Use the experiment and file designators (from step one) to adjust the input lines of *gfiles*. The *gfiles* output lines let you assign a unique filename to each experiment / file you extract (this filename will be used by *migsget* in step four). The following sample command file listing shows the first few lines of *gfiles* (as you would see them in a text editor). Input lines are italicized and output lines are in bold type; none of the other lines require editing:

```
# QSUB -IT 60 -q prem -eo -s /bin/csh -r gfiles
date
ja
cd $TMPDIR
cat << EOF >! in$$
/ ISRADAR / MLH860331A           1 2
```

```

DISPOSE
/ ISRADAR / MLH860827A      1  2
DISPOSE
/ ISRADAR / MLH860827A      3  4
DISPOSE
/ ISRADAR / MLH860827A      5  6
DISPOSE
/ ISRADAR / MLH860827A      7  8
DISPOSE
/ ISRADAR / MLH860827A      9 10
DISPOSE
LASTIN
/ ISRADAR / MLH860401
/ ISRADAR / MLH860828
/ ISRADAR / MLH860924
/ ISRADAR / MLH861008
/ ISRADAR / MLH861030
/ ISRADAR / MLH861211
LASTOUT
ms.input.vsn.name.max30chars__ 1st 1st (file to write to current output)
DISPOSE - forces write of current output vol after finishing previous vsn rd
LASTIN - terminates input list
ms.output.vsn.name.max30chars_ retpd=__ virtual=__ passwd=,__
LASTOUT - terminates output list (optional, EOF is encountered gracefully)
EOF

```

Referring to the input lines, the *MLHYMMDDA* designators (following / ISRADAR /) are the experiment designators, and the numbers to the right of these designators are the desired file numbers for the given experiment. The output lines show the user-determined output filenames. The data requested on the first input line will be written to the output file specified on the first output line, and so on. For example, in the listing above, the data contained in MLH860331A, files one and two, will be written to the output file MLH860401.

3. Execute the *gfiles* command file by typing *shjob gfiles* at the UNIX command prompt. This initiates the extraction process. The command *shstat [your login ID]*

queries the status of the extraction process. The extraction is complete when the *shstat* command returns the following message:

no batch entries

no pipe entries

no queue entries

4. Now you must move the extracted information into a user-accessible directory. This is accomplished with the command *migsget* [*filename*], where [*filename*] is the user-defined output filename from step two. Use a separate *migsget* command for each output filename. Execution of *migsget* will give the output file a ".cbf" extension and move the file to the / *local* / *home* / *madrigal* / *files* / *stage* directory of the CEDAR database computer.

5. Copy each ".cbf" file to your DECstation using the following remote copy command:

```
rcp filename.cbf [E-mail address:directory path]
```

For example, the E-mail address / directory path I used was:

```
aeronomy.cass.usu.edu:/usr/users/devin
```

APPENDIX 3
SONDRESTROM DATA

This appendix contains tables of the T_e algorithm output for the 23 days of Sondrestrom data we analyzed. Each table consists of four columns. The first column is UT time, the second column is the solar zenith angle at Sondrestrom, the third column is conjugate point solar zenith angle, and the fourth column is the downward heat flux (in $\text{eV cm}^{-2} \text{s}^{-1}$) valid at 600 km (see Section 4.2).

A WARNING TO POTENTIAL USERS OF THIS DATA: The heat flux values listed in this appendix are "raw," i.e., no attempt has been made to remove the heat flux values which correspond to a poor agreement between the calculated and ISR T_e profiles. Therefore, as a rule-of-thumb, disregard all heat flux values which are less than 1×10^7 or greater than 1×10^{12} .

TABLE A3.1. Sondrestrom Heat Flux Values for 24 April 1983

<u>UT HRS</u>	<u>SZA</u>	<u>CPSZA</u>	<u>HEAT FLUX</u>
0.2833	94.1743	107.9411	2.216E+10
1.2167	97.5589	106.4986	7.012E+09
1.6833	98.8397	105.6858	5.057E+09
2.1667	99.8355	104.8082	5.705E+09
2.6500	100.5074	103.8739	4.249E+09
3.1000	100.8018	102.9901	1.851E+10
3.5667	100.7742	102.1031	3.148E+10
4.0333	100.4100	101.2060	6.399E+09
4.5000	99.7162	100.3285	7.806E+09
5.5167	97.1264	98.5626	1.094E+10
5.9667	95.5726	97.8726	1.050E+10
7.3167	89.5241	96.2025	3.788E+10
7.7833	87.0758	95.8024	2.039E+10
10.4667	71.4545	95.5513	1.945E+10
11.4333	65.8729	96.3359	8.564E+09
11.9000	63.4742	96.8441	2.175E+10
12.3667	61.1971	97.4511	2.175E+10
12.8333	59.1481	98.1372	2.727E+10
13.7667	55.9056	99.7039	3.127E+11
14.2167	54.8380	100.5186	3.288E+10
14.7000	54.0704	101.4329	1.071E+11
15.1500	53.7290	102.3464	6.195E+10
15.6167	53.7998	103.2684	3.875E+10
16.0833	54.2634	104.1627	5.793E+10
16.5500	55.1299	105.0618	8.202E+10
17.0167	56.3653	105.9301	4.125E+10
17.4833	57.9379	106.7536	2.865E+10
17.9500	59.8105	107.5188	2.654E+10

TABLE A3.2. Sondrestrom Heat Flux Values for 18 May 1983

<u>UT HRS</u>	<u>SZA</u>	<u>CPSZA</u>	<u>HEAT FLUX</u>
0.7833	89.6884	113.8685	7.674E+09
1.2500	91.1491	113.0942	8.703E+09
2.1833	93.1995	111.4203	3.831E+09
2.6500	93.7855	110.5243	6.504E+09
3.1167	94.0532	109.6142	8.202E+09
4.0500	93.6076	107.7848	3.875E+09
4.9667	91.9595	106.1231	2.244E+09
6.6667	86.0864	103.5931	6.425E+09
7.1333	83.9335	103.0738	8.033E+09
9.6167	70.1259	101.9810	1.033E+10
10.0833	67.3989	102.1062	1.136E+10
10.5500	64.6201	102.3406	1.136E+10
11.4833	59.2636	103.1124	1.495E+10
11.9500	56.7688	103.6395	1.311E+10
12.4333	54.4017	104.2688	1.401E+10
12.9000	52.2766	104.9775	1.450E+10
13.4000	50.4063	105.7760	1.349E+10
13.8667	48.9635	106.5939	1.514E+10
14.3667	47.8302	107.5224	1.799E+10
14.8333	47.2008	108.4189	2.074E+10
15.3167	47.0041	109.3568	2.263E+10
15.7833	47.2576	110.2767	2.067E+10
16.2500	47.9400	111.1884	1.746E+10
16.7167	48.9978	112.0558	1.707E+10
17.2333	50.6987	113.0343	1.759E+10
17.7000	52.4759	113.8125	3.632E+10
18.2000	54.7360	114.6007	2.106E+10
18.6667	57.0720	115.2551	3.374E+10
19.1333	59.5812	115.8232	2.039E+10
19.6000	62.2225	116.2942	1.524E+10
20.0667	64.8802	116.6534	2.004E+10
20.5333	67.6567	116.9114	2.738E+10
21.0000	70.4473	117.0531	2.293E+10
21.5000	73.4836	117.0746	1.829E+10
21.9833	76.2523	116.9646	2.363E+10
22.4333	78.7302	116.7546	2.484E+10
22.9167	81.3444	116.4033	2.151E+10
23.3667	83.5653	115.9848	1.963E+10
23.8333	85.7269	115.4490	1.371E+10

TABLE A3.3. Sondrestrom Heat Flux Values for 15 June 1983

<u>UT HRS</u>	<u>SZA</u>	<u>CPSZA</u>	<u>HEAT FLUX</u>
11.7167	54.8350	107.0926	2.934E+10
12.1833	52.3642	107.6434	1.136E+10
12.6500	50.0855	108.2761	1.436E+10
13.1167	48.0493	108.9825	6.561E+10
13.5833	46.3093	109.7528	4.940E+10
14.0500	44.9173	110.5761	1.970E+10
14.5167	43.9179	111.4420	1.695E+10
14.9833	43.3489	112.3371	1.985E+10
15.4500	43.2286	113.2263	2.242E+10
15.9167	43.5560	114.1428	2.472E+10
16.3833	44.3263	115.0497	2.067E+10
16.8500	45.5117	115.9340	1.707E+10
17.3167	47.1149	116.8026	1.690E+10
17.7833	49.0039	117.5986	1.456E+10
18.2500	51.1075	118.3140	1.495E+10
18.7167	53.4800	118.9732	1.603E+10
19.1833	56.0235	119.5460	2.092E+10
19.6500	58.6897	120.0223	2.039E+10
20.1167	61.4354	120.3935	1.681E+10
20.5833	64.1509	120.6478	1.739E+10
21.0500	66.9364	120.7938	1.353E+10
21.5167	69.7632	120.8196	1.394E+10
21.9833	72.4568	120.7236	1.663E+10
22.4500	75.0578	120.5094	1.899E+10
22.9167	77.5337	120.1817	1.495E+10
23.4000	79.9115	119.7346	2.106E+10
23.8500	81.9499	119.2258	2.395E+10

TABLE A3.4. Sondrestrom Heat Flux Values for 13 July 1983

<u>UT HRS</u>	<u>SZA</u>	<u>CPSZA</u>	<u>HEAT FLUX</u>
2.1000	90.2760	114.3735	4.850E+09
2.5667	91.0125	113.4818	8.406E+09
3.0333	91.4408	112.5699	1.123E+10
3.5000	91.5542	111.6513	1.551E+10
3.9833	91.3405	110.7171	2.214E+09
4.4333	90.8320	109.8479	7.674E+09
4.9167	89.9602	108.9468	4.493E+09
5.4333	88.7008	108.0565	7.619E+09
5.9000	87.3054	107.3251	9.752E+09
7.3000	81.5822	105.5134	2.761E+09
7.7667	79.2747	105.0840	1.739E+10
11.8833	55.7447	105.7526	1.279E+10
12.3500	53.3189	106.3154	4.125E+10
12.8167	51.0450	106.9753	2.235E+10
13.3333	48.9017	107.7683	1.589E+10
13.8000	47.2797	108.5521	3.059E+10
14.3167	45.9098	109.4731	2.196E+10
14.7833	45.0893	110.3482	2.834E+10
15.2500	44.7067	111.2251	2.506E+10
15.7167	44.7565	112.1374	1.899E+10
16.1833	45.2531	113.0483	1.681E+10
16.6500	46.1780	113.9443	1.792E+10
17.1167	47.5359	114.8320	1.905E+10
17.5833	49.1711	115.6358	2.365E+10
18.1000	51.4142	116.4979	1.488E+10
18.5500	53.5531	117.1564	9.356E+09
19.0333	56.0609	117.7855	1.695E+10
19.5000	58.6612	118.3082	9.838E+09
19.9667	61.3658	118.7294	1.820E+10
20.4333	64.1334	119.0416	1.120E+10
20.9000	66.8574	119.2370	1.630E+10
21.3667	69.7102	119.3213	1.752E+10
21.8333	72.4503	119.2834	1.538E+10
22.3000	75.1149	119.1270	1.495E+10
22.7667	77.6725	118.8544	9.435E+09
23.2333	80.0958	118.4714	1.349E+10
23.7000	82.3011	117.9978	1.518E+10

TABLE A3.5. Sondrestrom Heat Flux Values for 26 June 1984

<u>UT HRS</u>	<u>SZA</u>	<u>CPSZA</u>	<u>HEAT FLUX</u>
0.3833	84.0111	118.6475	8.169E+09
0.5333	84.5896	118.4268	1.045E+10
0.6667	85.0602	118.2335	2.726E+10
0.8500	85.7111	117.9426	1.384E+10
1.1000	86.5039	117.5446	1.065E+10
1.2833	87.0598	117.2298	9.618E+09
1.4167	87.4166	117.0082	9.838E+09
1.5667	87.8117	116.7411	9.657E+09
1.7333	88.2041	116.4478	6.383E+09
1.9167	88.6103	116.1055	7.764E+09
2.0500	88.8619	115.8670	4.102E+09
2.2167	89.1502	115.5595	6.328E+09
2.3667	89.3852	115.2704	8.202E+09
2.5000	89.5586	115.0244	9.815E+09
2.6833	89.7701	114.6628	2.305E+10
2.8167	89.8868	114.4130	1.690E+10
2.9667	89.9946	114.1159	1.899E+10
3.1333	90.0738	113.7951	1.094E+10
3.2833	90.1130	113.4972	8.613E+09
3.4167	90.1197	113.2220	8.202E+09
3.5833	90.0919	112.9019	1.307E+10
3.7333	90.0317	112.6057	1.812E+10
3.8667	89.9552	112.3564	7.962E+09
4.0500	89.8016	111.9958	8.302E+09
4.2000	89.6542	111.7279	1.963E+10
4.3333	89.4628	111.4400	3.259E+10
4.5000	89.2212	111.1339	7.620E+09
4.7833	88.7220	110.6195	4.125E+09
4.9667	88.3301	110.2847	2.768E+09
5.2667	87.6258	109.7767	6.484E+09
5.6000	86.6737	109.2141	1.028E+10
5.7333	86.2753	109.0088	6.081E+09
5.9000	85.7397	108.7545	1.216E+10
6.0500	85.2156	108.5261	7.764E+09
6.1833	84.7101	108.3222	7.619E+09
6.3667	84.0452	108.0760	6.425E+09
6.5167	83.4428	107.8714	8.482E+09
6.6500	82.9161	107.7051	8.956E+09
6.8167	82.1707	107.4881	8.613E+09
6.9667	81.5539	107.3232	1.681E+10
7.1000	80.9192	107.1662	2.304E+10

TABLE A3.5. Sondrestrom Heat Flux Values for 26 June 1984

<u>UT HRS</u>	<u>SZA</u>	<u>CPSZA</u>	<u>HEAT FLUX</u>
7.4167	79.4271	106.8422	4.125E+09
7.5667	78.6821	106.7015	1.374E+10
8.0167	76.4026	106.3481	8.716E+09
8.2167	75.3389	106.2191	8.716E+09
9.2667	69.3213	105.8471	1.707E+10
9.7667	66.4177	105.8609	1.216E+10
9.9000	65.5807	105.8865	2.302E+10
10.0667	64.6040	105.9284	3.437E+10
10.2167	63.6986	105.9787	1.759E+10
10.3500	62.9307	106.0302	1.913E+10
10.5333	61.8174	106.1191	1.401E+10
10.6667	61.0559	106.1896	1.582E+10
10.8000	60.2256	106.2760	1.061E+10
10.9833	59.1982	106.3962	1.577E+10
11.1333	58.3161	106.5117	1.272E+10
11.2667	57.5756	106.6177	1.505E+10
11.4500	56.5141	106.7843	1.326E+10
11.5833	55.7946	106.9076	1.567E+10
11.7333	54.9544	107.0629	9.085E+09
11.9000	54.0678	107.2405	1.142E+10
12.0500	53.2618	107.4150	1.302E+10
12.1833	52.5328	107.5845	1.017E+10
12.3667	51.6480	107.8061	1.231E+10
12.5000	50.9589	107.9922	1.203E+10
12.6500	50.2911	108.1849	1.222E+10
12.8167	49.4847	108.4360	1.642E+10
12.9667	48.8177	108.6607	1.235E+10
13.1000	48.2255	108.8755	1.128E+10
13.2833	47.4775	109.1708	1.401E+10
13.4167	46.9916	109.3798	1.353E+10
13.5500	46.5314	109.5927	1.061E+10
13.7333	45.9072	109.9104	1.222E+10
13.8667	45.5117	110.1333	1.045E+10
14.0167	45.0796	110.4023	1.171E+10
14.1833	44.6609	110.6967	1.142E+10
14.3333	44.3162	110.9745	1.339E+10
14.4667	44.0582	111.2130	1.128E+10
14.6500	43.7413	111.5636	1.231E+10
14.7833	43.5487	111.8303	1.349E+10
14.9167	43.4073	112.0767	1.420E+10
15.1000	43.2629	112.4369	1.114E+10

TABLE A3.5. Sondrestrom Heat Flux Values for 26 June 1984

<u>UT HRS</u>	<u>SZA</u>	<u>CPSZA</u>	<u>HEAT FLUX</u>
15.2500	43.2020	112.7097	1.142E+10
15.4167	43.1842	113.0510	1.216E+10
15.5833	43.2255	113.3717	1.154E+10
15.7333	43.3139	113.6684	1.296E+10
15.8667	43.4263	113.9210	1.128E+10
16.0500	43.6502	114.2863	1.203E+10
16.2000	43.8642	114.5589	1.263E+10
16.3333	44.1174	114.8307	1.045E+10
16.5167	44.4870	115.1676	1.267E+10
16.6500	44.8234	115.4338	1.150E+10
16.8000	45.2297	115.7213	1.165E+10
16.9667	45.7107	116.0252	1.142E+10
17.1333	46.2371	116.3251	1.203E+10
17.2667	46.7237	116.5791	1.016E+10
17.5667	47.8753	117.1116	1.110E+10
17.7167	48.5000	117.3698	1.098E+10
17.8667	49.1554	117.6222	9.618E+09
18.0333	49.8918	117.8860	1.226E+10
18.1833	50.6026	118.1235	1.919E+10
18.3167	51.2227	118.3184	3.437E+10
18.5000	52.1557	118.5926	2.962E+10
18.6333	52.8152	118.7737	1.518E+10
18.7833	53.6101	118.9787	1.714E+10
18.9500	54.4872	119.1899	1.407E+10
19.1000	55.3191	119.3765	1.518E+10
19.4667	57.3541	119.7799	1.114E+10
19.6333	58.2942	119.9428	1.384E+10
19.8167	59.3804	120.1131	1.079E+10
19.9500	60.1351	120.2207	9.384E+09
20.1833	61.5162	120.3948	1.017E+10
20.3333	62.4206	120.4934	9.979E+09
20.5333	63.6064	120.6040	1.008E+10
20.7000	64.5839	120.6793	6.383E+10
20.8500	65.4898	120.7361	1.864E+10
20.9833	66.3272	120.7780	1.799E+10
21.2000	67.5799	120.8207	2.031E+10
21.3500	68.4781	120.8363	2.166E+10
21.4833	69.3025	120.8395	2.160E+10
21.6833	70.4623	120.8256	9.781E+09
21.8333	71.3412	120.8004	9.139E+09
21.9667	72.0768	120.7692	1.058E+10

TABLE A3.5. Sondrestrom Heat Flux Values for 26 June 1984

<u>UT HRS</u>	<u>SZA</u>	<u>CPSZA</u>	<u>HEAT FLUX</u>
22.1500	73.1341	120.7077	1.120E+10
22.2833	73.9195	120.6494	1.114E+10
22.4333	74.6910	120.5806	8.346E+09
22.6000	75.6425	120.4800	7.862E+09
22.7500	76.3913	120.3880	7.787E+09
22.8833	77.1263	120.2860	8.983E+09
23.0667	78.0271	120.1446	7.886E+09
23.5167	80.2621	119.7076	1.114E+10
23.6500	80.8624	119.5669	8.372E+09
23.8333	81.7092	119.3492	8.008E+09

TABLE A3.6. Sondrestrom Heat Flux Values for 27 June 1984

<u>UT HRS</u>	<u>SZA</u>	<u>CPSZA</u>	<u>HEAT FLUX</u>
0.1167	82.9185	118.9950	7.012E+09
0.2833	83.5883	118.7739	9.407E+09
0.4333	84.1847	118.5598	7.177E+09
0.5667	84.6716	118.3717	6.817E+09
0.7500	85.3478	118.0877	6.541E+09
0.9000	85.8667	117.8492	6.699E+09
1.0333	86.2860	117.6413	5.877E+09
1.2167	86.8597	117.3309	6.399E+09
1.3500	87.2302	117.1117	6.672E+09
1.4833	87.6103	116.8681	6.081E+09
1.6667	88.0502	116.5573	9.868E+09
1.8167	88.4261	116.2604	6.875E+09
1.9500	88.6958	116.0242	8.613E+09
2.1167	89.0282	115.6974	5.057E+09
2.2667	89.2645	115.4320	6.953E+09
2.4000	89.4731	115.1647	7.126E+09
2.5833	89.6956	114.8274	1.136E+10
2.7167	89.8425	114.5553	7.012E+09
2.8667	89.9702	114.2597	7.484E+09
3.0333	90.0711	113.9397	9.085E+09
3.1833	90.1305	113.6419	8.983E+09
3.3167	90.1549	113.3896	1.388E+10
3.5000	90.1482	113.0234	8.660E+09
3.6333	90.1143	112.7719	7.458E+09
3.9500	89.9312	112.1594	5.760E+09
4.4000	89.4348	111.3136	2.843E+10
4.6833	88.9576	110.7715	8.453E+09
4.8667	88.6153	110.4535	9.021E+09
5.3167	87.5371	109.6577	7.294E+09
5.4667	87.1522	109.4230	1.158E+10
5.9167	85.7356	108.6976	9.618E+09
6.0500	85.2498	108.4868	5.289E+09
6.2333	84.5687	108.2159	7.110E+09
6.3667	84.0790	108.0366	1.038E+10
6.6833	82.8034	107.6215	9.248E+09
7.1333	80.7898	107.0887	6.953E+09
7.2833	80.0765	106.9296	1.158E+10
7.6000	78.5361	106.6308	9.566E+09
7.7333	77.8878	106.5215	1.739E+10
7.8833	77.1060	106.4018	5.127E+09
8.2000	75.4322	106.1867	1.963E+10

TABLE A3.6. Sondrestrom Heat Flux Values for 27 June 1984

<u>UT HRS</u>	<u>SZA</u>	<u>CPSZA</u>	<u>HEAT FLUX</u>
8.5000	73.8307	106.0290	4.126E+09
13.4500	46.9417	109.3795	2.302E+10
13.6000	46.4061	109.6327	1.495E+10
13.7333	45.9805	109.8520	1.841E+10
13.9000	45.4798	110.1356	2.242E+10
14.2000	44.6708	110.6792	2.845E+10
14.3667	44.3047	110.9795	1.642E+10
14.6500	43.7801	111.5253	1.617E+10
15.1167	43.2961	112.4220	1.436E+10
15.4333	43.2263	113.0355	1.469E+10
15.6500	43.2953	113.4474	1.131E+10
16.2833	44.0714	114.7014	1.524E+10
16.5667	44.6656	115.2395	1.199E+10
17.0333	45.9745	116.1152	1.110E+10
17.3500	47.0638	116.6850	1.258E+10
17.5167	47.6868	116.9711	1.188E+10
17.8333	48.9954	117.5061	1.123E+10
18.6167	52.7372	118.7006	1.807E+10
18.7667	53.4697	118.8921	1.154E+10
18.9000	54.2795	119.0905	1.285E+10
19.0833	55.2343	119.3079	9.085E+09
19.2333	56.0784	119.4860	1.371E+10
19.3667	56.8677	119.6410	1.050E+10
19.5333	57.7998	119.8103	8.346E+09
19.6833	58.6767	119.9567	1.523E+10
19.8333	59.4947	120.0824	1.339E+10
20.0000	60.5234	120.2254	1.222E+10
20.1500	61.3549	120.3295	1.358E+10
20.3500	62.6062	120.4663	1.196E+10
20.5167	63.5823	120.5565	1.970E+10
20.6667	64.4912	120.6280	1.970E+10
20.8167	65.3273	120.6824	1.841E+10
21.0000	66.4432	120.7390	2.013E+10
21.1333	67.2087	120.7670	1.681E+10
21.2833	68.1090	120.7883	1.551E+10
21.4500	69.0735	120.7971	1.937E+10
21.6000	69.9630	120.7921	1.193E+10
21.7333	70.7777	120.7763	1.420E+10
21.9167	71.7884	120.7415	1.296E+10
22.0667	72.6531	120.6977	1.254E+10
22.2000	73.3766	120.6509	1.538E+10

TABLE A3.6. Sondrestrom Heat Flux Values for 27 June 1984

<u>UT HRS</u>	<u>SZA</u>	<u>CPSZA</u>	<u>HEAT FLUX</u>
22.3667	74.3524	120.5730	1.339E+10
22.5167	75.1200	120.4988	1.171E+10
22.6500	75.8765	120.4143	9.435E+09
22.8333	76.8058	120.2945	1.366E+10
22.9667	77.5356	120.1874	1.114E+10
23.1167	78.3098	120.0604	1.971E+10
23.3000	79.2397	119.8887	1.864E+10
23.4667	80.0308	119.7248	9.868E+09
23.6000	80.6921	119.5745	7.311E+09
23.7833	81.5467	119.3606	6.817E+09
23.9333	82.1664	119.1903	9.868E+09

TABLE A3.7. Sondrestrom Heat Flux Values for 28 June 1984

<u>UT HRS</u>	<u>SZA</u>	<u>CPSZA</u>	<u>HEAT FLUX</u>
0.0667	82.7676	119.0118	8.008E+09
0.2333	83.4459	118.7934	7.862E+09
0.3833	84.0505	118.5816	9.727E+09
0.5167	84.5422	118.3960	9.272E+09
0.7000	85.2281	118.1150	8.613E+09
0.8333	85.6768	117.9150	6.561E+09
0.9667	86.1052	117.7104	9.188E+09
1.1500	86.6953	117.4033	1.017E+10
1.2833	87.1111	117.1662	8.091E+09
1.4333	87.5014	116.9245	8.033E+09
1.6000	87.9547	116.6157	7.592E+09
1.7500	88.2891	116.3635	7.620E+09
1.8833	88.5970	116.1080	7.012E+09
2.0500	88.9241	115.8046	8.065E+09
2.2000	89.1952	115.5194	9.407E+09
2.3333	89.3998	115.2757	8.302E+09
2.5167	89.6570	114.9169	7.311E+09
2.6500	89.8052	114.6687	7.585E+09
2.8000	89.9504	114.3735	7.674E+09
3.0000	90.0909	113.9852	6.468E+09
3.1500	90.1603	113.6876	7.417E+09
3.2833	90.1933	113.4355	5.793E+09
3.4500	90.1999	113.0917	5.811E+09
3.6000	90.1700	112.7945	7.806E+09
3.7333	90.1128	112.5208	1.366E+10
3.9167	90.0015	112.1804	5.705E+10
4.0500	89.8811	111.9101	1.296E+10
4.2000	89.7331	111.6421	8.197E+09
4.3667	89.5092	111.3104	1.114E+10
4.5167	89.2996	111.0483	1.420E+10
4.6500	89.0629	110.7893	1.114E+10
4.8167	88.7521	110.4912	1.919E+10
4.9667	88.4329	110.2197	1.609E+10
5.1000	88.1387	109.9936	1.279E+10
5.4167	87.3238	109.4542	8.848E+09
5.5667	86.8887	109.2041	1.145E+10
5.7333	86.3865	108.9414	1.642E+10
5.8833	85.8937	108.7049	1.247E+10
6.2667	84.5209	108.1366	1.284E+10
6.4167	83.9348	107.9263	1.094E+10
6.8667	82.0888	107.3603	9.979E+09

TABLE A3.7. Sondrestrom Heat Flux Values for 28 June 1984

<u>UT HRS</u>	<u>SZA</u>	<u>CPSZA</u>	<u>HEAT FLUX</u>
7.0000	81.5171	107.2104	9.815E+09
7.3167	80.0581	106.8714	1.085E+10
7.4500	79.3825	106.7340	1.746E+10
7.9167	76.9591	106.3293	3.731E+10
8.0833	76.0958	106.2147	1.542E+10
11.6667	55.4068	106.9063	4.723E+10
12.0333	53.3906	107.3179	3.945E+10
12.2167	52.4836	107.5294	7.417E+10
12.3833	51.6004	107.7536	5.616E+10
12.5333	50.8604	107.9564	9.909E+10
12.6667	50.2532	108.1343	2.906E+10
12.8500	49.4015	108.4036	3.520E+10
12.9833	48.8408	108.5950	7.556E+10
13.1333	48.2035	108.8287	7.364E+10
13.3000	47.5541	109.0869	1.279E+11
13.4500	46.9832	109.3345	4.443E+10
13.5833	46.5273	109.5488	5.192E+10
13.7500	45.9865	109.8266	5.327E+10
13.9000	45.5219	110.0913	7.229E+10
14.0333	45.1283	110.3401	1.263E+11
14.2167	44.6862	110.6562	2.271E+10
14.3500	44.3737	110.9130	2.323E+10
14.5167	44.0561	111.2169	9.537E+09
14.7000	43.7733	111.5476	1.714E+10
14.8333	43.5920	111.8143	1.769E+10
14.9667	43.4611	112.0605	1.231E+10
15.1500	43.3310	112.4219	1.724E+10
15.3000	43.2789	112.7177	1.374E+10
15.4333	43.2730	112.9676	2.041E+10
15.6000	43.3151	113.2875	2.632E+10
15.7500	43.4042	113.5855	3.632E+10
15.9167	43.5537	113.9055	3.316E+10
16.1000	43.7917	114.2711	2.484E+10
16.2333	43.9959	114.5205	3.578E+10
16.3833	44.3027	114.8365	1.962E+10
16.7333	45.1310	115.5053	1.776E+10
16.8667	45.4894	115.7453	7.830E+09
17.0333	46.0255	116.0702	2.378E+10
17.1833	46.4901	116.3254	8.372E+09
17.3167	46.9855	116.5767	1.332E+10
17.5000	47.6474	116.8856	9.785E+09

TABLE A3.7. Sondrestrom Heat Flux Values for 28 June 1984

<u>UT HRS</u>	<u>SZA</u>	<u>CPSZA</u>	<u>HEAT FLUX</u>
17.6333	48.2082	117.1273	1.179E+10
17.7667	48.7437	117.3431	1.071E+10
17.9500	49.5629	117.6509	1.267E+10
18.1000	50.2570	117.8920	1.110E+10
18.2500	50.9220	118.1091	1.702E+10
18.4500	51.8967	118.4044	1.085E+10
18.5833	52.6083	118.6051	1.050E+10
18.7333	53.3961	118.8132	9.475E+09
18.9000	54.2673	119.0285	8.983E+09
19.0500	55.0934	119.2185	8.406E+09
19.1833	55.8025	119.3712	8.908E+09
19.3667	56.8534	119.5814	8.274E+09
19.5167	57.6530	119.7285	7.764E+09
19.6500	58.4586	119.8657	8.596E+09
19.8333	59.4784	120.0248	1.114E+10
19.9833	60.3698	120.1505	1.388E+10
20.1167	61.1989	120.2566	1.175E+10
20.3000	62.2398	120.3750	2.955E+10
20.4500	63.1437	120.4643	2.472E+10
20.5833	63.9834	120.5370	9.248E+09

TABLE A3.8. Sondrestrom Heat Flux Values for 15 January 1985

<u>UT HRS</u>	<u>SZA</u>	<u>CPSZA</u>	<u>HEAT FLUX</u>
13.2000	91.3265	64.6269	3.617E+09
13.5167	90.3900	65.1584	3.501E+09
13.6667	89.9838	65.4233	3.875E+09
13.8000	89.6353	65.6728	4.849E+09
14.0000	89.1860	66.0337	4.738E+09
14.1500	88.9010	66.2926	5.030E+09
14.3333	88.5625	66.6432	4.612E+09
16.1000	87.8424	70.1028	1.114E+10
16.5667	88.4114	70.9964	1.323E+10
16.9000	88.9925	71.6036	5.930E+09
18.0000	91.9771	73.4735	1.086E+10
18.4833	93.7352	74.1820	2.992E+09
18.6167	94.2959	74.3748	5.072E+09
19.4333	97.8900	75.3389	2.351E+09
21.5833	109.7428	76.5059	4.544E+09

TABLE A3.9. Sondrestrom Heat Flux Values for 16 January 1985

<u>UT HRS</u>	<u>SZA</u>	<u>CPSZA</u>	<u>HEAT FLUX</u>
13.6000	89.9536	65.5072	4.232E+09
13.7833	89.5077	65.8171	5.030E+09
13.9333	89.1539	66.0915	8.276E+09
14.0667	88.8787	66.3270	5.647E+09
14.8833	87.6637	67.8848	6.515E+09
15.0333	87.5434	68.1814	5.647E+09
15.5000	87.3832	69.1000	9.838E+09
15.6833	87.4054	69.4446	8.908E+09
15.9833	87.5490	70.0394	5.664E+09
16.3167	87.8543	70.6722	3.831E+09
16.6500	88.3317	71.3147	6.817E+09
17.1167	89.2528	72.1706	4.246E+09
21.5833	109.4918	76.6978	1.247E+09
22.1333	112.8292	76.6360	2.398E+07

TABLE A3.10. Sondrestrom Heat Flux Values for 17 January 1985

<u>UT HRS</u>	<u>SZA</u>	<u>CPSZA</u>	<u>HEAT FLUX</u>
12.6500	92.9215	64.1359	1.551E+10
12.8333	92.2272	64.4147	1.475E+10
12.9833	91.6919	64.6498	2.757E+10
13.1333	91.1834	64.8922	2.918E+10
13.3167	90.6310	65.1804	2.520E+10
13.4667	90.1828	65.4372	1.851E+10
13.6000	89.7948	65.6797	2.151E+10
13.9333	88.9886	66.2628	2.318E+10
14.0833	88.6627	66.5412	3.777E+10
15.3667	87.2019	69.0166	1.993E+10
15.5167	87.1870	69.3157	3.531E+10
16.9333	88.6533	72.0264	1.820E+10
17.4167	89.7804	72.8771	1.970E+10
17.6000	90.3035	73.1942	1.551E+10
17.7500	90.7578	73.4458	1.674E+10
17.9000	91.2031	73.6720	1.469E+10
18.0833	91.8343	73.9646	8.848E+09
18.2333	92.3763	74.1944	1.475E+10
18.3667	92.8545	74.3831	7.269E+09
18.5500	93.5835	74.6472	3.118E+09
18.8500	94.8458	75.0498	3.363E+09
20.3833	102.4097	76.5073	2.585E+09
20.5667	103.4406	76.6139	3.015E+09
20.7167	104.2940	76.6875	3.632E+09
20.8500	105.0199	76.7423	1.527E+09
21.0333	106.0925	76.8064	1.659E+09

TABLE A3.11. Sondrestrom Heat Flux Values for 18 January 1985

<u>UT HRS</u>	<u>SZA</u>	<u>CPSZA</u>	<u>HEAT FLUX</u>
6.6500	125.1795	64.2339	8.425E+08
7.1333	122.6170	63.5792	5.616E+09
7.4167	121.0760	63.2504	6.904E+09
7.6167	119.9561	63.0367	2.796E+09
7.7500	119.2208	62.9078	2.091E+09
8.0833	117.2518	62.6065	8.716E+09
8.3667	115.5272	62.3925	1.443E+09
8.7167	113.4372	62.1923	4.044E+09

TABLE A3.12. Sondrestrom Heat Flux Values for 21 March 1985

<u>UT HRS</u>	<u>SZA</u>	<u>CPSZA</u>	<u>HEAT FLUX</u>
0.1000	104.6086	96.0536	2.457E+08
0.4333	106.1093	95.6402	8.354E+08
0.7833	107.5887	95.1556	2.565E+08
5.2667	110.5798	87.0238	9.767E+08
10.4333	83.9297	82.9823	4.073E+09
10.7833	81.9088	83.1729	6.504E+09
11.8000	76.4219	84.0591	6.838E+09
12.1500	74.7076	84.4709	6.195E+09
12.5000	73.1092	84.9330	7.556E+09
12.8333	71.7358	85.4044	6.010E+09
13.1833	70.4056	85.9479	8.613E+09
13.5167	69.3076	86.4887	7.294E+09
13.8667	68.2959	87.1009	7.334E+09
14.2000	67.4681	87.7392	8.564E+09
14.5500	66.8336	88.3993	8.312E+09
14.8833	66.4225	89.0305	8.276E+09
15.2333	66.1821	89.7172	8.908E+09
15.5833	66.1499	90.4104	7.458E+09
15.9167	66.3101	91.0567	8.406E+09
16.2667	66.6830	91.7434	7.620E+09
16.6167	67.2588	92.4191	7.458E+09
16.9500	67.9705	93.0360	7.556E+09
17.3000	68.9156	93.6745	9.216E+09
17.6533	69.9959	94.2661	8.453E+09
17.9833	71.2740	94.8465	6.758E+09
18.3333	72.7014	95.3900	6.526E+09
18.6667	74.2091	95.8762	1.061E+10
19.0167	75.8870	96.3341	7.886E+09
19.5500	78.5954	96.9271	1.086E+10
19.8833	80.4410	97.2451	2.776E+10
20.2333	82.4133	97.5187	1.247E+10
20.5667	84.3025	97.7195	1.058E+10
20.9167	86.3656	97.8736	7.311E+09
21.2500	88.3110	97.9611	4.429E+09
21.6000	90.3985	97.9960	1.120E+10
21.9333	92.4099	97.9694	2.835E+09
22.2833	94.4754	97.8765	3.979E+09
22.6333	96.5024	97.7224	1.289E+09
23.9000	103.2670	96.6781	1.676E+08

TABLE A3.13. Sondrestrom Heat Flux Values for 12 April 1985

<u>UT HRS</u>	<u>SZA</u>	<u>CPSZA</u>	<u>HEAT FLUX</u>
11.4333	69.8673	92.2105	1.128E+10
14.6833	58.1158	97.2090	8.738E+09
16.6000	59.0960	100.9567	9.021E+09
17.0667	60.3004	101.8291	8.786E+09
17.5333	61.8377	102.6572	8.276E+09
18.4667	65.7565	104.1344	1.240E+10
18.9333	68.0580	104.7606	3.788E+09
19.8500	73.0151	105.7170	1.208E+10
20.3333	75.7857	106.0651	8.848E+09
20.7833	78.4806	106.2885	8.406E+09
21.2667	81.4049	106.4093	6.136E+09
21.7167	84.0371	106.4099	8.302E+09
22.6500	89.4113	106.0702	4.443E+09
23.1167	91.9431	105.7344	2.413E+09

TABLE A3.14. Sondrestrom Heat Flux Values for 22 May 1985

<u>UT HRS</u>	<u>SZA</u>	<u>CPSZA</u>	<u>HEAT FLUX</u>
0.1167	86.2285	115.9274	5.010E+09
0.6333	88.2081	115.1967	5.793E+09
1.1000	89.7502	114.4542	4.304E+09
1.6333	91.1597	113.5487	2.122E+09
2.0833	92.0864	112.7151	2.593E+09
2.7833	92.9514	111.3535	3.437E+09
4.2500	92.4132	108.5283	4.631E+09
4.8333	91.3671	107.4759	3.239E+09
5.3000	90.1850	106.6651	5.057E+09
5.8500	88.4444	105.7854	9.475E+09
10.7167	62.8459	103.3285	4.815E+09

TABLE A3.15. Sondrestrom Heat Flux Values for 13 August 1985

<u>UT HRS</u>	<u>SZA</u>	<u>CPSZA</u>	<u>HEAT FLUX</u>
13.6167	54.9519	100.8669	8.578E+09
14.3833	52.9640	102.2292	3.852E+10
14.7667	52.3571	102.9511	1.619E+10
15.1333	52.0396	103.6447	1.251E+10
15.5167	51.9778	104.3918	1.475E+10
15.8833	52.1797	105.0960	1.098E+10
16.9833	54.2662	107.1887	1.972E+10
18.4500	59.9949	109.6322	6.817E+09
18.8167	61.8485	110.1469	3.875E+09

TABLE A3.16. Sondrestrom Heat Flux Values for 12 November 1985

<u>UT HRS</u>	<u>SZA</u>	<u>CPSZA</u>	<u>HEAT FLUX</u>
20.9833	105.8094	79.6401	9.658E+09
21.1500	106.7810	79.6495	4.643E+09
21.3167	107.8261	79.6439	1.953E+09
21.5000	108.9436	79.6204	3.148E+09
21.6500	109.7828	79.5916	5.030E+09
21.8167	110.8321	79.5433	1.343E+09
22.0167	112.0174	79.4688	1.721E+09
22.1667	112.9207	79.3999	2.158E+09
22.3333	113.8878	79.3126	1.208E+09
22.5333	115.0522	79.1889	9.020E+08
22.6833	115.9345	79.0829	6.851E+08
22.8500	116.8733	78.9554	6.588E+08
23.0500	117.9973	78.7855	1.055E+09
23.2000	118.8423	78.6434	9.693E+07
23.3667	119.7366	78.4793	2.776E+08
23.5667	120.7981	78.2651	8.624E+08
23.8833	122.4201	77.8907	9.987E+08

TABLE A3.17. Sondrestrom Heat Flux Values for 28 August 1986

<u>UT HRS</u>	<u>SZA</u>	<u>CPSZA</u>	<u>HEAT FLUX</u>
0.1167	95.8442	105.6960	1.392E+09
0.3333	96.7591	105.4196	1.721E+09
0.5000	97.4865	105.1750	4.972E+08
0.6667	98.1347	104.9375	7.556E+08
0.8500	98.8376	104.6550	8.864E+08
1.0167	99.4190	104.3972	2.929E+08
1.1833	99.9660	104.1331	5.462E+08
1.3667	100.5495	103.8211	2.259E+08
5.7833	99.1903	95.5664	3.355E+09
9.7833	78.5282	92.2563	3.437E+09
10.1000	76.6526	92.3177	6.195E+09
10.4500	74.5866	92.4449	8.521E+09
10.9833	71.4922	92.7570	3.512E+09
11.1667	70.4456	92.8979	9.085E+09
11.3500	69.4210	93.0535	1.358E+10
11.5167	68.5409	93.2034	8.346E+09
11.6833	67.6771	93.3666	1.150E+10
11.8667	66.7193	93.5644	2.106E+10
12.0333	65.9013	93.7518	8.197E+09
12.2000	65.1076	93.9501	6.953E+09
12.3833	64.2365	94.1865	7.674E+09
12.5500	63.5005	94.4066	9.979E+09
12.7333	62.7000	94.6671	9.658E+09
12.9333	61.8923	94.9587	9.815E+09
13.0833	61.3534	95.1713	7.620E+09
13.2500	60.7152	95.4463	6.953E+09
13.4333	60.1196	95.7302	8.956E+09
13.6000	59.5686	96.0223	8.065E+09
13.7667	59.0963	96.3018	7.806E+09
13.9500	58.6366	96.6083	6.925E+09
14.1167	58.2267	96.9212	9.618E+09
14.3000	57.8680	97.2401	8.308E+09
14.4833	57.5431	97.5861	1.065E+10
14.6500	57.3111	97.8909	5.414E+09
14.8333	57.1005	98.2475	6.346E+09
15.0500	56.9355	98.6724	1.072E+10
15.2167	56.8700	98.9899	6.081E+09
15.3833	56.8558	99.3301	9.566E+09
15.5833	56.9089	99.7153	1.085E+10
15.7333	56.9981	100.0105	5.551E+09
15.9000	57.1409	100.3282	6.219E+09

TABLE A3.17. Sondrestrom Heat Flux Values for 28 August 1986

<u>UT HRS</u>	<u>SZA</u>	<u>CPSZA</u>	<u>HEAT FLUX</u>
16.1000	57.3789	100.7133	1.603E+10
16.2500	57.6087	101.0052	4.376E+10
16.4167	57.9002	101.3193	3.788E+10
16.6167	58.3164	101.6955	2.776E+10
16.9333	59.1118	102.2803	1.296E+10
17.1333	59.6929	102.6407	2.865E+10
17.2833	60.1782	102.9086	8.513E+09
17.4500	60.7369	103.1952	3.071E+10
17.6500	61.4656	103.5332	4.191E+10
17.8000	62.0585	103.7823	1.926E+10
17.9833	62.8271	104.0827	1.970E+10
18.1667	63.5853	104.3546	1.456E+10
18.3500	64.4313	104.6354	9.979E+09

TABLE A3.18. Sondrestrom Heat Flux Values for 1 April 1987

<u>UT HRS</u>	<u>SZA</u>	<u>CPSZA</u>	<u>HEAT FLUX</u>
2.6833	108.7586	96.0649	3.916E+08
3.8500	108.9967	93.8084	1.862E+08
4.0000	108.8739	93.5374	3.211E+08
4.1667	108.6763	93.1994	1.126E+05
4.3333	108.4471	92.8862	1.703E+08
4.4833	108.1973	92.5963	6.765E+08
11.5333	73.6694	87.8510	8.848E+09
12.7167	68.0357	89.2743	1.048E+10
12.9000	67.2758	89.5483	8.197E+09
13.0500	66.6898	89.7799	1.033E+10
13.2167	66.0919	90.0374	1.050E+10
13.3833	65.5297	90.3029	1.263E+10
13.5333	65.0409	90.5564	1.033E+10
13.7000	64.5526	90.8351	8.637E+09
13.8833	64.0420	91.1635	1.353E+10
14.0333	63.6680	91.4348	1.216E+10
14.2000	63.2803	91.7555	1.017E+10
14.4833	62.7658	92.2785	1.079E+10
14.6333	62.5418	92.5672	9.407E+09
14.8000	62.3447	92.8814	2.013E+10
14.9833	62.1766	93.2439	1.759E+10
15.1333	62.0912	93.5173	1.226E+10
15.2833	62.0353	93.8168	1.231E+10
15.4667	62.0246	94.1852	1.145E+10
15.6167	62.0622	94.4847	1.139E+10
15.7833	62.1455	94.8091	9.589E+09
15.9667	62.2900	95.1541	1.251E+10

TABLE A3.19. Sondrestrom Heat Flux Values for 27 August 1987

<u>UT HRS</u>	<u>SZA</u>	<u>CPSZA</u>	<u>HEAT FLUX</u>
0.2000	95.7623	106.0904	3.731E+09
0.5167	97.0899	105.6646	2.091E+09
9.7833	78.1657	92.6871	1.556E+10
10.1167	76.2223	92.7420	8.091E+09
10.7667	72.3261	93.0213	3.288E+10
11.1000	70.4681	93.2387	8.596E+09
11.7500	66.9394	93.8186	1.670E+10
12.0833	65.2916	94.1798	1.759E+10
12.4167	63.6927	94.5965	1.272E+10
12.7500	62.2577	95.0441	1.642E+10
13.0667	61.0007	95.5058	1.759E+10
13.4000	59.8308	96.0211	1.524E+10
13.7333	58.7851	96.5832	1.216E+10
14.0667	57.9394	97.1570	1.690E+10
14.3833	57.2969	97.7260	1.142E+10
14.7167	56.7968	98.3576	1.017E+10
15.0500	56.5031	99.0033	1.442E+10
15.3667	56.4194	99.6125	2.943E+10
15.7000	56.5317	100.2748	3.131E+10
16.0333	56.8435	100.9085	1.945E+10
16.3500	57.3249	101.5160	1.332E+10
16.6833	58.0336	102.1589	1.776E+10
17.0167	58.8968	102.7663	3.131E+10
17.6667	61.1079	103.9179	2.527E+10
18.0000	62.4301	104.4534	2.293E+10

TABLE A3.20. Sondrestrom Heat Flux Values for 10 November 1987

<u>UT HRS</u>	<u>SZA</u>	<u>CPSZA</u>	<u>HEAT FLUX</u>
0.0167	122.2132	78.7864	4.831E+08
0.2333	123.2654	78.4959	2.648E+08
0.6500	125.0608	77.9130	9.534E+07
0.8500	125.9039	77.5916	1.110E+05
1.4833	128.0564	76.5504	1.196E+10
1.9000	129.1124	75.8236	1.203E+10
2.1000	129.5199	75.4583	1.180E+08
2.5167	130.1428	74.6635	1.039E+05
2.7333	130.3274	74.2579	1.098E+08
3.1500	130.4391	73.4348	1.589E+10
3.3667	130.3636	73.0207	2.943E+09
3.7833	129.9570	72.1915	4.475E+09
4.4000	128.7537	70.9893	2.385E+09
5.6500	124.4241	68.7433	4.631E+09
5.8667	123.4321	68.3858	4.993E+08
6.4833	120.4679	67.4869	2.335E+09
7.1167	117.0717	66.7027	2.672E+09
7.5333	114.6797	66.2764	4.815E+09
7.7333	113.5222	66.1049	8.406E+09
8.1500	111.1116	65.8110	9.167E+09
8.3667	109.7217	65.6810	2.244E+10
8.7833	107.2132	65.5195	3.027E+10
9.0000	105.9616	65.4745	2.413E+10
9.4167	103.4813	65.4561	1.567E+10
9.6167	102.3311	65.4785	5.365E+09
10.0333	100.0018	65.5943	6.038E+09
10.2500	98.7701	65.6939	2.411E+10
10.6667	96.5747	65.9433	2.458E+10
10.8667	95.5433	66.0969	1.296E+10
11.5000	92.4781	66.7039	2.105E+10
11.9167	90.6296	67.2070	1.296E+10
12.1167	89.8156	67.4712	1.235E+10
12.5333	88.1979	68.0931	7.764E+09
12.7500	87.4901	68.4178	8.596E+09
13.1667	86.2372	69.1081	1.702E+10
13.3833	85.6991	69.4687	9.669E+09
13.8000	84.7959	70.2260	7.965E+09
14.0000	84.4595	70.5912	8.824E+09
14.4167	83.9421	71.3652	9.380E+09
14.6333	83.7649	71.7921	1.033E+10
15.0500	83.6308	72.5865	1.663E+10

TABLE A3.20. Sondrestrom Heat Flux Values for 10 November 1987

<u>UT HRS</u>	<u>SZA</u>	<u>CPSZA</u>	<u>HEAT FLUX</u>
15.2500	83.6559	72.9742	1.603E+10
15.6667	83.9047	73.7921	1.603E+10
15.8833	84.1286	74.1955	1.420E+10
16.3000	84.7692	74.9897	1.216E+10
16.5000	85.1599	75.3552	1.247E+10
16.9167	86.1970	76.1291	1.216E+10
17.1333	86.7915	76.4909	1.514E+10
17.5500	88.1480	77.1778	1.388E+10
17.7667	88.9055	77.5037	1.038E+10

TABLE A3.21. Sondrestrom Heat Flux Values for 25 November 1987

<u>UT HRS</u>	<u>SZA</u>	<u>CPSZA</u>	<u>HEAT FLUX</u>
0.7167	128.6536	74.2355	2.498E+08
1.0333	129.9174	73.7505	1.180E+09
3.5500	133.9082	69.1049	6.170E+08
5.4333	129.0032	65.5588	7.105E+08
9.5000	106.6168	61.8214	8.124E+09
11.0667	98.1954	62.6000	1.521E+09
11.3833	96.6822	62.9062	1.906E+09
11.7000	95.2569	63.2564	5.688E+09
12.0167	93.8748	63.6665	3.995E+09
12.3167	92.6920	64.0838	6.699E+09
12.6333	91.5696	64.5535	8.008E+09
12.9500	90.5654	65.0544	7.585E+09
13.2667	89.6841	65.5839	8.716E+09
13.5833	88.9316	66.1379	3.211E+10
13.8833	88.3325	66.6918	3.579E+10
14.2000	87.8469	67.2823	2.646E+10
14.5167	87.5026	67.8851	3.685E+10
14.8333	87.3022	68.4962	2.363E+10
15.1500	87.2470	69.1113	2.251E+10
15.4667	87.3375	69.7262	2.489E+10
15.7667	87.5498	70.2939	1.222E+10
16.0833	87.9187	70.8958	9.085E+09
16.4000	88.4495	71.5088	7.764E+09
16.7167	89.1013	72.0835	1.017E+10
17.0167	89.8544	72.6193	1.296E+10
17.3333	90.7620	73.1521	7.585E+09
17.6500	91.7915	73.6584	1.188E+10
17.9667	92.9362	74.1351	6.504E+09
18.2833	94.1893	74.5791	6.219E+09
18.5833	95.4917	74.9740	4.829E+09
18.9000	96.9352	75.3460	5.229E+09

TABLE A3.22. Sondrestrom Heat Flux Values for 15 January 1988

<u>UT HRS</u>	<u>SZA</u>	<u>CPSZA</u>	<u>HEAT FLUX</u>
0.3333	125.7872	74.6192	3.728E+08
0.6000	127.1079	74.2879	4.570E+08
0.8833	128.4068	73.9134	2.971E+08
1.7167	131.6671	72.6547	8.279E+08
2.0000	132.5732	72.1636	2.847E+08
2.2667	133.2503	71.7150	8.908E+08
13.4833	90.5710	64.7608	7.229E+09
14.0500	89.2093	65.7453	9.939E+09
14.3333	88.6863	66.2627	6.817E+09
14.6167	88.2732	66.7924	7.620E+09
15.1833	87.7775	67.9019	3.201E+09
15.4667	87.7084	68.4526	8.276E+09
17.1333	89.6426	71.6552	3.731E+09
17.4167	90.3441	72.1540	9.216E+09
17.7167	91.2191	72.6737	9.838E+09
18.0000	92.1252	73.1321	9.048E+09
18.5667	94.2099	73.9777	7.556E+09
18.8667	95.4783	74.3915	5.127E+09
19.2333	97.1052	74.8400	2.222E+09
19.5167	98.4439	75.1516	2.871E+09
19.8000	99.8993	75.4423	1.472E+09
20.0833	101.3588	75.6854	1.760E+09
20.3667	102.8703	75.8926	1.616E+09
21.2000	107.6312	76.2949	1.065E+08
22.0333	112.5379	76.3543	7.957E+08

TABLE A3.23. Sondrestrom Heat Flux Values for 17 March 1988

<u>UT HRS</u>	<u>SZA</u>	<u>CPSZA</u>	<u>HEAT FLUX</u>
0.3500	107.0598	94.4803	7.484E+08
0.5000	107.7366	94.2914	1.172E+09
0.6667	108.4454	94.0727	1.512E+08
0.8500	109.2612	93.7973	1.148E+05
1.0000	109.8055	93.5972	6.608E+08
1.1667	110.4576	93.3333	4.112E+08
1.3500	111.0657	93.0630	3.239E+09
1.5167	111.5997	92.7993	6.390E+08
1.6667	112.0598	92.5497	4.122E+08
1.8667	112.6105	92.2148	3.088E+09
2.0167	112.9943	91.9500	5.487E+09
2.1833	113.3644	91.6625	7.054E+08
2.3667	113.7403	91.3232	8.562E+08
2.5167	114.0003	91.0467	7.876E+08
2.6833	114.2419	90.7409	8.347E+09
2.8667	114.4603	90.3902	1.301E+10
3.1833	114.6979	89.7860	7.588E+09
3.5167	114.7626	89.1535	1.191E+09
3.6833	114.7232	88.8393	2.527E+09
3.8667	114.6266	88.4735	2.934E+09
4.0333	114.4903	88.1577	1.621E+09
4.1833	114.3265	87.8604	1.721E+09
4.3833	114.0505	87.4790	8.197E+08
4.5333	113.7959	87.1890	1.007E+09
4.7000	113.4800	86.8791	1.719E+09
4.8833	113.0674	86.5286	5.598E+08
5.0333	112.6927	86.2464	1.231E+08
5.2000	112.2157	85.9290	4.259E+08
5.3833	111.6946	85.6156	1.187E+09
5.5333	111.2077	85.3498	5.571E+08
5.7000	110.6488	85.0674	5.710E+08
5.8833	109.9659	84.7561	7.990E+08
6.0333	109.3790	84.5093	9.987E+08
6.2000	108.7164	84.2490	2.299E+09
6.3833	107.9213	83.9632	1.260E+09
6.5500	107.1939	83.7245	2.632E+09
6.7000	106.4946	83.5080	1.289E+09
7.0500	104.7970	83.0436	3.097E+09
7.2167	103.9681	82.8450	2.269E+09
7.4000	103.0570	82.6422	7.556E+09
7.5500	102.2496	82.4758	8.703E+09

TABLE A3.23. Sondrestrom Heat Flux Values for 17 March 1988

<u>UT HRS</u>	<u>SZA</u>	<u>CPSZA</u>	<u>HEAT FLUX</u>
7.7167	101.3627	82.3092	2.158E+09
7.9000	100.3293	82.1346	1.030E+09
8.0500	99.4758	82.0037	2.538E+09
8.2167	98.5441	81.8731	6.541E+09
8.4000	97.4654	81.7407	4.306E+09
8.5500	96.5794	81.6463	6.219E+09
8.7167	95.6175	81.5571	4.789E+09
8.9000	94.5794	81.4762	6.573E+08
9.0667	93.5355	81.4093	4.241E+08
9.2167	92.6974	81.3703	4.219E+09
9.4167	91.3676	81.3254	6.038E+09
9.7333	89.4783	81.3070	3.118E+09
9.9167	88.4326	81.3202	9.435E+09
10.0667	87.5303	81.3423	4.044E+09
10.4167	85.4692	81.4412	3.097E+09
10.5667	84.5881	81.5039	8.882E+09
10.7333	83.6493	81.5843	2.187E+10
10.9167	82.5912	81.6922	1.175E+10
11.0667	81.8093	81.7851	1.734E+10
11.2333	80.8476	81.9140	5.229E+09
11.4167	79.9050	82.0576	6.275E+09
11.5667	79.1050	82.1939	1.582E+10
11.7333	78.2629	82.3512	1.188E+10
11.9167	77.3262	82.5478	1.323E+10
12.0833	76.5313	82.7314	1.110E+10
12.2333	75.8152	82.9122	1.193E+10
12.4333	74.9127	83.1632	1.061E+10
12.5833	74.2505	83.3640	8.308E+09
12.7500	73.5653	83.5911	7.229E+09
12.9333	72.8195	83.8631	1.098E+10
13.1000	72.2018	84.1102	1.025E+10
13.2667	71.6184	84.3550	1.008E+10
13.4500	70.9942	84.6671	1.004E+10
13.6000	70.5219	84.9203	9.537E+09
13.7667	70.0168	85.2208	9.658E+09
13.9500	69.5571	85.5280	9.537E+09
14.1000	69.1966	85.7991	8.956E+09
14.2667	68.8462	86.0984	1.128E+10
14.4833	68.4399	86.5105	1.038E+10
14.6500	68.1896	86.8207	9.979E+09
14.8167	67.9862	87.1318	9.727E+09

TABLE A3.23. Sondrestrom Heat Flux Values for 17 March 1988

<u>UT HRS</u>	<u>SZA</u>	<u>CPSZA</u>	<u>HEAT FLUX</u>
15.0000	67.8047	87.4941	1.050E+10
15.1500	67.7007	87.7906	9.216E+09
15.3167	67.6337	88.1106	9.658E+09
15.5000	67.6100	88.4799	9.042E+09
15.6667	67.6386	88.8032	9.589E+09
15.8167	67.7070	89.1028	7.962E+09
16.0000	67.8313	89.4499	6.991E+09
16.1667	68.0100	89.7939	8.824E+09
16.3333	68.2209	90.1144	9.356E+09
16.5167	68.4937	90.4562	1.017E+10
16.6667	68.7709	90.7493	1.022E+10
16.8333	69.1121	91.0606	1.175E+10
17.0167	69.5490	91.4134	1.040E+10
17.1667	69.9453	91.6945	8.963E+09
17.3333	70.4060	91.9942	1.154E+10
17.5167	70.9815	92.3285	1.033E+10
17.6667	71.4856	92.5936	1.054E+10
17.8333	72.0606	92.8736	7.269E+09
18.0167	72.7598	93.1846	6.608E+09
18.1667	73.3583	93.4304	9.435E+09
18.3333	74.0330	93.6870	1.071E+10
18.5167	74.8408	93.9694	1.216E+10
18.6667	75.5231	94.1905	1.501E+10
18.8333	76.2838	94.4192	1.394E+10
19.0167	77.1842	94.6682	8.453E+09
19.1833	77.9963	94.8752	1.028E+10
19.3333	78.7671	95.0590	9.979E+09
19.5333	79.8082	95.2816	9.216E+09
19.7500	80.9351	95.5009	3.355E+10
19.9000	81.7688	95.6457	1.926E+10
20.0833	82.8081	95.8115	2.413E+10
20.2500	83.7331	95.9425	1.136E+10
20.4167	84.6697	96.0607	9.909E+09
20.6000	85.7531	96.1795	1.085E+10
20.7500	86.6405	96.2638	9.979E+09
20.9167	87.6033	96.3416	6.991E+09
21.1000	88.7082	96.4148	8.482E+09
21.2500	89.5459	96.4551	1.384E+10
21.4167	90.5878	96.4952	1.028E+10
21.6000	91.6331	96.5182	5.987E+09
21.7500	92.5376	96.5257	6.904E+09

TABLE A3.23. Sondrestrom Heat Flux Values for 17 March 1988

<u>UT HRS</u>	<u>SZA</u>	<u>CPSZA</u>	<u>HEAT FLUX</u>
21.9167	93.5073	96.5216	9.838E+09
22.1000	94.6169	96.4966	7.200E+09
22.2500	95.5767	96.4630	1.654E+10
22.4167	96.5344	96.4128	1.966E+09
22.6000	97.6162	96.3400	2.263E+09
22.7500	98.4176	96.2746	7.377E+08
22.9167	99.4058	96.1799	2.927E+09
23.1000	100.3837	96.0671	2.920E+09
23.2667	101.2808	95.9485	6.046E+08
23.4167	102.0938	95.8303	9.594E+08
23.6167	103.1380	95.6564	2.806E+08
23.7667	103.9133	95.5138	3.683E+08
23.9333	104.7352	95.3435	2.389E+08

APPENDIX 4

MILLSTONE HILL DATA

This appendix contains tables of the T_e algorithm output for the 25 days of Millstone Hill data we analyzed. Each table consists of four columns. The first column is UT time, the second column is the solar zenith angle at Millstone Hill, the third column is conjugate point solar zenith angle, and the fourth column is the downward heat flux (in $\text{eV cm}^{-2} \text{s}^{-1}$) valid at 600 km (see Section 4.2).

A WARNING TO POTENTIAL USERS OF THIS DATA: The heat flux values listed in this appendix are "raw," i.e., no attempt has been made to remove the heat flux values which correspond to a poor agreement between the calculated and ISR T_e profiles. Therefore, as a rule-of-thumb, disregard all heat flux values which are less than 1×10^7 or greater than 1×10^{12} .

TABLE A4.1. Millstone Hill Heat Flux Values for 15 January 1985

<u>UT HRS</u>	<u>SZA</u>	<u>CPSZA</u>	<u>HEAT FLUX</u>
0.7000	123.5579	79.2583	2.579E+09
1.8167	135.7079	83.9737	3.222E+09
2.5500	143.4019	86.4845	2.974E+09
3.2000	149.6455	88.2235	2.595E+09
3.8667	154.8754	89.4670	2.186E+09
4.5333	158.1004	90.1430	1.738E+09
5.1833	158.4090	90.2385	1.832E+09
5.9333	155.1991	89.6562	1.080E+09
6.5833	150.1814	88.5557	7.335E+08
7.2500	143.8963	86.8991	6.680E+08
7.9167	136.8598	84.7071	9.405E+08
8.5667	129.8900	82.2131	8.562E+08
9.2333	122.5427	79.2677	9.720E+08
9.9000	115.1839	76.0231	9.405E+08
10.5500	108.1688	72.6879	1.180E+09
11.2167	101.0687	69.1001	1.566E+09
12.4667	88.3963	62.2487	3.316E+09
13.6500	78.0141	56.2948	6.081E+09
14.8667	69.6389	51.3225	8.033E+09
16.0333	64.7177	48.3274	8.091E+09
16.4833	63.8121	47.7598	9.135E+09
17.8333	64.7501	48.2453	8.312E+09
18.2833	66.2144	49.1000	5.688E+09
18.7833	68.5001	50.4420	7.311E+09
19.3000	71.4596	52.1823	1.042E+10
20.2000	77.9212	55.9570	6.195E+09
20.7333	82.4184	58.5487	7.764E+09
21.4833	89.2899	62.4301	5.793E+09
21.9833	94.2184	65.1440	5.072E+09
22.2667	97.0636	66.6776	4.518E+09
22.8333	102.9120	69.7472	3.437E+09
23.1167	106.0271	71.3324	3.110E+09
23.5500	110.7025	73.6404	2.520E+09

TABLE A4.2. Millstone Hill Heat Flux Values for 16 January 1985

<u>UT HRS</u>	<u>SZA</u>	<u>CPSZA</u>	<u>HEAT FLUX</u>
0.5333	121.4930	78.5982	2.808E+09
1.1000	127.8145	81.2298	2.835E+09
1.7000	134.3202	83.7005	1.730E+09
2.2667	140.2714	85.7312	3.593E+09
2.8333	146.0251	87.4694	3.901E+09
3.1167	148.6499	88.1863	6.925E+10
3.6833	153.3123	89.3372	3.461E+09
4.2500	156.8200	90.1034	1.535E+09
4.8167	158.4103	90.4363	2.028E+09
6.2667	152.6458	89.3438	7.105E+08
7.0000	146.2965	87.7883	1.359E+09
7.5667	140.5631	86.1253	1.081E+09
8.1333	134.6248	84.1656	8.588E+08
8.7000	128.5056	81.9071	9.383E+08
9.3167	121.5368	79.0679	9.434E+08
9.9833	114.1847	75.7929	8.164E+08
10.2667	111.1122	74.3467	5.961E+08
10.8333	105.0463	71.3710	1.153E+09
11.1167	101.9419	69.7908	4.372E+08
11.6833	96.1153	66.7280	1.106E+09
12.2500	90.5191	63.6817	2.378E+09
12.8167	85.1054	60.6476	3.241E+09
13.2000	81.7721	58.7432	4.323E+09
13.7000	77.4970	56.2632	5.093E+09
14.9000	69.3408	51.4334	6.608E+09
15.4167	66.7118	49.8472	6.399E+09
16.0000	64.6614	48.5979	7.334E+09
16.5000	63.6243	47.9504	5.010E+09
17.5167	63.8343	48.0193	1.025E+10
18.0167	65.0720	48.7309	8.564E+09
18.5167	67.0127	49.8614	8.487E+09
19.0333	69.6556	51.4109	8.453E+09
19.6833	73.8763	53.8774	9.752E+09
20.2000	77.7534	56.1322	8.674E+09
20.7000	81.8510	58.4890	1.142E+10
21.2000	86.3778	61.0566	7.830E+09
21.7167	91.2891	63.7925	5.909E+09
22.4500	98.8491	67.8724	4.286E+09
23.0167	104.7629	70.9343	3.027E+09
23.5833	110.8203	73.9350	3.929E+09

TABLE A4.3. Millstone Hill Heat Flux Values for 17 January 1985

<u>UT HRS</u>	<u>SZA</u>	<u>CPSZA</u>	<u>HEAT FLUX</u>
0.1500	117.0994	76.8812	2.372E+09
0.7167	123.2989	79.6040	3.027E+09
1.0000	126.3933	80.8889	2.609E+09
1.5667	132.6672	83.3268	2.448E+09
2.1333	138.6661	85.4357	2.056E+09
2.7000	144.5038	87.2629	1.664E+09
3.2667	149.8356	88.7247	2.082E+09
3.8333	154.2160	89.7721	1.352E+09
4.1167	155.9270	90.1469	1.535E+09
5.3000	157.8042	90.5834	1.798E+09
5.8667	155.3063	90.1264	1.483E+09
6.1500	153.4496	89.7455	1.743E+09
6.7167	148.7665	88.6584	1.416E+09
7.0000	146.1619	87.9801	1.659E+09
7.5667	140.4439	86.3187	1.400E+09
8.1333	134.5106	84.3563	1.546E+09
8.7667	127.6239	81.7956	1.760E+09
9.0500	124.5306	80.5547	1.448E+09
9.6167	118.1950	77.8482	2.448E+09
10.2167	111.6376	74.8358	1.766E+09
10.7833	105.5580	71.8717	5.491E+08
11.1667	101.3265	69.7183	1.055E+09
11.7333	95.5149	66.6585	4.698E+09
12.1000	91.7630	64.6234	1.868E+09
12.6000	87.0276	61.9971	4.443E+09
13.1000	82.4465	59.4018	5.343E+09
13.6167	78.0936	56.8906	5.045E+09
14.1167	74.2329	54.6307	9.838E+09
14.6167	70.9084	52.6649	1.098E+10
15.1333	67.9107	50.8743	8.033E+09
15.6333	65.6699	49.5235	1.139E+10
16.1500	64.0784	48.5533	1.071E+10
16.6500	63.2620	48.0396	1.114E+10
17.1500	63.1979	47.9740	8.596E+09
17.6667	63.9361	48.3833	9.318E+09
18.2167	65.5200	49.2976	1.216E+10
18.7167	67.7114	50.5720	1.045E+10
19.2333	70.5872	52.2510	1.222E+10
19.7333	74.0333	54.2569	1.033E+10
20.2500	77.9634	56.5323	1.150E+10
20.7500	82.1985	58.9610	7.830E+09

TABLE A4.3. Millstone Hill Heat Flux Values for 17 January 1985

<u>UT HRS</u>	<u>SZA</u>	<u>CPSZA</u>	<u>HEAT FLUX</u>
21.2500	86.6515	61.4793	9.537E+09
21.7333	91.3700	64.0973	8.716E+09
22.0167	94.1642	65.6208	5.664E+09
22.8833	103.1288	70.3505	5.466E+09
23.1667	106.1315	71.8716	3.316E+09
23.7333	112.3460	74.9107	4.304E+09

TABLE A4.4. Millstone Hill Heat Flux Values for 20 March 1985

<u>UT HRS</u>	<u>SZA</u>	<u>CPSZA</u>	<u>HEAT FLUX</u>
0.6500	109.2228	98.8597	1.557E+09
1.4500	117.4183	102.6876	9.351E+08
1.8667	121.3051	104.4358	9.802E+08
2.3000	125.1418	106.1107	6.988E+08
3.3833	133.0582	109.3759	8.399E+08
3.8000	135.2219	110.2249	7.431E+08
4.2167	136.7512	110.8178	8.588E+08
4.6500	137.5821	111.1519	8.320E+08
5.0667	137.6359	111.2066	8.784E+08
5.5000	136.9199	110.9820	5.710E+08
6.0833	134.7599	110.2352	3.473E+08
6.5167	132.3841	109.3631	4.164E+08
7.0333	128.8439	107.9955	2.825E+08
7.4500	125.4762	106.6339	2.537E+08
7.8833	121.6629	105.0279	2.282E+08
8.3000	117.6803	103.2876	1.007E+09
8.7333	113.3666	101.3382	5.330E+08
9.1667	108.8847	99.2590	4.847E+08
9.5833	104.4033	97.1347	5.508E+08
10.0167	99.7054	94.8653	4.831E+08
10.4333	95.2077	92.6674	1.019E+09
10.9500	89.5180	89.8671	1.019E+09
11.3833	84.7353	87.5110	3.330E+09
11.8167	79.9831	85.1792	3.979E+09
12.2333	75.4199	82.9642	6.038E+09
12.6667	70.6999	80.7070	6.195E+09
13.0833	66.4758	78.7276	8.091E+09
13.8667	58.8628	75.2861	8.453E+09
14.3000	55.0246	73.6252	9.216E+09
14.7167	51.6252	72.2019	1.078E+10
15.1667	48.4837	70.9347	1.098E+10
15.6000	45.9601	69.9483	8.406E+09
16.0333	44.0625	69.2248	1.061E+10
16.4500	42.9013	68.7845	1.193E+10
16.8833	42.4699	68.6143	9.135E+09
17.3000	42.8182	68.7249	1.188E+10
17.7333	43.9459	69.1179	1.199E+10
18.1500	45.7296	69.7699	1.117E+10
18.5833	48.1914	70.7016	1.150E+10
19.5833	55.7291	73.7598	1.518E+10
20.0167	59.6232	75.4394	1.397E+10

TABLE A4.4. Millstone Hill Heat Flux Values for 20 March 1985

<u>UT HRS</u>	<u>SZA</u>	<u>CPSZA</u>	<u>HEAT FLUX</u>
20.4333	63.6657	77.2441	1.235E+10
21.0667	70.2057	80.2714	1.123E+10
21.5000	74.7826	82.4543	1.094E+10
21.9167	79.2016	84.5997	9.589E+09
22.3333	83.8085	86.8638	9.021E+09
22.7667	88.5791	89.2264	8.882E+09
23.1833	93.0948	91.4709	6.383E+09
23.6167	97.8571	93.8285	4.179E+09

TABLE A4.5. Millstone Hill Heat Flux Values for 23 April 1985

<u>UT HRS</u>	<u>SZA</u>	<u>CPSZA</u>	<u>HEAT FLUX</u>
4.2000	124.4942	123.6128	8.320E+08
4.8167	124.9981	123.9098	9.955E+12
5.4333	124.1560	123.5521	5.848E+08
6.0500	122.1120	122.5898	3.366E+08
9.1333	98.5537	110.6224	1.802E+05
9.7500	92.1018	107.2876	2.850E+05
10.3667	85.5141	103.9226	9.955E+12
10.9833	78.8896	100.6121	1.505E+09
11.5833	72.3111	97.4289	6.081E+09
12.2000	65.4588	94.2504	8.065E+09
13.1333	55.2917	89.8702	5.365E+09
13.7500	48.9620	87.3863	8.765E+09
14.3667	42.8279	85.1893	6.561E+09
14.9833	37.5030	83.4639	8.202E+09
15.6000	33.3160	82.2343	1.071E+10
16.2167	30.5801	81.4899	1.025E+10
16.8333	29.8275	81.2778	9.167E+09
17.4500	31.1765	81.5988	1.326E+10
18.0667	34.4087	82.4497	1.538E+10
18.6833	39.0342	83.8089	1.142E+10
19.3000	44.5990	85.6357	9.909E+09
19.9500	51.0077	87.9724	9.216E+09
20.5500	57.4286	90.5375	1.061E+10
21.1667	64.0433	93.3876	1.120E+10
21.7833	70.8764	96.5196	7.674E+09
22.4000	77.5790	99.7480	9.172E+09
23.0167	84.4677	103.1901	5.259E+09
23.6333	91.0644	106.5805	4.544E+09

TABLE A4.6. Millstone Hill Heat Flux Values for 21 May 1985

<u>UT HRS</u>	<u>SZA</u>	<u>CPSZA</u>	<u>HEAT FLUX</u>
0.3000	92.7229	117.1179	6.695E+09
0.9167	98.2898	120.2673	1.045E+09
1.5333	103.5637	123.3114	2.169E+08
2.1500	108.0299	125.9300	1.014E+05
2.7667	111.8292	128.1851	1.158E+08
3.3833	114.7292	129.9265	7.273E+07
3.9833	116.5443	131.0392	1.483E+09
4.6000	117.3296	131.5496	2.305E+08
6.4500	112.8801	129.0812	1.506E+08
7.0667	109.3598	127.0615	2.381E+08
11.0167	73.2092	107.3300	1.488E+09
11.6333	66.4488	104.0713	7.126E+09
12.3000	59.0930	100.7555	5.909E+09
14.2667	37.9368	92.8535	7.830E+09
14.8833	31.9908	91.1481	8.406E+09
15.5000	26.9357	89.8931	6.139E+09
16.1167	23.4682	89.1391	8.812E+09
16.7333	22.2126	88.8721	8.605E+09
17.3333	23.5336	89.1007	7.554E+09
17.9500	27.1334	89.8376	1.071E+10
18.5667	32.2328	91.0641	1.145E+10
19.1833	38.2086	92.7485	1.488E+10
19.8167	44.7948	94.8931	7.588E+09
20.4333	51.5141	97.3685	1.021E+10
21.0500	58.2132	100.0998	8.169E+09
21.6667	65.0531	103.1330	6.425E+09
22.2667	71.5725	106.2300	5.289E+09
22.8833	78.3405	109.6323	7.126E+09
23.5000	84.6533	112.9580	4.249E+09

TABLE A4.7. Millstone Hill Heat Flux Values for 25 June 1985

<u>UT HRS</u>	<u>SZA</u>	<u>CPSZA</u>	<u>HEAT FLUX</u>
0.3500	89.9058	119.9008	2.808E+09
0.9667	95.3655	123.0800	1.244E+09
1.5667	100.3447	126.0646	3.341E+08
2.1833	104.7321	128.7584	7.453E+08
2.7833	108.4160	131.0678	4.427E+08
3.4000	111.2667	132.8883	7.436E+07
4.0000	113.1513	134.1170	1.058E+07
4.6167	114.0722	134.7448	1.327E+08
5.2167	113.8846	134.6667	1.014E+05
5.8333	112.6099	133.8994	5.171E+07
6.4333	110.4045	132.5440	3.164E+08
7.0500	107.1892	130.5675	3.689E+07
7.6500	103.3224	128.2095	1.126E+05
10.2667	80.1093	114.8693	9.118E+08
10.8667	73.9170	111.6227	1.142E+09
11.4833	67.2839	108.3267	3.131E+09
12.0833	60.7724	105.2937	1.798E+09
12.7000	53.9315	102.3468	5.030E+09
13.3000	47.2250	99.7189	6.326E+09
13.9167	40.4911	97.3637	8.564E+09
14.5167	34.2385	95.4511	4.544E+09
15.1833	27.8064	93.7761	7.294E+09
15.7833	23.0056	92.7265	3.229E+09
16.4000	19.8142	92.1188	5.127E+09
17.0000	19.2432	91.9926	6.635E+09
17.6167	21.5712	92.3625	1.045E+10
18.2167	25.8531	93.1856	1.123E+10
18.8333	31.5190	94.5043	6.038E+09
19.4333	37.6009	96.1923	7.364E+09
20.0500	44.2494	98.3396	6.422E+09
20.6500	50.8007	100.7434	9.135E+09
21.2667	57.6487	103.5377	9.868E+09
21.8667	64.3317	106.5192	5.987E+09
22.4833	71.0312	109.7376	5.877E+09
23.0833	77.3202	112.9493	7.387E+09

TABLE A4.8. Millstone Hill Heat Flux Values for 1 April 1986

<u>UT HRS</u>	<u>SZA</u>	<u>CPSZA</u>	<u>HEAT FLUX</u>
0.4333	104.3459	102.4335	1.697E+09
0.8000	108.0629	104.2628	1.477E+09
1.1833	111.8843	106.1226	1.021E+09
1.5667	115.5301	107.8739	9.832E+08
1.9333	118.7716	109.4015	7.744E+08
2.3167	121.9807	110.8847	8.763E+08
2.6833	124.7208	112.1286	7.933E+08
3.0667	127.3013	113.2754	8.354E+08
3.4500	129.4120	114.1999	6.200E+08
3.8167	131.0890	114.9252	6.526E+08
4.2000	132.3085	115.4554	6.813E+08
4.5667	132.9609	115.7490	7.484E+08
4.9667	133.0535	115.8200	6.526E+08
5.3500	132.5504	115.6484	6.136E+08
5.7333	131.5213	115.2597	6.046E+08
6.1000	129.9933	114.6593	5.655E+08
6.4833	128.0132	113.8547	4.332E+08
6.8500	125.6326	112.8552	4.481E+08
7.2333	122.9045	111.6762	5.326E+08
7.6167	119.7811	110.2879	4.259E+08
7.9833	116.6067	108.8433	4.662E+08
8.3667	113.0138	107.1703	4.456E+08
8.7333	109.3556	105.4316	3.245E+08
9.1167	105.4380	103.5392	4.089E+08
9.5500	100.9091	101.3255	3.014E+08
9.9333	96.7738	99.2842	3.954E+08
10.3000	92.8301	97.3304	3.059E+09
10.6833	88.5901	95.2311	2.325E+09
11.0667	84.4553	93.1925	3.520E+09
11.4333	80.3140	91.1653	6.792E+09
11.8167	76.1859	89.1688	5.171E+09
12.1833	72.0918	87.2222	6.305E+09
12.5667	68.0496	85.3373	7.148E+09
12.9500	63.3396	83.4229	1.760E+09
13.3167	60.1054	81.7742	9.781E+09
13.7000	56.2743	80.1384	7.592E+09
14.0833	52.6329	78.6406	1.025E+10
14.7167	47.2216	76.5274	9.216E+09
15.0833	44.5170	75.5287	8.812E+09
15.4667	42.0472	74.6507	8.276E+09
15.8500	40.0820	73.9717	8.316E+09

TABLE A4.8. Millstone Hill Heat Flux Values for 1 April 1986

<u>UT HRS</u>	<u>SZA</u>	<u>CPSZA</u>	<u>HEAT FLUX</u>
16.2167	33.7677	73.5285	8.372E+09
16.6000	37.9979	73.2687	9.499E+09
16.9667	37.9088	73.2280	1.045E+10
17.3500	38.5021	73.4027	1.222E+10
17.7333	39.7079	73.7828	1.220E+10
18.1000	41.4818	74.3634	1.158E+10
18.4833	43.7502	75.1383	1.216E+10
18.8500	46.4337	76.0990	1.193E+10
19.2333	49.4650	77.2328	1.145E+10
19.6167	52.8842	78.5706	1.150E+10
19.9833	56.3090	79.9704	1.216E+10
20.3667	60.1408	81.5960	1.272E+10
20.7333	63.8730	83.2362	1.110E+10
21.1167	67.9517	85.0861	8.564E+09
21.5000	72.2398	87.0853	1.007E+10
21.8667	76.2030	88.9740	8.820E+09
22.2500	80.4512	91.0364	9.318E+09
22.6167	84.4559	93.0062	8.716E+09
23.0000	88.7096	95.1204	6.652E+09
23.3833	92.8120	97.1701	5.010E+09
23.7500	96.8710	99.2023	4.161E+09

TABLE A4.9. Millstone Hill Heat Flux Values for 2 April 1986

<u>UT HRS</u>	<u>SZA</u>	<u>CPSZA</u>	<u>HEAT FLUX</u>
0.1333	100.8637	101.1997	2.975E+09
0.5000	104.7719	103.1449	2.538E+09
0.8833	108.5781	105.0197	2.105E+09
1.2667	112.3550	106.8612	1.652E+09
1.6333	115.8472	108.5391	1.535E+09
2.0167	119.2389	110.1389	1.550E+09
2.3833	122.1875	111.5044	1.212E+09
2.7667	125.0245	112.7946	1.428E+09
3.1333	127.3618	113.8374	1.566E+09
3.9000	131.0542	115.4535	1.754E+09
4.2667	132.0889	115.9078	7.335E+08
5.4000	132.0752	115.9960	1.785E+09
5.7833	130.9060	115.5482	8.811E+08
7.2833	122.0464	111.8169	2.247E+08
8.0333	115.6820	108.9253	3.606E+08
8.4167	112.1763	107.2785	1.085E+05
8.8000	108.3880	105.4675	1.671E+08
9.1667	104.6976	103.6761	3.005E+08
9.5500	100.6586	101.6951	4.354E+08
11.5667	78.5251	90.7794	4.429E+09
11.9333	74.5330	88.8611	3.015E+09
12.3167	70.3239	86.8764	3.804E+09
12.6833	66.4283	85.0808	4.864E+09
13.0667	62.3671	83.2557	8.316E+09
13.4667	58.3103	81.4902	8.276E+09
13.8500	54.5369	79.9087	7.311E+09
14.2167	51.1791	78.5528	7.588E+09
14.6000	47.7616	77.2295	8.276E+09
14.9833	44.7757	76.1227	7.674E+09
15.3500	42.3364	75.2530	8.202E+09
15.7333	40.2087	74.5219	7.012E+09
16.1000	38.7248	74.0224	7.269E+09
16.4833	37.7620	73.7026	8.008E+09
16.8667	37.4832	73.6024	7.764E+09
17.2333	37.8659	73.7088	8.202E+09
17.6167	38.8888	74.0219	9.356E+09
17.9833	40.5018	74.5379	8.564E+09
18.3667	42.6325	75.2512	8.308E+09
19.0167	47.4806	76.9787	1.339E+10
19.4000	50.6597	78.1870	8.144E+09
19.7667	54.0903	79.5500	1.188E+10

TABLE A4.9. Millstone Hill Heat Flux Values for 2 April 1986

<u>UT HRS</u>	<u>SZA</u>	<u>CPSZA</u>	<u>HEAT FLUX</u>
20.1500	57.7238	81.0528	1.193E+10
20.5333	61.6350	82.7336	9.356E+09
20.9000	65.4215	84.4190	9.908E+09
21.2833	69.5493	86.3090	1.085E+10
21.6500	73.4853	88.1593	8.008E+09
22.0333	77.7227	90.1911	8.716E+09
22.4167	81.9828	92.2695	1.028E+10
22.7833	85.9831	94.2479	6.139E+09
23.1667	90.3549	96.4282	4.940E+09
23.5333	94.3124	98.4087	3.071E+09
23.9167	98.4675	100.4913	1.766E+09

TABLE A4.10. Millstone Hill Heat Flux Values for 28 August 1986

<u>UT HRS</u>	<u>SZA</u>	<u>CPSZA</u>	<u>HEAT FLUX</u>
0.0333	96.6640	105.7436	1.260E+09
0.4667	101.0943	108.0071	5.309E+08
0.8000	104.3396	109.6653	6.716E+08
1.0833	107.0307	111.0342	3.888E+08
1.4167	110.1569	112.6200	4.771E+08
1.8667	114.0022	114.5507	1.152E+05
2.0167	115.2435	115.1691	5.293E+08
2.9000	121.5699	118.2765	7.484E+08
3.0500	122.4670	118.7113	3.415E+08
3.3833	124.2415	119.5609	2.021E+08
3.8167	126.0088	120.4050	1.715E+08
4.0000	126.5545	120.6648	2.676E+08
4.4500	127.4814	121.1107	6.368E+07
4.7833	127.6935	121.2212	1.382E+08
5.0667	127.5694	121.1747	1.049E+05
5.4000	127.0418	120.9481	1.549E+08
5.8333	125.7953	120.3885	8.230E+07
6.0000	125.1659	120.0994	7.715E+07
6.6500	121.8393	118.5502	6.897E+07
6.9833	119.6680	117.5152	1.047E+05
7.1167	118.7749	117.0841	1.081E+05
7.4500	116.2453	115.8553	5.329E+07
7.8833	112.7050	114.1069	1.055E+08
8.0500	111.2817	113.3984	3.200E+06
8.3833	108.3274	111.9118	1.298E+08
8.8167	104.2114	109.8252	1.932E+08
9.0000	102.3651	108.8864	1.187E+05
9.4500	97.8649	106.5857	1.160E+05
9.7833	94.3282	104.7780	2.238E+08
10.0667	91.3505	103.2586	1.532E+08
10.4000	87.8256	101.4697	4.847E+08
10.8333	82.9744	99.0338	1.411E+09
11.0167	80.9210	98.0115	2.430E+09
11.4500	76.1476	95.6702	2.808E+09
11.7833	72.3993	93.8705	1.766E+09
12.0667	69.3072	92.4140	4.405E+09
12.4000	65.7227	90.7620	3.979E+09
12.8500	60.7931	88.5651	4.149E+09
13.0000	59.2960	87.9175	7.088E+09
13.3333	55.7418	86.4138	3.520E+09
13.7833	51.2337	84.5920	6.504E+09

TABLE A4.10. Millstone Hill Heat Flux Values for 28 August 1986

<u>UT HRS</u>	<u>SZA</u>	<u>CPSZA</u>	<u>HEAT FLUX</u>
14.0833	48.2808	83.4540	4.911E+09
14.4167	45.2623	82.3354	7.732E+09
14.8667	41.3987	80.9807	8.613E+09
15.0167	40.2187	80.5852	8.605E+09
15.3667	37.7557	79.7831	8.197E+09
15.8000	35.3031	79.0175	5.208E+09
16.1167	34.0012	78.6206	9.909E+09
16.4500	33.1245	78.3524	8.202E+09
16.8833	32.8625	78.2482	9.435E+09
17.0333	33.0037	78.2753	8.346E+09
17.3833	33.7451	78.4545	9.318E+09
17.8167	35.4868	78.9221	9.139E+09
18.0000	36.4878	79.2053	5.760E+09
18.4333	39.2908	80.0423	1.272E+10
18.7667	41.7930	80.8357	5.365E+09
19.0500	44.2511	81.6550	1.021E+10
19.3833	47.3187	82.7314	1.123E+10
19.8333	51.6152	84.3326	7.990E+09
20.0167	53.4967	85.0631	8.596E+09
20.4500	57.9794	86.8775	1.058E+10
20.7833	61.5917	88.4082	1.033E+10
21.2333	66.4134	90.5331	1.150E+10
21.5667	70.0087	92.1723	8.983E+09
22.0000	74.7875	94.4133	8.990E+09
22.3333	78.5412	96.2201	8.564E+09
22.7833	83.4413	98.6245	5.057E+09
23.0833	86.7684	100.2811	2.918E+09
23.4167	90.3169	102.0654	2.905E+09
23.8667	95.2990	104.5908	1.381E+09

TABLE A4.11. Millstone Hill Heat Flux Values for 23 September 1986

<u>UT HRS</u>	<u>SZA</u>	<u>CPSZA</u>	<u>HEAT FLUX</u>
20.9667	71.9276	80.7043	8.983E+09
21.4167	76.7972	83.0273	7.764E+09
21.8667	81.6346	85.3746	8.738E+09
22.3167	86.5274	87.7738	8.202E+09
22.7667	91.5735	90.2603	5.155E+09
23.2167	96.4828	92.6767	4.723E+09
23.6667	101.4784	95.1159	2.385E+09

TABLE A4.12. Millstone Hill Heat Flux Values for 24 September 1986

<u>UT HRS</u>	<u>SZA</u>	<u>CPSZA</u>	<u>HEAT FLUX</u>
0.1167	106.2769	97.4348	3.593E+09
1.0167	115.7330	101.8660	1.081E+09
1.4667	120.0539	103.8120	8.516E+08
1.9167	124.2068	105.6183	5.824E+08
2.3667	127.9044	107.1708	3.258E+08
2.8167	131.1671	108.4912	5.568E+08
3.2833	134.0208	109.6025	3.077E+08
3.7333	136.1131	110.3967	3.060E+08
4.1833	137.3943	110.8770	2.988E+08
4.6333	137.8557	111.0585	2.517E+08
5.0833	137.4258	110.9232	1.382E+08
5.5333	136.1761	110.4852	2.988E+08
5.9833	134.1108	109.7340	1.733E+08
6.0000	134.0480	109.7109	8.211E+07
6.4333	131.4379	108.7205	1.808E+08
6.9000	128.0369	107.3739	1.102E+08
7.3500	124.3555	105.8514	2.270E+08
7.8000	120.2157	104.0691	6.608E+08
8.7000	111.3987	100.0641	1.028E+09
9.6000	101.6865	95.4232	3.888E+08
10.0500	96.6972	92.9770	3.077E+08
10.5000	91.8005	90.5522	1.893E+09
12.7333	67.7163	78.7644	4.191E+09
13.1833	63.2873	76.7010	4.698E+09
13.6333	58.9828	74.7507	9.537E+09
14.0833	54.9943	72.9998	5.512E+09
14.5333	51.4970	71.5123	7.012E+09
14.9833	48.3979	70.2375	8.983E+09
15.4333	45.9657	69.2612	6.484E+09
15.8833	44.2103	68.5672	8.346E+09
16.3333	43.2060	68.1617	8.983E+09
16.7833	43.0605	.0728	5.305E+09
17.2333	43.7758	2965	7.269E+09
17.6833	45.3221	55.8372	6.275E+09
18.1333	47.5493	69.6569	6.383E+09
18.5833	50.4700	70.7806	6.038E+09
19.0333	53.8296	72.1338	8.008E+09
19.4833	57.7032	73.7594	8.812E+09
19.9333	61.8085	75.5537	1.022E+10
20.3833	66.1661	77.5194	1.075E+10
20.8333	70.8421	79.6928	8.935E+09

TABLE A4.12. Millstone Hill Heat Flux Values for 24 September 1986

<u>UT HRS</u>	<u>SZA</u>	<u>CPSZA</u>	<u>HEAT FLUX</u>
21.3000	75.7982	82.0535	8.882E+09
21.7500	80.6088	84.3815	5.417E+09
22.2000	85.6147	86.8319	8.033E+09
22.6500	90.6584	89.3183	5.343E+09
23.1000	95.5717	91.7360	3.967E+09
23.5500	100.5856	94.1904	2.992E+09

TABLE A4.13. Millstone Hill Heat Flux Values for 7 October 1986

<u>UT HRS</u>	<u>SZA</u>	<u>CPSZA</u>	<u>HEAT FLUX</u>
0.3833	113.4514	94.3902	2.490E+09
0.8833	118.7419	96.7552	2.105E+09
1.3667	123.7018	98.8811	1.543E+09
1.8667	128.3691	100.7832	9.405E+08
2.3667	132.7367	102.4728	5.020E+08
2.8667	136.5418	103.8624	2.913E+08
3.3667	139.5492	104.9027	2.335E+08
3.8667	141.7164	105.6264	1.367E+08
4.3667	142.7938	105.9833	2.806E+08
4.8667	142.7000	105.9714	3.617E+08
5.3667	141.3941	105.5786	4.005E+08
5.8667	139.0468	104.8237	3.299E+08
6.3500	135.9771	103.7814	2.565E+08
7.9000	122.4519	98.5415	1.768E+08
8.3833	117.5568	96.4339	4.134E+08
8.8833	112.2337	94.0389	4.797E+08
9.3833	106.6524	91.4330	4.151E+08
9.8833	101.2539	88.8379	4.611E+08
10.3833	95.6980	86.1120	9.118E+08
10.8833	90.1644	83.3563	2.752E+09
11.3833	84.8204	80.6754	3.437E+09
11.8833	79.4559	77.9827	2.788E+09
12.3833	74.2512	75.3848	6.425E+09
12.8833	69.3791	72.9801	5.760E+09
13.3833	64.6760	70.6972	6.541E+09
13.8833	60.2494	68.5938	6.672E+09
14.7000	54.3572	65.8761	5.414E+09
15.2000	51.5145	64.6033	7.806E+09
15.6833	49.5372	63.7250	6.383E+09
16.1833	48.3306	63.1801	9.188E+09
16.6833	48.0809	63.0345	8.564E+09
17.1833	48.7757	63.2812	8.453E+09
17.6833	50.4057	63.9272	1.384E+10
18.1833	52.9442	64.9785	5.093E+09
18.6833	56.0741	66.3250	1.040E+10
19.1833	59.8727	68.0197	1.136E+10
19.6833	64.1557	69.9893	1.048E+10
20.1833	68.7109	72.1438	9.435E+09
20.6833	73.6718	74.5441	9.868E+09
21.1667	78.6123	76.9683	9.727E+09
21.6667	83.9618	79.6221	7.674E+09

TABLE A4.14. Millstone Hill Heat Flux Values for 8 October 1986

<u>UT HRS</u>	<u>SZA</u>	<u>CPSZA</u>	<u>HEAT FLUX</u>
2.5167	134.3531	102.5776	8.993E+08
3.0167	137.8860	103.8378	1.024E+09
3.5000	140.6619	104.7763	7.556E+08
4.0000	142.5022	105.3806	5.638E+08
4.5000	143.2648	105.6348	7.054E+08
5.0000	142.8251	105.5134	5.462E+08
5.5000	141.2672	105.0406	4.662E+08
6.0000	138.6600	104.1997	2.169E+08
6.5000	135.2103	103.0177	1.465E+08
7.0000	131.1118	101.5176	1.421E+08
7.5000	126.5282	99.7297	2.882E+08
8.0000	121.5849	97.6887	1.875E+08
8.4833	116.6310	95.5401	2.510E+08
8.9833	111.2653	93.1102	2.645E+08
9.4833	105.9149	90.5997	2.676E+08
10.2833	97.0167	86.2795	5.145E+08
10.7833	91.6068	83.5908	1.505E+09
11.2833	85.9961	80.7766	2.244E+09
11.7833	80.6167	78.0709	3.804E+09
12.2833	75.5100	75.5116	4.581E+09
12.7833	70.4917	73.0190	6.195E+09
13.2833	65.7417	70.7001	7.178E+09
13.7833	61.4575	68.6431	7.592E+09
14.2667	57.6834	66.8742	8.202E+09
14.7667	54.2780	65.3099	8.346E+09
15.2667	51.5539	64.0796	7.764E+09
15.7667	49.6254	63.2160	9.752E+09
16.2667	48.5934	62.7426	9.356E+09
16.7667	48.5223	62.6685	9.727E+09
17.2667	49.3806	62.9870	1.078E+10
17.7667	51.1598	63.7051	1.038E+10
18.2667	53.7576	64.7986	1.017E+10
18.7667	56.9721	66.1977	9.589E+09
20.4333	71.5933	73.0309	1.050E+10
21.3667	81.0776	77.6996	9.537E+09
21.8667	86.4724	80.3824	9.048E+09
22.3667	91.9700	83.1179	8.346E+09
22.8667	97.3913	85.7931	6.275E+09
23.3667	102.9553	88.5005	4.249E+09
23.8667	108.4841	91.1284	3.705E+09

TABLE A4.15. Millstone Hill Heat Flux Values for 29 October 1986

<u>UT HRS</u>	<u>SZA</u>	<u>CPSZA</u>	<u>HEAT FLUX</u>
14.9500	59.8964	57.1898	7.938E+09
15.4000	58.0068	56.1962	8.008E+09
15.8500	56.6906	55.4963	8.812E+09
16.3000	56.0622	55.1407	1.104E+10
16.7500	56.1060	55.1241	9.537E+09
17.2000	56.8492	55.4589	9.188E+09
17.6500	58.2202	56.1127	7.229E+09
18.1000	60.2422	57.1062	1.021E+10
18.5500	62.7526	58.3636	1.247E+10
19.0000	65.7315	59.8787	1.142E+10
19.4667	69.3015	61.7167	1.328E+10
19.9167	73.1445	63.7139	1.079E+10
20.3667	77.1781	65.8245	8.846E+09
21.0333	83.7685	69.2723	1.025E+10
21.8833	92.4890	73.7876	7.417E+09
22.3333	97.3847	76.2735	5.395E+09
22.7833	102.2317	78.6852	4.112E+09
23.2333	107.2575	81.1231	3.032E+09
23.6833	112.1734	83.4318	2.527E+09

TABLE A.4.16. Millstone Hill Heat Flux Values for 30 October 1986

<u>UT HRS</u>	<u>SZA</u>	<u>CPSZA</u>	<u>HEAT FLUX</u>
1.6833	133.7112	92.3618	1.405E+09
2.1333	138.0058	93.8534	1.495E+09
2.5833	141.9554	95.1267	1.652E+09
3.0333	145.5056	96.1843	1.721E+09
3.4833	148.2994	96.9595	1.690E+09
4.4000	151.1579	97.7111	1.832E+09
4.8500	150.8433	97.6524	1.157E+09
5.3000	149.3723	97.3024	1.208E+09
5.7500	146.8999	96.6685	5.568E+08
6.2000	143.7310	95.7861	1.332E+09
6.6500	140.0036	94.6552	8.197E+08
7.1000	135.7519	93.2541	9.262E+08
7.5500	131.3174	91.6730	8.562E+08
8.0000	126.5614	89.8505	6.608E+08
8.4500	121.7859	87.9036	1.055E+09
8.9000	116.9337	85.8112	9.383E+08
9.3500	111.9087	83.5385	1.011E+09
9.8167	106.6160	81.0423	4.681E+08
10.2667	101.7326	78.6588	9.118E+08
10.7167	96.9013	76.2357	1.116E+09
11.1667	92.0296	73.7367	2.752E+09
11.6167	87.3926	71.3190	3.685E+09
12.0667	82.7862	68.8868	5.760E+09
12.5167	78.4788	66.5960	7.592E+09
12.9667	74.3944	64.4155	8.716E+09
13.4167	70.4837	62.3268	9.135E+09
13.8667	66.9181	60.4246	7.806E+09
14.3167	63.7563	58.7453	1.222E+10
14.7667	61.1346	57.3558	8.065E+09
15.2167	59.0236	56.2411	6.991E+09
15.6667	57.4592	55.4071	8.882E+09
16.1167	56.5659	54.9183	8.772E+09
16.5667	56.3311	54.7615	9.537E+09
17.0167	56.7762	54.9469	8.124E+09
17.4667	57.8688	55.4640	1.054E+10
17.9167	59.6255	56.3248	5.072E+09
18.8500	65.0728	59.0773	7.556E+09
19.3000	68.3282	60.7571	8.091E+09
19.7500	71.9435	62.6390	6.081E+09
20.2000	75.9691	64.7478	4.376E+09
20.6500	80.1476	66.9429	6.010E+09

TABLE A4.16. Millstone Hill Heat Flux Values for 30 October 1986

<u>UT HRS</u>	<u>SZA</u>	<u>CPSZA</u>	<u>HEAT FLUX</u>
21.1000	84.6507	69.3037	3.685E+09
22.4667	99.0622	76.7034	3.275E+09
22.9167	104.0505	79.1665	2.538E+09
23.3667	108.9549	81.5228	1.671E+09
23.8167	113.8706	83.8048	1.906E+09

TABLE A4.17. Millstone Hill Heat Flux Values for 10 December 1986

<u>UT HRS</u>	<u>SZA</u>	<u>CPSZA</u>	<u>HEAT FLUX</u>
15.4167	67.5695	47.1156	1.521E+09
15.8500	66.3226	46.3043	6.383E+09
16.2833	65.6007	45.8182	7.989E+09
16.7333	65.4231	45.6721	6.038E+09
17.1667	65.8039	45.8791	7.387E+09
17.6000	66.7220	46.4234	6.038E+09
18.0333	68.1535	47.2877	7.200E+09
18.4667	70.0688	48.4524	6.953E+09
18.9000	72.4940	49.9253	9.589E+09
19.4167	75.8236	51.9370	1.456E+10
19.8500	79.0039	53.8407	8.372E+09
20.2833	82.4860	55.9005	6.561E+09
20.7167	86.2299	58.0823	9.356E+09
21.1500	90.1989	60.3534	6.139E+09
21.5833	94.3575	62.6813	3.632E+09
22.0167	98.6779	65.0388	2.279E+09
22.4500	103.1357	67.4004	2.876E+09
22.8833	107.8264	69.7998	3.027E+09
23.3333	112.6135	72.1516	2.654E+09
23.7667	117.3342	74.3651	2.005E+09

TABLE A4.18. Millstone Hill Heat Flux Values for 11 December 1986

<u>UT HRS</u>	<u>SZA</u>	<u>CPSZA</u>	<u>HEAT FLUX</u>
0.1833	121.9693	76.4297	1.953E+09
0.6167	126.7511	78.4383	1.616E+09
1.0500	131.5235	80.3115	2.556E+09
1.4833	136.2506	82.0287	1.939E+09
1.9167	140.8935	83.5744	1.202E+09
2.3500	145.3905	84.9314	9.118E+08
2.7833	149.6461	86.0825	1.314E+09
3.2167	153.5212	87.0138	5.571E+08
3.6500	156.8156	87.7184	1.469E+10
4.0833	159.2242	88.1840	1.344E+09
4.5167	160.4117	88.4070	4.771E+08
5.5333	157.6355	87.9622	1.121E+09
5.9667	154.5719	87.3668	1.065E+09
6.4000	150.8437	86.5382	1.081E+09
6.8333	146.6805	85.4855	7.105E+08
7.2833	142.0000	84.1475	2.214E+09
7.7167	137.3907	82.6770	5.192E+08
8.1500	132.6758	81.0253	1.919E+08
8.5833	127.9148	79.2127	3.285E+08
9.0167	123.1373	77.2566	2.546E+08
9.4500	118.3688	75.1761	3.728E+08
9.9000	113.3820	72.8720	3.025E+08
10.3333	108.7133	70.6040	3.448E+08
10.7667	104.1275	68.2790	3.639E+08
11.2000	99.6472	65.9210	1.808E+08
11.6333	95.2994	63.5562	7.689E+08
12.0667	90.9940	61.1458	1.252E+09
12.9500	83.1100	56.5684	3.545E+09
13.3833	79.5903	54.4615	2.423E+09
13.8167	76.3638	52.4978	2.808E+09
14.2500	73.4770	50.7143	4.126E+09
14.6833	70.9701	49.1449	7.674E+09
15.1167	68.8879	47.8247	4.864E+09
15.5667	67.2390	46.7635	5.414E+09
16.0000	66.1196	46.0291	6.635E+09
16.4333	65.5694	45.6494	2.342E+09
16.8667	65.5623	45.6116	6.699E+09
17.3000	66.0997	45.9178	4.850E+09
17.7333	67.1683	46.5580	6.866E+09
18.1667	68.7418	47.5131	1.033E+10
18.6000	70.7864	48.7588	7.806E+09

TABLE A4.18. Millstone Hill Heat Flux Values for 11 December 1986

<u>UT HRS</u>	<u>SZA</u>	<u>CPSZA</u>	<u>HEAT FLUX</u>
18.9333	72.6925	49.9188	5.688E+09
19.7833	78.4228	53.3726	9.188E+09
20.2167	81.9443	55.4638	7.059E+09
20.6667	85.8490	57.7469	5.343E+09
21.1000	89.7910	60.0098	3.316E+09
21.5333	93.9265	62.3329	3.501E+09
21.9667	98.1111	64.6261	3.306E+09
22.4000	102.5467	66.9874	2.646E+09
22.8500	107.3482	69.4564	2.138E+09
23.2833	111.9979	71.7535	2.717E+09
23.7167	116.7123	73.9799	3.520E+09

TABLE A4.19. Millstone Hill Heat Flux Values for 3 June 1987

<u>UT HRS</u>	<u>SZA</u>	<u>CPSZA</u>	<u>HEAT FLUX</u>
0.5000	92.8898	120.0256	4.149E+09
0.9833	97.1435	122.4953	1.267E+09
1.4833	101.2702	124.9406	1.135E+09
1.9667	104.8305	127.0871	1.739E+08
2.4667	108.0368	129.0488	2.193E+08
2.9667	110.7901	130.7558	5.842E+07
3.4500	112.8491	132.0508	1.022E+05
3.9500	114.3584	133.0165	1.035E+05
4.4500	115.1517	133.5454	5.672E+07
4.9500	115.2033	133.6171	1.010E+05
5.4333	114.5357	133.2424	8.853E+06
5.9333	113.1803	132.4435	7.644E+07
6.4333	111.1237	131.2144	1.010E+05
6.9167	108.5889	129.6966	9.419E+07
7.4167	105.3925	127.7877	1.207E+08
8.4167	97.7352	123.2796	5.192E+09
8.9000	93.4187	120.7918	3.754E+08
9.4000	88.7068	118.1297	1.349E+10
9.9000	83.7580	115.4056	2.672E+10
10.4000	78.7352	112.7241	3.087E+10
10.8833	73.5610	110.0590	1.847E+10
11.3833	68.2746	107.4501	2.342E+10
11.8833	62.7780	104.8711	2.744E+10
12.3667	57.4888	102.5299	2.473E+10
12.8667	51.9323	100.2327	3.099E+10
13.3667	46.2823	98.0809	2.400E+10
13.8500	41.1059	96.2841	3.127E+10
14.3500	35.8578	94.6454	2.604E+10
14.8500	31.0265	93.3068	3.716E+10
15.3500	26.5917	92.2278	4.928E+10
15.8333	23.1472	91.4907	5.466E+10
16.3333	20.8012	91.0337	4.405E+10
16.8333	20.2055	90.9086	4.884E+10
17.3333	21.4805	91.1107	4.161E+10
17.8167	24.2794	91.6274	1.488E+10
18.3167	28.2448	92.4750	4.985E+10
18.8000	32.6808	93.5704	2.983E+10
19.3000	37.7520	95.0028	2.224E+10
19.7833	42.8291	96.6195	1.979E+10
20.2833	48.2944	98.5528	1.603E+10
20.7667	53.5753	100.5985	1.702E+10

TABLE A4.19. Millstone Hill Heat Flux Values for 3 June 1987

<u>UT HRS</u>	<u>SZA</u>	<u>CPSZA</u>	<u>HEAT FLUX</u>
21.2667	59.1293	102.9260	1.263E+10
21.7500	64.5333	105.3504	9.453E+09
22.2500	70.0020	107.9524	7.556E+09
22.7333	75.1284	110.5157	1.008E+10
23.2333	80.3708	113.2521	7.126E+09
23.7167	85.2169	115.8749	5.072E+09

TABLE A4.20. Millstone Hill Heat Flux Values for 25 November 1987

<u>UT HRS</u>	<u>SZA</u>	<u>CPSZA</u>	<u>HEAT FLUX</u>
0.0667	120.4038	78.5857	1.997E+09
0.4167	124.2804	80.2376	2.138E+09
0.9333	129.9405	82.5039	2.244E+09
1.1167	131.8548	83.2292	1.879E+09
1.4667	135.6442	84.6004	2.111E+09
2.0167	141.4021	86.5066	6.193E+09
2.5167	146.3712	87.9733	2.843E+09
3.0333	150.9607	89.1730	2.797E+09
3.5667	154.8913	90.0792	3.374E+09
4.0833	157.3708	90.5959	3.180E+09
4.6167	158.1353	90.7627	2.364E+09
5.1500	156.9008	90.5496	2.065E+09
5.6667	153.9846	89.9715	3.451E+09
6.2000	149.8857	89.0381	5.057E+09
6.7167	145.1504	87.7982	5.616E+09
7.2500	139.7331	86.1794	3.545E+09
7.7667	134.1527	84.3040	2.865E+09
8.3000	128.4267	82.1722	2.413E+09
8.8333	122.5005	79.7632	1.359E+09
9.0000	120.6919	78.9897	1.868E+09
9.3500	116.8196	77.2770	1.424E+09
9.8833	111.0469	74.5885	1.069E+09
10.0500	109.1386	73.6665	1.007E+09
10.4000	105.4810	71.8560	1.686E+09
10.9333	99.7869	68.9328	8.081E+08
11.1000	98.0868	68.0369	1.358E+09
11.4500	94.5068	66.1176	2.423E+09
11.9833	89.0922	63.1394	6.139E+09
12.0167	88.8671	63.0140	4.884E+09
12.5000	84.2904	60.4290	1.058E+10
13.0333	79.7008	57.7872	1.068E+10
13.5500	75.6029	55.3883	1.050E+10
14.0833	71.8066	53.1359	1.171E+10
14.6167	68.6630	51.2477	1.285E+10
15.1333	66.2147	49.7598	1.061E+10
15.6667	64.3950	48.6380	6.817E+09
16.1833	63.4265	48.0205	6.932E+09
16.7167	63.2609	47.8771	1.161E+10
17.2333	63.9417	48.2411	1.263E+10

TABLE A4.21. Millstone Hill Heat Flux Values for 3 February 1989

<u>UT HRS</u>	<u>SZA</u>	<u>CPSZA</u>	<u>HEAT FLUX</u>
19.1500	65.8874	55.9324	4.304E+09
19.6000	68.9354	57.5810	1.154E+10
19.9667	71.6505	59.0575	8.716E+09
20.1333	72.9538	59.7669	1.120E+10
20.4833	75.8942	61.3662	1.401E+10
20.8500	79.1118	63.1169	1.311E+10
21.0167	80.6233	63.9357	2.431E+10
21.3833	84.1830	65.8601	1.769E+10
21.8333	88.7023	68.2828	1.895E+10
22.1000	91.4509	69.7391	9.955E+12
22.4667	95.2338	71.7196	2.334E+10
22.9000	99.8412	74.0892	1.081E+10
23.0000	100.9765	74.6640	1.495E+10
23.4500	105.8109	77.0707	5.909E+09
23.8167	109.7969	78.9967	7.488E+09

TABLE A4.22. Millstone Hill Heat Flux Values for 9 May 1989

<u>UT HRS</u>	<u>SZA</u>	<u>CPSZA</u>	<u>HEAT FLUX</u>
14.3000	39.6707	90.0432	2.136E+10
14.7333	35.4889	88.7678	1.045E+10
15.0167	33.0587	88.0809	1.739E+10
15.3833	30.1612	87.3143	1.301E+10
15.8167	27.4611	86.6537	1.094E+10
16.0833	26.2742	86.3792	1.681E+10
16.4667	25.2000	86.1324	1.537E+10
16.9000	25.1158	86.0976	1.690E+10
17.0000	25.2776	86.1286	1.905E+10
17.4333	26.6571	86.4112	1.513E+10
17.8167	28.6643	86.8585	2.431E+10
18.0833	30.4856	87.2938	2.092E+10
18.5167	33.9299	88.1876	1.807E+10
18.9000	37.5133	89.2105	1.776E+10
19.1000	39.4190	89.7906	2.605E+10
19.4667	43.0393	90.9607	2.661E+10
19.9000	47.5471	92.5345	1.945E+10
20.0000	48.6662	92.9446	1.888E+10
20.4500	53.4587	94.7843	1.945E+10
20.8167	57.4236	96.4031	2.136E+10
21.0833	60.3836	97.6648	1.878E+10
21.5333	65.4249	99.9069	1.937E+10
21.9000	69.4225	101.7657	2.125E+10
22.0667	71.2174	102.6230	1.175E+10
22.4333	75.1738	104.5540	1.455E+10
22.8833	80.0942	107.0289	1.017E+10
23.1500	82.9495	108.5008	1.807E+10
23.5167	86.8506	110.5496	9.955E+12
23.9500	91.2422	112.9004	2.153E+10

TABLE A4.23. Millstone Hill Heat Flux Values for 10 May 1989

<u>UT HRS</u>	<u>SZA</u>	<u>CPSZA</u>	<u>HEAT FLUX</u>
0.0667	92.4042	113.5292	1.222E+10
0.5000	96.5911	115.8164	8.487E+09
0.8667	99.9429	117.6695	6.425E+09
1.0333	101.4035	118.4823	3.118E+09
1.4167	104.6999	120.3266	2.860E+09
1.8500	108.1222	122.2521	1.191E+09
2.1167	110.0829	123.3594	2.768E+08
2.4833	112.4954	124.7269	1.613E+09
2.9333	115.0564	126.1821	1.202E+09
3.0333	115.5912	126.4879	2.082E+09
4.0000	119.1171	128.5161	1.286E+09
4.4500	119.8036	128.9358	1.779E+09
4.8167	119.8846	129.0094	1.647E+09
5.0833	119.6755	128.9136	1.074E+09
5.5333	118.8314	128.4850	2.138E+09
5.9000	117.7022	127.8882	2.312E+09
6.0667	117.0203	127.5233	9.757E+08
6.4333	115.3468	126.6212	3.703E+08
6.8833	112.8449	125.2579	1.172E+09
7.1500	111.1124	124.3099	2.570E+09
7.5167	108.4546	122.8485	1.030E+09
7.9667	104.8717	120.8757	6.046E+08
8.0667	104.0948	120.4482	9.955E+12
8.5000	100.3395	118.3871	1.608E+09
8.8667	96.8958	116.5055	5.429E+08
9.0333	95.3384	115.6580	2.556E+09
9.4167	91.5645	113.6213	2.305E+09
9.8500	87.1820	111.2887	1.963E+10
10.1167	84.5121	109.8878	7.294E+09
10.5000	80.4337	107.7829	5.909E+09
10.9333	75.7742	105.4354	8.716E+09
11.0333	74.6274	104.8667	4.518E+09
11.3667	71.0461	103.1246	6.760E+09
11.8000	66.1504	100.8214	9.955E+12
12.0667	63.1758	99.4693	9.955E+12
12.4500	59.0428	97.6582	1.008E+10
12.8833	54.2844	95.6718	9.939E+09
13.1500	51.3562	94.5085	9.172E+09
13.5167	47.4656	93.0363	9.424E+09
13.9667	42.7074	91.3570	9.955E+12
14.0667	41.7547	91.0364	1.609E+10

TABLE A4.23. Millstone Hill Heat Flux Values for 10 May 1989

<u>UT HRS</u>	<u>SZA</u>	<u>CPSZA</u>	<u>HEAT FLUX</u>
14.5000	37.5093	89.6855	9.955E+12
14.8667	34.0966	88.6854	1.008E+10
15.0500	32.6069	88.2741	1.628E+10

TABLE A4.24. Millstone Hill Heat Flux Values for 20 September 1990

<u>UT HRS</u>	<u>SZA</u>	<u>CPSZA</u>	<u>HEAT FLUX</u>
16.3333	41.6960	69.7153	7.126E+09
16.9833	41.7000	69.6658	9.345E+09
17.0000	41.7337	69.6763	1.407E+10
17.7500	44.0119	70.4303	9.172E+09
18.4333	47.8344	71.8143	1.203E+10
19.0833	52.7487	73.7270	1.456E+10
19.8000	59.1968	76.4149	1.120E+10
20.4667	65.6494	79.2731	2.542E+10
21.1333	72.6188	82.5029	4.698E+09
21.8000	79.8395	85.9629	1.030E+10
22.4667	87.1879	89.5569	1.216E+10
23.1167	94.5567	93.1885	2.092E+10
23.8167	102.0955	96.8851	4.072E+09

TABLE A4.25. Millstone Hill Heat Flux Values for 18 December 1990

<u>UT HRS</u>	<u>SZA</u>	<u>CPSZA</u>	<u>HEAT FLUX</u>
13.3667	80.4764	54.4410	2.673E+05
13.8667	76.7937	52.1917	1.685E+05
14.3833	73.3294	50.0370	3.171E+09
15.0167	69.9415	47.8905	4.304E+09
15.5500	67.8060	46.5120	3.025E+09
16.0833	66.4600	45.6231	3.193E+09
16.6333	65.8879	45.2198	5.395E+09
17.1667	66.1750	45.3633	6.484E+09
17.7167	67.3219	46.0525	7.861E+09
18.2500	69.1876	47.1964	9.955E+12
18.7833	71.8745	48.8482	1.025E+10
19.3333	75.2278	50.8984	1.171E+10
19.8667	78.9835	53.1702	9.868E+09
20.4167	83.3884	55.7934	1.123E+10
20.9500	88.1030	58.5441	1.324E+10
21.4833	93.0312	61.3476	1.016E+10
22.0333	98.4564	64.3399	9.706E+09
22.5667	103.9794	67.2732	6.608E+09
23.1167	109.9248	70.2907	7.806E+09